ANALYSIS OF CALCIUM AND HYDROGEN PEROXIDE FREQUENCY RESPONSES IN T CELLS AT SINGLE-CELL RESOLUTION VIA MICROFLUIDIC TRAPS

A Dissertation
Presented to
The Academic Faculty

by

Ariel Seitz Kniss-James

In Partial Fulfillment
of the Requirements for the Degree
Doctor of Philosophy in Biomedical Engineering in the
Wallace H. Coulter Department of Biomedical Engineering

Georgia Institute of Technology
August 2016

ANALYSIS OF CALCIUM AND HYDROGEN PEROXIDE FREQUENCY RESPONSES IN T CELLS AT SINGLE-CELL RESOLUTION VIA MICROFLUIDIC TRAPS

Approved by:

Dr. Melissa L. Kemp, Advisor
Department of Biomedical Engineering
Georgia Institute of Technology and Emory University

Dr. Hang Lu, Advisor
School of Chemical and Biomolecular Engineering
Georgia Institute of Technology

Dr. Eberhard O. Voit
Department of Biomedical Engineering
Georgia Institute of Technology and Emory University

Dr. Cheng Zhu
Department of Biomedical Engineering
Georgia Institute of Technology and Emory University

Dr. Magnus Egerstedt
School of Electrical and Computer Engineering
Georgia Institute of Technology

Dr. Dean P. Jones
Department of Medicine
Emory University

Date Approved: April 18, 2016

To my family

ACKNOWLEDGEMENTS

For their invaluable support and guidance over the past five years, I wish to thank my advisors, Dr. Melissa Kemp and Dr. Hang Lu. I am forever grateful for their investment of time and energy into my development as a scientific researcher and young professional. I would also like to thank my committee members for all of their input and suggestions throughout this process: Dr. Eberhard Voit, Dr. Cheng Zhu, Dr. Magnus Egerstedt, and Dr. Dean Jones. I would also like to thank my financial support through NSF Graduate Research Fellowship Grant DGE-1148903, P.E.O. Scholar Award, NIH Training Grant 32GM105490, NIH R01AI088023, and EBICS.

Finally, it is with my sincerest gratitude that I wish to thank my family and friends for their unwavering support and enthusiasm for all of my endeavors through life. I am fortunate to have such an amazing group of people setting an example of kindness, compassion, and dedication. I hope to exemplify these qualities while never losing sight of all the opportunities I have been given to reach this point in my career.

TABLE OF CONTENTS

LIST OF TABLES

LIST OF FIGURES

LIST OF SYMBOLS AND ABBREVIATIONS

APC	Antigen Presenting Cell
Ca^{2+}	Calcium
CaMKII	Ca^{2+}/Calmodulin-Dependent Protein Kinase II
CD3 mAB	CD3 Monoclonal Antibody
CRAC	Calcium Release-Activated Channels
DAG	Diacylglycerol
ER	Endoplasmic Reticulum
GPx	Glutathione Peroxidase
GSSG	Glutathione Disulfide
GSH	Glutathione
H_2O_2	Hydrogen Peroxide
HIF1α	Hypoxia Inducible Factor 1 α
IP_3	Inositol Triphosphate
IP_3R	IP_3 Receptor
LAT	Linker of Activated T cells
LCK	Lymphocyte-specific Protein Tyrosine Kinase
NFAT	Nuclear Factor of Activated T cells
NF-κB	Nuclear Factor Kappa-light-chain-enhancer of Activated B Cells
ODE	Ordinary Differential Equations
PIP_2	Phosphatidylinositol Biphosphate
PM	Plasma Membrane
ROS	Reactive Oxygen Species
RyR	Ryanodine Receptor
SERCA	Sarco/Endoplasmic Reticulum Ca^{2+} ATPase
smFISH	Small Molecule Fluorescent In Situ Hybridization
SOCE	Store Operated Ca^{2+} Entry
STIM1	Stromal Interaction Molecule 1
TCR	T Cell Receptor
ZAP70	Zeta-chain Associated Protein Kinase 70kDa
$\Delta\Psi_m$	Mitochondrial Membrane Potential

SUMMARY

As a key component of the adaptive immune response, T cell lymphocytes are widely studied but often difficult to isolate and visualize for experimentation with single-cell resolution. Intracellular signaling upon activation of the T cell receptor by antigen presenting cells is necessary for proper immune function. The resulting cytosolic calcium (Ca^{2+}) concentration has been shown to oscillate, differentially encoding downstream transcription factors. Activation also requires the concurrent signaling of hydrogen peroxide (H_2O_2) and Ca^{2+}, with implications on protein and channel functions between these networks. Frequency response analysis, originally developed in control engineering, has been shown to be useful for analyzing biological systems and allows us to probe intracellular Ca^{2+} dynamics in the frequency domain to better investigate the relationship between H_2O_2 and Ca^{2+}. To enable single-cell studies of intracellular T cell signaling dynamics, we first developed computational and microfluidic tools necessary for single-cell trapping, imaging, and analysis. This novel platform provides a systematic approach for analyzing T cell signaling in the frequency domain and is applicable for assessing many biological questions.

Stimulation with oscillatory H_2O_2 solutions identified specific input frequencies that facilitate entrainment of Ca^{2+} signaling. We observed heterogeneous responses of cells upon stimulation with dynamic H_2O_2, illustrating the necessity of single-cell analysis to understand the realm of potential responses and ultimately better identification of diseased states. Jurkat T cells were found to respond robustly to input oscillations of 2.78 mHz frequency, corresponding to a period of 6 minutes. The resulting transfer functions for subpopulations had different characteristics, mainly in the damping

coefficient. This illustrates the potential for high and low responding cells to display different filtering characteristics to H_2O_2 signaling upon T cell activation.

We extended this analysis and switched the input and output signals such that cells were exposed to oscillatory Ca^{2+} solutions and localized intracellular H_2O_2 was measured using two variants of the reporter protein, HyPer. Post-stimulation, cells were fixed and hybridized on-chip with smFISH probes, enabling us to track single-cells from signaling events to the downstream transcriptional response. Differences arise in Ca^{2+} stimulated H_2O_2 dynamics depending on location of the reporter within the cell; we observed a clear reduction in cytoplasmic H_2O_2 levels while mitochondrial H_2O_2 was shown to initially increase. This difference in signaling dynamics suggests different regulatory mechanisms for Ca^{2+}-H_2O_2 crosstalk dependent on subcellular localization. We report the first investigation of the downstream transcriptional response using smFISH analysis following oscillatory stimulation with cytoplasmic Ca^{2+} signaling. These findings uphold our previous results with a natural frequency identified to be approximately 2.78 mHz as our smFISH response was maximal at this frequency, connecting the functional consequence with upstream frequency-based signaling.

In summary, we developed experimental and computational techniques to robustly deliver oscillatory stimulation to cells, monitor the response of various reporters, and automatically analyze these single-cell traces through time, highlighting a previously unexplored domain of Ca^{2+} signaling in T cell lymphocytes. We found a natural frequency of the system in response to H_2O_2 and validated that this dominant frequency encodes the maximal transcriptional response, indicating a functional change for activated T cells. By visualizing the previously uncharacterized H_2O_2 response to Ca^{2+}

stimulation, we found differences in redox environments between the cytoplasm and mitochondria. Overall, through the use of innovative microfluidic platforms, localized reporter proteins, computational models, and frequency response analysis techniques, we were able to perturb Jurkat T cells in an unprecedented fashion, uncovering new insight into the dynamic signaling of Ca^{2+} and H_2O_2.

CHAPTER 1 INTRODUCTION

Immune response to specific pathogens includes the activation of T cell lymphocytes, which will subsequently differentiate into effector cells and secrete specific cytokine panels to help eliminate the identified threat [1]. Ca^{2+} has been shown to increase upon stimulation, with heterogeneous, dynamic, and spatially localized responses seen across a population of cells [2]. With such complex signals, it is difficult to (1) understand the possible responses, and (2) correlate these with downstream effectiveness. Successful T cell activation includes the concurrent signaling of multiple, interconnected molecules such as Ca^{2+} and reactive oxygen species (ROS), yet the spatiotemporal resolution of this signaling has not been fully characterized [3].

ROS such as H_2O_2 and superoxide act as secondary messengers within the cell and are involved in numerous cellular processes such as signal transduction, protein expression, and gene expression [4, 5]. Modification of ROS production and regulation within the cell has been implicated in many diseases such as cancer and autoimmune disorders and thus poses a relevant target to study [6-13]. ROS can be produced in distinct locations within the cell and act locally; yet most studies of ROS production currently consider global averages within the cell. Furthermore, these values are often obtained with techniques that only allow for population averages through time. It has been shown that ROS may tune Ca^{2+} signaling, providing evidence that Ca^{2+} proteins and channels are redox sensitive and modification helps orchestrate the complex behavior [14]. Through the technologies of microfluidics and computational modeling, it is possible to study individual cells through time and elucidate key network features and fundamental phenotypic differences between cells within a population.

This study sought to understand H_2O_2 regulation and the effects of connections with Ca^{2+} during T cell activation with the overarching hypothesis that frequency response analysis provides a novel understanding of the complex signaling network. The main rationale for this work is that single-cell analysis of H_2O_2 production and Ca^{2+} signaling dynamics in T cells will better enable understanding of the realm of potential single-cell responses to give insight into the underlying network of complex regulatory factors.

1.1 Research Objectives and Specific Aims

The main objectives of this research are to further develop and create new computational and microfluidic tools for use in better understanding T cell activation by: (1) developing the experimental and computational framework for dynamically stimulating and subsequently analyzing single-cell signals of intracellular fluorescent reporters, (2) measuring the filter characteristics of Ca^{2+} in response to H_2O_2 using frequency response analysis, and (3) uncovering localized H_2O_2 dynamics in response to oscillatory Ca^{2+} signaling while simultaneously observing the downstream transcriptional response.

To address these research objectives, this dissertation has three specific aims as follows:

Aim 1: Develop computational and microfluidic tools to investigate intracellular T cell Ca^{2+} signaling: This aim sought to develop computational tools for characterizing both a novel microfluidic platform capable of applying robust frequency stimulation to individual T cells and the response of cells to these oscillatory stimuli using small molecule dyes and fluorescent reporter proteins. We created stably transfected Jurkat T

cell lines with a recently developed recombinant protein capable of subcellular localization and H_2O_2 tracking. Utilizing these cells and a previously developed microfluidic device, we show the utility of single-cell analysis techniques and the multitude of responses that exist. Further, we built on this cell trapping microfluidic device and characterized a device capable of dynamic stimulation with oscillatory input signals. The initial creation of the stably transfected cell lines and methods of analysis is reported in Chapter 3. Chapter 4 builds upon a previously developed computational model to systematically interrogate cells *in silico* to elucidate novel underlying protein modifications during T cell signaling. Finally, Chapter 5 discussed two microfluidic devices and the characterization that confirmed our ability to deliver dynamic stimulation and tightly control the cellular environment of T cells with single-cell resolution.

Aim 2: Extract filter characteristics of T cell Ca^{2+} signaling in response to frequency based stimulation with H_2O_2: In this aim we continued to monitor single-cell dynamics through time to more completely characterize the response of Ca^{2+} to H_2O_2 in the frequency domain. To accomplish this, we extended our analysis methods to include a spectral analysis component that highlights frequencies of interest from single-cell traces, enabling an unprecedented view into the frequency domain of Ca^{2+} signaling. We used this data to create Bode plots of the cellular response, which give an indication for cell behavior across multiple frequencies sampled. This visualization enabled comparison both between cells within the population, highlighting heterogeneity, and between different experimental frequencies. We were able to derive transfer function fits to the experimental data and partitioned the data into different subsets to visualize differences in

the resulting systems. We also expanded the computational model from Chapter 4 and created an *in silico* method to perturb the model to reflect experimental conditions. Ultimately, we provide a new view of Ca^{2+} signaling in response to oscillatory stimulation and demonstrate the utility of computationally modeling complex kinetics to begin understanding new aspects of the signaling network. This work is presented in Chapter 6.

Aim 3: Characterize H_2O_2 production and transcriptional response to Ca^{2+} oscillation with single-cell resolution: The goal of this aim was to determine the immediate response of localized H_2O_2 production to Ca^{2+} signaling by exchanging the input and output signals from Aim 2 such that cells received a well characterized, oscillatory pattern of Ca^{2+} signaling while H_2O_2 production was measured. We further developed the microfluidic protocol from Aim 2 to utilize on chip smFISH methods for downstream transcription factor measurement. We found from these experiments a better understanding of the H_2O_2 response to intracellular Ca^{2+} signaling. Using the microfluidic device, we subsequently fixed and hybridized cells on-chip for measurement of downstream transcription factors FOS and HIF1α, which we could then relate to position within the trap to compare data for cells at both timescales post stimulation. With this approach, we gained understanding for multiple levels of regulation within the cell: immediate signaling events encoding downstream regulation of gene expression. This work is highlighted in Chapter 7.

1.2 Significance of Results

T cell signaling involves the orchestration of a myriad of signaling molecules with disease ramifications for temporal or spatial inaccuracies of signaling events [15-19]. Ca^{2+} and H_2O_2, two secondary messengers, have been shown to be important for T cell activation [20, 21], but a clear understanding of their connections is elusive with conventional experimental techniques. Further, Ca^{2+} signaling has been shown to oscillate through time with differential downstream transcriptional activation dependent on the frequency of signaling [22]. Yet these spatiotemporal dynamics have not been explored in a systematic fashion due to technical limitations. Taken together, analysis of this system requires a tunable platform for the delivery of dynamic stimulation coupled with a frequency based spectral analysis counterpart to perturb and analyze cellular responses that give rise to a successful immune response.

Within this work, we develop computational and microfluidic tools to enable a frequency response analysis approach for studying T cell activation, a platform necessary for a more complete understanding of this complex network of signaling molecules. We were able to model the response of Ca^{2+} to H_2O_2, investigating the natural frequency that exists in this signaling connection and ultimately providing models capable of generating future experimental hypotheses. Further, we imaged the response of H_2O_2 production to Ca^{2+} using subcellular localized reporter proteins to examine differences in H_2O_2 response within the cytoplasm and mitochondria, providing a more complete spatiotemporal understanding of the redox environment of Jurkat T cells. Finally, we found that the natural frequency of Ca^{2+} signaling identified in Jurkat T cells also elicited the highest level of transcriptional response by combining signaling studies with

downstream transcriptional information using a single microfluidic device. Taken together, we have highlighted the utility of these complementary experimental and computational approaches in providing additional signaling information and foresee additional applications in analyzing other fundamental signaling pathways. Future work can also build on these platforms with applications in drug screens or better characterization of population heterogeneity that may be responsible for differential disease progression or prognosis.

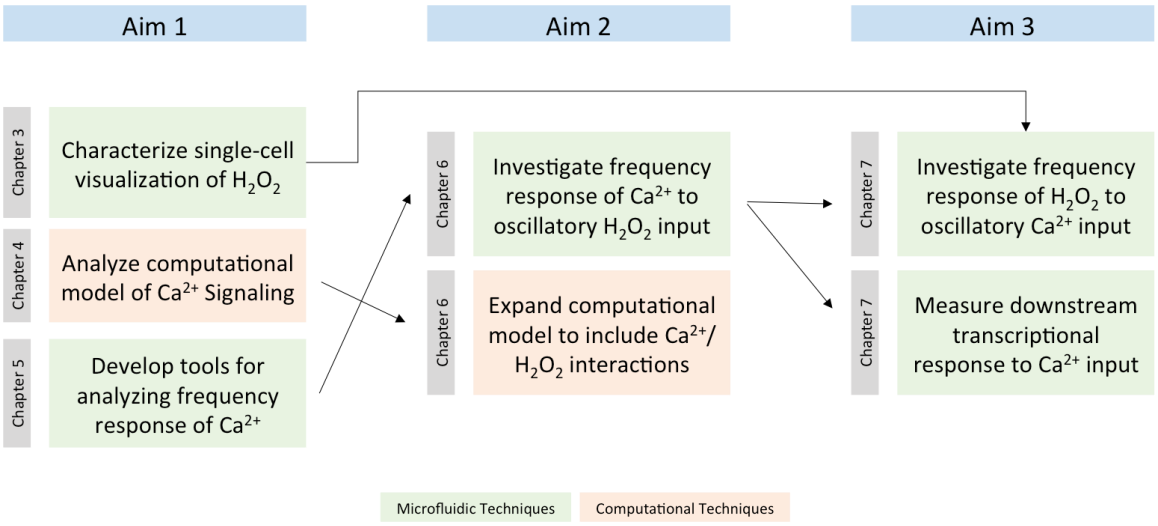

Figure 1-1. Overview of dissertation.

CHAPTER 2 BACKGROUND

2.1 Immune Cells and Diseases

T cell lymphocytes are a part of the adaptive immune response and dysregulation of their activation has been implicated in many diseased states. T cells are characterized by a peptide-recognizing receptor, known as the T cell receptor (TCR), on the plasma membrane. Maturation of T cell occurs in the thymus, and they reside as suspension cells primarily in the bloodstream for activation by antigen presenting cells (APCs) to fight pathogens and to store immunological memory [20, 23, 24]. T cells are classified as a variety of subtypes, each capable of producing a unique cytokine repertoire to fulfill their function within the immune system [25-29]. When T cells are not activated appropriately, it is thought to contribute to the progression of cancer as the aberrant cells are able to avoid death by cytotoxic $CD8^+$ T cells [30]. Dysregulation of $CD4^+$ T cells are also associated with a host of diseases such as asthma [15], allergic reactions [16], autoimmunity [17], lupus [18], and tumor immunity [19].

Activation induces rapid proliferation and a change in signaling cascades to alter gene expression and ultimately cytokine release [20]. More specifically, when an APC engages the TCR, the kinases Lck, LAT, and Zap70 are recruited to the complex to activate phospholipase-Cγ (PLC-γ) [31]. Once phosphorylated, PLC-γ cleaves PIP_2 to generate IP_3, which will then bind to IP_3 Receptors (IP_3R) and release calcium into the cytoplasm [32]. T cell activation is also associated with an increase in glucose metabolism and a subsequent burst of ROS from the mitochondria [20]. Although not completely understood, these molecules work in concert to help orchestrate cell signaling

and the resulting immune functions of T cells following activation. Jurkat T cells were used throughout this dissertation, and experiments were performed on this immortal cell line unless otherwise stated.

2.2 ROS and Calcium as Secondary Messengers

2.2.1 Mitochondria as a Source of ROS

Reactive oxygen species (ROS), such as H_2O_2 and superoxide, have been shown to play critical roles in numerous cellular processes such as signal transduction [4] and homeostatic regulation [5]. Many diseases, such as cancer [6], diabetes [7], aging [8], Alzheimer's disease [9-12], and autoimmune disorders [13], are associated with an abnormally high level of ROS. Mammalian cells generally maintain energy requirements through aerobic respiration, which requires oxygen (O_2) for the biochemical reaction to take place [33]. Oxidative phosphorylation, through the electron transport chain within the mitochondria, is a major source of both H_2O_2 and superoxide with a production rate of approximately 50-500 μmol kg^{-1} min^{-1}, depending on the current metabolic rate of the cell [34].

Superoxide is produced as a by-product of complex III in the electron transport chain and is disproportionated to H_2O_2 through superoxide dismutases (SOD1 or SOD2). Superoxide is unable to diffuse through the membrane, but it has not been conclusively excluded from anion transporters [35]. In contrast to the limited mobility of superoxide, H_2O_2 is able to both diffuse passively through the membrane and be transported through aquaporins [35]. H_2O_2 and superoxide have both been implicated in a multitude of signaling processes such as proliferation, apoptosis, and the cell cycle [36].

2.2.1.1 ROS Signaling in T Cell Activation

Mitochondrial ROS production is necessary for T cell activation both in early stages from NADPH oxidase production [37] and later stages from mitochondrial ROS production [20, 38]. This initial burst of ROS is involved with many cellular processes during T cell activation. H_2O_2 was found in one report to dampen the MEK-ERK activation pathway [39] while in other reports it indirectly induces mitogen-activated protein kinases (MAPK) activation [40]. H_2O_2 treatment of Jurkat cells elicits a response similar to TCR engagement and it was found that protein tyrosine kinase ZAP-70 was phosphorylated in a dose dependent fashion with increasing H_2O_2 concentrations [41]. This activation of ZAP-70 was required for the observed activated ERK response upon H_2O_2 stimulation in T cells [42]. Clear targets of H_2O_2 that have emerged in literature are protein tyrosine phosphatases (PTPs) [43, 44]. PTPs have H_2O_2 sensitive cysteine residues in their catalytic center that inhibits activity upon reaction with H_2O_2 [45]. It is thought that with PTPs inhibited, protein tyrosine kinases (PTKs) are able to remain active during early T cell signaling initiation [45]. There is additional evidence in literature that H_2O_2 may oxidize cysteine residues on PTKs directly. Examples of susceptible PTKs include Src and Lyn, two Src family kinases [46-48]. One of the main technical limitations of measuring these interactions is the low concentration and spatially localized distribution of ROS during T cell activation. Even more confounding are studies that use populations of T cells that, upon isolation from blood, may have small amounts of phagocytes present, which create large amounts of H_2O_2 and can give faulty results for T cell production [49, 50]. Single-cell analysis is imperative for better understanding these interactions.

Oxidative stress is characterized by the imbalance between ROS present within the cell and the cell's ability to consume that ROS or repair the malfunctions associated with ROS [33]. The redox state of the cell is affected through the antioxidant enzyme systems capable of reducing ROS and repairing damage caused by ROS within the cell [51]. A few components of these antioxidant systems are superoxide dismutases, glutathione peroxidases, catalases, and peroxiredoxins. The main reducing equivalent for many intracellular reactions involving these enzymes is NADPH, with the oxidized form of $NADP^+$ [52, 53].

2.2.2 Calcium as a Secondary Messenger

Ca^{2+} is a ubiquitous intracellular secondary messenger that holds a plethora of roles in a diversity of cells. These roles encompass biological processes from conception to death, and are involved in proper maintenance of cells, tissues, and organisms [54-57]. Many examples include excitable cells, such as cardiac or muscle cells, where Ca^{2+} is the driver for contraction of cells [58-60], and neurons for propagation of action potentials [61]. However, Ca^{2+} is also involved with many non-excitable cells, where it can control gene expression and cell death [62]. Ca^{2+} cannot be chemically altered as other complex signaling molecules can, and as a result cells must expend large amounts of energy trying to properly chelate, expel, or localize Ca^{2+} ions within intracellular organelles to coordinate signaling events [55]. Many proteins exist to control calcium signaling and are often found on the plasma or organellular membranes, a position which allows them to gate calcium flux by different activation means, such as voltage, ligand, or a decrease in intracellular storage [55, 63].

2.2.2.1 Calcium Signaling in T Cell Activation

Ca^{2+} is critical for the orchestration of the diverse functionality of immune T cell lymphocytes, such as activation upon antigen recognition, differentiation, proliferation, and death [2, 21, 56, 64]. Within T cells, Ca^{2+} is actively sequestered into the endoplasmic reticulum (ER) until T cell activation triggers its release [2, 64]. When unstimulated, T cells maintain a cytoplasmic Ca^{2+} concentration of ~50-100 nM, which is ~104 fold lower than serum Ca^{2+} concentrations [31]. Through the store-operated Ca^{2+} entry (SOCE) mechanism, the cytoplasmic Ca^{2+} concentration can then rise to ~1 µM [65] from the release of internal stores of Ca^{2+} via protein channels, such as IP_3R, as well as an influx of Ca^{2+} from external sources through CRAC channels [2, 21, 64, 66]. SOCE is thought to be mediated through the endoplasmic reticulum (ER) Ca^{2+} sensing molecule STIM1 and a plasma membrane protein, ORAI1, which is capable of forming pores [2, 64, 67-69]. Following stimulation, the Ca^{2+} concentration can return to the baseline within ~100 sec [65].

2.2.2.2 Oscillatory Calcium Signaling

With such a diverse array of downstream events coordinated with the same upstream Ca^{2+} ion, the field of Ca^{2+} studies is shifting to investigate the temporal and spatial aspects of Ca^{2+} signaling, taking into consideration not only the amplitude of response, but also the temporally varying oscillatory pattern [21, 70]. Such a view of the system helps to determine how specificity can be achieved despite the universality of Ca^{2+} signaling. In other words, specific dynamic signals can be decoded by the cell to interpret what information a particular Ca^{2+} signal is conveying for the appropriate downstream response [71].

The unexpected phenomena of cytoplasmic Ca^{2+} oscillation is thought to be a result of the stochastic distribution of IP_3R within the membrane and the result of calcium flooding the cytoplasm from external sources [72, 73]. This feature of Ca^{2+} signaling profiles illustrates the ability for calcium signals to produce complex signals as opposed to molecules that produce binary state switches [65]. It has been shown that low levels of stimulation results in 5-10 mHz Ca^{2+} oscillations within the T cell [74]. The importance of these oscillations can be seen in studies highlighting differences in activation of specific transcription factors, such as NFAT and NF-κB [22, 32]. It is hypothesized that Ca^{2+} decoding is achieved through the on-off kinetics of Ca^{2+} interactions with kinases and phosphatases [70]. Many proteins are thought to have this capability to decode signals, such as PLC-γ [75, 76], protein kinase Cβ [77], and the mitochondrial calcium uniporter [70, 78]. Yet these molecules will show differences in dependence on frequency, duration of signaling, and duty cycle, demanding technology capable of applying accurate, finely tuned input signals for large screens of Ca^{2+} signaling. Further, with such complex and heterogeneous signaling behavior, analysis techniques are required for determining the response of cells in the frequency domain, a facet of signaling only recently explored for non-excitable biological cells.

2.2.3 Cross-talk Between Calcium and ROS

As Ca^{2+} and ROS molecules are described in isolation above, we now shift to the cross talk between the two signaling molecules. In muscle cells containing both ER and a specialized organelle sarcoplasmic reticulum (SR), ROS is able to activate calcium release channels [79-81]. Furthermore, there are reviews that generalize these interactions to encompass more cell types [82-84].

More specifically, oxidation of both ER membrane channels, IP_3R and RyR, increases the channel activity in early calcium signaling events [85-87]. It has been shown that mitochondrial relocalization occurs during T cell activation, potentially bringing these ROS molecules closer to the area and creating stochastic modulation of the Ca^{2+} release channels [88]. Mitochondria are also noted for their ability to buffer the increase in cytoplasmic Ca^{2+} concentration through the VDAC channel during this translocation [89] and the increase in mitochondrial Ca^{2+} concentration triggers mitochondrial permeability transition pore opening and enhances ROS production [90]. Two other molecules mentioned above, STIM1 and ORAI1, are susceptible to oxidation and may implicate ROS in being responsible for the delay in opening of the CRAC channel [91]. Other channels, such as SERCA [92], [93] and PMCA [94, 95] have also been shown to be affected by ROS through oxidative posttranslational modifications [96].

The molecules STIM1 and ORAI1, part of the SOCE, have conflicting evidence of ROS regulation in the literature. As reported in [97], oxidation is thought to play a positive role in STIM1 signaling as S-glutathionylation of STIM1 is thought to decrease Ca^{2+} binding, leading to constitutive activation of CRAC channels. However, conflicting evidence in [98] suggested a negative role of oxidation through binding of STIM1 to ERp57, the ER oxidoreductase, and ultimately inhibition of SOCE. Similarly, ORAI1 was reported to be both positively [3] and negatively [14] regulated by H_2O_2. It was shown in [3] that ORAI1 is activated in a STIM1 dependent manner after being exposed to H_2O_2, whereas [14] suggests ORAI1 in inhibited by oxidation of Cys195 by H_2O_2. These conflicting reports demonstrate the difficulty in identifying specific roles of molecules during intracellular signaling and highlight the opportunity for a more

mechanistic way of analyzing these events through a systems biology approach of investigating the cross talk between calcium and ROS.

For this project, we used microfluidic platforms to garner single-cell data to be used in conjunction with a computational modeling approach to systematically investigate the frequency dependence of Ca^{2+} signaling to an oscillatory H_2O_2 stimulus. Although interactions are observed between these signaling molecules, most techniques study one facet of studying in isolation, and often utilize end point population assays, such that populations of cells are lysed and analyzed as a bulk measurement. Often, these measurements of ROS cannot be contributed to specific oxidants and provide very little, if any, detail of cellular localization within the cell. Thus, innovative platforms combining technology for single-cell analysis with proper H_2O_2 probes will precipitate novel biological understanding of the connections between signaling molecules with respect to their spatiotemporal dynamics, giving a more complete picture of intracellular T cell signaling and ultimately potential targets for therapeutic use.

2.3 Technology for Analyzing T Cell Signaling

Stochastic fluctuations in gene expression can create differences in protein expression and ultimately in phenotype [99, 100]. Such differences in phenotype can lead to different cell fates [101] or cell functionality [100]. Current techniques, such as flow cytometry, mask the heterogeneity within a population of cells by analyzing populations of cells instead of single-cells. Flow cytometry will measure a single-cell at a given time point, but cannot measure that cell through time, thus preventing the ability to get time course data on single-cells. For adherent cells, it is possible to use high-resolution microscopy through time but this technique is difficult on suspension cells, such as T

cells, which can drift out of the focal plane. To overcome this challenge, we will be utilizing and modifying an existing microfluidic device capable of passively trapping suspension T cells [102]. Once trapped, we are able to collect data that allows for the quantification of signaling network components using a systems biology approach to shed light on the overall system [103].

2.3.1 Microfluidic Techniques

Biological samples can be manipulated on the micron length scale, in volumes in the pL range, with the growing field of microfluidics [104]. Many techniques in microfluidics have introduced their use in studying complex biological systems [105-108] and creating more uniform handling and precise environmental treatment as a result of easily attainable laminar flow conditions on chip [109, 110]. Microfluidic devices for suspension cells have been developed to lyse and analyze cells on chip [111].

Advances in design have led to chips capable of imaging single-cells through time [107, 108], although it was historically more difficult to trap individual suspension cells as they would float and thus not maintain a constant position within the trap. A microfluidic device was previously developed in a collaboration with our lab that is capable of trapping up to 4000 individual T cells in 8 different chambers through passive hydrodynamic focusing [102]. Once loaded, these T cells can be imaged through time using an epifluorescent microscope [102, 112]. The 8 cell traps can be placed downstream other device features such as a linear serial dilution generator creating different solute concentrations while maintaining an internal control for flow rate on chip [113]. However, applying dynamic stimulation is thwarted from high residence time of solutes traveling to the chambers due to the limitation of shear stress on the cells. This

high residence time allows the solutes to diffuse and not maintain the plug like delivery of dynamic soluble cues. Other microfluidic devices are capable of delivering tunable stimulation profiles to adherent cells due to the higher allowable flow rate [114, 115].

2.3.2 Computational Modeling Techniques

As previously mentioned, cells are constantly collecting and reviewing information from their external environment to be processed through a set of connected intracellular signaling networks, ultimately resulting in phenotypic changes when deemed necessary by the cell. In other words, cells receive these inputs from a variety of sources and cells constantly review them to produce appropriate outputs. Complicating factors of this system are nonlinear, stochastic, and redundant properties of signaling pathways [116]. It is thought that although there are hundreds of reactions within a given signaling network, only a few of them drive system dynamics although it is difficult to ascertain which ones. Many models have attempted to account for all known reactions, but are only occasionally successful [117-119]. This approach is often hindered from missing parameters or interactions [117]. Control-based computational models have been developed to try to unveil complex interconnected networks of signaling molecules to identify and model only dominant interactions within the network by characterizing the behavior of a system to its response to sinusoidal inputs.

Frequency response models exist for the osmotic stress response in *S. cerevisiae*, in which simulated oscillations were delivered to the organism and amplitude and phase responses were measured [117]. Another model of *S. cerevisiae* focused on the galactose response pathway and discovered a previously unknown level of regulation by using periodic changes in carbon source to drive changes in gene regulation [120]. Other

frequency response models have focused on *E. coli* and the chemotactic response to varying environmental stimuli and the interaction between signaling modules [121]. The key to these control theory based modeling approaches comes in the experimental design in which techniques were developed to deliver these time varying stimuli [116]. These platforms require the ability to finely tune dynamic stimulation while enabling time course measurement of fluorescent reporter proteins of interest. Current techniques do not allow this manipulation for suspension T cells without first binding cells to the coverslip, an action that could render signaling alterations. To overcome these experimental limitations, I present the techniques developed in our lab to deliver robust, tunable dynamic stimulation to suspension cells *in vitro* and the subsequent analysis that reveals Ca^{2+} signals encoded in the frequency domain.

2.4 Motivations for Research

Cells are continuously integrating dynamic environmental cues and altering their signaling pathways to reflect the environment. Many current biological techniques involve bolus addition of stimulants, resulting in a single step concentration profile change. New techniques, founded in control theory engineering, seek to deliver dynamic stimulations, to observe a phenomenon of interest in the frequency domain. This approach seeks to interrogate complex signaling environments in an unprecedented fashion to ultimately better understand dominant pathways within intracellular networks. While experimental protocols exist for frequency response analysis in particular model organisms and cell systems, a technique has not previously been developed for suspension cells with low shear stress capable of being paired with time-lapse fluorescent microscopy. The *innovation* of this research comes with the concerted efforts of

microfluidics, frequency response analysis, computational analysis techniques, such as modeling and single-cell analysis, and fluorescent reporters within T cells for Ca^{2+} and H_2O_2. These new experimental and computational approaches lead to the *significance* of the research in further advancing the understanding of T cell activation and the role of Ca^{2+} and H_2O_2 interplay, potentially highlighting or predicting therapeutic targets to explore in future studies. This dissertation seeks to expand the applicability of frequency response analysis by introducing a microfluidic device capable of delivering robust, easily tunable dynamic stimulation profiles and collecting single-cell T cell data through time using fluorescent microscopy.

The frequency response analysis platform created was then utilized to combine signaling response with downstream transcriptional outcome to oscillatory Ca^{2+} stimulation; illuminating downstream effects of these encoded oscillatory Ca^{2+} signals. Overall, we sought to explore the connections between Ca^{2+} and H_2O_2 in intracellular T cell signaling by utilizing dynamic, oscillatory perturbations and subsequent spectral analysis. We highlight previously uncharacterized filter characteristics of the system with an innovative platform combining microfluidics and computational approaches for data analysis and modeling. Further, we combine a recently developed H_2O_2 sensor with our platform to demonstrate the universality of the platform to different applications while furthering our understanding of H_2O_2 signaling in response to Ca^{2+} oscillations. Finally, we again utilize the device to connect downstream transcriptional responses to upstream signaling using smFISH for single-cell mRNA transcript counts. Taken together, this dissertation represents advancement in the technological tools necessary for a frequency

response analysis approach for capturing single-cell dynamics and computational methods for a more systematic method to address complex biological questions.

.

CHAPTER 3 SINGLE-CELL ANALYSES AND OBSERVED HETEROGENEITY OF REDOX SIGNALING IN RESPONSE TO ANTIMYCIN A

This chapter was adapted from Kniss, A., et al., A microfluidic systems biology approach for live single-cell mitochondrial ROS imaging. Methods Enzymol, 2013. 526: p. 219-30. [112]

3.1 Introduction

Reactive oxygen species (ROS), such as hydrogen peroxide and superoxide, have critical roles in numerous cellular processes including signal transduction and have been found to be abnormally high in many diseases such as cancer [6] and autoimmune disorders [13]. A major source of ROS is the electron transport chain in the mitochondria, which produces superoxide and hydrogen peroxide. It has been estimated that mitochondrial respiration accounts for 50-500 μmol kg^{-1} min^{-1} cellular ROS, depending upon the metabolic rate of the cell [34].

Two ROS produced in the mitochondria are superoxide and hydrogen peroxide. Superoxide is generated in the mitochondria as a by-product of complex III in the electron transport chain (Figure 3-1) and can be disproportionated to H_2O_2 via manganese superoxide dismutase (MnSOD1 or SOD2) [122, 123].

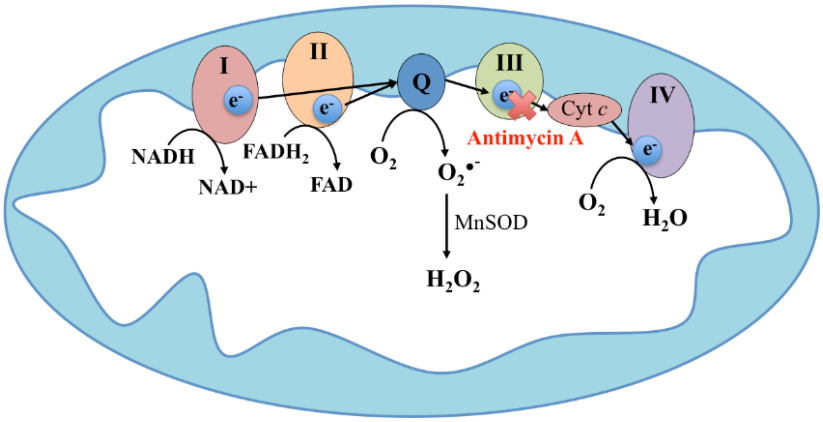

Figure 3-1: Schematic of mitochondrial ROS production.
The electron transport chain is composed of four main complexes that allow electrons to be transferred, driving ATP production. Superoxide is a by-product of respiration and can be disproportionated to hydrogen peroxide via SOD2. Antimycin A is a complex III inhibitor shown to increase the rate of production of mitochondrial ROS by inhibiting the flow of electrons to cytochrome c.

H_2O_2 can both diffuse through the mitochondrial membrane and be transported via aquaporins [35, 124-126]. Although superoxide cannot diffuse through the membrane, transport has not been definitively excluded from anion transporters. They are both implicated in different signaling processes, such as proliferation, apoptosis, and the cell cycle [36]. Fluorescent indicators exist for both reactive oxygen species. MitoSOX is an irreversible small molecule dye capable of localizing to the mitochondria and fluorescing upon oxidation by superoxide. This dye is commonly used as it is well studied and shows exclusive sensitivity to superoxide with 4 x 10^6 $M^{-1}s^{-1}$ as the rate-limiting step of oxidation by superoxide [127, 128]. H_2O_2 has historically been more difficult to image with controversy surrounding H_2DCF-DA measurements [129]. The recombinant protein, HyPer, has been developed from cpYFP and Oxy-R and is capable of changing conformation upon oxidation by H_2O_2 [130-132]. Once transfected into cells,

the reporter protein is capable of providing ratiometric measurements with the correct microscope set-up with two excitation filters and one emission filter [130-132].

Stochastic fluctuations in transcriptional and translational regulators within a cell are now considered influential to differences in cell behavior [99, 133, 134]. Such differences can be masked by techniques that analyze populations of cells instead of single-cells. For instance, flow cytometry analyzes individual cells at single time points but cannot track a single-cell through multiple time points. With single time point measurements, kinetic differences between individual cells in the response to a stimulus are not observed. High magnification imaging through time can address this problem for adherent cells, but for T cells and other suspension cells, this can be difficult as the cells may drift out of the focal plane. Advances in microfluidic design offer an alternative approach to studying these differences by i) passively trapping and analyzing the fluorescence of cells through time [102] and ii) allowing quantification of components of signaling networks within a single-cell and then applying these findings to an overall system [103].

The ability to track individual cells through time will lead to a more complete understanding of redox signaling and ultimately more insight into diseased states. In this chapter, we discuss methods for utilizing microfluidics to analyze mitochondrial superoxide and H_2O_2 responses to an oxidative stimulant, antimycin A, among single-cells in a high-throughput manner. While our analysis is limited to one reporter molecule at a time, ultimately other fluorescent measurements can simultaneously be performed in multicolor live imaging microscopy (e.g. calcium, pH, mitochondrial membrane

potential, etc.) to provide insight in how variations in mitochondrial function influences behavior across an array of cells.

3.2 Materials and Methods

3.2.1 Microfluidic Platform

3.2.1.1 Densely Arrayed Single-cell Trapping Device

A previously developed microfluidic device was utilized for imaging mitochondrial ROS production in the Jurkat T cell line through time [102]. This high-throughput single-cell trapping device has the capability to hold approximately 4000 total cells in eight different trap arrays [102]. Each array contains 25 traps per row and 20 rows. The device is compatible with any mode of optical microscopy, so imaging can be done at different magnifications and, with a motorized stage, multiple chambers can be imaged within seconds (Figure 3-2). The traps can also be placed downstream of different microfluidic platforms, allowing for different stimulus conditions. In this study, a linear serial dilution generator [113] was used upstream to create a range of stimulus concentrations while simultaneously maintaining consistency in flow rate, dye loading, etc. between chambers containing cells from the same cultured population.

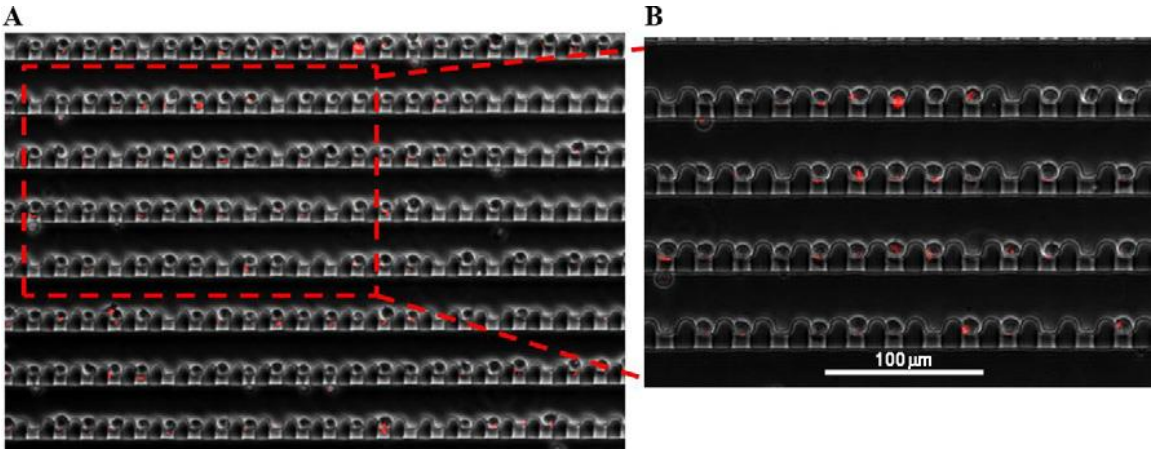

Figure 3-2: Device loaded with cells.
Single-cell analysis of mitochondrial superoxide production using MitoSOX Red Mitochondrial Superoxide Indicator (Invitrogen) dye in microfluidic cell traps. (A) 10x view of approximately 160 single-cell traps with MitoSOX labeled Jurkat cells. (B) 20x view of traps.

3.2.1.2 Device Preparation

Devices were molded in a polydimethylsiloxane (PDMS) A and B mixture of 10:1 using a SU-8 master mold developed in previously described methods [102]. Devices were cut and holes were punched using a 19-gauge needle. The prepared devices were bonded via oxygen plasma to a 1 mm glass slide for imaging and polyethylene (PE3) tubing (Scientific Commodities) was used for all connections with solutions. Initially, the device was primed with a 2% bovine serum albumin (BSA) in PBS solution. This removes any air bubbles from the channels and prevents unintentional cell adhesion to the walls or glass slide. Once primed, the cells were loaded at a concentration of 4 x 10^6 cells/mL using gravity flow and the optimized flow rate of ~ 2 µL/hour found previously was used for all treatments [102].

3.2.2 Microscope System and Image Analysis

3.2.2.1 Microscope Setup

Once bonded to a glass slide, the cell trap device is placed on a 37°C heated stage and imaged using a Nikon Eclipse Ti inverted epifluorescent microscope (Figure 3-3). Inlet tubing for flow of buffer and/or stimulus was set approximately 40 cm above the outlet tubing to allow for a gravity-based pressure-driven flow of liquid through the chip. Time-lapse microscopy was performed on an automated stage with a 0.7 s delay between imaging the separate chambers with an exposure time of 900 ms. Images were collected every 30 s for 70 minutes. All images within a given video were set to the same look-up tables (LUTs) to avoid digital differences between images during image analysis.

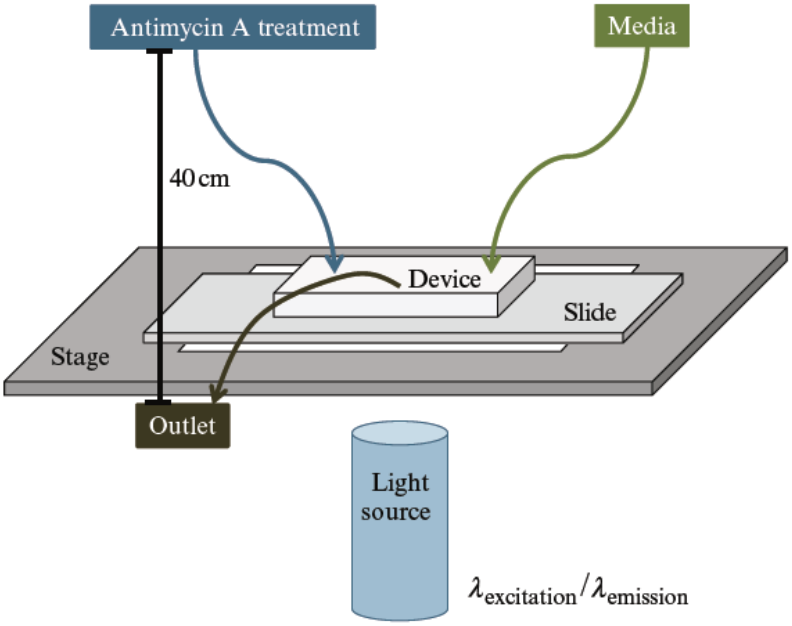

Figure 3-3: Device position with respect to microscope.
Device is plasma bonded to a glass slide with tubing connections to treatment solutions and outlet. Slide is placed on a motorized stage set to 37°C. Filter cubes are utilized for appropriate excitation and emission wavelengths.

3.2.2.2 Image Analysis

MATLAB® (MathWorks) scripts were written and utilized for image analysis of the time-lapse videos. The fluorescent image was converted to a binary image to identify the fluorescent cells in the trap array. To ensure cells present during the entire experiment were selected, both the first and last images were converted to a binary image using a MATLAB® built-in global threshold function, "graythresh". Next, manual selection was performed to select the cell areas to analyze, based on presence in both the first and last binary images. The mean fluorescence was then calculated for each region of interest. To remove differences in background fluorescence between frames, the average fluorescence of a non-occupied portion of the trap was calculated and subtracted from each region of interest at each time point. This ensures differences in intensities were less reliant on

background noise. To normalize each cell individually, measurements are divided by the first mean intensity for that region of interest.

3.2.3 Cellular Conditions

3.2.3.1 Cell Culture

The Jurkat E6-1 human acute T cell lymphoma cell line (American Type Culture Collection) was cultured at 37°C in a humidified 5% CO2 incubator in RPMI 1640 Medium without Phenol Red and with L-glutamine (Sigma-Aldrich), with 10 mM HEPES buffer, 1 mM sodium pyruvate, 100 units/mL penicillin-streptomycin (Cellgro), 1x MEM Non-Essential Amino Acids, and 10% fetal bovine serum (Sigma-Aldrich).

3.2.3.2 MitoSOX Treatment

To visualize the presence of mitochondrial superoxide, Jurkat cells were incubated with 5 μM MitoSOX Red Mitochondrial Superoxide Indicator (Invitrogen) for 10 minutes at 37°C, according to previous protocols [127]. Following incubation, cells were washed three times with 4°C sterile phosphate-buffered saline (PBS) and resuspended in 250 μL RPMI Phenol Red-free media to be loaded in the device at a final concentration of 4 x 10^6 cells/mL. Once loaded in the device, cells were imaged using the TRITC (540/605 nm) filter cube (Nikon) and stimulated with antimycin A (Sigma-Aldrich) at various concentrations. Individual cells were tracked through time and a heat map ("imagesc") was created to visualize the change in intensity, related to change in mitochondrial superoxide production, through time.

3.2.3.3 Stable Transfection of Jurkat Cell Line with HyPer Plasmid

To visualize the dynamics of mitochondrial H_2O_2 through time, the pHyPer-dMito plasmid (Evrogen) was transfected into Jurkat cells using the Neon Transfection System (Life Technologies). Jurkat cells were cultured until logarithmic growth was observed and then washed in PBS without Ca^{2+} and Mg^{2+}.

Cells are resuspended in Resuspension Buffer R (Invitrogen Neon Kit) at a final concentration of 1 x 10^7 cells/mL with 10 μg DNA per 100 μL transfection. Four 100 μL transfections were completed using the Neon protocol of 3 pulses of 1325 V with a 10 ms pulse width. Once transfected, cells were cultured for 3 days without antibiotics. Selection was completed using the neomycin resistant gene on the pHyPer-dMito plasmid. On day 4, 1.4 mg/mL active neomycin (G418) (KSE Scientific) was added to the media with a cell concentration of approximately 0.2 x 10^6 cells/mL. The selection was continued for 14 days with washing and addition of fresh media and antibiotics every 3 days, maintaining the cell concentration between 0.2-0.6 x 10^6 cells/mL. The concentration of G418 was calibrated via a cytotoxicity curve with the same lot of G418 (KSE Scientific) using the reported active concentration. Following selection, a maintenance concentration of 0.6 mg/mL G418 was continued in cell culture. Cells were loaded into the device at a concentration of 4 x 10^6 cells/mL. Once sufficiently loaded, antimycin A (Sigma-Aldrich) was introduced at various concentrations. Cells were imaged using the QMAX GR TE-10 filter set (Omega Optical), as recommended by Evrogen for non-ratiometric imaging of the Hyper reporter protein. The filter set for excitation between 450-490 nm and emission filter at 535 nm primarily represents the oxidized form of the mitochondrial H_2O_2 sensor, HyPer-Mito.

3.3 Results

3.3.1 Imaging Mitochondrial Superoxide Production

Within a chamber with uniform antimycin A concentration, we observed individual cellular differences in mitochondrial superoxide production (Figure 3-4). With an irreversible dye, a monotonic increase is expected over the 70 min experiment. In several instances, lower fluorescence was observed with time; this may be due to rotation of the trapped cell with respect to the focal plane of imaging, photo bleaching of the dye, or inaccuracies in creation of the binary images. On average, we observed an increase in MitoSOX Red oxidation with increasing antimycin A concentration (Figure 3-4 a,c) as well as the number of cells that respond to the stimulatory condition as defined by an increase greater than 40% the original fluorescence. In the example shown, there were 7 responsive cells in the 1.6 μM inhibitor treatment compared to 16 responsive cells in the 50 μM inhibitor concentration.

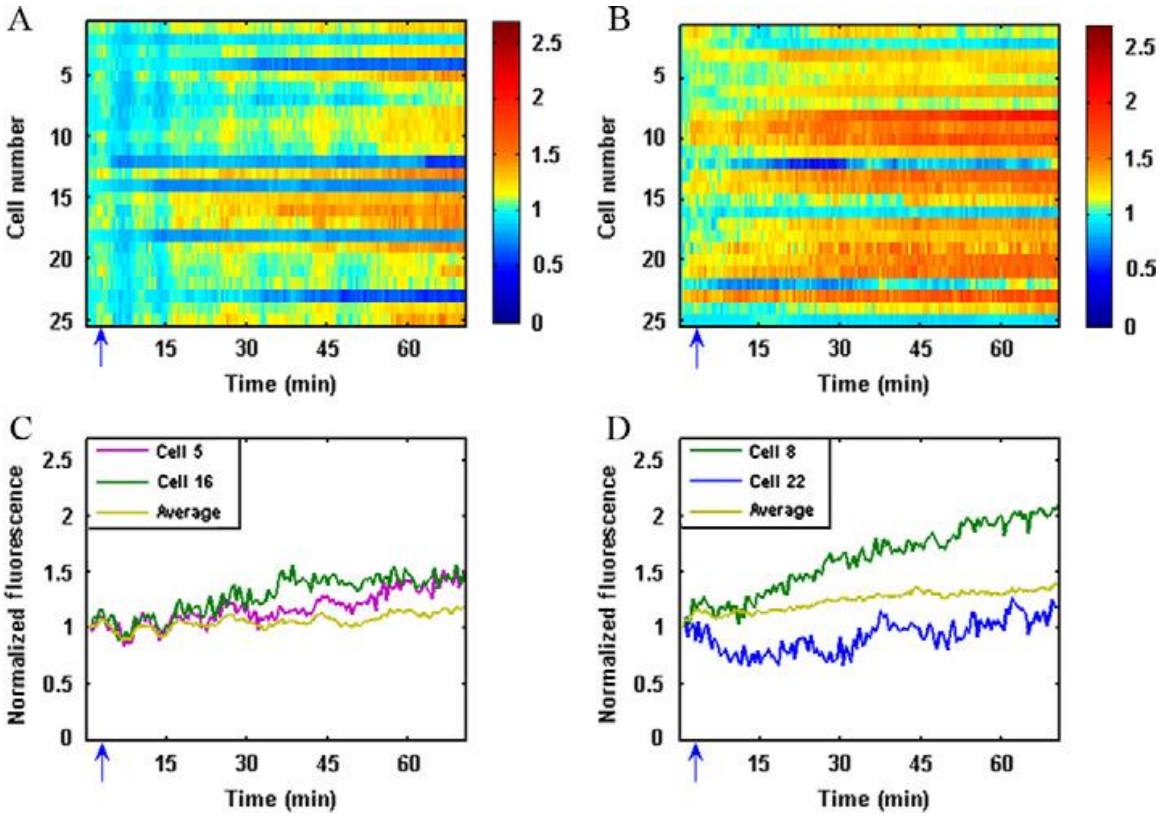

Figure 3-4: Mitochondrial superoxide production with antimycin A stimulation.
(A, C) 1.6 µM antimycin A treated cells (blue arrow). (C, D) 50 µM antimycin A treated cells (blue arrow). (A, B) Heat map of normalized mean fluorescence of 25 analyzed cells through time. (C, D) Average and single-cell traces of mean fluorescence.

3.3.2 Imaging Mitochondrial Hydrogen Peroxide Production

Images were collected over the course of 70 min and reveal differences in H_2O_2 signaling between different cells under the same antimycin A concentration (Figure 3-5). As with the MitoSOX Red, we observed an increase in fluorescence intensity associated with oxidized HyPer-Mito as the concentration of antimycin A increased (Figure 3-5 a,c). With a reversible ROS reporter, however, the observed kinetics were more diverse at the single-cell level. At the 1.6 µM inhibitor concentration, the cells that respond tend to do so similarly in a steadily increasing manner (Figure 3-5 a,c), whereas cells at the 50 µM concentration vary in both the time to respond, and whether the H_2O_2 is sustained or changes with time.

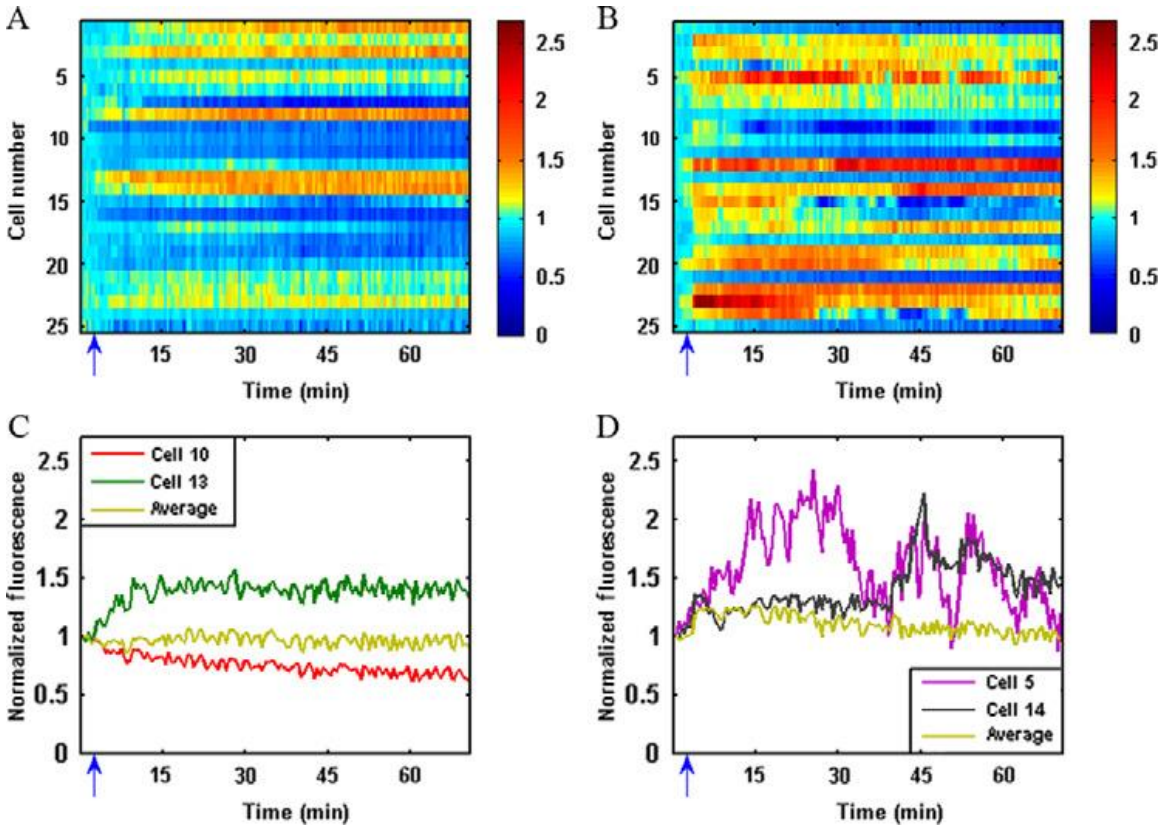

Figure 3-5: Mitochondrial hydrogen peroxide production with antimycin A stimulation. (A, C) 1.6 µM antimycin A treated cells (blue arrow). (C, D) 50 µM antimycin A treated cells (blue arrow). (A, B) Heat map of normalized mean fluorescence of 25 analyzed cells through time. (C, D) Average and single-cell traces of mean fluorescence.

Differences can also be seen in the number of cells to respond, as defined by a 40% change from baseline. In the example shown, there were 5 responsive cells in the 1.6 µM inhibitor treatment compared to 12 responsive cells in the 50 µM inhibitor concentration. The quantity of cells responding was lower than that observed with MitoSOX.

3.4 Discussion

We have demonstrated the potential to use microfluidics to study time-dependent changes of two different mitochondrial ROS in single-cells, thus supporting redox systems biology at the level of single-cells. Further, we provide the ability to study

heterogeneity of these processes in different cells within a population. We report that cells exposed to the same concentration of stimulus exhibited variation in mitochondrial ROS production, which could ultimately result in different cellular responses. This variation could be the result of stochastic processes within the cell, such as transcriptional or translational regulation of key components of the mitochondrial ROS pathway. Additionally, the nature of the responses differed between O_2^- and H_2O_2 kinetics. Because two different types of fluorescent reporters (irreversible small molecule vs. YFP-fusion protein) were used, it is difficult to ascertain without further analysis whether variation at the single-cell level is attributed to properties of the reporter or due to subcellular concentrations of the respective ROS. To our knowledge, this is the first description of the use of microfluidics to image and quantify single-cell redox states in mammalian T cells, a method that may help elucidate underlying dysfunctions in different cell types and diseases. Accounting for distributions of mitochondrial redox state within populations of cells will ultimately allow for a better understanding of signaling processes associated with diseases that implicate mitochondrial dysfunction, such as Alzheimer's disease [9], autoimmune disorders [135], and cancer [6].

CHAPTER 4 COMPUTATIONAL MODELING OF AGE DEPENDENT DIFFERENTIAL INTRACELLULAR CALCIUM SIGNALING DURING T CELL ACTIVATION

4.1 Introduction

4.1.1 T Cell Activation and Immunosenescence

There are two facets of the immune system in humans with over 1600 genes involved in regulation: the innate and adaptive response [136, 137]. Innate immunity is the first defense mechanism against pathogens and is comprised of many cell types, such as dendritic cells, macrophages, and neutrophils [136, 138]. Innate immunity becomes activated through an inflammatory response and, if unable to control and eradicate an infection, contributes to the activation of the adaptive immune response [138]. During the adaptive immune system stimulation, T cells become activated by antigen presenting cells (APCs), such as dendritic cells, which help to inform the adaptive immune system of the pathogenic threat [139, 140].

APCs ligate and activate the TCR via peptide presentation on the major histocompatibility complex (MHC) [141]. TCR ligation provokes the activation of tyrosine kinases and ultimately the phosphorylation of PLC-γ [142, 143]. PLC-γ cleaves phosphatidylinositol 4,5-bisphosphate (PIP_2), present on the plasma membrane, to form IP_3 and DAG. IP_3 binds to IP_3R on the ER membrane to rapidly release Ca^{2+} from intracellular ER stores and store-operated Ca^{2+} entry (SOCE) channels on the plasma membrane enable a sustained calcium response, ultimately dictating gene expression and T cell function [54]. SOCE channel activation is dependent on STIM1, an ER Ca^{2+}

sensing molecule and its partner, ORAI1, which is a pore-forming plasma membrane protein [144]. Together, these molecules activate SOCE via CRAC channels on the plasma membrane [2, 69].

Immunosenescence encompasses the age-related alterations within the immune system that result in a less effective immune response in elderly individuals [145, 146]. Most notably, these changes include a reduction in naïve peripheral T cells from 3×10^9 to 7×10^8 as well as a decrease in repertoire diversity by two orders of magnitude [145, 147, 148]. In addition to the number of cells, T cell function also declines with age leaving elderly individuals with fewer and less effective T cells at warding off cancer, infections, and autoimmune disorders [149, 150]. It has been shown that T cells undergo a redox shift upon activation with CD28 with decreased levels of reduced glutathione and increased reactive oxygen species (ROS) production [4, 151], which may upregulate TNFα [152]. Another redox protein, thioredoxin, has been shown to be differentially regulated, based on age, and is involved with redox pathways within T cells [153]. T cell responses are attenuated in elderly individuals, potentially due to low but persistent levels of pro-inflammatory cytokines and increased ROS production [154-159]. Ultimately, the underlying mechanisms of T cell functional decline have not been fully elucidated, but studies confirm development of defects in Ca^{2+} signaling in response to mitogenic stimulation during immunosenescence [160, 161]. Many proximal events in TCR signaling or cytokine responses are differentially regulated with age, such as reduced protein tyrosine kinase activation, ultimately reducing Ca^{2+} signaling and subsequent NF-κB and NF-AT levels [23, 145, 152, 154, 156]. $CD8^+$ T cells from aged mice are shown to have a diminished activation-induced Ca^{2+} flux [162, 163], and this was mirrored in

$CD4^+$ T cells in elderly humans [164, 165], but $CD8^+$ T cells from elderly humans showed a significantly greater Ca^{2+} response upon activation with CD3 mAB [166]. Interestingly, the proliferation response of activation between elderly and younger donors showed no difference in $CD4^+$ T cells and a reduction in $CD8^+$ T cells in elderly humans, suggesting the reduced proliferation in $CD8^+$ T cells does not contribute to the decrease in Ca^{2+} signaling function [166]. Due to the complexity of signaling events and plethora of data suggesting changes in aging T cells, computational modeling was used to provide new experimentally testable predictions.

4.1.2 ODE Mechanistic Models of T Cell Activation

Due to the universality of Ca^{2+} signaling in numerous cell types, there is a substantial body of literature available for modeling Ca^{2+} dynamics. Ca^{2+} signaling is often described via models in excitable cells, most notably neurons [167-171], cardiomyocytes [172-181], and muscle cells [182-185]. Ca^{2+} signaling, specifically during T cell activation, is less often modeled. Two deterministic models have been published describing Ca^{2+} kinetics in Jurkat [186] and murine T cells [187], but these models do not include extracellular space or mitochondrial Ca^{2+} buffering and the complex protein interactions of SOCE. Maurya *et al.* introduced a more detailed mechanistic model of Ca^{2+} signaling in immune cells that is capable of predicting Ca^{2+} concentration temporal profiles in RAW 264.7 macrophages for different stimulation and network alterations [188, 189].

Previous experimental work in our lab has used an *in vitro* aging framework for $CD8^+$ T cells to unveil decreased protein phosphorylation after TCR ligation [160, 190-193]. It was hypothesized, based on *in vivo* data and the finding of decreased protein phosphorylation, that Ca^{2+} signaling would be reduced in older T cells. Instead, our lab

observed both a faster Ca^{2+} rise and subsequent decay as T cells aged. After gene expression analysis by RT-qPCR revealed overexpression of the plasma membrane CRAC channel, ORAI1, and PMCA in older T cells, we adapted the Maurya model [188, 189] to include additional details to determine if these changes were sufficient to explain the differences in the Ca^{2+} dynamics of older T cells. Through this process, we found that the results of the model show upregulation of ORAI1 and PMCA are not sufficient to recreate the observed dynamics and predicts changes in kinetic parameters associated with the IP_3R and SERCA channels as potential causes of altered Ca^{2+} signaling. Through computational modeling, we uncovered previously unexplored interactions of Ca^{2+} kinetic parameters, ultimately providing a novel understanding of ROS modulation of STIM1 in immunosenescence.

4.2 Materials and Methods

The model description is modified, with permission from [194] to include updates to equations and optimization framework.

4.2.1 Model Description

We expanded previously developed computational models [188, 195-197] for calcium signaling after T cell receptor ligation, which now consists of a simplified model for IP_3 formation and calcium fluxes for the cytosol, ER, mitochondria, and extracellular space. As can be seen in Figure 4-1, the mechanistic model we compiled and characterized incorporates the binding of peptide presented on MHC with TCR to recruit tyrosine kinases Lck, LAT, and Zap70 to the TCR/CD3 complex, which activates PLC-γ, as a one step input to phosphorylated PLC-γ levels. Once activated, PLC-γ is modeled as cleaving PIP_2 on the plasma membrane to generate both DAG and IP_3. IP_3 subsequently binds to

the IP_3 receptor, releasing Ca^{2+} stored in the ER (J_{IP3}). Once ER Ca^{2+} levels drop, the ER Ca^{2+} sensor, STIM1 is activated, translocates to the interface between the ER and plasma membrane (ER-PM) to activate a longer lasting, sustained influx of Ca^{2+} to the cytosol from extracellular space via CRAC channels (J_{crac}) [68, 198]. PMCA on the plasma membrane pumps Ca^{2+} to extracellular space and maintains the concentration gradient between the cytosol and the cellular environment (J_{pmca}). With such a steep gradient, one assumption of the model is a small Ca^{2+} leak through the plasma membrane back into the cytosol (J_{PMleak}). SERCA pumps on the ER membrane pump Ca^{2+} from the cytosol into the ER, again maintaining a gradient between the ER organellular Ca^{2+} concentration and the cytosol (J_{serca}). As with the plasma membrane, we assume a small leak back to the cytosol with such a steep gradient (J_{ERleak}). Mitochondria play a role in buffering cytosolic Ca^{2+} to enable proper activation and maintenance function of SOCE, thus preventing the negative feedback of increasing Ca^{2+} concentrations on the CRAC channels [88, 199, 200]. Ca^{2+} uptake into the mitochondria is accomplished through the Ca^{2+} uniporter (J_{mitin}) and released back into the cytosol via the Na^+/Ca^{2+} exchanger (J_{mitout}).

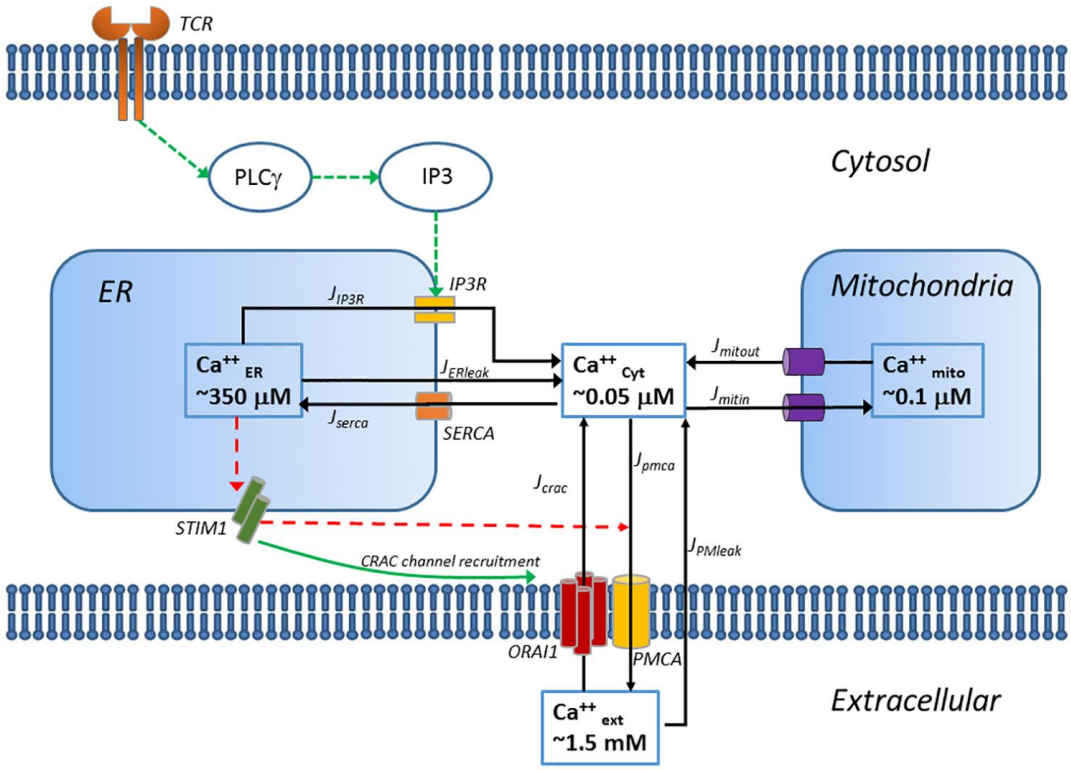

Figure 4-1: Model schematic showing included species and interactions involved with T cell activation.

These fluxes are combined to describe the fundamental Ca^{2+} signaling kinetics between multiple cellular compartments and extracellular spaces as follows:

$$\frac{dCa_{cyt}}{dt} = \beta_i((J_{IP3} - J_{serca} + J_{ERleak}) + (-J_{mitin} + J_{mitout}) + (J_{crac} - J_{pmca} + J_{PMleak})) \quad \text{Equation 4-1}$$

$$\frac{dCa_{ER}}{dt} = \frac{\beta_{er}}{\rho_{er}}(-J_{IP3} + J_{serca} - J_{ERleak}) \quad \text{Equation 4-2}$$

$$\frac{dCa_{mit}}{dt} = \frac{\beta_{mit}}{\rho_{mit}}(J_{mitin} - J_{mitout}) \quad \text{Equation 4-3}$$

Ca_{cyt} and β_i represent the concentration of Ca^{2+} and the ratio of free to total Ca^{2+} in the cytosol, respectively. Ca_{mit} and β_{mit} represent the concentration of Ca^{2+} and the ratio of free to total Ca^{2+} in the mitochondria. Similarly, Ca_{ER} and β_{ER} represent the concentration of Ca^{2+} and the ratio of free to total Ca^{2+} in the ER [188, 197]. From these relationships, the assumption is made that the ratio of free to total Ca^{2+} in each of the compartments does not fluctuate with time. We use ρ_{mit} and ρ_{er} to correct for the difference in volume between the ER and mitochondria compared to the cytosol.

4.2.1.1 IP_3 Production

As noted previously, IP_3 is formed upon phosphorylation of PLC-γ following TCR ligation. PLC-γ phosphorylation is modeled through simplified mass action kinetics with ligand (R) interacting with the TCR, with k_{PLCact} representing the rate constant for PLC-γ phosphorylation and, conversely, $k_{PLCdeact}$ represents the rate for PLC-γ dephosphorylation.

$$\frac{dR}{dt} = -k_{PLCact} \cdot R \qquad \text{Equation 4-4}$$

$$\frac{dPLC\gamma}{dt} = k_{PLCact} \cdot R - k_{PLCdeact} \cdot pPLC\gamma \qquad \text{Equation 4-5}$$

IP_3 production varies based on activated PLC-γ and the cytosolic Ca^{2+} concentration, as described below:

$$\frac{dIP3}{dt} = k_{IP3prod} \cdot pPLC\gamma \cdot Ca_{cyt} - k_{IP3deg} \cdot IP3 \qquad \text{Equation 4-6}$$

with the rate constant for IP_3 production and degradation, $k_{IP3prod}$ and k_{IP3deg}, respectively.

4.2.1.2 Cytosolic Ca^{2+} Flux

Cytosolic Ca^{2+} increases as Ca^{2+} is released from the ER through the IP_3R. This model builds off of previous mathematical models of IP_3R activation [201-205] and is given by:

$$J_{IP3} = V_{IP3} \cdot P_{IP3} \cdot Ca_{ER} \qquad \text{Equation 4-7}$$

such that VIP_3 is the maximal flow rate and PIP_3 is the IP_3R open probability. PIP_3 is described as a function of Ca^{2+}, IP_3, and the portion of available IP_3R, defined as not having the inhibitory site bound by Ca^{2+}:

$$P_{IP3} = \left(\left(\frac{IP3}{IP3 + K_{IP3}}\right)\left(\frac{Ca_{cyt}}{Ca_{cyt} + K_{act}}\right)h\right)^3 \qquad \text{Equation 4-8}$$

with K_{IP3} defined as the concentration of IP_3 at which the half maximal observed reaction rate is achieved and K_{act} is the midpoint of Ca^{2+}-dependent channel activation.

The inactivated portion of IP_3R is also modeled, by (1-h), as a function dependent on cytosolic Ca^{2+} and Q, defined as the effective affinity of Ca^{2+} to the site of inhibition.

$$\frac{dh}{dt} = A((1-h)(Q + Ca_{cyt}) - Ca_{cyt})$$ Equation 4-9

$$Q = K_{inh}\left(\frac{IP3 + K_{IP3}}{IP3 + K_{IP3inh}}\right)$$ Equation 4-10

with the coefficient A controlling the difference in time scales between equations. K_{inh} represents the Ca^{2+} affinity to the Ca^{2+} inhibitory site, and K_{IP3inh} is the affinity of IP_3 to the IP_3 binding site when the Ca^{2+} inhibitory site is occupied.

4.2.1.3 Continuous Leak of Ca^{2+} from ER

It is assumed that there is a continuous leak from the ER due to the concentration gradient of Ca^{2+} between the ER and cytosol:

$$J_{ERleak} = K_{ERleak} \cdot Ca_{ER}$$ Equation 4-11

4.2.1.4 Ca^{2+} Flux into ER

Ca^{2+} is sequestered in the ER via SERCA channels as modeled with:

$$J_{serca} = V_{serca} \cdot \frac{{Ca_{cyt}}^2}{{Ca_{cyt}}^2 + {K_{serca}}^2}$$ Equation 4-12

where V_{serca} is the maximal flux of Ca^{2+} through the SERCA pump and K_{serca} is the concentration of Ca_{cyt} at which the reaction rate is half of V_{serca}. Isoforms of SERCA are combined into a single, average SERCA pump.

4.2.1.5 Mitochondrial Ca^{2+} Flux

Ca^{2+} uptake by the mitochondria is modeled according to a 4th order Hill function [206, 207] through the mitochondrial uniporter where V_{mitin} is the maximal rate of uptake and K_{mitin} is the concentration of Ca_{cyt} at which the reaction rate is half of V_{mitin}:

$$J_{mitin} = V_{mitin} \cdot \frac{{Ca_{cyt}}^4}{{Ca_{cyt}}^4 + {K_{mitin}}^4} \qquad \text{Equation 4-13}$$

Ca^{2+} is extruded from the mitochondria via the Na^+/Ca^{2+} exchanger and permeability transition pores (PTP), which are combined in the equation below with V_{mitout} representing the maximal flow rate and K_{mitout} is the concentration of Ca_{cyt} at which the reaction rate is half of V_{mitout} [197, 208]:

$$J_{mitout} = V_{mitout} \cdot Ca_{mit} \cdot \frac{{Ca_{cyt}}^2}{{Ca_{cyt}}^2 + {K_{mitout}}^2} \qquad \text{Equation 4-14}$$

4.2.1.6 Plasma membrane Ca^{2+} Fluxes

Previous models and findings of Ca^{2+} entry to the cytosol through SOCE [196, 208-211] were simplified to assume the binding of STIM1 and ORAI1 is at steady state and only depends on the concentration of Ca^{2+} in the ER:

$$J_{crac} = V_{crac} \cdot \frac{K_{stim}^3}{Ca_{ER}^3 + K_{stim}^3} \cdot \frac{Ca_{ext}}{Ca_{ext} + K_{soc}} \qquad \text{Equation 4-15}$$

with the maximal Ca^{2+} influx through CRAC defined by V_{crac}, K_{soc} is the concentration of Ca_{ext} at which the half maximal observed reaction rate is achieved, and K_{stim} is the dissociation constant of ER Ca^{2+} to STIM1.

Similar to the ER membrane, because of the steep Ca^{2+} gradient, it is assumed there is a small leak of Ca^{2+}, at a given rate K_{PMleak}, through the plasma membrane, represented by:

$$J_{PMleak} = K_{PMleak} \cdot Ca_{ext} \qquad \text{Equation 4-16}$$

Lastly, Ca^{2+} can be extruded from the cytosol via PMCA pumps into the extracellular space. This can be described with the following equation where V_{pmca} is the maximal rate of this efflux and K_{pmca} is the concentration of Ca_{ext} at which the reaction rate is half of V_{pmca}:

$$J_{pmca} = V_{pmca} \cdot \frac{{Ca_{cyt}}^2}{{Ca_{cyt}}^2 + {K_{pmca}}^2} \qquad \text{Equation 4-17}$$

4.2.2 Parameter Optimization

The described system of differential equations was solved using ode23s in MATLAB® R2014b (Mathworks, Natick, MA). This model was first developed for Jurkat T lymphocytes, an immortal T cell line, and subsequently fit to primary $CD8^+$ T cells that were aged in culture to represent young vs. old characteristics of Ca^{2+} signaling. Overall, the model consists of 7 state variables and 29 parameters and encompasses a simplified

version of TCR activation and subsequent Ca^{2+} kinetics that arise from orchestrated phosphorylated proteins and activated channels. The Jurkat model was fit concurrently to experimental data from the literature of IP_3 signaling in the presence of EGTA [212] and dynamic Ca^{2+} recordings in the presence or absence of EGTA and TMB-8. EGTA, a Ca^{2+} chelator was applied to reduce extracellular Ca^{2+} entry through the CRAC channels and PM leakage. TMB-8, an IP_3R inhibitor, reduces the amount of Ca^{2+} released from the ER upon activation. To mimic these experimental conditions, two parameters λ_1 and λ_2, were introduced to the model equations to represent the percent reduction in extracellular Ca^{2+} and activity of JIP_3, respectively. λ_1 is set to 0.33 and λ_2 was fit to 0.30.

Parameter estimation was achieved via a sum of squared error (SSE) function, taking into account the difference between collected experimental data and the model prediction for different parameter sets Equation 4-18. This was achieved by using either the genetic algorithm (*ga*) algorithm or a combination of the genetic algorithm (*ga*), constrained nonlinear programing (*fmincon*) and pattern search (*patternsearch*) algorithms in the MATLAB® Optimization Toolbox™. For the Jurkat model, all three optimization algorithms were used for optimal results whereas for the Young and Old models, only the genetic algorithm was used because further optimization algorithms did not drastically reduce the error value. For estimating modeling predictions against different experimental conditions, the objective function was estimated below for the Jurkat and Young $CD8^+$ Model:

$$S = \sum_{t=1}^{t_{sim}} \sum_{n=1}^{N} \sum_{c=1}^{C} \left(\frac{x_{pred}(c,n,t) - x_{exp}(c,n,t)}{x_{exp}(c,n,t)} \right)^2 \qquad \text{Equation 4-18}$$

In this equation, t_{sim} is the maximum time of simulation, N is the number of species used for optimization and C is the number of experimental conditions for computed comparison. The Old CD8$^+$ Model was fit with a similar, slightly altered error function to account for differences in peak amplitude ($peak_{Amp}$ and $peak_{ExpAmp}$ for the model and experimental data, respectively):

$$S = \sum_{t=1}^{t_{sim}} \sum_{n=1}^{N} \sum_{c=1}^{C} \left(\frac{\frac{x_{pred}(c,n,t)}{peak_{Amp}} - \frac{x_{exp}(c,n,t)}{peak_{ExpAmp}}}{\frac{x_{exp}(c,n,t)}{peak_{ExpAmp}}} \right)^2 \qquad \text{Equation 4-19}$$

Initial concentrations of species were chosen from published experimental data or computed at steady state and used for the initial parameter optimization with the Jurkat model (Table 4-1) and were allowed to vary within specified bounds (Table 4-2).

Table 4-1: Initial conditions for all Jurkat model runs.

State Variable	Jurkat Model Initial Condition	Primary CD8$^+$ T Cell Model Initial Condition
PLCγ	70 nM	70 nM
IP_3	0.54 μM	0.54 μM
Ca_{cyt}	50 nM	50 nM
Ca_{ER}	350 μM	280 μM
Ca_{mit}	0.1 μM	0.1 μM
h	0.1	0.1
R	10	10

Table 4-2: Original bounds set on parameter values for parameter estimation.

Parameter	Bounds	Source/Explanation
$\boldsymbol{\beta_i}$	[0.001 1]	SS value: 0.009 [68]
$\boldsymbol{\beta_{er}}$	[0.001 1]	SS value: 0.196 [68]
$\boldsymbol{\beta_{mit}}$	[0.001 1]	0.0025 [68, 198]
$\boldsymbol{\rho_{er}}$	0.015	[213]
$\boldsymbol{\rho_{mit}}$	0.08	[213]
$\boldsymbol{k_{PLCact}}$	[0.001 0.01] s^{-1}	0.047 [187]
$\boldsymbol{k_{PLCdeact}}$	[0.01 0.1] s^{-1}	
$\boldsymbol{k_{IP3prod}}$	[0.1 1] $\mu M^{-1} s^{-1}$	1 [187]
$\boldsymbol{k_{IP3deg}}$	[0.01 0.1] s^{-1}	
$\boldsymbol{V_{IP3}}$	[0.05 80] s^{-1}	0.189 [208], 3 [207], 1.11 [209], 66.6 [211]
$\boldsymbol{K_{IP3}}$	[0.1 1] μM	0.136 [208], 0.13 [209], 1 [211], 3 [207]
$\boldsymbol{K_{act}}$	[0.05 0.5] μM	0.0814 [208], 0.08 [209], 0.4 [211], 0.13 [207]
$\boldsymbol{A}$	[0.01 0.5]	0.104 [208], 0.032 [209], 0.5 [211]
$\boldsymbol{K_{inh}}$	1 μM	1 [208]
$\boldsymbol{K_{IP3inh}}$	[0.5 1.5] μM	1.05 [208]
$\boldsymbol{K_{ERleak}}$	[0.0005 0.05] s^{-1}	0.002 [208], 0.02 [209], 0.0009 [211], 0.01 [207], 0.002 [196]
$\boldsymbol{V_{serca}}$	[0.2 250] μM s^{-1}	114 [208], 0.9 [209], 1 [211], 0.27 [207], 1 [187]
$\boldsymbol{K_{serca}}$	[0.15 0.8] μM	0.754 [208], 0.1 [209], 0.15 [211], 0.175 [207], 0.2 [187]
$\boldsymbol{V_{mitin}}$	[100 800] μM s^{-1}	300 [197], 506 [208]
$\boldsymbol{K_{mitin}}$	[0.5 1.5] μM	0.8 [197], 1 [208], 0.6 [207]
$\boldsymbol{V_{mitout}}$	[50 500] μM s^{-1}	125 [197], 476 [208]
$\boldsymbol{K_{mitout}}$	[1 10] μM	5 [197, 208]
$\boldsymbol{V_{crac}}$	[0.01 10] μM s^{-1}	0.226 [208], 8.85 [196], 0.01 [186]
$\boldsymbol{K_{soc}}$	[50 1000] μM	500 [196]

Table 4-2 continued.

K_{stim}	[150 250] μM	152.3 [214]
K_{PMleak}	[2.5e-7 3.5e-5] s^{-1}	5.6e-6 [186], 2.6e-7 [209], 4.6e-7 [207], 3.3e-5 [208]
V_{pmca}	[0.01 50] μM s^{-1}	0.05 [186], 0.01 [209], 0.013 [207], 0.0893/0.59 [208], 38 [196]
K_{pmca}	[0.1 0.5] μM	0.12 [209], 0.2 [207], 0.113/0.44 [208], 0.5 [196]
$K_{STIMpmca}$	[5 450] μM	Range in ER Ca^{2+} concentration

Ca^{2+} kinetic traces were analyzed for peak time, peak amplitude, integral under the curve, and decay constants. Decay constants were calculated by fitting the decay portion of Ca^{2+} traces to a sum of exponentials using MATLAB® scripts:

$$Decay = A_1 e^{\frac{t}{\tau_1}} + A_2 e^{\frac{t}{\tau_2}} \qquad \text{Equation 4-20}$$

4.2.3 Sensitivity Analysis

To determine which parameters affected specified characteristics of Ca^{2+} kinetics, sensitivity analysis was performed on the Young $CD8^+$ Model by varying one parameter, p, at a time between 1 and 20% of the original value. The resulting features included peak time, amplitude, and decay constant of the Ca^{2+} kinetics and these values were compared to the original state of the model according to the following equation:

$$Sensitivity = \frac{\frac{\Delta feature}{feature}}{\frac{\Delta p}{p}} \qquad \text{Equation 4-21}$$

4.3 Results

4.3.1 Jurkat Model Shows Adequate Fit

Upon optimization with three MATLAB® Optimization Toolbox™ algorithms, parameters were found to recapitulate the cytosolic Ca^{2+} dynamics under described experimental conditions in the presence or absence of EGTA or TMB-8 (Figure 4-2). The model is able to predict IP_3, Ca_{ER}, and Ca_{mit} concentrations but appropriate experiments in the literature were unavailable to compare (Figure 4-2).

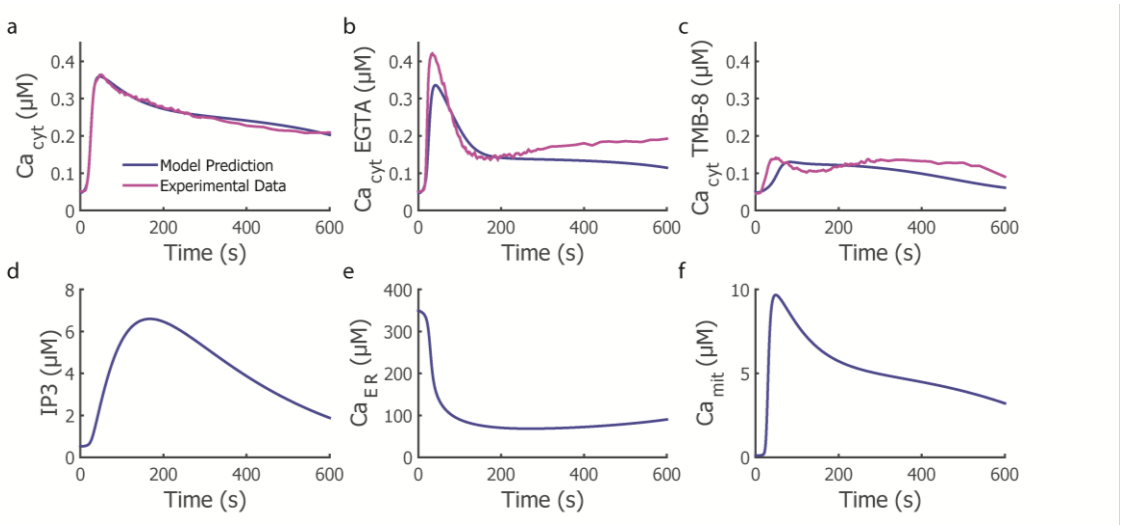

Figure 4-2: Optimization of Jurkat Model Fit.
The fit is performed between model and experimental conditions of Jurkat T cells stimulated with TCR ligation in the presence or absence of inhibitors, EGTA and TMB-8. Parameters represented here can be found in Table 4-4.

Concerned with the abundance of parameters and scarcity of data for fitting, we iterated through this optimization pipeline 17 times to arrive at a unique set of parameters every time. We compared the parameter values to create a confidence interval for each (Table 4-3) and results can be seen for the resulting Ca^{2+} traces that show a tight range of dynamics attained (Figure 4-3).

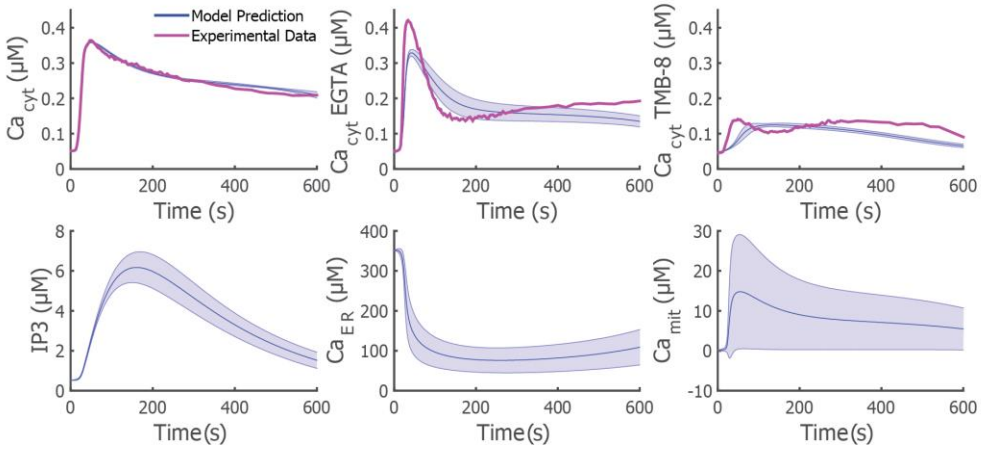

Figure 4-3: Multiple iterations of Jurkat model optimization shows tight Ca^{2+} dynamics. 17 different parameter sets are combined here with the average value (blue line) +/- standard deviation (blue shading). Results appear to be tight for Ca^{2+} traces with or without inhibitors present.

It can be seen that overall, throughout all parameter sets obtained, the Ca^{2+} dynamics do not vary substantially when compared in Figure 4-3. From this exercise we conclude that although many parameter sets can be obtained, with values varying between different runs to give the 95% confidence interval (Table 4-3), the overall network topology is robust to these alterations and nicely reflects the physiological Ca^{2+} response in Jurkat T cells upon TCR activation as all runs show qualitatively similar results when compared to experimental data (Figure 4-3).

Table 4-3: 95% confidence interval for parameter values in Jurkat T cells. 17 simulations were compiled to compute confidence intervals.

Parameter	**Jurkat T cells**
$\boldsymbol{\beta_i}$*	(0.015, 0.071)
$\boldsymbol{\beta_{er}}$*	(0.060, 0.094)
$\boldsymbol{\beta_{mit}}$	(0.10, 0.30)
$\boldsymbol{\rho_{er}}$	0.015

Table 4-3 continued.

ρ_{mit}	0.08
k_{PLCact}	(0.0033, 0.0043) s^{-1}
$k_{PLCdeact}$	(0.037, 0.057) s^{-1}
$k_{IP3prod}$	(0.38, 0.56) $\mu M^{-1} s^{-1}$
k_{IP3deg}*	(0.0094, 0.012) s^{-1}
V_{IP3}	(1.4, 5.3) s^{-1}
K_{IP3}	(0.31, 0.43) μM
K_{act}	(0.12, 0.16) μM
A	(0.077, 0.10)
K_{inh}	1 μM
K_{IP3inh}*	(0.76, 0.99) μM
K_{ERleak}*	(0.0023, 0.0038) s^{-1}
V_{serca}*	(49.57, 85.43) μM s^{-1}
K_{serca}	(0.32, 0.42) μM
V_{mitin}	(315.9, 497.2) μM s^{-1}
K_{mitin}	(0.74, 0.92) μM
V_{mitout}*	(140.5, 191.7) μM s^{-1}
K_{mitout}*	(3.21, 4.92) μM
V_{crac}	(1.04, 1.48) μM s^{-1}
K_{soc}*	(284, 448) μM
K_{stim}	(201, 230) μM
K_{PMleak}	(2.18e-5, 3.42e-5) s^{-1}
V_{pmca}*	(1.25, 1.99) μM s^{-1}
K_{pmca}	(0.13, 0.22) μM

4.3.2 Young Model Recreates Experimental Data

Our computational model of TCR-induced Ca^{2+} signaling in Jurkat T cells was then adapted to describe Ca^{2+} signaling in low passage primary $CD8^+$ T cells. The model was

optimized to fit Ca^{2+} time courses from low passage primary $CD8^+$ T cells while keeping many parameters conserved between both cell types and allowing the starred species in Table 4-4 to vary within the original bounds. For the young $CD8^+$ T cell model, parameter estimation was performed with a genetic algorithm in MATLAB® R2014b (Mathworks, Natick, MA). The initial parameter set was populated from the best parameter fit +/- 20% of the Jurkat Ca^{2+} model. The model was fit to conditions without inhibitors and was validated by predicting Ca^{2+} dynamics in the presence of chemical inhibitors.

Table 4-4: Parameters chosen for plotting and subsequent model fitting or sensitivity analysis

Parameter	Jurkat T cells	Young $CD8^+$ T cells
β_i*	0.056	0.047
β_{er}*	0.049	0.98
β_{mit}	0.033	0.033
ρ_{er}	0.015	0.015
ρ_{mit}	0.08	0.08
k_{PLCact}	0.0033 s^{-1}	0.0033 s^{-1}
$k_{PLCdeact}$	0.042 s^{-1}	0.042 s^{-1}
$k_{IP3prod}$	0.48 $\mu M^{-1} s^{-1}$	0.48 $\mu M^{-1} s^{-1}$
k_{IP3deg}*	0.010 s^{-1}	0.018 s^{-1}
V_{IP3}	4.0 s^{-1}	4.0 s^{-1}
K_{IP3}	0.57 μM	0.57 μM
K_{act}	0.13 μM	0.13 μM
A	0.079	0.079
K_{inh}	1 μM	1 μM
K_{IP3inh}*	0.82 μM	1.5 μM
K_{ERleak}*	0.0043 s^{-1}	0.048 s^{-1}
V_{serca}*	112.75 $\mu M\, s^{-1}$	103.88 $\mu M\, s^{-1}$

Table 4-4 continued.

K_{serca}	0.43 μM	0.43 μM
V_{mitin}	388.6 μM s^{-1}	388.6 μM s^{-1}
K_{mitin}	0.81 μM	0.81 μM
V_{mitout}*	188.9 μM s^{-1}	244.7 μM s^{-1}
K_{mitout}*	4.03 μM	4.7 μM
V_{crac}	2.4 μM s^{-1}	2.4 μM s^{-1}
K_{soc}*	363.5 μM	358.8 μM
K_{stim}	178.1 μM	178.1 μM
K_{PMleak}	1.1e-6 s^{-1}	1.1e-6 s^{-1}
V_{pmca}*	2.14 μM s^{-1}	2.08 μM s^{-1}
K_{pmca}	0.11 μM	0.11 μM

Upon fitting, we found the primary young $CD8^+$ T cell model was able to predict IP_3 and Ca^{2+} dynamics in different cellular compartments, as shown in Figure 4-4. With such different time scales of Ca^{2+} dynamics between the two cell types, it is not surprising that the resulting optimized parameter values are different between the models, especially the maximal velocities (Table 4-4).

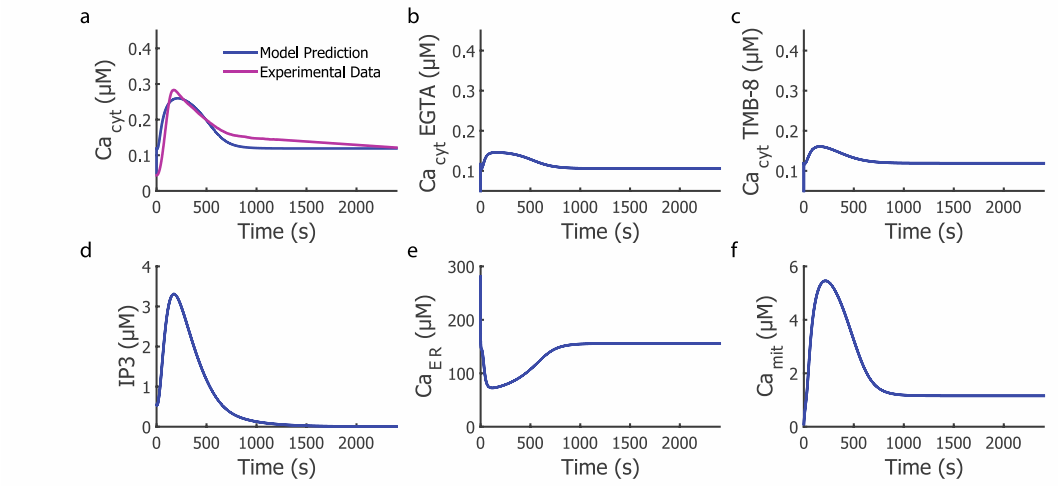

Figure 4-4: Model results for young primary $CD8^+$ T cell model compared to experimental data.
Cytosolic Ca^{2+} dynamics in the absence (a) or presence of inhibitors (b,c) at the same concentration as for Jurkat cells. (d-f) Model predictions for other state variables in the no inhibitor simulation.

We similarly ran multiple iterations of the parameter optimization and arrived at confidence intervals for the parameters that were allowed to vary between the Jurkat and young $CD8^+$ T cell model and from the shaded plot summarizing all runs, it is clear that a wide range of parameters give rise to similar Ca^{2+} dynamics (Table 4-5, Figure 4-5). One notable exception is in the dynamics of Ca^{2+} signaling in the ER, which has a wide range and qualitatively does not match intuition. In further inspection, there appeared to be two different qualitative responses that the model could give. The first was qualitatively similar to what appears in Figure 4-4, where the concentration of Ca_{ER} drops upon initial activation and slowly recovers through time. This matches all literature evidence of T cell activation mechanisms and was chosen for performing the sensitivity analysis and subsequent fit with the old T cell data. The second qualitative behavior of the model showed an initial increase in Ca_{ER} that seems to level off through time, but ultimately reaching a level that was greater than is physiologically relevant (> 500 μM). These were

deemed less accurate due to literature evidence of Ca^{2+} release from the ER during T cell activation but were nonetheless included in parameter calculations for the confidence intervals (Table 4-5).

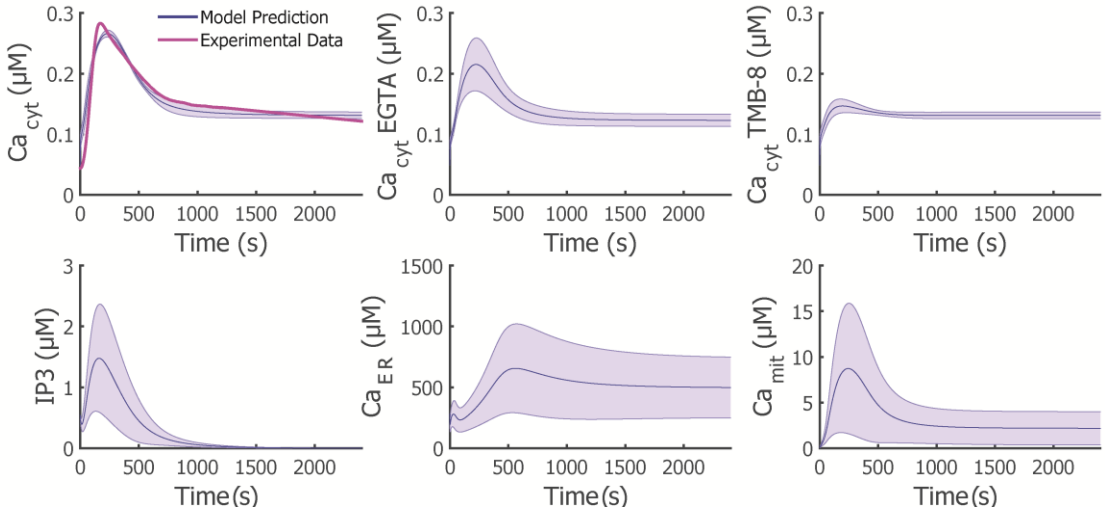

Figure 4-5: Primary young $CD8^+$ T cell model results from 15 iterations of optimization. The average response (blue line) is compared to +/- one standard deviation in model results.

Table 4-5: 95% confidence interval for parameter values in primary young $CD8^+$ T cells. 15 simulations were compiled to compute confidence intervals.

Parameter	Young $CD8^+$ T cells
$\boldsymbol{\beta_i}$*	(0.0065, 0.027)
$\boldsymbol{\beta_{er}}$*	(0.36, 0.73)
$\boldsymbol{k_{IP3deg}}$*	(0.040, 0.063) s^{-1}
$\boldsymbol{K_{IP3inh}}$*	(1.29, 1.47) μM
$\boldsymbol{K_{ERleak}}$*	(0.028, 0.041) s^{-1}
$\boldsymbol{V_{serca}}$*	(145, 200) μM s^{-1}
$\boldsymbol{V_{mitout}}$*	(222, 369) μM s^{-1}
$\boldsymbol{K_{mitout}}$*	(4.25, 6.62) μM
$\boldsymbol{K_{soc}}$*	(197, 455) μM
$\boldsymbol{V_{pmca}}$*	(0.088, 0.95) μM s^{-1}

Previously collected experimental data suggested mRNA levels of plasma membrane channels were upregulated, mainly PMCA and ORAI1 showed significant increase with age [194]. To determine if these changes were sufficient to explain differences in young vs. old $CD8^+$ T cells, we used the model described above to vary V_{crac} and V_{pmca} within the original bounds to compare with the old $CD8^+$ T cell data. Varying these two parameters alone did not create substantial changes between the models to recapitulate experimental differences in amplitude, time to peak, and decay time, as can be seen by the best fit in Figure 4-6.

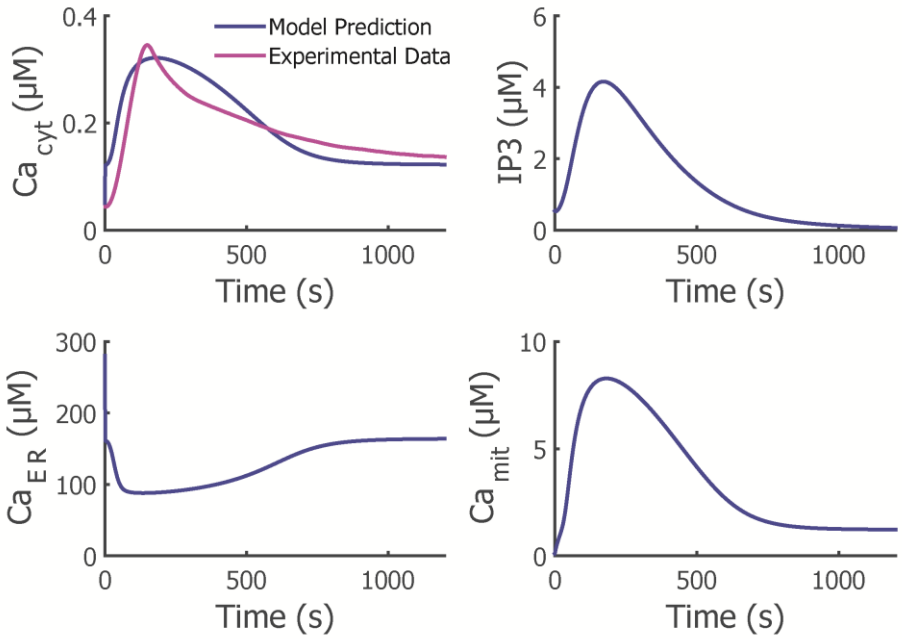

Figure 4-6: Best fit of Old $CD8^+$ T cell model varying only two parameters, V_{crac} and V_{pmca}.

4.3.3 Sensitivity Analysis of Young Model

With changes in levels of PMCA and CRAC channels being unable to recreate the old $CD8^+$ T cell experimental data, we identified which parameters were most implicated in being responsible for our characteristics of interest: time-to-peak and decay time

constant. We achieved this through performing sensitivity analysis on the young CD8$^+$ T cell model (Figure 4-7).

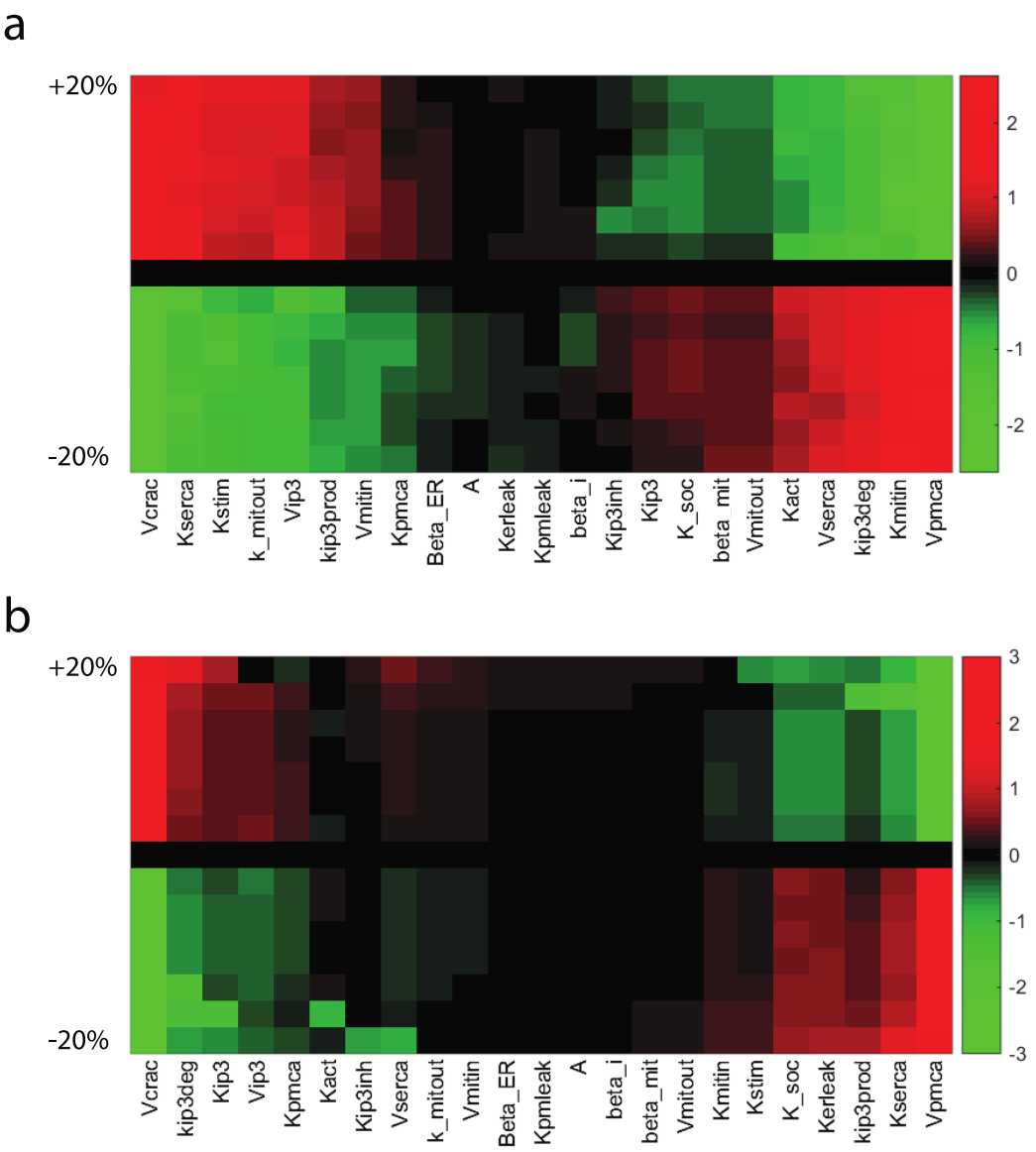

Figure 4-7. Model sensitivity analysis of Ca^{2+} trace features implicated in immunosenescence.
(a) Parameter sensitivity to peak time and (b) parameter sensitivity to the decay time constant, τ_1. Parameters were perturbed +/- 20% from their initial value individually and results are reported as compared to the original feature value and clustered for easier visualization.

For these two features, any non-linear behaviors, such as oscillatory Ca^{2+} traces that may result in certain regions of the parameter space, would alter the calculation but results appear to be fairly consistent with very few nonlinear behaviors seen in the heatmap. After clustering, higher parameter sensitivity can be seen for either of the features, but the parameters involved in altering both are mainly consistent between features, i.e. most parameters implicated in one feature are also highly indicative in the second feature.

Among the initial 24 parameters tested, seven parameters were identified as being the most responsible for the observed changes with age, many of which are involved with Ca^{2+} exchange with the ER stores (Figure 4-7). The seven parameters found to have the most effect on peak time and the decay constant were K_{serca}, V_{pmca}, V_{crac}, K_{stim}, K_{IP3}, $K_{IP3prod}$, and K_{IP3deg} (Figure 4-7).

4.3.4 Old Model Recreates Experimental Data

To ensure these parameters were the drivers involved with the experimentally observed old $CD8^+$ T cell phenotype, we allowed these seven parameters to vary from the original young $CD8^+$ T cell model using the genetic algorithm approach mentioned above. The objective function was varied slightly from previous fits with additional constraints for peak time and peak amplitude (Figure 4-8). The new optimized parameter set, shown in Figure 4-8, shows differences compared to the young $CD8^+$ T cell model best parameter set, with 1% upregulation for K_{serca}, 35% upregulation for V_{pmca}, 59% upregulation for V_{crac}, 2% upregulation for K_{stim}, 76% downregulation for K_{IP3}, 22% upregulation for $K_{IP3prod}$, and 434% upregulation in K_{IP3deg}. From this point, we were motivated to investigate redox metabolic reprogramming during this aging protocol because we

typically associate altered protein abundance with differences in maximal velocity, but our mRNA experiments did not implicate all of these parameters. Specifically, SERCA, IP_3 and STIM1 appeared with altered kinetics despite not appearing as significantly different in mRNA experiments.

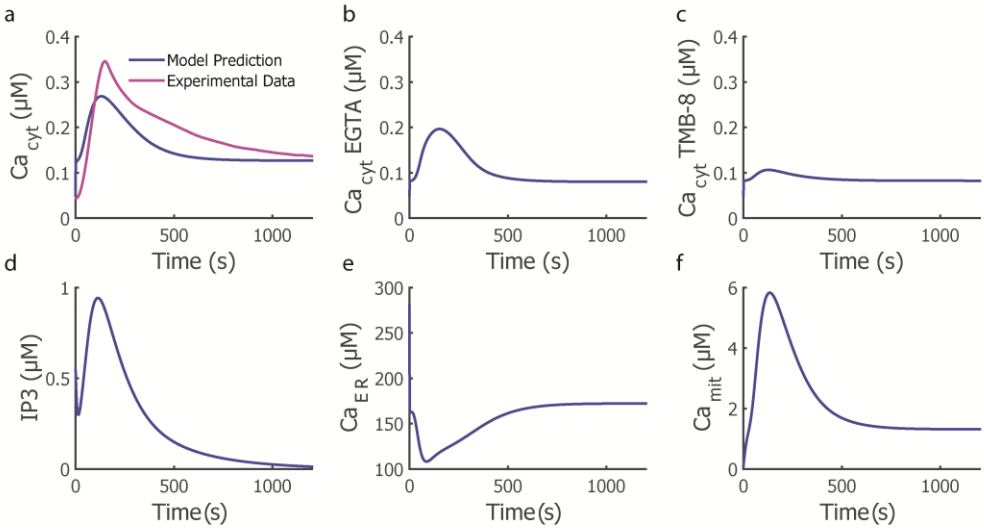

Figure 4-8: Best fit of old $CD8^+$ T cell model with allowing seven parameters to vary from the young $CD8^+$ T cell model, as identified through sensitivity analysis.

In Figure 4-9 and Figure 4-10, we varied the two main parameters associated with STIM1, V_{crac} and K_{stim}, individually to determine the effect on the calcium traces. We found that both of these parameters alone altered the peak time and decay of the calcium signaling when varied +/- 20% of the optimized young $CD8^+$ T cell model, which supports our model predictions that STIM1 may be involved with age related changes in T cells.

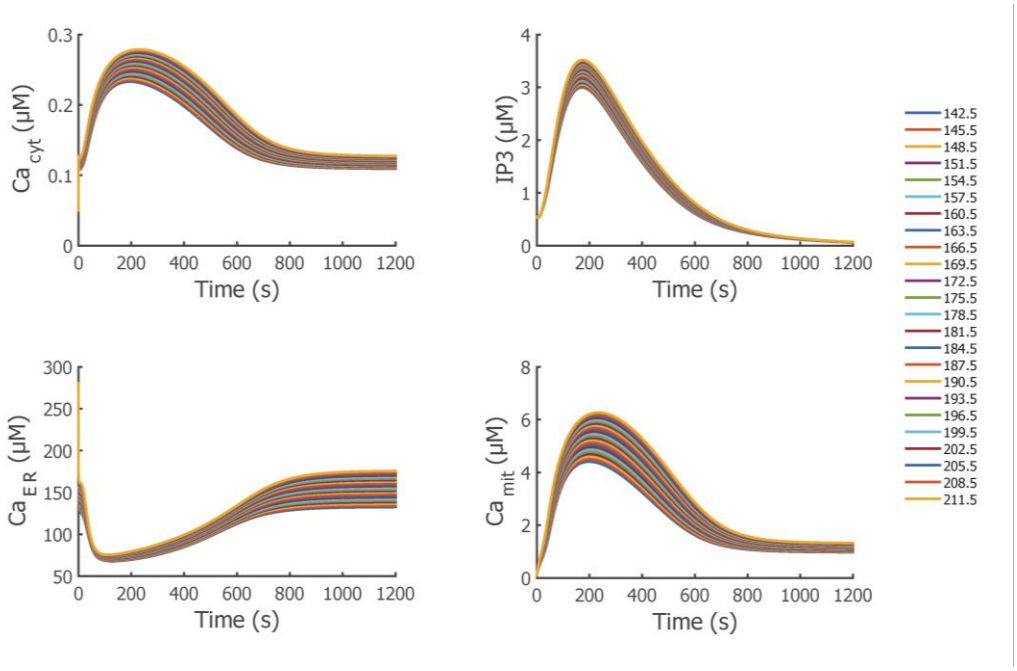

Figure 4-9: Varying K_{stim} from the "young T cell" model fit to investigate the effects on calcium traces.
K_{stim} was varied +/- 20% the fit value of 178.

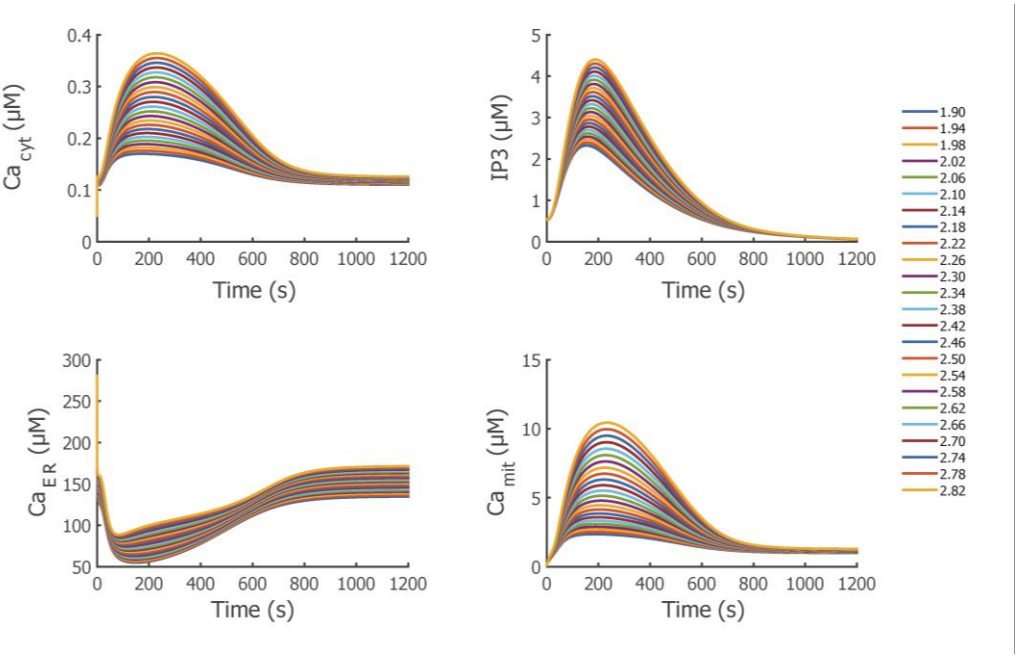

Figure 4-10: Varying V_{crac} from the young $CD8^+$ T cell model fit to investigate the effects on calcium traces.
V_{crac} was varied +/- 20% the fit value of 2.37.

4.3.5 Models Capture Dynamic Response of Senescing T Cells

For the final step of our modeling pipeline, we investigated the changes in identified Ca^{2+} trace features between the young and old $CD8^+$ T cell models compared to the experimental observations (Figure 4-11). As can be seen in Figure 4-11a, the fold change between the young and old $CD8^+$ T cell models reflect the experimental data well and thus validates this modeling technique.

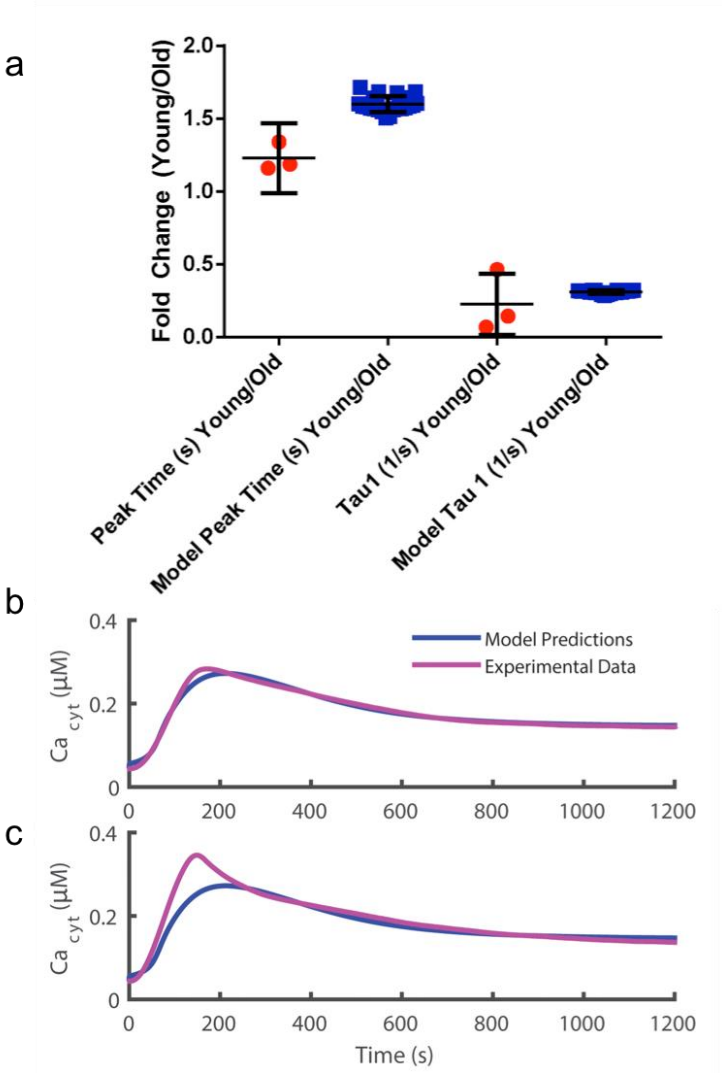

Figure 4-11: Model predictions compared to experimental data of Ca^{2+} dynamics between young and old $CD8^+$ T cells.
a) Comparison of experimental data to the model predictions for the two identified parameters, Peak Time and Decay Constant τ1. Error bars represent mean and 95% confidence interval represented in the above error bar b) Young $CD8^+$ T cell cytosolic Ca^{2+} model trace (blue) compared to experimental data (pink). c) Old $CD8^+$ T cell cytosolic Ca^{2+} model trace (blue) compared to experimental data (pink).

4.4 Discussion

Previous experimental evidence suggests primary $CD8^+$ T cells, aged in culture, exhibit differences in Ca^{2+} kinetics between young and old cells. Specifically, the Peak Time and Decay Constant τ1 were found to be significantly different between ages.

Further, there were two Ca^{2+} channels shown to be slightly upregulated with age. If Ca^{2+} channels and pumps lose activity through time, this upregulation potentially acts as a compensatory effect to keep T cell signaling kinetics similar to younger cells. To explore this intricate web of a multifactorial signaling network to determine if these differences in gene expression could account for the changes in Peak Time and Decay Constant $\tau 1$, we utilized computational modeling and built upon previous models to successfully recreate the kinetic Ca^{2+} dynamics upon TCR ligation.

Since parameter sets were combined from different cell types and conditions, we first started with a Jurkat model of immortal T cells and fit the model to experimental data that was either previously collected or found in literature. This closely related model was then modified to fit the young $CD8^+$ T cell experimental data by allowing a subset of parameters to vary. The modeling work shows good concordance between experimental traces and model predictions, and a robust qualitative behavior for many different parameter sets suggesting we haven't drastically overfit the model (Figure 4-3). Because the model fit experimental data well, we were confident moving forward to compare differences in the kinetic parameters between models of different ages, investigating the differences as potential explanations of the underlying biological mechanisms behind the altered function.

Our first attempt was to see if the mRNA data differences were enough to affect the observed changes in kinetics (Figure 4-9 and Figure 4-10). When modeling found this was not enough as the models did not fit the old $CD8^+$ T cell traces well, we moved on to see which parameters drive the observed experimental changes and allowed those to vary to fit an old model of $CD8^+$ T cell activation (Figure 4-7). Upon running this

optimization, we found a much more appropriate fit of the model to the experimental data and felt comfortable the seven parameters that we allowed to vary were responsible for the purported change in Ca^{2+} kinetics. We completed many replicates of the optimization to arrive at a range of parameter values and calculated the characteristics of interest, Peak Time and $\tau 1$.

When comparing the young and old $CD8^+$ T cell models, it was found that the fold change in the characteristics of interest, Peak Time and $\tau 1$, aligned well with the experimental findings, thus validating the model. The activity of STIM1 was pulled out of the sensitivity analysis as a potential driver for these changes. As there was no significant difference in mRNA level of this protein found, it must be concluded that this suggests the activity of STIM1 is altered through *in vitro* aging of T cells. It was later confirmed that STIM1 is differentially oxidized between young and old $CD8^+$ T cells, thus demonstrating the utility of a mechanistic model in extracting mechanistic differences and highlighting potential targets. From this exercise, we have created a model capable of recapitulating multiple T cell states, thus informing us of potential redox modified components of the system which were previously difficult to ascertain.

While these models are able to capture the observed differences between young and old $CD8^+$ T cells, it may be possible to further capture responsible entities in this signaling cascade by introducing more complexity, specifically that involved with redox modification of these proteins of interest. The model is also written as a deterministic ODE model, but there is a great deal of literature on all the stochastic events which play a role in T cell activation, and it would be interesting to incorporate some of this stochasticity into the model. With a stochastic component of the model, it may be

possible to see how these noisy events can emerge as functional alterations in T cell Ca^{2+} kinetics.

The model shown here represents an average T cell in the body. Future explorations could include single-cell analysis approaches to determine if there are different subsets of the population that account for different Ca^{2+} kinetics. This model would be amenable to this type of study by altering the parameters for each subset; potentially identifying which parameters should be experimentally investigated for potentially driving subsets of the population. These parameters may be of interest in diseases that show a different portion of cells in these subpopulations compared to healthy individuals. This example highlights the ability of modeling to answer many complex questions and using this to drive many future experiments. Computational modeling provides a unique framework for hypothesis driven experimentation by allowing us to intelligently probe complex signaling networks in an unprecedented fashion. These experiments may be difficult or impossible to perform with current technology in the lab, thus opening the door to a more complete understanding of T cell signaling in response to TCR engagement, hopefully identifying key regulatory networks that can be targeted for cell therapies in the future.

CHAPTER 5 MICROFLUIDIC TECHNIQUES FOR OSCILLATORY STIMULATION AND SINGLE-CELL FREQUENCY RESPONSE ANALYSIS

5.1 Introduction

Parts of this chapter were adapted from He, L, Kniss, A*, et al., An automated programmable platform enabling multiplex dynamic stimuli delivery and cellular response monitoring for high-throughput suspension single-cell signaling studies. Lab on a Chip, 2015. 15(6): p. 1497-1507. [215]*

5.1.1 Frequency Based Stimulation

T cell lymphocytes are a critical component of the adaptive immune response and become activated upon presentation with a foreign peptide through the T cell receptor [64]. Activation induces rapid signaling through multiple kinase cascades to alter gene expression and ultimately leads to functional changes, such as proliferation and cytokine release, that enable T cells to ward off pathogens and store immunological memory for future diseases [23, 150]. The time dependent, dynamic features of these signaling pathways is crucial for full functionality of T cells [74, 216]. Improper intracellular signaling of T cells during activation has been implicated in numerous diseases, thus providing an important cascade to study [15-19]. There is a great body of literature on elucidating components of the signal transduction cascades, yet many complex interactions remain unknown and are difficult to study with conventional experimental

methods, which typically measure responses to a bolus stimulus concentration step change.

To better understand the structure and dominant feedback controls in complex signaling networks, system identification methods, originally developed in control engineering, have recently been applied to biological systems [115-117, 120, 217]. With dynamic stimulation, it is possible to analyze the gain and delay of the output signal and analyze signal transduction pathways in an unprecedented fashion [218]. This analysis technique requires experimental systems amenable to fast, fluid switching mechanisms to interrogate cellular systems on a short timescale, capturing signaling events that occur on the order of seconds to minutes [66, 219]. Further, measurements done in bulk can mask these oscillatory or dynamic responses of a heterogeneous population by averaging different signaling phenotypes [100, 219]. To utilize this control theory approach, two devices have been designed and implemented in our research group to enable repeatable delivery of dynamic stimuli while enabling single-cell resolution analysis of T cells through time [215, 220].

5.1.2 Experimental Techniques For Oscillatory Manipulation

Microfluidics provide new opportunities for studying cellular signaling dynamics [102, 107, 221-226]. Multiple techniques have been utilized for trapping suspension cells, such as dielectrophoresis (DEP) [227, 228], optical tweezers [229], valves [230-232], microarray [233, 234], or hydrodynamic focusing [223, 235]. Yet the quick alteration of cellular microenvironment is difficult with these platforms. Several microfluidic designs exist in this functional domain, one such device is capable of a spatially varying but temporally static chemical gradient to study cellular processes such as chemotaxis [113].

Other devices enable oscillatory stimulation [236, 237], specifically for the nematode organism [238, 239], yeast cells [117], and bacteria [236]. This research utilizes two microfluidic devices that were invented to not only capture individual non-adherent cells, but also deliver robust and operationally simple dynamic chemical stimulation. The first device is a one layer device that uses on-chip valves to vary the microenvironment. The second device is a two layer device that uses a perforated PDMS membrane combined with a high-density cell trap for uniform stimulation of the entire population of cells.

5.2 Materials and Methods

5.2.1 Device Design: Device for Multiplex Cell Stimulation

Previous microfluidic devices are unable to provide dynamic stimulation with high frequency due to external fluid switching technology that may introduce undesirable pressure surges and create large fluid switching times, enabling diffusion of the square wave dynamic stimulation [114]. To create a microfluidic device capable of delivering robust dynamic stimuli, a previously developed cell trap [102] was modified with pneumatic valves (Figure 5-1). While different valve systems exist for microfluidic devices, such as screw valves and solenoid valves [240], pneumatic valves were chosen because it was possible to include them on a single-layer device with only the addition of an external pressure source box. The single-layer PDMS device consists of 2 compartments: the pressurized liquid valves capable of fluid switching and cell trapping chambers with flow channels to hydrodynamically attract a single-cell to each trap site when it is empty [102]. The flow rate is determined by an adjustable, external pressure source that can be tuned to reduce shear stress on the cells.

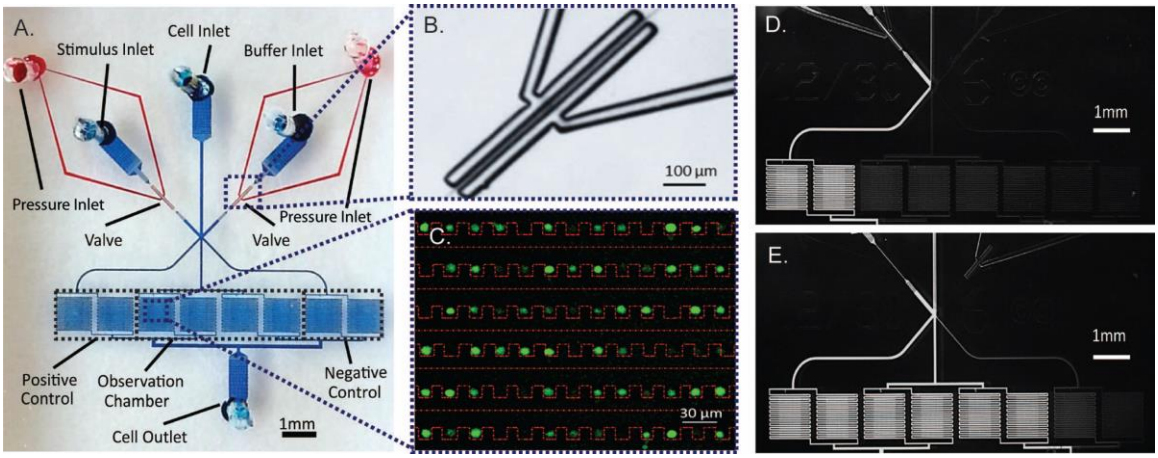

Figure 5-1: One layer device overview.
(A) Micrograph of microfluidic device: pneumatic valves (red) and fluid flow module (blue). (B) Enlarged bright field image of pneumatic valves when actuated. (C) False color image of Jurkat cells (green) trapped in cell chamber (red dotted line). (D & E) Fluorescent image of alternate switching between fluorescein solution (bright) and PBS (dark).

This device consists of a cell trap layer (Figure 5-1A, blue) where cells are loaded into individual traps for the experiment duration and the pneumatic valves (Figure 5-1A, red), which close and open to allow either stimulus or buffer to be delivered to the cells (Figure 5-1B). There are four observation chambers in the middle of the device as well as two chambers for a positive control and negative control on either side, which receive stimulus or buffer only, respectively. This provides suitable experimental controls within a single device.

5.2.2 Methods: Device for Multiplex Cell Stimulation

5.2.2.1 Device Setup

All solutions and cell suspensions were prepared and contained in 15 mL tubes (Falcon tube, BD biosciences, San Jose, CA). Tubes were connected to the device through polystyrene tubing (PE4, Scientific Commodities). Pneumatic valves were initially filled

with water at 30 psi through the valve inlet; during the experiment, valves were alternatively actuated at 50 psi. To prime the device and create a liquid environment, filtered 2% bovine serum albumin (BSA, Fisher Scientific) in 1× phosphate buffered saline (PBS, Boston BioProducts) was pressurized simultaneously from all ports into the device using a pressure of approximately 5 psi. This priming step removed any air bubbles and prevented undesired adhesion of cells to channel walls. To load cells after priming the device, the cell inlet was replaced with tubing connecting to the cell suspension, while all other ports stayed connected to priming solution.

The cell suspension was driven into the device by applying 1 psi at the cell inlet and no pressure at the outlet. Pressures were adjusted at stimulus and buffer inlets to keep priming solution flowing into device, which ensured unidirectional loading of cells to trapping chambers. After cells were loaded, the stimulus solution and cell media replaced priming solutions at the stimulus and buffer inlets, respectively. After closing the cell inlet by pinching the tubing, stimulus and buffer were driven to their respective inlets by a constant pressure between 1 and 5 psi to stimulate cells with a dynamic signal. An air compressor regulated through solenoid valves in a customized pressure control box provided the pressure source. A custom MATLAB® (MathWorks) GUI controlled these solenoid valves that modulate the actuation or shutoff of pressure.

5.2.2.2 Cell Culturing and Treatment

The Jurkat E6-1 human acute T cell lymphoma cell line (American Type Culture Collection) was cultured in RPMI 1640 Medium without Phenol Red and with L-glutamine (Sigma-Aldrich) at 37 °C in a humidified 5% CO_2 incubator. The media was supplemented with 10 mM HEPES buffer, 1 mM sodium pyruvate, 50 units mL^{-1}

penicillin–streptomycin (Cellgro), 1× MEM nonessential amino acids, and 10% fetal bovine serum (Sigma-Aldrich).

Cytoplasmic Ca^{2+} concentration was monitored using Fluo-3, AM, cell permeant (Life Technologies). Cells were incubated for 40 minutes with 5 μM Fluo-3 and 0.05% w/v Pluronic F127 at 37°C before being washed 3 times with PBS and resuspended in white RPMI without Phenol Red. Cells were loaded into the device at 0.5×10^6 cells mL^{-1} for approximately 20 minutes before they received stimulation.

5.2.2.3 Time Lapse Microscopy and Cell Identification

Once cells were loaded in the device, images were acquired with a Nikon Eclipse Ti inverted fluorescent microscope using a FITC filter cube (Omega XF22). Time-lapse microscopy was performed using Elements Software (Nikon) with frame rates of 0.1 Hz to avoid photo bleaching of the Ca^{2+} dye, Fluo-3.

Images were analyzed in an automated fashion using custom MATLAB® (MathWorks) scripts. Analyzed cells were manually chosen based on presence in the first and final frame using the overlay command in MATLAB® (MathWorks). The mean fluorescence intensity was calculated for each region of interest (ROI) with the removal of background fluorescence at each time point.

5.2.2.4 Characterizing Device Performance

To assess the performance of our device in various experimental conditions, we empirically characterized the chemical stimulus profiles at various flow rates, temporal resolutions and concentration levels. We recorded the fluorescent intensity by acquiring images (Infinity 3, Leica) at a frame rate of 5 Hz. Image analysis was done using custom

MATLAB® (MathWorks) scripts. With these scripts, we manually identified a ROI for each row and calculated the mean intensity in that ROI for all frames.

To characterize the temporal resolution of stimulus profiles, we alternated fluorescein solution (0.05 mg mL^{-1}) and PBS at 4 frequencies: 5, 10, 100, and 500 mHz, while pressurizing both solutions at 3 psi. The alternation was automated by a customized pressure control box and controlled through a customized MATLAB® GUI communicating to the box.

5.2.3 Device Design: Modularized Device for Uniform Cell Stimulation

A previously characterized microfluidic device was used for the trapping and subsequent fluorescent imaging of suspension Jurkat immune cells [220]. The two-layer design of this device enables fast, robust switching of fluids while cells are maintained in a low shear stress environment for the duration of the experiment. As can be seen in Figure 5-2a-d, this published device consists of cell trap layer, capable of trapping and holding cells for subsequent analysis, connected to a large stimulus delivery layer, capable of enabling fast fluid switching, via small pores [220]. Together, we are able to image individual T cells through time with precise, uniform control of the cellular environment. Taking a frequency response analysis approach, we probed Jurkat lymphocyte cells with an oscillatory input of H_2O_2 (Figure 5-2e). To complement this enabling experimental pipeline, analysis techniques were developed to enable an unprecedented view of calcium signaling in T cells.

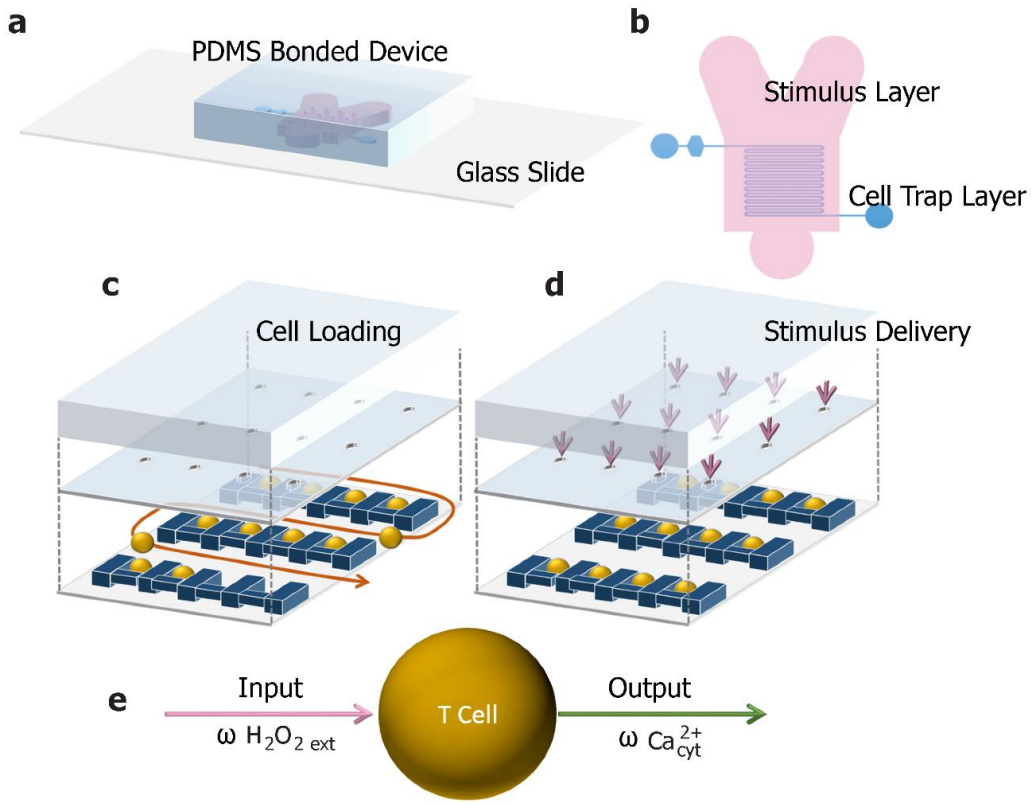

Figure 5-2: Microfluidic device description and experimental setup.
(a) 3D representation of the two-layer device plasma bonded to a glass slide. (b) Depiction of the two layers of the device: red is the stimulus layer, which allows for orthogonal bulk fluid flow and blue is the cell trap layer, which traps individual cells for time-lapse fluorescent microscopy. (c) Example of the cell loading phase of the experiment. Cells are loaded into the traps (shown in blue) via hydrodynamic focusing and a porous membrane connects this layer to the stimulus layer. (d) Example of the stimulus application phase of the experiment. Stimulus (shown in red) is flowed through the top chamber and permeates the bottom through the porous membrane while cells remain trapped. (e) Cells trapped in the device receive an oscillatory H_2O_2 input signal and we measure the resulting dynamic cytoplasmic calcium signal.

5.2.4 Methods: Modularized Device for Uniform Cell Stimulation

5.2.4.1 Device Fabrication and Cell Loading

Devices were molded with PDMS (Sylgard 184, Dow Corning) and two master wafers as previously described [220]. Both layers were molded with a 10:1 mixture of PDMS pre-

polymer to cross linker. The first layer of PDMS was spun on the master with cell traps to a level of ~10-12 μm so the pore structures that connect the two layers were above the PDMS and thus created holes for fluid to flow through. This layer was baked at 70°C for approximately 15 minutes, until partially cured. The second layer was poured on the stimulus chamber wafer to a height of ~2-3 mm and also partially cured at 70°C for 20 minutes. Once both layers were partially cured, the stimulus chamber layer was cut, aligned with the cell trap layer, and thermally bonded for an additional 40 minutes at 70°C. Once cured, holes were punched with a 19-gauge needle and the two-layer PDMS device was plasma bonded onto a clean glass slide.

5.2.4.2 Single-cell Identification and Analysis

As experimental design becomes increasingly complex and capable of collecting large quantities of single-cell data, analysis is becoming dependent on automated techniques to identify cells and collect metrics of interest over time. Many techniques available are unable to discern anomalous or unrelated features that are similar to those of interest. To combat this, our research first utilizes a manual approach for identifying cells of interest, and then builds on a combination of Relative Difference Filtering and Clustering (RDFC), which has shown to be useful for numerous systems with a predictable pattern of signal. Collected images were analyzed using custom MATLAB® scripts (MathWorks). First, cells were automatically identified in one of the initial images using a previously described relative difference filtering and clustering (RDFC) approach (Zhao *et al.*, In Prep). Once the mask was created, it was applied to the entire image sequence and the average fluorescent intensity of the cells was calculated and the local background was subtracted, based on a small area to the top left of each identified cell. Cell traces

were discarded if the average fluorescent intensity was negative for any value in the measured time points. This indicated the background subtraction was above the mean fluorescent intensity, suggesting the identified cell may have squeezed through the trap and was no longer present. For the cells that remained in the trap through the duration of the experiment, the average intensity was normalized via a linear transformation such that each cell's signal varies from 0 to 1. This step helped to reduce variation in initial loading of cell dye.

Once the normalized fluorescent intensity was calculated for each cell, it was then analyzed via a modified spectral analysis GUI, as originally developed by Uhlén in 2004 [241]. This GUI takes the single-cell signals and first fits a second order polynomial to each individually and subtracts this from the signal to remove artifacts from the experimental conditions [241], such as photo-bleaching of the cytoplasmic calcium indicator, Fluo-3. The Fourier transform is then taken of the signal to identify dominant frequencies in the signals. For each cell, the power spectral density is normalized to a total area of 1 and the area under the curve for each frequency is calculated to determine these dominant frequencies. It is then compiled into weighted histograms [242] with each identified frequency being multiplied by the relative power of the frequency and combined with the frequency information from all other cells in the population and plotted in a weighted histogram. This histogram is then normalized such that the total area under the curve is equal to 1 with bins of width 0.5 mHz.

5.3 Results

5.3.1 Device for Multiplex Cell Stimulation

5.3.1.1 Device is Capable of Delivering Robust and Tunable Stimulation

To perform frequency response analysis, the goal of the device is to interrogate cells with oscillatory signals, which span a broad portion of the frequency space. To ensure this device was capable of achieving this, we visualized the alternation of PBS and a fluorescent signal, PBS with fluorescein, at varying frequencies. We quantified the fluorescent intensity through time for various rows of the device and compiled it in Figure 5-3. It can be seen in the resulting spatial-temporal profiles that dispersion affects the fluorescent profiles to different extents. For instance, lower frequencies (below 10 mHz) shows the oscillatory profile for all rows within the device, although those rows towards the bottom of the device have a more sinusoidal profile when compared to the step profile in the first rows. For higher frequencies, the residence time of 8 s in this experiment is much higher than that of the alternating period. At these frequencies, the desired waveforms are only resolved for the first few rows and beyond that the microenvironment becomes homogenized into an average, constant stimulus level.

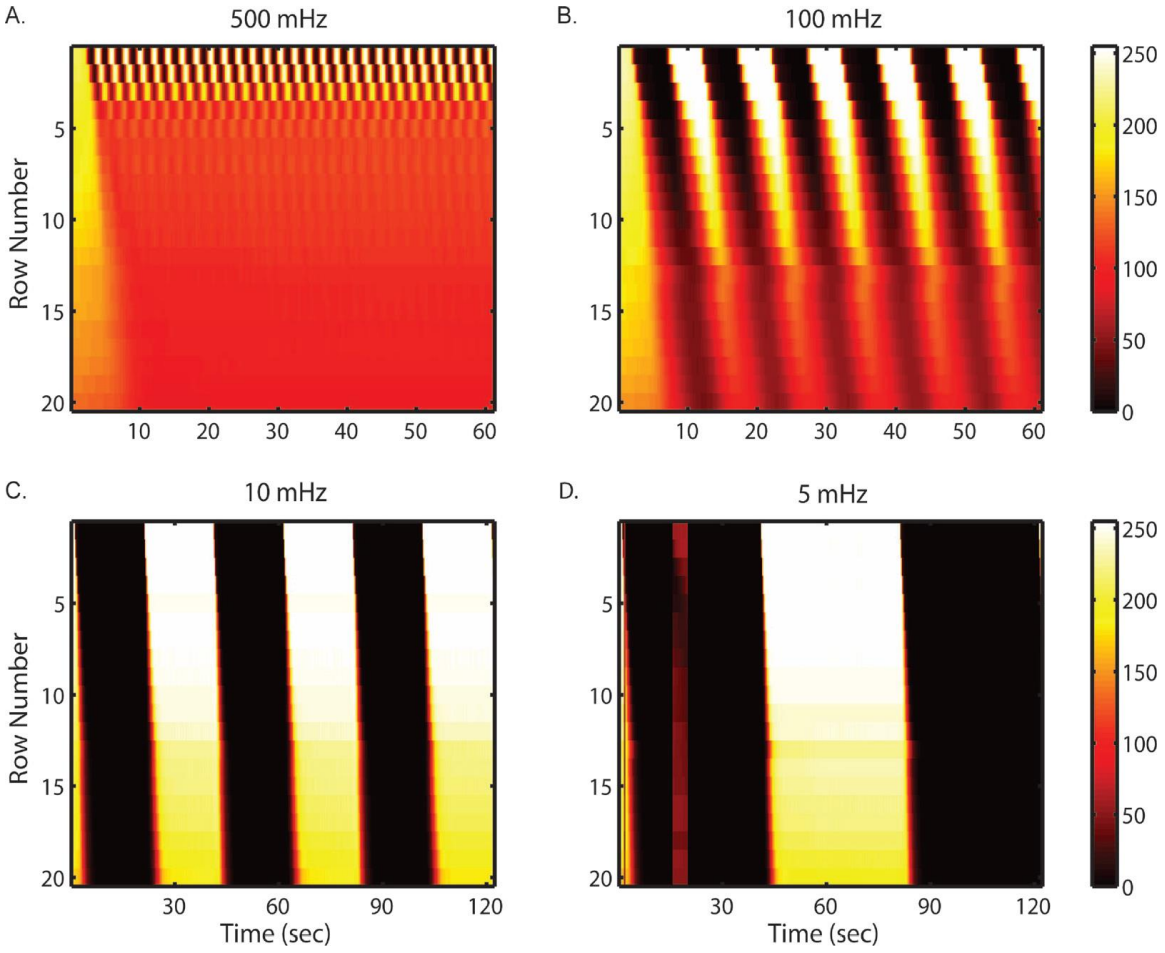

Figure 5-3: Varying frequencies in one layer device.
The temporal resolution is revealed by stimulus profiles oscillating in wide temporal ranges: (A) 500 mHz (2 s), (B) 100 mHz (10 s), (C) 10 mHz (100 s) and (D) 5 mHz (200 s). Profiles were generated by alternatively delivering fluorescein solution and PBS at a driving pressure of 3 psi. Heat maps show spatial (Y axis) and temporal (X axis) average ROI fluorescent intensity (color bar) in single observation chamber.

This dispersion and mixing through the device limits the attainable temporal resolution, and also introduces variability within a given experiment between cells of different rows.

5.3.1.2 Preliminary Study of Calcium Signaling in Response to Dynamic Stimulation of H_2O_2

Ca^{2+} is actively sequestered in the endoplasmic reticulum (ER) until T cell activation triggers its release [2, 64]. Upon stimulation, cytoplasmic Ca^{2+} concentration has been shown to oscillate through time, which is thought to be the result of stochastic distribution of receptor proteins within the membrane[72, 73, 243]. This dynamic calcium signaling ultimately leads to nucleation of NFAT and production of cytokine interleukin-2 (IL-2) [150]. Studies suggest a role of ROS in T cell activation, especially involved in calcium flux that follows TCR recognition [20, 37, 45].

We used our device to examine the response of Jurkat cells to dynamic stimulation by alternating 100 μM H_2O_2 solution with RPMI media without Phenol Red at 2 psi. The shear stress experienced by these cells is estimated from flow velocity data to be around 1 dyne cm^{-2}, much lower than the high shear stress blood cells are subjected to normally in the bloodstream [244]. Previous studies also indicated no recognizable effect on T cell signaling with the shear stresses estimated in the cell trapping chamber [102, 245]. Thus we assume signaling is unimpaired with the observed continuous flow conditions. Cytoplasmic Ca^{2+} concentration was monitored using fluorescence microscopy of Fluo-3 while cells experienced stimulation at a frequency of either 5 mHz or 50 mHz. Under 10x magnification (e.g. for monitoring of cytosolic calcium dye such as Fluo-3), only a few rows within an observation chamber can be monitored at the same time. These cells are assumed to be under approximately the same stimulation profiles, because for each of the two frequencies the concentration profile has been experimentally shown to be similar in adjacent rows (Figure 5-3). Individual cell traces were analyzed

over time, and a heat map of fluorescent intensity from 50 cells is shown in Figure 5-4. The cell number is not associated with location information.

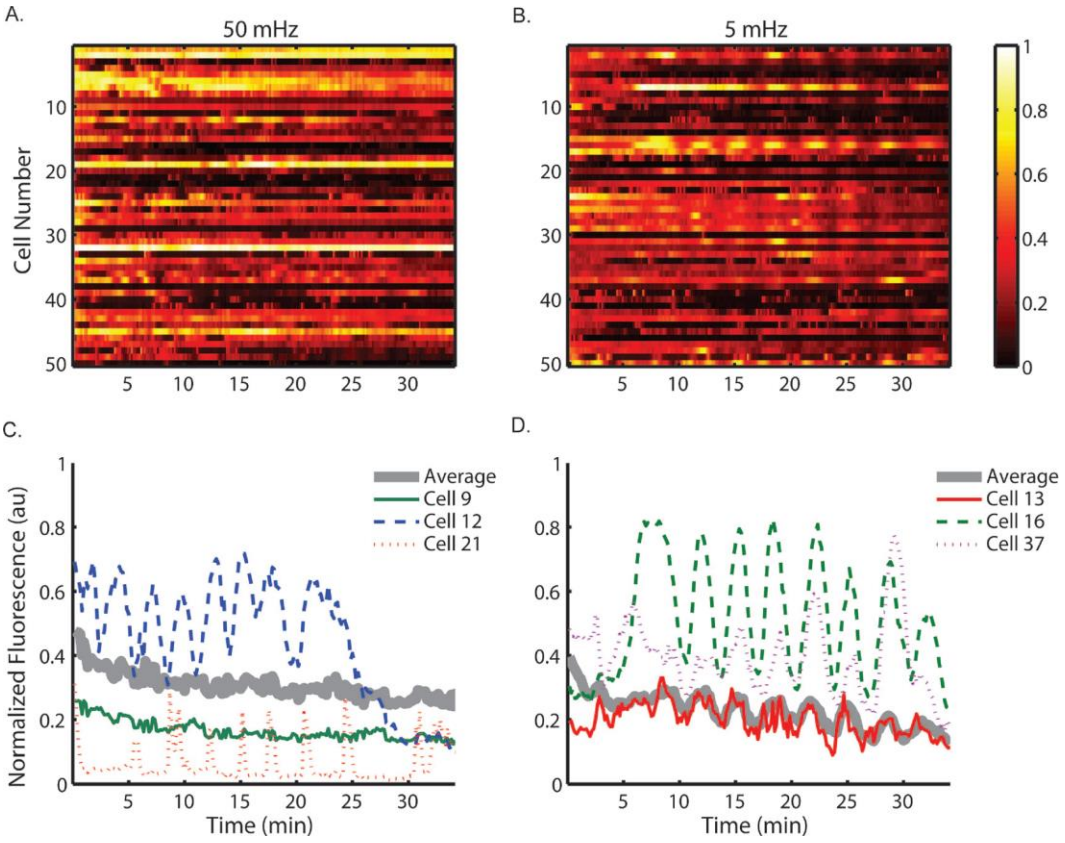

Figure 5-4: Cytoplasmic calcium signalling synchronizes with low frequency oscillating stimulus.
Heat map of 50 cells responding to (A) 50 mHz (20 s) and (B) 5 mHz (200 s) stimulation of 100 μM H_2O_2. Single-cell traces are graphed from selected cells responding to (C) 50 mHz and (D) 5 mHz stimulation of 100 μM H_2O_2. The population is visibly synchronizing to the stimulus at 5 mHz, while response heterogeneity exists among populations under each stimulation condition.

The heat maps clearly show heterogeneity within the population of monitored cells under each stimulation condition and select individual cell traces are shown Figure 5-4. The 5 mHz signal entrained some cells within the population to exhibit cytoplasmic Ca^{2+} concentration oscillations at approximately the same frequency. In contrast, the cells experiencing 50 mHz stimulation do not appear to exhibit oscillations of cytoplasmic

Ca^{2+} concentration at the same frequency as the driving frequency. These results suggest the Ca^{2+} signaling pathway of Jurkat T cells acts as a low-pass filter, not responding to stimulation at high frequencies while faithfully reflecting low frequency signals. The cut-off frequency of this particular pathway was shown to be between 50 mHz and 5 mHz.

Given these results, we demonstrated the value of this device to generate biologically relevant signals in order to interrogate cellular signaling pathways and probe its signal transduction properties. With a full spectrum of frequencies sampled, this device is capable of garnering the experimental data necessary for frequency response analysis and provides a more systematic approach to analyzing the underlying feedback control in a complex biological network.

5.3.2 Modularized Device for Uniform Cell Stimulation

5.3.2.1 Uniform Stimulation for All Rows with Robust Delivery

With the two-layer nature of this device, stimulation is delivered from the top layer at a faster rate while keeping the cells in a low shear stress environment. Due to the top down delivery, all rows receive uniform stimulation and there are no delays or dispersion of chemical stimulation that may contribute to experimental artifacts within a device. As can be seen in Figure 5-5 for the sampled frequencies, there is uniform, repeatable stimulation for all rows sampled, which span from top to bottom of the device, controlling for stimulation profile during experiments.

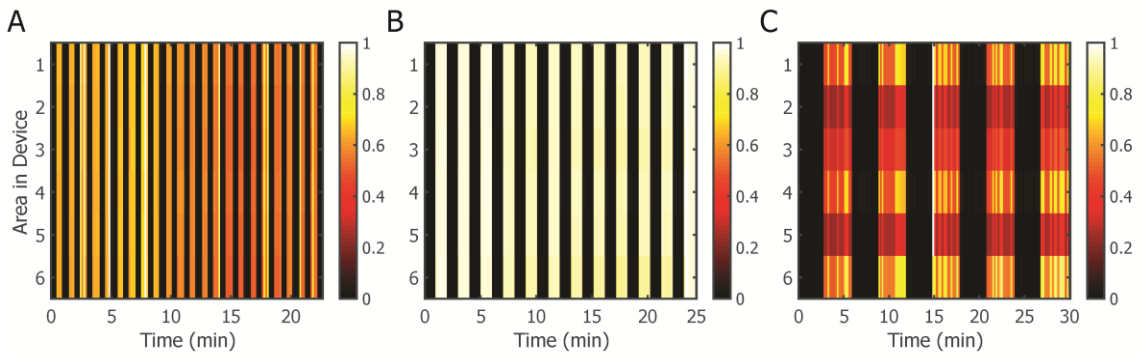

Figure 5-5: Characterization of different frequencies in two layer device.
The characterization of the two layer device revealed robust and uniform stimulation in all rows sampled in the device. (A) 1 min period, corresponding to a frequency of 16.7 mHz, (B) 2 minute period, corresponding to a frequency of 8.3 mHz, and (C) 6 minute period, corresponding to a frequency of 2.8 mHz. Results were obtained from switching PBS and fluorescein solution at 1 psi. Heat maps represent the average fluorescent intensity (au) in a single row of the device.

5.3.2.2 Cells are Automatically Identified with RDFC

For each experiment, images were compiled into a video, which was subsequently analysed for mean fluorescent intensity of a single-cell through time. To identify cells located in the trap, one of the images from the video went through a combination of relative difference filtering and clustering (RDFC) (Zhao *et al.*, In Prep). Briefly, this algorithm uses a standard 3x3 media filter to reduce sparse noise and assigns the value zero to regions with intensity lower than an identified threshold (Zhao *et al.*, In Prep). Following this, uneven illumination is reduced by using a relative difference filter and a threshold is then applied to identify pixels above the local background (Zhao *et al.*, In Prep). The resulting pixels of interest are further filtered based on size, shape, and position in an ordered array with respect to other cells using k-means clustering, as the cells are loading in a predictable manner within the trap (Zhao *et al.*, In Prep).

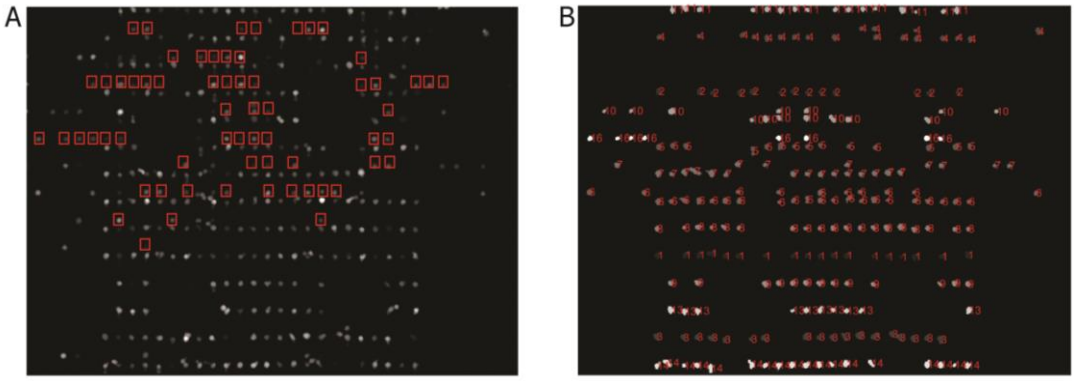

Figure 5-6: Example analyzed frame for identifying single T cells in two-layer device. (A) Cells can be seen loaded in traps in a deterministic way, but some have been trapped in pores that connect the two layers (red boxes). (B) RDFC result where the majority of boxed cells from A have been removed, leaving only cells properly trapped for subsequent analysis.

5.3.2.3 Single-cell Traces Show Heterogeneity Within the Population

Once cells have been identified in the cell trap array, a mask is created and then applied to all images in a given experimental video. The average intensity is recorded with a local background identified and subtracted for each specific cell. This helps to reduce the variation in the event of uneven illumination during the fluorescent recording. The average intensity is min-max normalized and each single-cell trace is put through a modified version of a previously published GUI for analyzing calcium oscillations [241]. The resulting single-cell calcium traces were recorded and heterogeneity can be seen in responses (Figure 5-7b,c). Traces were analyzed for dominant frequencies, as defined by exhibiting an area under the curve greater than a designated threshold in the PSD (Figure 5-7f,g). Interestingly, for given input frequencies, the average trace can be seen entrained to the driving frequency, exhibiting a single dominant frequency at the corresponding driving frequency (Figure 5-7d,h). When viewing individual cells, some will be entrained similarly to the population average (Figure 5-7b,f) while others exhibit alternative

frequency responses (Figure 5-7c,g), illustrating the necessity to use single-cell analysis in this approach.

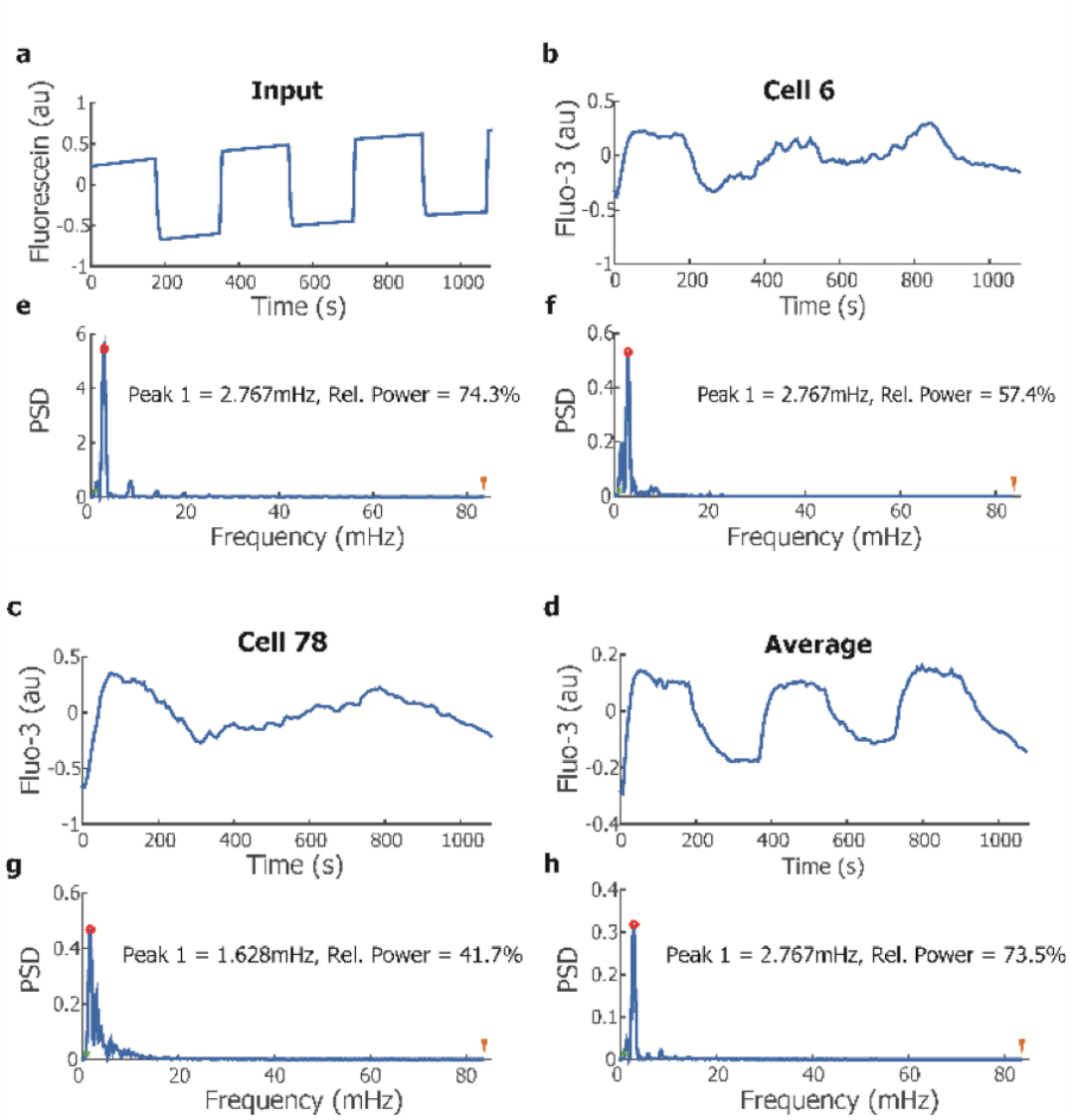

Figure 5-7: Data analysis pipeline of example 2.78 mHz experiment.
(a) The input signal was characterized using fluorescein media and oscillates at the desired frequency of 2.78 mHz. (b) and (c) Two single-cell calcium traces illustrate the dynamic information we receive from the experimental system: (b) Cell 6 and (c) Cell 78. (d) The single-cell traces from a given experiment are combined to yield a population average. (e-h) 207 calcium signals are then analyzed [241] by FFT and resulting dominant frequencies are identified for frequencies above a chosen threshold (see Methods). The power spectral densities (PSDs) are plotted for (e) the input signal, (f) Cell 6, (g) Cell 78, (h) the average signal of all 207 individual cells.

During this analysis, we also extract the gain and phase for each individual cell and combine them for further, population-based analyses. This analysis pipeline allows us to view individual calcium traces as signals in the frequency domain, ultimately providing additional information about the response of cytoplasmic calcium to the experimental perturbation that cannot be captured with dose-response, bulk measurements.

5.4 Discussion

In this chapter, I introduce two enabling technologies from the Lu lab, both of which are capable of delivering a range of profiles that were previously unobtainable for cells not adhered to a surface. This ability was captured in two elegant solutions. The first device kept fabrication and operational simplicity by combining pneumatic valves with the previously developed cell trapping module for suspension cells [215]. I developed MATLAB® scripts to characterize the delivery of signals within the device, finding the phenomena of dispersion and mixing as the signal moves through the device. Due to the one-layer nature, not all cells within the device receive exactly the same stimulation: the top rows receive a square wave whereas lower rows receive a more sinusoidal shape while controlling for the average level of stimulant throughout the experiment. Further, the device had positive and negative experimental controls built into the design, simplifying the number of experiments necessary and controlling for variation between devices. The variability of stimulation throughout the device may prove useful in certain biological systems that can be perturbed dynamically for known responses. It would reduce the number of experiments necessary while providing otherwise unobtainable stimulation profiles.

The second device, which was previously developed by our group, incorporated a second layer on top of the cell trapping module separated only by a perforated PDMS membrane, enabling quick delivery of stimulation from fast, bulk flow down to the cell trapping layer while maintaining a low shear stress environment [220]. We chose to switch to this design for future chapters because of the uniform nature of the stimulus delivery. Not only was the device capable of delivering finely tuned oscillatory input signals, but it can be easily seen there is very little variation between rows, thus reducing the amount of experimental artifacts for any given set of cells.

Development of both devices was driven by an experimental need to perturb suspension cells in a dynamic fashion. We confirmed this need was met by characterizing the devices and subsequently investigating the role of ROS in Jurkat human T cells' calcium signaling network. In this chapter I have demonstrated the utility of the one layer device for perturbing Jurkat T cells. To accomplish this, we stimulated cells with two dynamic patterns of H_2O_2 signals. The acquired results showed the heterogeneity among cell population and allowed us to roughly estimate the cut-off frequency of the Ca^{2+} signaling network in Jurkat cells. Our results would not be observable in population-average based, bulk experiments and emphasized the unique value of our platform to enable the study of cellular signaling network properties.

These experimental results were obtained through the development of a complementary data analysis pipeline capable of accumulating single-cell data and analyzing it through time. This analysis technique reduced the time it takes to compile such data with conventional technologies and demonstrates its utility when examining single-cell responses compared to the population average of the cells, showing a wide

range of responses that were previously uncharacterized. This method of analysis, while providing new insight into the range of responses, also makes it difficult to make conclusions while controlling for population heterogeneity versus experimental variation. To help reduce the latter, we switched to the two-layer device and characterized less variability between the rows. This device was chosen for all subsequent signaling studies due to the uniform nature of stimulation.

Although we demonstrated the concept of these devices with T cells, as the signal generation modules are independent from the cell-trapping module, the cell-trapping modules can be replaced to adapt to most cell sizes and types. Similarly, the analysis techniques shown here can be used for different cell types and fluorescent reporters, thus providing a complete package for single-cell analysis in response to dynamic stimulation. We envision this platform to be applied to broad single-cell analyses, such as in pharmacodynamics, immunology, stem cells and cancer research.

CHAPTER 6 T CELL RESPONSE TO OSCILLATORY STIMULATION

6.1 Introduction

As part of the adaptive immune response, T cell lymphocytes function to recognize and respond to pathogens present in the body. With a multitude of functions, T cells have been implicated in numerous diseased conditions, such as autoimmune disorders [17]. T cell activation induces rapid proliferation and a change in intracellular signaling cascades to alter gene expression and ultimately cytokine release [20]. More specifically, when an antigen-presenting cell (APC) engages the T cell receptor (TCR), a cascade of activated kinases phosphorylates phospholipase-C γ (PLC-γ) [31], which cleaves PIP_2 to generate IP_3. IP_3 subsequently binds IP_3 receptors (IP_3R) and calcium is released from intracellular stores into the cytoplasm [32]. The subsequent calcium signaling involves oscillations, thought to be the result of the stochastic distribution of IP_3R within the membrane and the result of calcium influx from external sources [72, 73]. This signaling profile illustrates the ability for calcium to produce complex signals as opposed to molecules that produce binary state switches [65]. Different frequencies have been shown with varying levels of stimulation[246] and have an effect on the activation of downstream transcription factors, such as NFAT and NF-κB [22, 32, 247].

The increased signaling capacity during T cell activation is also associated with an increase in glucose metabolism and subsequent burst of reactive oxygen species (ROS) from NADPH oxidases [37] and the mitochondria [20]. ROS, such as hydrogen peroxide (H_2O_2) and superoxide, are produced within the cell and act as secondary

messengers in numerous cellular processes. Alteration of ROS production and regulation has been implicated in diseases such as cancer [6] and autoimmune disorders [248]. However, it is often difficult to measure ROS within the cell and many techniques only allow for population averages through time. There is known cross talk between calcium and H_2O_2 during T cell activation; ROS is able to activate calcium release channels [79-81] and increase the channel activity of two ER membrane channels, IP_3R and RyR [85, 87, 249]. The connections between these signaling molecules are difficult to analyze due to the fast, dynamic kinetics and subcellular localization. We seek to better understand these connections in the context of frequency encoding, looking to answer the question of whether dynamic stimulation with H_2O_2 is able to affect Ca^{2+} signaling in the frequency domain within T cell lymphocytes. Furthermore, we seek to determine which frequencies of input oscillatory conditions of H_2O_2 elicit the best Ca^{2+} response.

Control-based computational methods have been developed for discerning complex, interconnected networks of signaling molecules that are difficult to interrogate with bulk measurements [218]. Ultimately, these techniques can help identify and model only dominant interactions within the network by characterizing the behavior of a system from its responses to sinusoidal inputs. This is accomplished by applying oscillatory stimuli to cells and measuring the resultant gain and phase shift of the output signal. This behavior can be modeled with a transfer function, reducing the parameters necessary to describe a biological system. We also attempt to compare this response to a large, mechanistic model of the interaction between ROS and Ca^{2+} molecules during T cell activation. We present here an approach to interrogating calcium dynamics with dynamic H_2O_2 input to elucidate characteristics of the signaling network.

T cells develop in the thymus and reside as suspension cells in the blood. As suspension cells, they have been historically difficult to analyze dynamically at a single-cell level because they often float out of the focal place during fluorescent microscopy imaging. There are techniques, such as flow cytometry, that enable single-cell analysis, but these are end-point assays that cannot monitor a single-cell through time.

Advances in microfluidics have enabled more advantageous methods for T cells, such that hundreds of single T cells can be loaded into a single device and monitored dynamically with fluorescent molecules [102, 250-253], providing insight into the underlying signaling networks with commonly available fluorescent probes and markers. Recent microfluidic devices have also enabled delivery of robust, time-varying chemical signals, in contrast to conventional experimental techniques which measure the response of cells to a single perturbation of step increase or bolus of stimulus [215, 220]. The enhanced experimental capability can be combined with frequency response analysis, originally developed in control engineering, such that the underlying complex signaling networks can be discerned more easily. As calcium signaling is an almost immediate response to T cell stimulation, occurring within seconds of stimulation, it is an appropriate molecular [254] candidate for this analysis technique. Examples of this approach include biological applications in the osmotic stress response [117] and the galactose response pathway [120] in *S. cerevisiae*.

In this study, we utilize a microfluidic device and frequency response analysis to investigate features of intracellular calcium dynamics in response to H_2O_2 stimulation in Jurkat cells, an immortal T cell lymphocyte line. We probed the dynamics between H_2O_2 and Ca^{2+} by varying the extracellular H_2O_2 environment of the cell and recording the

intracellular cytoplasmic Ca^{2+} response to varying frequencies. Cells in any given experiment received a single frequency of stimulation and cells were combined across conditions for an experimental Bode Plot, which provides insight into the filter dynamics of cytoplasmic Ca^{2+} signaling in response to H_2O_2. We report that Ca^{2+} responds to H_2O_2 with second order filtering characteristics exhibiting a natural frequency of 2.78 mHz, corresponding to known downstream effector functions.

6.2 Materials and Methods

6.2.1 Cell Culture and Treatments

Experiments were performed on the Jurkat E6-1 human acute T cell lymphoma cell line (American Type Culture Collection) grown in conditions as described before [215]. Briefly, the cells were cultured in RPMI 1640 without Phenol Red (Lonza) and with L-glutamine (Sigma-Aldrich), supplemented with 10 mM HEPES buffer (Corning), 1 mM sodium pyruvate (Cellgro), 50 units mL-1 penicillin-streptomycin (Cellgro), 1x MEM nonessential amino acids (Cellgro), and 10% fetal bovine serum (Sigma-Aldrich).

To visualize cytoplasmic calcium in response to varying experimental conditions, the cells were loaded with 5 μM Fluo-3 AM, cell permeant (Life Technologies) and 0.05% w/v Pluronic F-127 (Sigma-Aldrich) for 30 minutes at 37°C. Cells were subsequently washed with PBS and resuspended in complete RPMI media without Phenol Red, as described above. Cells were loaded into the device at a density of 1×10^6 cells/mL.

6.2.2 Device Operation

Devices were primed with 2% BSA in PBS to prevent unintentional cell-adhesion and non-specific binding. Once all bubbles were removed, the top, stimulus chamber, was

connected to two pressurized reservoirs of fluid at 1 psi. Specifically, these reservoirs contained either complete media or complete media with the addition of 10, 25, 50, or 100 μM H_2O_2. Cells were loaded into the device via gravity driven flow as previously described [220]. Once cells were loaded, the different solutions were delivered at alternating frequencies, as defined with user input to custom MATLAB® (MathWorks) scripts, which controlled off-chip pinch solenoid valves.

6.2.3 ROS and Calcium Model: System of Differential Equations

The model description is modified, with permission from [194] to include updates to equations and optimization framework.

There are many known interactions between Ca^{2+} signaling and ROS metabolism during T cell activation. To better elucidate some of these key interactions we built upon the model presented in Chapter 5 and added interactions, such as proteins regulating ROS and Ca^{2+} metabolism, into the different compartments of the model. As can be seen in the model depiction in Figure 6-1, there are two major modules of the model: ROS production and Ca^{2+} fluxes between organelles. In this model, we assume all species concentrations are spatially uniform within any given compartment. Many Ca^{2+} and ROS modulation interactions described here have not been mathematically derived in previous work, and we have assumed these biological processes can be described using Michaelis-Menten and Hill-type functions.

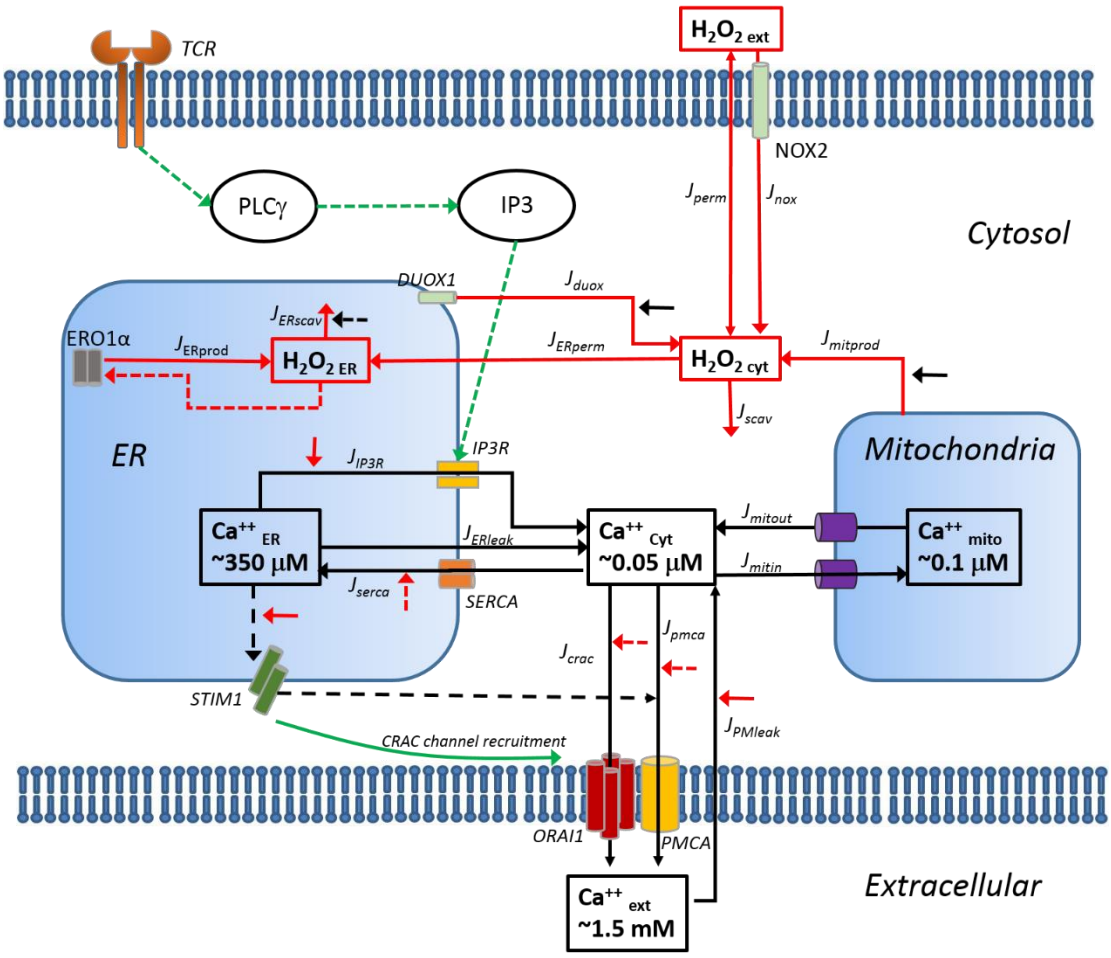

Figure 6-1: Schematic of Species and Connections Within the ROS/Ca^{2+} Model. Connections between the Ca^{2+} Module (Black) and ROS Module (Red) are depicted here with dashed arrows representing inhibition and solid arrows representing activation. Modifications are described in the text for equations subjected to regulation.

6.2.4 Model Equations: ROS Module

The first module of the model comprises ROS production and clearance mechanisms within T cell lymphocytes. ROS are lumped together; there is no distinction between different species present within the cell. Previous work in our group has encompassed a more detailed model of cytosolic H_2O_2 and its clearance from Jurkat cells, including mechanisms involving catalase, glutathione peroxidase, peroxiredoxin, glutaredoxin, thioredoxin and glutathione [255]. In this approach, many of these interactions are either

simplified or removed such that only major production and clearance mechanisms in each compartment are in place.

The fundamental equations, describing ROS concentration in the cytosol, ER, and extracellular spaces are described below for ROS_{cyt}, ROS_{ER}, and ROS_{ext}, respectively:

$$\frac{dROS_{ext}}{dt} = -J_{perm} \quad \text{Equation 6-1}$$

$$\frac{dROS_{cyt}}{dt} = J_{perm} + J_{nox} + J_{duox} + J_{mitprod} - J_{ERperm} - J_{scav} \quad \text{Equation 6-2}$$

$$\frac{dROS_{ER}}{dt} = \frac{1}{\rho_{ER}}(J_{ERperm} + J_{ERprod} - J_{ERscav}) \quad \text{Equation 6-3}$$

where $\rho_{ER}$is the ratio of the volume of the ER compared to the cytosolic volume.

6.2.4.1 ROS Flux Across the Plasma Membrane

The rate of ROS transport across the plasma membrane from extracellular space to the cytosol is described based on [255]:

$$J_{perm} = K_{perm}\,(ROS_{ext} - ROS_{cyt}) \quad \text{Equation 6-4}$$

where Kperm is the coefficient to describe the permeability of ROS through the plasma membrane and is adjusted to reflect the surface area of the cell, as was done in [255].

6.2.4.2 Production of ROS

ROS is produced as a result of many reactions within the cell. NADPH oxidases are commonly activated to produce either superoxide or H_2O_2 during T cell signaling and two exist in T cells: Nox2 (J_{nox}), and Duox1 (J_{duox}), which is also sensitive to Ca^{2+} [37, 256].

Nox2 has been extensively studied due to its importance in phagocytic oxidative burst during T cell activation, which subsequently controls many interwoven aspects of the signaling cascade. Nox2 activation occurs as a result of a series of complex protein-protein interactions and proper phosphorylation is required for full activity [52, 257]. We further simplified previous models of NOX activation in epithelial cells [258] to be dependent solely upon IP_3 for activation since the same upstream effector for IP_3 is also responsible for activating protein kinase C (PKC), which phosphorylates downstream targets through RAS [259, 260], ultimately activating Nox2:

$$J_{nox} = V_{nox}\left(\frac{IP3}{IP3 + K_{nox}}\right) \qquad \text{Equation 6-5}$$

In this equation, V_{nox} is the maximal rate of ROS production via Nox2 and K_{nox} is the concentration of IP_3 at which the reaction rate is half of V_{nox}.

The other NAPDH oxidase studied here, duox1, is dependent on Ca^{2+} and has been shown to be important during the initial, rapid production of H_2O_2 upon TCR engagement. ROS production via Duox1 is described as linear with respect to IP_3 and a 2nd order Hill function with respect to cytosolic Ca^{2+} levels based on its activation via Ca^{2+} binding to EF hand motifs and phosphorylation through PKC/PKA-dependent routes [261]:

$$J_{duox} = V_{duox} IP3 \left(\frac{Ca_{cyt}^2}{Ca_{cyt}^2 + K_{Duox}^2} \right)$$ Equation 6-6

where V_{duox} is the maximal rate of ROS production by Duox1 and K_{duox} is the concentration of Ca_{cyt} at which the reaction rate is half of V_{duox}.

Another notable source of ROS is from the electron transport chain in the mitochondria. It has been shown previously that ROS production is increased, specifically from the mitochondria, but the connection to Ca^{2+} signaling is still being discerned. There are currently conflicting reports suggesting under some inhibitory conditions, Ca^{2+} induced ROS production in the mitochondria, but under normal conditions it may be reduced upon Ca^{2+} signaling [90, 262]. Due to this discrepancy, mitochondrial production was described with a constant rate with no dependence on Ca^{2+}:

$$J_{mitprod} = V_{mitprod}$$ Equation 6-7

6.2.4.3 Cytoplasmic Scavaging of ROS

Previously generated models [255] were combined into a single 1st order mass action kinetic equation to describe the redox reactions and other protein thiol modifications responsible for metabolizing H_2O_2, with k_{scav} representing the scavenging rate constant:

$$J_{scav} = k_{scav} ROS_{cyt}$$ Equation 6-8

6.2.4.4 Permeability of ER Membrane

It has been shown that ER ROS levels increase in response to bolus additions of H_2O_2, suggesting the ER membrane is somewhat permeable to this molecule [263]. We model this as being dependent on the difference in concentration through time:

$$J_{ERperm} = K_{ERperm}(ROS_{cyt} - ROS_{cytinit}) \quad \text{Equation 6-9}$$

with k_{ERperm} being the permeability of the ER membrane to ROS.

6.2.4.5 ER Production of ROS

The ER is the site of protein folding and requires a highly oxidative environment to ensure the proper post translational modifications can occur. To create this environment, there are many sources of ROS present in the ER, including oxygenases and oxidases [264]. Ero1α is also a significant source of ROS in the ER and helps to set the highly oxidized state while reducing fluctuations via a feedback mechanism [265-267]. We have simplified this production rate below:

$$J_{ERprod} = V_{ero1}\left(\frac{K_{ero1}^{nprod}}{ROS_{ER}^{p_{10}} + K_{ero1}^{nprod}}\right) \quad \text{Equation 6-10}$$

where V_{ero1} maximum production rate of ROS by Ero1, K_{ero1} is concentration of ROS_{ER} at which the reaction rate is half of V_{ero1}, and the Hill coefficient is represented with n_{prod}.

6.2.4.6 ER Scavanging of ROS

The ER is also able to reduce ROS, by means such as the thiol/disulfide system that includes glutathione, newly synthesized proteins, pyridine nucleotides, and glucose-6-phosphate (G6P) [259]. It was shown in [263] that ER levels decrease after Ca^{2+} mobilization, without ERO1α activity, suggesting Ca_{ER} levels affect ROS degradation [261]. This aligns with other work that suggests low intraluminal Ca^{2+} can lead to an altered redox status and ultimately misfolded proteins. Simplifying these interactions, we arrive at the following equation:

$$J_{ERscav} = k_{ERscav} ROS_{ER} \left(\frac{K_{ERscav}^{nscav}}{Ca_{ER}^{nscav} + K_{ERscav}^{nscav}} \right) \qquad \text{Equation 6-11}$$

where k_{ERscav} is the maximum rate of ROS scavenging in the ER and K_{ERscav} is the concentration of Ca_{ER} at which the reaction rate is half of k_{ERscav} and nscav is the associated Hill coefficient.

6.2.4.7 Model Equations: Ca^{2+} Module

The second module contains interactions involved with Ca^{2+} signaling and represents the same mathematical description as in Chapter 5 for the main fluxes between intracellular compartments, with the addition of ROS modulatory parameters, described below. Reflecting those in Chapter 5, the main equations of Ca^{2+} kinetics are given here:

$$\frac{dCa_{cyt}}{dt} = \beta_i \big((J_{IP3} - J_{serca} + J_{ERleak}) + (-J_{mitin} + J_{mitout}) + (J_{crac} - J_{PMCA} + J_{PMleak}) \big) \qquad \text{Equation 6-12}$$

$$\frac{dCa_{ER}}{dt} = \frac{\beta_{ER}}{\rho_{ER}}(-J_{IP3} + J_{serca} - J_{ERleak}))$$ Equation 6-13

$$\frac{dCa_{mit}}{dt} = \frac{\beta_{mit}}{\rho_{mit}}(J_{mitin} - J_{mitout})$$ Equation 6-14

Ca_{cyt} and β_i represent the concentration of Ca^{2+} and the ratio of free to total Ca^{2+} in the cytosol, respectively. Ca_{mit} and β_{mit} represent the concentration of Ca^{2+} and the ratio of free to total Ca^{2+} in the mitochondria. Similarly, Ca_{ER} and β_{ER} represent the concentration of Ca^{2+} and the ratio of free to total Ca^{2+} in the ER [188, 197]. We use ρ_{mit} and ρ_{er} to correct for the difference in volume between the ER and mitochondria compared to the cytosol. There are many proteins involved with Ca^{2+} buffering that have the potential to be redox sensitive, but oxidation of various proteins results either increased or decreased affinity for Ca^{2+}, and thus these mixed effects have been left out of the equations.

6.2.4.8 <u>Ca^{2+} Flux into the ER</u>

Ca^{2+} flux from the cytosol to the ER is modulated through IP_3R channels, which have the ability to be redox regulated at several cysteine residues. For example, IP_3R1 has 60 cysteine residues, with 70% shown to be in the reduced state with diverse regulatory significance and accessibility [268]. IP_3R activation can also be sensitized via oxidation of thiol groups by thimesoral or GSSG such that lower levels of IP_3 are able to activate channel activity [85, 269, 270]. Duox1 is also co-expressed with IP_3R in T cells, suggesting Duox1 activity may provide a positive feedback necessary for IP_3R activity [271]. Finally, some studies found a potential link between ER redox state and the

functional activity of IP_3R, even without specific purported cysteine residues that would give rise to these specific modifications [272-274]. From these interactions, we describe the ROS modulation as a redox dependent modification of the IP_3 affinity constant:

$$J_{IP3} = V_{IP3} Ca_{ER} \mathrm{P_{IP3}} \qquad \text{Equation 6-15}$$

where V_{IP3} is the maximal flux of Ca^{2+} through IP_3R into the ER, and P_{IP3} is the probability that IP_3R is open. The open probability can be described as a function of Ca_{cyt}, IP_3 concentration, and h, which is the fraction of IP_3R that does not have Ca^{2+} bound to the inhibitory site:

$$P_{IP3} = \left(\left(\frac{IP3}{IP3 + \mathrm{K_{IP3ros}}} \right) \left(\frac{Ca_{cyt}}{Ca_{cyt} + K_{act}} \right) h \right)^3 \qquad \text{Equation 6-16}$$

where K_{act} is the midpoint of Ca^{2+}-dependent channel activation and K_{IP3ros} represents the ROS dependent dissociation of IP_3 from the IP_3 binding site:

$$K_{IP3ros} = K_{IP3} \left(\frac{k_{IP3ros}^{nrosIP3}}{ROS_{cyt} + k_{IP3ros}^{nrosIP3}} \right) \qquad \text{Equation 6-17}$$

with K_{IP3} representing the concentration of IP_3 at which the half maximal observed reaction rate is achieved, k_{IP3ros} is the concentration of ROS_{ER} that leads to half maximal altered IP_3 binding affinity and nrosIP3 is the Hill coefficient for this process.

We also define the fraction of inactivated IP_3R, (1-h), to be a function of Ca_{cyt} and the affinity of Ca^{2+} for the inhibitory site, Q:

$$\frac{dh}{dt} = A\left((1-h)\left(Q + Ca_{cyt}\right) - Ca_{cyt}\right) \qquad \text{Equation 6-18}$$

$$Q = \frac{K_{inh}(IP3 + \mathrm{K_{IP3ros}})}{IP3 + K_{IP3inh}} \qquad \text{Equation 6-19}$$

where A is a factor to control the relative time scales, K_{inh} is the affinity of Ca^{2+} for the inhibitory site, and K_{IP3inh} is the altered IP_3 affinity to its binding site when Ca^{2+} is bound to the inhibitory site.

6.2.4.9 <u>Ca^{2+} Flux into the ER via SERCA</u>

Ca^{2+} is actively sequestered into the ER via SERCA pumps, which have between 22 and 28 cysteine residues that are redox sensitive to inhibit pump activity during high ROS_{cyt} levels [92, 271, 275]. For simplicity, we modeled a general modification of combined SERCA isoforms dependent on ROS_{cyt}:

$$J_{serca} = V_{serca}\left(\frac{Ca_{cyt}^2}{Ca_{cyt} + K_{serca}^2}\right)\left(\frac{k_{sercaros}^{nsercaros}}{ROS_{cyt}^{nsercaros} + k_{sercaros}^{nsercaros}}\right) \qquad \text{Equation 6-20}$$

where V_{serca} is the maximal velocity of Ca^{2+} through SERCA pumps, K_{serca} is the concentration of Ca_{cyt} at which the reaction rate is half of V_{serca}, $k_{sercaros}$ is the concentration of ROS_{cyt} concentration for half maximal pump inhibition and nsercaros is the associated Hill coefficient.

6.2.4.10 ER Ca^{2+} Leak

Due to the increase in nonselective membrane permeability upon high levels of ROS_{ER}, we modified J_{ERleak}:

$$J_{ERleak} = K_{ERleak} Ca_{ER} \left(1 + \frac{ROS_{ER} - ROS_{ERinit}}{ROS_{ERinit}}\right) \quad \text{Equation 6-21}$$

where K_{ERleak} is the constant leak of Ca^{2+} through the ER membrane and ROS_{ERinit} is the initial level of ROS in the ER.

6.2.4.11 Mitochondrial Control of Ca^{2+}

The mitochondrial control of Ca^{2+} remains unaltered from Chapter 5 because there are no confirmed reports of redox modification of the channels and pumps involved with Ca^{2+} transport across the mitochondrial membrane:

$$J_{mitin} = V_{mitin} \left(\frac{Ca_{cyt}^4}{Ca_{cyt}^4 + K_{mitin}^4}\right) \quad \text{Equation 6-22}$$

$$J_{mitout} = V_{mitout} Ca_{mit} \left(\frac{Ca_{cyt}^2}{Ca_{cyt}^2 + K_{mitout}^2}\right) \quad \text{Equation 6-23}$$

6.2.4.12 Ca^{2+} Transport Through the Plasma Membrane

SOCE is dependent on ER Ca^{2+} depletion to activate STIM1. STIM1 dimerizes and associates with ORAI1 at the plasma membrane to activate CRAC channels. It is not

clear from literature what role redox regulation plays in SOCE, and conflicting reports led us to keep the flux identical to that described in Chapter 5.

$$J_{crac} = V_{crac}\left(\frac{K_{stim}^3}{Ca_{ER}^3 + K_{stim}^3}\right)\left(\frac{Ca_{ext}}{Ca_{ext} + K_{soc}}\right) \quad \text{Equation 6-24}$$

Similarly, the leak of Ca^{2+} ions through the plasma membrane is not thought to be redox regulated and hence was kept the same as in Chapter 5:

$$J_{PMleak} = K_{PMleak} Ca_{ext} \quad \text{Equation 6-25}$$

Similar to SERCA pumps, PMCA pumps are thought to be inhibited by oxidation in the presence of high levels of ROS [276, 277]. As such, Ca^{2+} flux through the plasma membrane into extracellular space has been modified:

$$J_{PMCA} = V_{pmca}\left(\frac{Ca_{cyt}^2}{Ca_{cyt}^2 + K_{pmca}^2}\right)\left(\frac{k_{pmcaros}^{npmcaros}}{ROS_{cyt}^{npmcaros} + k_{pmcaros}^{npmcaros}}\right) \quad \text{Equation 6-26}$$

where V_{pmca} is the maximum rate of efflux of Ca^{2+} via PMCA pumps, K_{pmca} is the concentration of Ca_{cyt} at which the reaction rate is half of V_{pmca}, $k_{pmcaros}$ is the concentration of ROS_{cyt} necessary for half maximal pump inhibition and $n_{pmcaros}$ is the associated Hill coefficient.

6.2.5 ROS and Calcium Model: Parameter Optimization

Parameter estimation was achieved via a sum of squared error function, taking into account the difference between collected experimental data and the model prediction for different parameter sets. This was achieved by using the genetic algorithm (*ga*) in the MATLAB® Global Optimization Toolbox. For estimating modeling predictions against different experimental conditions, the objective function was estimated below as in Chapter 5:

$$S = \sum_{t=1}^{t_{sim}} \sum_{n=1}^{N} \sum_{c=1}^{C} \left(\frac{x_{pred}(c,n,t) - x_{exp}(c,n,t)}{x_{exp}(c,n,t)} \right)^2 \qquad \text{Equation 6-27}$$

We kept the parameters from Module 2 consistent with the Jurkat Model results from Chapter 5 where possible, and varied Module 1 parameters while fitting to data available in the literature. The model was simultaneously fit to three different datasets found in literature on the ROS_{ER} concentration changes through time [263]. The first dataset was captured in response to DTT and we represented this ROS scavenger with an 8-fold increase in the scavenging rate of the cytosol and ER. The second dataset was collected in the presence of thapsigargin and we represented this with an 85% reduction in V_{serca}. The third data set was recorded in response to histamine treatment, and because this time course was reminiscent of Ca^{2+} kinetics following TCR ligation, we increased the IP_3 input function for the first 5 minutes of treatment to accommodate the experimental perturbation. Parameters were simultaneously allowed to vary with the initial conditions for each species. Many parameters identified in Chapter 5 were kept constant.

Table 6-1: Optimized Initial Conditions for ROS/Ca^{2+} Model.
Initial conditions were allowed to vary in physiological ranges according to literature to best fit the experimental data.

Parameter	Optimized Initial Condition	Bounds
ROS_{ext}	0.012 μM	[0.0005, 0.05] μM
ROS_{ER}	79.2 μM	[60, 100] μM
ROS_{cyt}	0.012 μM	[0.0005 0.05] μM
Ca_{cyt}	0.0376 μM	[0.01, 0.1] μM
Ca_{ER}	338 μM	[250 550] μM
Ca_{mit}	0.108 μM	[0.05, 2] μM
h	0.97	[0.5, 0.99]

Table 6-2: Optimized Parameter Values for ROS/Ca^{2+} Model.
Many parameters were set constant to the Jurkat model values from Chapter 5. Some values were modified or introduced based on ROS interactions within the network of equations.

Parameter	Optimized Parameter Value	Bounds	Source/Explanation
β_i	0.056	0.056	Chapter 5
β_{er}	0.049	0.049	Chapter 5
β_{mit}	0.033	0.033	Chapter 5
ρ_{er}	0.015	0.015	[213]
ρ_{mit}	0.08	0.08	Chapter 5
V_{IP3}	4.0 s-1	4.0 s-1	Chapter 5
K_{act}	0.13 μM	0.13 μM	Chapter 5
A	0.079	0.079	Chapter 5
K_{inh}	1 μM	1 μM	Chapter 5
K_{IP3inh}	0.82 μM	0.82 μM	Chapter 5
K_{ERleak}	0.0043 s-1	0.0043 s-1	Chapter 5
K_{serca}	0.43 μM	0.43 μM	Chapter 5
V_{mitin}	388.6 μM s-1	388.6 μM s-1	Chapter 5
K_{mitin}	0.81 μM	0.81 μM	Chapter 5
V_{mitout}	188.9 μM s-1	188.9 μM s-1	Chapter 5

Table 6-2 continued.

K_{mitout}	4.03 μM	4.03 μM	Chapter 5
V_{crac}	2.4 μM s-1	2.4 μM s-1	Chapter 5
K_{soc}	363.5 μM	363.5 μM	Chapter 5
K_{stim}	178.1 μM	178.1 μM	Chapter 5
K_{PMleak}	1.1e-6 s^{-1}	1.1e-6 s^{-1}	Chapter 5
K_{pmca}	0.11 μM	0.11 μM	Chapter 5
K_{perm}	0.096 s^{-1}	[1e-2 1e-1] s^{-1}	Adapted from [278], according to [194]
V_{nox}	1.03e-5 μM s^{-1}	[1e-7 1e-4] μM s^{-1}	[194]
K_{nox}	4.00 μM	[1 8] μM	[194]
V_{duox}	6.00e-5 μM s^{-1}	[1e-7 1e-4] μM s^{-1}	[194]
K_{duox}	0.052 μM	[0.05 1] μM	[194]
K_{ERperm}	0.098 μM	[1e-4 0.1] μM	[194]
V_{ero1}	0.0021 μM s^{-1}	[1e-4 1e-2] μM s^{-1}	Adapted from [279] according to [194]
K_{ero1}	120 μM	[85 120] μM	[194]
$nprod$	6	[1 6]	[194]
k_{ERscav}	5.74e-5 s^{-1}	[4e-5 7e-5]	[194]
K_{ERscav}	306 μM	[150 350] μM	[194]
$nscav$	3	[1 6]	[194]
K_{IP3}	1.77 μM	[0.1 5] μM	Modulated from Chapter 5
V_{serca}	300 μM s^{-1}	[85.8 300] μM s^{-1}	Modulated from Chapter 5
V_{pmca}	2.22 μM s^{-1}	[1.5 10] μM s^{-1}	Modulated from Chapter 5
$V_{MitProd}$	1.2e-6 μM s^{-1}	1.2e-6 μM s^{-1}	[194]
k_{scav}	1.2e-3 s^{-1}	1.2e-3	Adapted from [278] according to [194]
k_{IP3ros}	0.0442 μM	0.0442 μM	Adapted from [280] according to [194]
$nrosIP3$	0.462	0.462	
$k_{sercaros}$	1.151 μM	1.151 μM	Adapted from [92], according to [194]
$nsercaros$	0.38	0.38	
$k_{pmcaros}$	0.258 μM	0.258 μM	Adapted from [277], according to [194]
$npmcaros$	1.147	1.147	

6.2.6 Fitting Transfer Function Model

Parameters to the 2nd order system function were fit to the median of the single-cell data at each frequency by using the same approach as for the ROS Ca^{2+} model. These parameters include K, the system gain, ζ, the damping coefficient, and ω_n, the systems

natural frequency in rad/s. The parameters are allowed to vary between given bounds while evaluating the genetic algorithm (ga) in the MATLAB® Optimization Toolbox™.

$$H(s) = K * \frac{1}{s^2 + 2\zeta\omega_n + \omega_n^2} \qquad \text{Equation 6-28}$$

Table 6-3: Optimized Parameter Values for Transfer Function Fit.

Parameter	Optimized Parameter Values			Bounds
	Population	Top 25%	Bottom 25%	
K	7.09e-7	7.80e-6	1.53e-7	[1e-8, 1e-3]
ζ	0.0220	0.104	0.00240	[1e-5, 1]
$\boldsymbol{\omega_n}$	0.0177 rad/s	0.0168 rad/s	0.0190 rad/s	[0.015, 0.019] rad/s
Error	3.7640	2.5980	3.4388	
Poles	-0.0004 +/- 0.0177i	-0.0017 +/- 0.0167i	-0.000045 +/- 0.0190i	
Stable?	Yes	Yes	Yes	

6.2.7 Frequency Response Analysis

Frequency response analysis does not require previous knowledge of a system, but rather treats the system as a black box and visualizes only the output response to the known sinusoidal input signal. To do this, the input and output signals must be decomposed into their frequency components. More specifically, any signal can be represented as a sum of sine waves using the Fourier transform. Mathematically, we derive the Fourier coefficient $\hat{R}(\omega)$ of an output signal R(t), at angular frequency, ω, with the following equation:

$$\hat{R}(\omega) = \frac{2}{nT}\int_0^{nT} e^{-i\omega t} R(t)\, dt \qquad \text{Equation 6-29}$$

where n is number of sampled periods. The resulting Fourier coefficient is a complex number whose amplitude and phase can be calculated for each frequency ω, by taking the norm and angle of the Fourier coefficient. While many systems utilize a noisy input signal composed of a wide range of sinusoidal inputs to calculate the resulting gain and phase for each frequency sampled in the output signal, it is difficult to apply this system to our complex signaling network as it will be difficult to ascertain if experimental signals are solely the result of underlying sinusoidal inputs presented to the cell or if they are a result of experimental noise. As such, we decided to sample the system with a sinusoidal input composed of a single frequency. The resulting gain and phase are calculated for each frequency and compiled for multiple sampled frequencies into a Bode Plot.

This Bode Plot can be investigated using a transfer function to mathematically describe the system's behavior. Transfer functions are represented in the Laplace Domain as:

$$H(s) = \frac{Y(s)}{U(s)} = K\frac{\prod_m s + z_m}{\prod_n s + p_n} \qquad \text{Equation 6-30}$$

Where H(s) is the quotient of the Laplace transform of the output signal y(t) and the Laplace transform of the input signal u(t). This can also be represented as the product of the zeros, z_m, and poles, p_n, of the system, where m is the number of zeros and n is the number of poles with $m \leq n$. K is the system gain. The frequency response, H(s) can be calculated for given frequencies, ω.

Due to the complex nature of our system and the many non-linearities present in the equations, we chose to instead probe the system with a given input to reverse engineer the transfer function estimation. The *in silico* frequency response was created by driving the model with an oscillatory H_2O_{2ext} input and calculating the gain and phase response of the output signal of interest, Ca_{cyt}. The gain and phase was computed for each frequency sampled using the fast Fourier transform (FFT) in MATLAB® (Mathworks).

6.3 Results

6.3.1 Single-cell Analysis Reveals Response to Oscillatory Stimulation

Once single-cell calcium traces were analyzed, they were compiled to provide insight to the response of cells to frequencies of interest. For cells receiving a frequency of 2.78 mHz, corresponding to a period of 6 minutes, we observed a wide range of dynamic responses and resulting dominant frequencies to a given stimulation, thus highlighting the emphasis to look at a single-cell response as opposed to the population average of these experiments (Figure 6-2a,d). This experimental condition was compared to two controls for mechanical switching of fluid flow: (1) media control where the cellular microenvironment switched at the same frequency but both solutions contained standard RPMI media and (2) H_2O_2 control where the two solutions were both 25 μM H_2O_2 supplemented RPMI media. We observed a clear entrainment of many cells to the oscillatory hydrogen peroxide stimulation; this was more pronounced than in the control conditions (Figure 6-2). It is evident from these single-cell traces that cells become entrained to specific driving frequencies, in particular the oscillating H_2O_2 condition as compared to the two controls (Figure 6-2d-f).

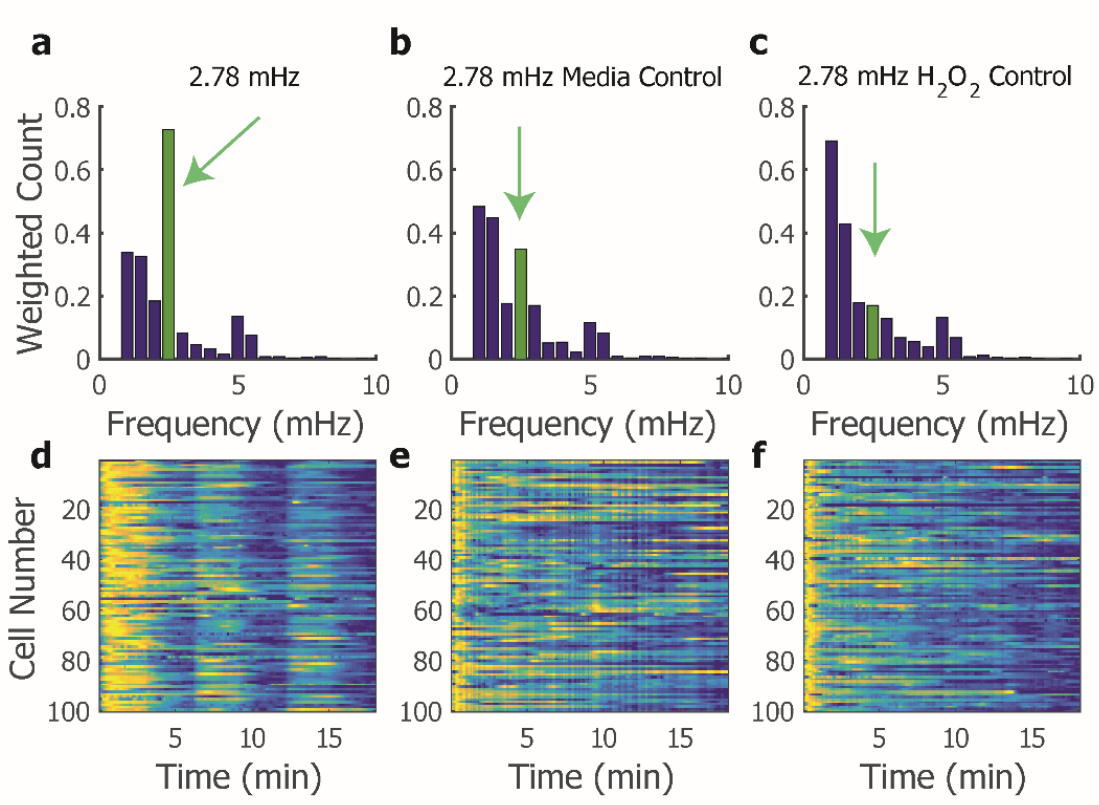

Figure 6-2: Single-cell analysis reveals observable entrainment to oscillatory H_2O_2 treatment when compared to controls.
Cells were stimulated with three different oscillatory conditions, all of which were performed at 2.78 mHz frequency. (a,d) For the treatment condition, the cellular environment alternated between 25 µM H_2O_2 supplemented RPMI media and RPMI media. (a) The resulting histogram of dominant frequencies shows a peak at the driving frequency (green arrow) and (d) the heatmap of cytoplasmic calcium concentration through time for cells shows the same entrainment characteristics. (b,e) For the media control, the cellular environment alternated at the same frequency, but both fluids contained only RPMI media. (b) The histogram of dominant frequencies shows a reduced peak as compared to the treatment condition and (e) the heatmap of cellular traces similarly shows less entrainment to the driving frequency. (c,f) The H_2O_2 control was also driven at 2.78 mHz frequency but both fluids contained 25 µM H_2O_2 supplemented RPMI media. (c) The histogram of dominant frequencies and (f) heatmap of cellular traces also show less entrainment to the driving frequency. For (a-c), the frequency domain is reduced to 10 mHz for easier visualization.

We also visualized the dominant frequencies present in cell signals when driven with a frequency of 2.78 mHz, and found a peak in dominant frequencies of the treated cells corresponding to the driving frequency. Both the media and H_2O_2 controls showed a

reduced peak in dominant frequency at the entrainment value (Figure 6-2a-c), indicating the experimental application of oscillatory H_2O_2 drives this Ca^{2+} response. This population-based visualization shows that although the population is heterogeneous in responses, there is an appreciable shift to correspond with the driving frequency of H_2O_2 stimulation in at least a subset of the population.

6.3.2 Input Amplitude Alters Cellular Entrainment for a Given Frequency

Experiments were repeated for different concentrations of H_2O_2 (10, 25, 50, and 100 μM) and we observed from the dominant frequency histograms that the entrainment is dependent on input amplitude (Figure 6-3a-d). These experiments were all driven at the same frequency, as shown before, of 2.78 mHz and only the 25 μM condition exhibits a large peak in output signal at this frequency (Figure 6-3b).

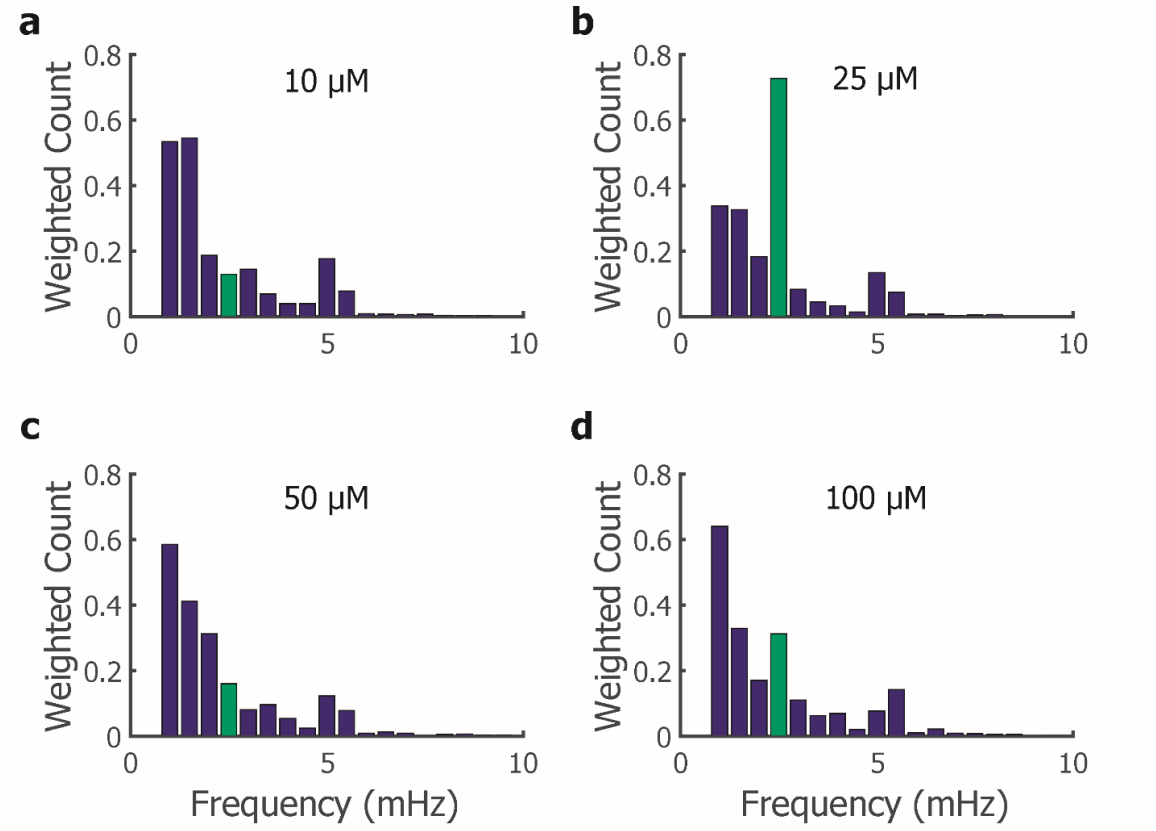

Figure 6-3: The amplitude of oscillatory stimulation differentially regulates the output signal with maximal entrainment at 25 μM.
We applied the same 2.78 mHz signal to cells but altered the amplitude of the input via H_2O_2 concentration. We repeated the same experiment at (a) 10 μM (b) 25 μM (c) 50 μM and (d) 100 μM. The dominant frequency histograms are shown for each experimental condition and clearly show entrainment only for the 25 μM condition. The frequency domain is reduced to 10 mHz for easier visualization.

We concluded this concentration was ideal for eliciting the Ca^{2+} signal; concentrations lower than 25 μM H_2O_2 were not able to elicit the robust response and similarly, those concentrations tested above 25 μM H_2O_2 also had diminished responsiveness at the driving frequency, potentially due to cytotoxic effects of high ROS. From these results, all subsequent experiments were done with 25 μM H_2O_2.

6.3.3 Cellular Entrainment is Dependent on Input Frequency

While keeping the concentration of H_2O_2 constant at 25 μM H_2O_2, the input frequency was varied in different experiments between 16.7 mHz (1 minute period) and 0.83 mHz (20 minute period). The cells responded to at least the initial input of H_2O_2 signal, but not all frequencies elicit the same entrainment seen with 2.78 mHz (Figure 6-4f-j). For instance, at the higher frequencies of 16.7 and 8.3 mHz cells did not respond to later inputs of hydrogen peroxide but instead appear to slowly diminish in intracellular calcium signaling (Figure 6-4f-g). This was corroborated by the histograms of dominant frequencies, which show very low or no response in the frequency domain at the driving frequency, as denoted with the green arrow (Figure 6-4a,b).

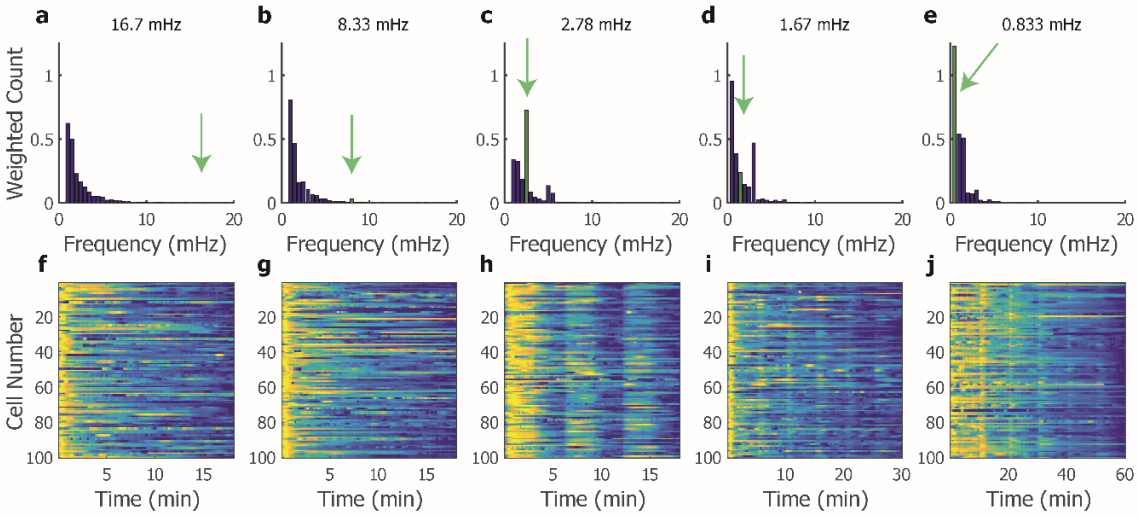

Figure 6-4: Differences can be seen in output signal with different input frequencies of H_2O_2.
We applied oscillating 25 μM H_2O_2 input signals to the cells at various frequencies: (a,f) 16.7 mHz, (b,g) 8.33 mHz, (c,h) 2.78 mHz, (d,i) 1.67 mHz, (e,j) 0.833 mHz. The dominant frequency histograms are shown in (a-e) with the respective driving frequency denoted by the green arrow. Corresponding heatmaps showing the first 100 cells from a representative experiment are shown in (f-j). The frequency domain is reduced to 20 mHz for easier visualization.

This could potentially be the result of fatigue of the system, such that the calcium signaling mechanistically cannot recover and respond at this rate. For experiments done at lower frequencies, the cells appear to recover between oscillations and exhibit an increase in calcium signaling when the environment is altered, although this increase was not sustained through the duration of H_2O_2 application (Figure 6-4i,j). These higher frequencies elevate the H_2O_2 in the cellular environment for longer periods, potentially harming the cell or exhausting the calcium signaling. The cellular response heatmaps also demonstrate the same theme of population heterogeneity; single-cells often have varying responses to the same input signal and this approach best captures those differences. The majority of cells can be seen responding in the 2.78 mHz frequency with the greatest entrainment.

6.3.4 Second Order System Model Describes the Behavior of T Cells in Response to Varying Stimulation

Once the above analysis was performed for each experimental condition (Figure 6-4), the gain and phase of individual cells was compiled across at least 3 independent experiments for each frequency (Figure 6a-d). It can be seen here that there is a definitive peak in the gain response and the 6 minute period emerges as compared to all others (Figure 6a,b). It should also be noted that there is a drop in phase as the frequency increases concomitant with an increase in variability.

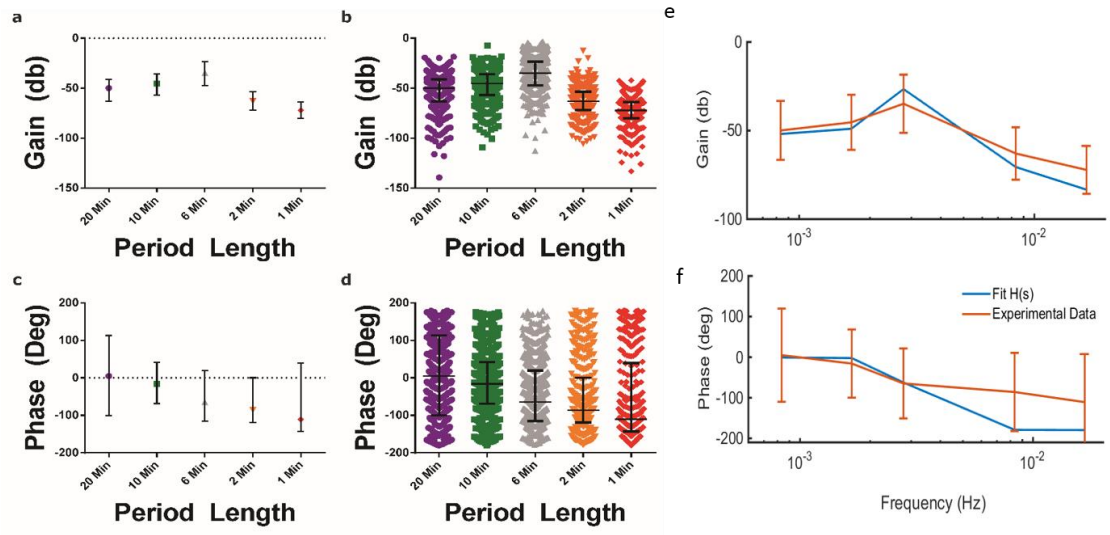

Figure 6-5: The Bode plot representation of the data is well approximated with second order behavior with a resonant frequency at approximately 6 minute oscillations (2.78 mHz).
All error bars are shown as median with the inter-quartile range to show the distribution of the population. Gain was calculated for individual cells and plotted as (a) the median with interquartile range and (b) a scattered dot plot where each dot represents a single-cell calculation. Phase was similarly calculated for individual cells and plotted as (c) the median with interquartile range and (d) a scattered dot plot where each dot represents a single-cell calculation. This experimental data was fit to a second order transfer function as shown in (e-f).

More specifically, there is a noticeable decline in gain and phase past the 2.78 mHz experimental condition, indicating a decrease in the cell's ability to entrain to periods lower than 6 minutes. This conclusion is in line with previous reports of biological systems behaving as low-pass filters [281]. As cells must filter out numerous environmental cues and assimilate them to mount a response [282-284]; it would require a great energy expenditure to respond to every fluctuation in the environment. As such, these cells appear to filter out signals above and below the experimental condition of 2.78 mHz, but can still be seen entrained slightly with the 10 and 20 minute period conditions. This visualization also provides an unparalleled view of single-cell responses within a

population of genetically similar Jurkat T cells, which has a surprisingly large variation in magnitude.

We sought a transfer function to enhance our understanding of the underlying biological network while providing a model for future hypothesis driven experimentation. The experimental data suggested a resonant frequency at approximately 2.78 mHz and damping. This data trend aligns with an overdamped, second order transfer function of the form:

$$H(s) = K * \frac{1}{s^2 + 2\zeta\omega_n + \omega_n^2} \qquad \text{Equation 6-31}$$

where K is the system gain, ω_n is the natural frequency in rad/s, and ζ is the damping factor. When fit to the median of the experimental conditions across various frequencies, and our resultant transfer function aligned well (Figure 6-5e,f).

We then subdivided the population of cells into quartiles based on the gain response and again fit the data to a second order band pass filter to compare the parameters between subpopulations (Figure 6-6 and Table 6-3). For the top 25% of cells, we see a much more damped system result, and a decrease in the range of phase values compared to both the population and to the bottom quartile. This interesting result suggests that the cells with highest gain values appears to have a less variable phase response, implying cells are more in phase with one another than when visualizing the entire population. This is not true for the bottom quartile, as the phase variation appears to be more similar to the population of cells. Although cells are not sampled for different

input frequencies, we highlight the potential for different cells within the population to have distinct and separate filtering capabilities.

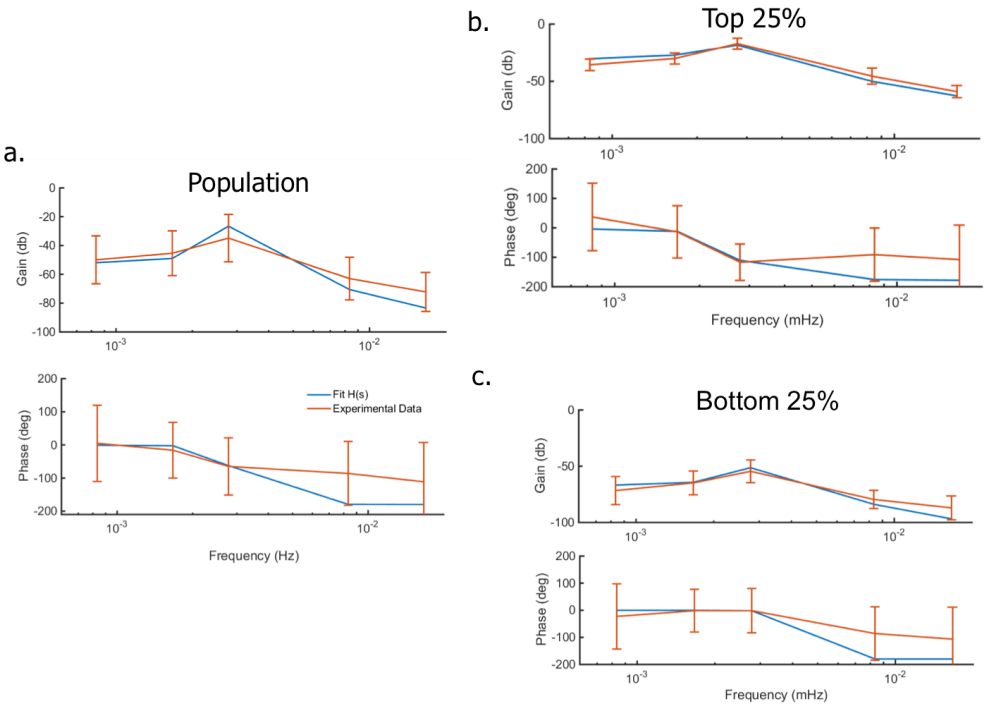

Figure 6-6: Bode Plot Fits for Different Portions of the Population.
We subdivided the population into quartiles based on the gain response and looked at the resulting transfer function fits for the (a) entire population, (b) top quartile, and (c) bottom quartile. Experimental Data is shown in orange as median +/- SD. The fit for H(s) is shown in blue.

6.3.5 ROS and Calcium Model: Fit and Frequency Response Analysis

Using the same genetic algorithm optimization approach as in 6.2.5, we fit the Ca^{2+} ROS model to data obtained in literature. As can be seen in Figure 6-7, we were able to optimize parameter values to obtain a good fit of the experimental data. This exercise showed the ability of our model to describe discrete changes in experimental conditions, such as the bolus addition of an inhibitor or H_2O_2.

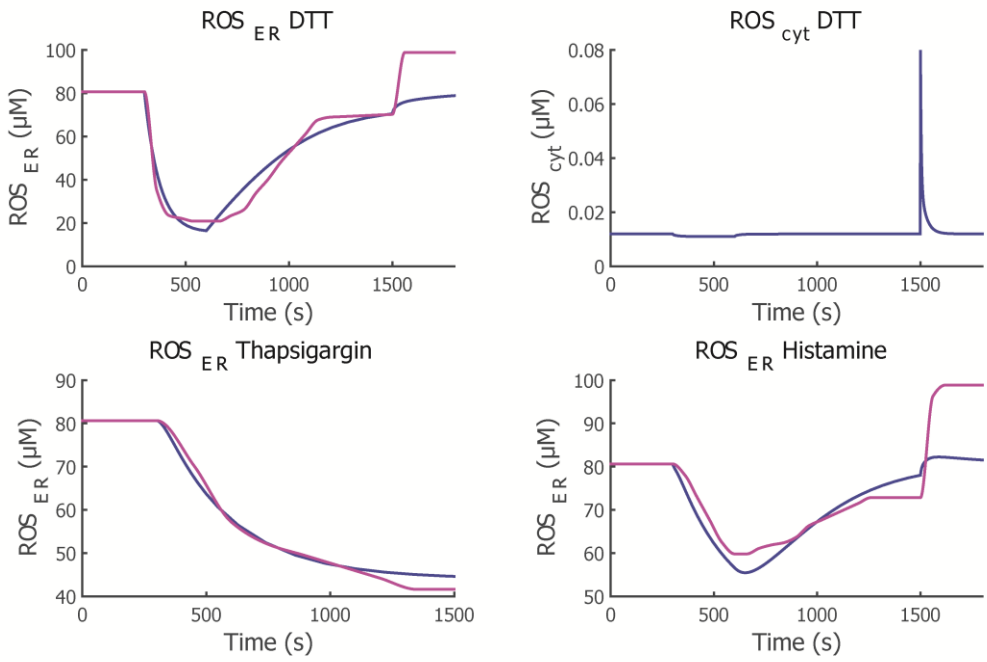

Figure 6-7: ROS Ca^{2+} Model Optimized Parameter Fit.

Furthermore, we found a steady state for the model, perturbed it with the application of a single bolus addition of H_2O_2 and observed the model behaved as expected and without an apparent nonlinear oscillatory behavior (Figure 6-8). This suggested the model was relatively stable in this regime and could potentially be driven with an oscillatory input without becoming unstable.

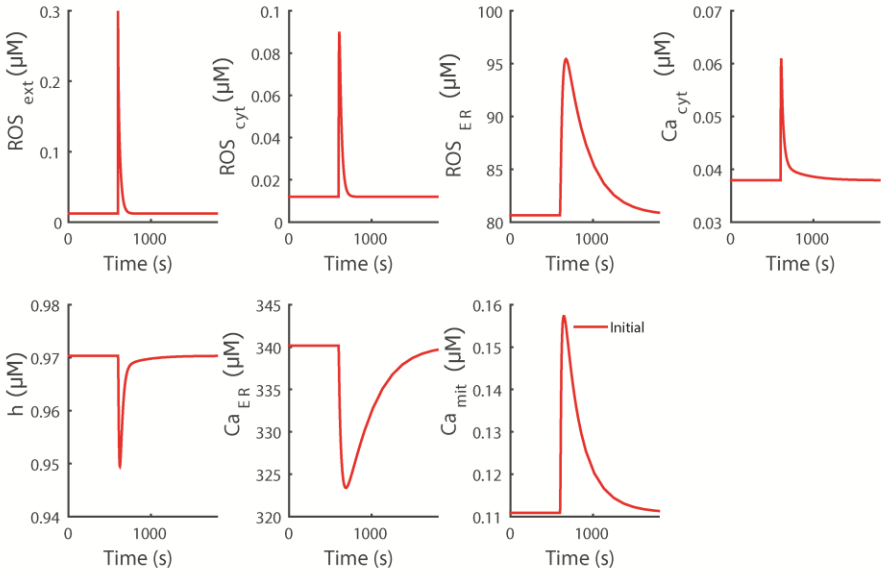

Figure 6-8: Optimized Model Perturbation with Bolus H_2O_2 Addition.

To test this hypothesis, and the stability of the model, we characterized and applied an oscillatory extracellular H_2O_2 condition, represented by a sine wave, and observed the behavior of intracellular species (Figure 6-9). In this exercise, we kept the lowest value of extracellular H_2O_2 consistent with the calculated steady state value and varied the height amplitude between 0.01 and 0.3, observing unexpected resulting behavior of the system. For instance, the steady state levels of Ca_{cyt} appear to vary based on the amplitude of ROS_{ext} (Figure 6-9). Although all responses exhibit the same oscillatory behavior, the minimum and maximum values vary between amplitude values, with the highest amplitudes resulting in average concentrations of Ca_{cyt} that are above the maximum level seen for lower amplitudes. From this, we propose the system can be modulated not only by the frequency applied, as witnessed from experimental results, but also the potential for the system to be modulated by the amplitude of signals it receives.

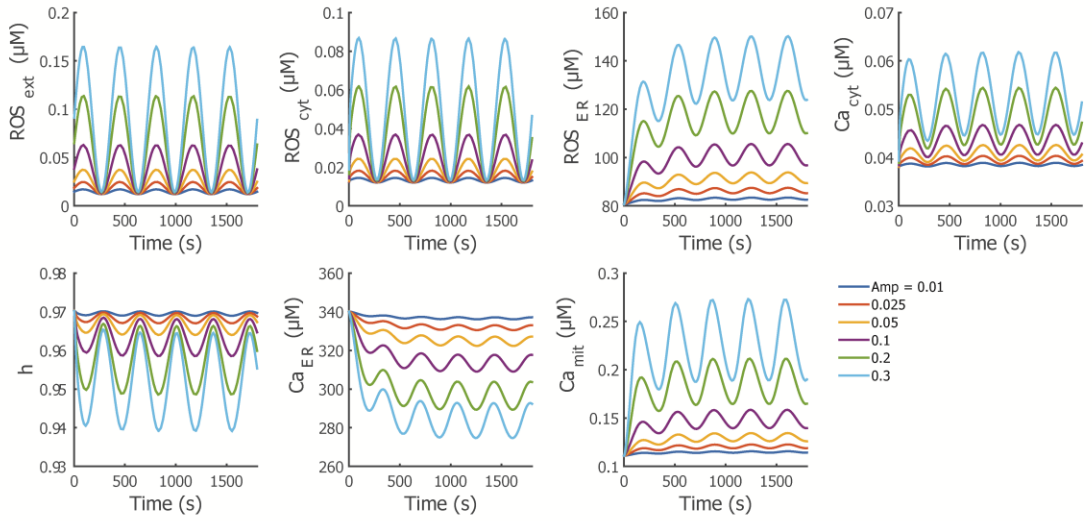

Figure 6-9: Frequency Response Analysis of the Optimized ROS Ca^{2+} Model.
The model was driven with a sinusoidal input of ROS_{ext} and the resulting dynamics were observed for other species in the model. Amplitude of the initial input signal was varied and is represented by the color of the response.

We also varied the frequency of the input signal for a given amplitude and compiled the results in a Bode Plot in Figure 6-10. This Bode Plot representation suggests the system acts as a low pass filter, attenuating signals of high frequency while exhibiting behavior to signals of low frequency. Not all species included in this model exhibit the same filter characteristics, and this suggests different components of the complex signaling network are receiving and encoding different aspects of the functional response of T cells in response to the oscillatory conditions. Another interesting finding from this *in silico* perturbation is that not all frequencies give rise to the same average steady state. In fact, it is easily seen that the higher amplitude inputs give rise to higher average levels of downstream signaling molecules, such as Ca_{cyt}. Corresponding to this increase in Ca_{cyt}, and ROS_{ER} we also observe a decrease in the average level of Ca_{ER}, indicating the ER stores are more depleted with higher amplitude oscillatory signals when compared to lower amplitude simulations. By using *in silico* perturbations, we are able to

generate testable hypotheses without running preliminary experiments. With the use of our microfluidic device, these experiments could be run *in vivo*.

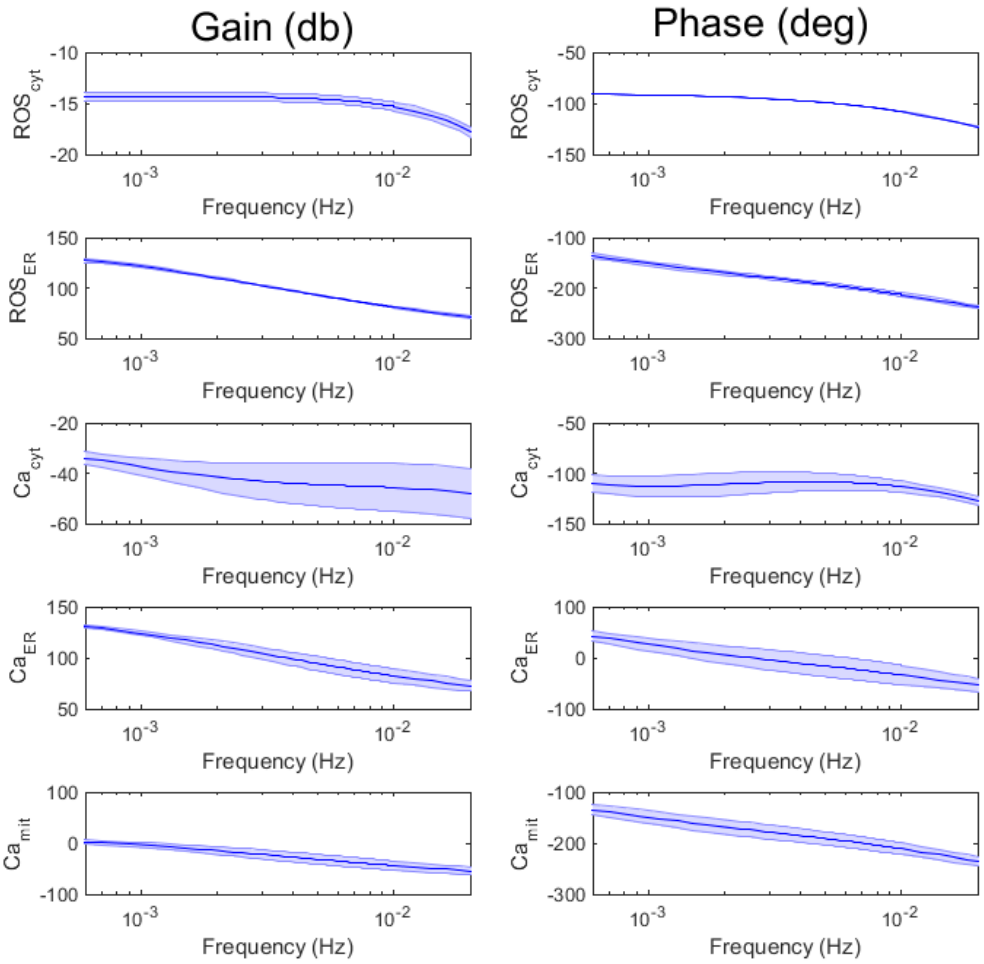

Figure 6-10: Bode Plot of the Optimized ROS Ca^{2+} Model.

6.4 Discussion

Cells are constantly responding to dynamic environmental conditions through intracellular Ca^{2+} signaling. Yet questions remain unanswered about how cells are able to use this secondary messenger to elicit a wide range of context dependent responses. Recent reports have indicated that the answer lies in better understanding the diverse

spatiotemporal dynamics giving rise to infinite patterns of Ca^{2+} responses [21, 70]. Ca^{2+} signaling is believed to increase information transmission by reducing extrinsic noise factors on the signal to noise ratio for intracellular signaling cascades [285]. However, current technological approaches limit the delivery of environmental cues and subsequent analysis of single-cell behavior. We contribute novel findings to the field by combining microfluidic and computational technologies to overcome this technical barrier and gain a better understanding of Ca^{2+} signaling in T cell lymphocytes through frequency response analysis.

Using frequency response analysis, it is possible to probe intracellular signaling networks, without prior knowledge of the system, by applying an oscillatory input stimulus and calculating the gain and phase of the resulting output signal. Using this approach, we were able to monitor cytoplasmic calcium in response to H_2O_2, a reactive oxygen species that has been shown to be upregulated in T cell activation and plays a role in signal transduction. This unprecedented view of the interplay between calcium and H_2O_2 also delineates differences between individual cells in response to the same, robustly controlled, environmental signals. Such a view provides novel insight both for intracellular signaling dynamics as well as for differences between cells in a relatively clonal population.

To examine the interplay between these two signaling molecules, we applied oscillatory H_2O_2 at varying frequencies and amplitudes and compiled a Bode Plot with the results to obtain the estimated resonant frequency and damping coefficient of this second order system. We found an oscillatory H_2O_2 signal was able to entrain the calcium dynamics unlike either constant media or H_2O_2 controls (Figure 6-2). Further, we

sampled different amplitudes, or concentrations, of the input H_2O_2 signal and found an optimal concentration of 25 μM H_2O_2 (Figure 6-3). This aligns with previous literature suggesting different concentrations of Ca^{2+} stimulation can result in oscillatory or refractory signaling [106] and suggests the 25 μM H_2O_2 concentration is within the oscillatory regime of stimulation for our sampled system. With this concentration held constant, a frequency sweep was performed for 5 different frequencies and results showed a damping of signals both above and below the optimal frequency of 2.78 mHz (Figure 6-4).

This was the first application of a sinusoidal input to T cells to our knowledge but can be compared to previous reports of T cell transcriptional encoding with Ca^{2+} spikes at varying frequencies. Observed Ca^{2+} frequencies vary based on cell type and stimulation, with values on the order of tens of Hz in excitable cells to the order of mHz for non-excitable cells [286]. Our observed system falls within this reported range, with the natural frequency estimated to be at approximately 2.78 mHz for our non-excitable T cell system. The cell must decode these frequencies, usually by sensing molecules that can appropriately modify their behavior [71]. On a molecular level, Ca^{2+} is binding to phosphatases and kinases to affect downstream targets and these on-off kinetics are most likely responsible for decoding a range of possible frequencies. With oscillations below appropriate frequencies, the signal cannot integrate to mount a response. Ca^{2+} binds to many effectors with high cooperatively and high dissociation, again supporting the idea that a range of moderate frequencies, corresponding to these kinetics, encodes more information than constant Ca^{2+} signals or high frequency signals [70]. Multiple proteins

involved in T cell activation are thought to be appropriate for this signaling, including PLC-γ [75, 76], PKCβ [77] and the mitochondrial Ca^{2+} uniporter [78].

The next step in this signaling pathway is transcription of appropriate genes, and one would assume this is maximally achieved within the range of natural frequencies, hence the necessity of appropriately timed Ca^{2+} oscillations. It has been shown for multiple genes that maximal expression is tuned to particular Ca^{2+} signaling characteristics. NFAT is activated by Ca^{2+} through dephosphorylation and subsequent nuclear translocation, and has been shown to decode Ca^{2+} oscillations in T cell lymphocytes with a maximal response of 2.5-10 mHz [22] or 1-11 mHz Ca^{2+} frequencies [287]. Although differences exist in experimental design, our data falls within these effective ranges and supports our conclusions of 2.78 mHz being the natural frequency of oscillation. NFκB is another potential decoder for Ca^{2+} oscillations and was shown to have its highest response between 0.56-10 mHz [22]. Differences in frequency decoding between NFAT and NFκB may lie in the ability of NFκB to remain in the nucleus longer, thus enabling faster dynamics to still increase expression [70, 216, 288]. Experimental techniques varied between studies, with differences in input signal shape as the previous reports stimulated with constant pulse widths and altered the inter-spike duration for a duty cycle between 0.028 and 0.5 whereas we chose to use a square wave with a duty cycle of 0.5, such that the stimulation and buffer would each be applied for an equal amount of time. The second clear difference is our investigation of Ca^{2+} signaling in response to H_2O_2 stimulation whereas Ca^{2+} has previously been directly controlled through chemical clamping. In our approach we conclude H_2O_2 signaling modulates Ca^{2+}

oscillatory kinetics within an effective range necessary for downstream transcription factor activation.

Our investigation of Ca^{2+} kinetics is the first to compare the Ca^{2+} response in T cells as a Bode plot across frequencies. In our system, we show a clear entrainment of cells with a 6 min period and a cutoff frequency between 1 and 2 minutes. We fit the gain and phase of the population of cells to a 2nd order transfer function for the system (Figure 6-5). With this model representation, we have reduced the number of parameters down to 3: ω_n, ζ, and K. Reducing the system to a smaller model while retaining the pertinent responses in the frequency domain provides a unique platform for *in silico* perturbation of the interactions between Ca^{2+} and H_2O_2 in future work. Further, it can be compared with subsets of the mechanistic model to determine dominant feedback controls of the large system through model reduction. This suggests that the pathways involved with Ca^{2+} signaling in response to H_2O_2 exhibit a natural frequency of approximately 2.78 mHz and suggest this is optimal for signal transmission to particular downstream effectors. This will be further explored in Chapter 7.

All experimental results showed great population heterogeneity, with a wide range of responses that could not be easily captured with any other experimental design. These single-cell differences could be the result of stochastic differences in gene expression, growth phase of the cells, or epigenetic alterations that keep a plethora of responses at the population level response for mounting an effective immune response [289]. Future experiments may attempt to control or visualize more of these levels of variability for a more complete understanding of the underlying mechanisms.

We observed from the modeling system that the resulting behavior of the system to an oscillatory input varies not only by applying different frequencies to the system, but also by applying different amplitudes as well. This suggests that the system can be modulated not only by the frequency applied, as witnessed from experimental results, but also from the amplitude of the signals it receives. This mechanism would provide yet another level of encoding for the ubiquitous Ca^{2+} signaling to overcome the universality of the ion in numerous signaling systems. In other words, there are multiple dimensions to which Ca^{2+} kinetics can encode important information about the environment for the cell to decode in a sophisticated, multifactorial process. Our approach not only recognizes some of these challenges, but also begins to understand how systems can behave differentially to these dynamic, oscillatory input signals.

Oscillating cytoplasmic calcium spikes have been shown to encode a variety of transcription factors in a complex way [247]. The ability to extract more of this encoded information using frequency response analysis will shed light on potential dominant feedback connections and new therapeutic targets. We report a widely applicable platform of technology advancements that enable complex and intelligent perturbation of Ca^{2+} signaling. This includes a microfluidic device enabling uniform, dynamic stimulation of suspension cells, and a set of analysis techniques to gain single-cell resolution. Together, this approach can be utilized for different cell types and signaling molecules of interest. We demonstrated this applicability on Jurkat T cells by probing Ca^{2+} dynamics with H_2O_2 and found novel biological insight that Ca^{2+} signals exhibit a natural frequency and our results align with literature reports of maximal downstream transcription.

CHAPTER 7 HYDROGEN PEROXIDE SIGNALING AND SUBSEQUENT TRANSCRIPTIONAL RESPONSE TO ROBUST CALCIUM OSCILLATIONS

7.1 Introduction

We showed in Chapter 6 that Jurkat T cells respond with oscillatory Ca^{2+} signaling when stimulated with dynamic H_2O_2 pulses and maximal entrainment is observed at 2.78 mHz, corresponding to a period of six minutes. We then sought to better understand the relationship by visualizing the time dependent H_2O_2 concentration in various organelles in response to oscillatory Ca^{2+}, switching the input and output signals from our previous work. Furthermore, we were able to couple this signaling behavior assay with the downstream transcriptional response.

We accomplished this using the same microfluidic platform, capable of uniform, dynamic stimulation of cells, paired with stably transfected Jurkat T cells. Following stimulation, cells were fixed on-chip and hybridized with smFISH probes for characterizing the downstream transcriptional response with single-cell resolution. We utilized the recombinant protein described in Chapter 3, HyPer-Mito, as well as the cytosolic localized version of the protein, HyPer-Cyto. These stably transfected Jurkat T cells enable us to visualize dynamic H_2O_2 traces with information on spatial localization and time dependent responses to Ca^{2+} signaling, a view that has been previously unachievable due to technically limitations. The innovative combination of microfluidics and the recombinant protein HyPer overcomes these experimental barriers and provides

novel biological understanding into the relationship between Ca^{2+} signaling and downstream H_2O_2 response.

7.1.1 ROS Production During T Cell Activation

The major source of ATP synthesis in eukaryotic cells is mitochondrial oxidative phosphorylation. This process includes a network of respiratory H^+ pumps, known as complexes I-IV, on the mitochondrial inner membrane that sustain a H^+ gradient across the membrane. During this process, electrons are removed from reducing substrates and transferred to O_2. The potential energy stored in this gradient is released to be used by complex V for ATP synthesis [90]. O_2 is chemically reduced via the following progression:

$$O_2 \rightarrow O_2^- \cdot \rightarrow H_2O_2 \rightarrow OH \cdot \rightarrow H_2O$$

where multiple reactive oxygen species (ROS) are formed in the process. There is a large body of evidence implicating ROS in damaging proteins, lipids, DNA, and other cellular components [290-293]. More recently, there have been reports of mitochondrial ROS acting as part of redox signaling within the cell, highlighting the shift in thinking to ROS behaving as potential secondary messengers [294, 295]. Thus, mitochondrial oxidative phosphorylation appears to delicately balance the maximal production of ATP by reducing O_2 to H_2O while simultaneously protecting the cell by producing only levels of ROS necessary for signaling and proper homeostasis within the cell [296]. Superoxide ($O_2^- \cdot$) is the primary ROS made within mitochondria, and this is quickly converted to H_2O_2, via the reaction above, by SOD or spontaneous dismutation. $O_2^- \cdot$ is mainly produced via the ubisemiquinone radical intermediate (QH·) at complex III of the

electron transport chain and complex III inhibitors, such as antimycin A shown in Chapter 3, increase ROS production by inhibiting subsequent steps of the process [297-299]. Other sources of ROS generation in the mitochondria include complex I, but the significance is not clear [90]. ROS production is also known to be regulated, with exponential dependence, on the mitochondrial membrane potential [300].

Mitochondria also play a role in many other important processes within the cell, such as steroid hormone synthesis, lipid metabolism, and Ca^{2+} homeostasis [301, 302]. During Ca^{2+} signaling, mitochondria are known to transport Ca^{2+} through their double membrane into the mitochondrial matrix, thus buffering the influx of Ca^{2+} into the cytoplasm. This transport is mediated via voltage-dependent anion channel (VDAC) on the outer membrane and the mitochondrial Ca^{2+} uniporter (MCU) on the inner membrane, in accordance with the membrane potential ($\Delta\Psi_m$) [89, 301]. There is also a "rapid-mode" uptake (RaM), which allows millisecond alteration of mitochondrial Ca^{2+} concentrations to mirror that in the cytosol [303].

Once Ca^{2+} enters the mitochondria, its primary function is to activate oxidative phosphorylation and drive ATP production [304-312]. This effect is manifested via a concerted effect of Ca^{2+} in induced allosteric effects on many proteins, such as pyruvate dehydrogenase and isocitrate dehydrogenase [308, 309]. This upregulation allows cells to respond to Ca^{2+} signaling by producing the high levels of ATP necessary for the resulting energy expenditure in the functional cellular response. Ca^{2+} can also trigger pathological effects, such as cytochrome c mediated apoptosis, in the presence of other stimulants through the permeability transition pore (PT) [313-315]. Mitochondrial function is also dependent on the structure of the organelle, which is quite dynamic in nature;

mitochondria go through fission, fusion, and change their shape [316, 317]. It is hypothesized this enables the proper distribution of mitochondria present in the cell to provide localized ATP delivery [90].

To better understand mitochondrial function and the how Ca^{2+} signaling can stimulate either physiological or pathological responses in the cell, we explore the ROS production in T cells in response to an oscillatory Ca^{2+} signal. Since ROS generation is dependent on QH·, it can be upregulated by either an increase in oxidative phosphorylation, or inhibition of the distal electron transport chain, as discussed above. ROS production by the mitochondria correlates with metabolic rate, suggesting an increase in electron chain leakage [318, 319]. Ca^{2+} is also known to stimulate nitric oxide synthase (NOS) to produce NO·, which inhibits complex IV, again increasing ROS production [296]. Yet these theoretical predictions do not capture the diverse set of ROS observations seen in response to Ca^{2+} signaling, suggesting there are other factors to consider. For instance, it appears application of Ca^{2+} alone actually reduces ROS production from complexes I and III. However, when Ca^{2+} is applied in conjunction with either complex inhibitors or uncouplers, the ROS generation was shown to increase [320]. For instance, Ca^{2+} added to rate heart mitochondria with antimycin A increased ROS generation, potentially because Ca^{2+} uptake mildly uncouples the mitochondria, or in other words, dissipates $\Delta\Psi_m$. This uncoupling could be attributed to changes in the pH gradient across the mitochondrial membrane, affecting downstream generation of $HO_2\cdot$/ $O_2^-\cdot$ [321]. However, another experiment showed a contrasting result where Ca^{2+} and antimycin A treatment of brain mitochondria did not stimulate complex III ROS generation [322]. There was some increase in complex I ROS formation, because upon

treatment with Ca^{2+} and rotenone (a complex I inhibitor), ROS generation was markedly decreased [323]. It was further noted that while the uncoupling of the $\Delta\Psi_m$ lasted only a few seconds from Ca^{2+} influx, the ROS decrease was continued for a few minutes, suggesting the mechanisms of ROS decrease was not from the alteration in $\Delta\Psi_m$ [300]. In summary, there appears to be a general consensus that ROS production is diminished by Ca^{2+} influx from both complex I and III, but increases upon treatment with inhibitors and it is not well understood what pathways account for these differences [262]. There are interactions between Ca^{2+} and mitochondrial energy metabolism, but it is not entirely clear what role ROS production plays into these complex signaling networks. In this work, we seek to visualize H_2O_2 with the redox sensitive reporter, HyPer, localized either within the cytoplasm or mitochondria. From this unprecedented view, we are able to make conclusions about Ca^{2+} induced ROS regulation in T cells that unveil some of the unknown aspects of signaling.

7.1.2 Ca^{2+} Frequencies and Transcriptional Changes

Upon activation, T cells undergo intracellular signaling that alters gene expression and downstream function of the cells to accomplish the multitude of tasks necessary for the adaptive immune response [1]. Throughout this work, we have demonstrated the utility of viewing Ca^{2+} signaling in the frequency domain, motivated by previous reports of the functional response of downstream effectors to oscillatory stimulation [22, 324]. In the literature, it's been shown in T cells that NF-κB, NF-AT and Oct/OAP are all activated at high frequency stimulation with Ca^{2+} and low frequencies activate only NF-κB [22]. This dependence of proinflammatory transcription factors on frequency of Ca^{2+} oscillation illustrates the necessity to investigate Ca^{2+} kinetics in the frequency domain. HEK293

cells were similarly investigated with application of an oscillatory GPCR signal, upstream of Ca^{2+}, and the resulting NF-AT localization demonstrated high pass filter characteristics in response to observed Ca^{2+} oscillation.

Different techniques are available to stimulate calcium, one of which includes the use of the small molecule inhibitor thapsigargin [22]. Thapsigargin depletes intracellular stores of Ca^{2+} by blocking endoplasmic reticulum Ca^{2+} ATPases while simultaneously and irreversibly activating CRAC channels on the cell membrane [325]. The resulting Ca^{2+} signaling is then dependent on the extracellular Ca^{2+} concentration the cells are immersed in. We will utilize this experimental framework to experimentally drive Ca^{2+} signaling in a robust manner to subsequently monitor simultaneous H_2O_2 signaling in response to Ca^{2+}. Downstream transcription can also be monitored on chip with smFISH, a revolutionary approach to monitor single-cell gene expression. Ultimately, with the use of microfluidics, we are able to combine multiple levels of regulation for single-cell observation; Ca^{2+} signaling and H_2O_2 production is monitored on the timescale of seconds and downstream transcriptional response can be monitored two hours post stimulation.

7.1.3 Single Molecule Fluorescent In Situ Hybridization

Cellular response to intracellular signaling usually includes an altered pattern of gene expression and single-cell expression levels often vary substantially form the population average [326]. Many methods provide the population average of cells, such as Northern blot, PCR, and RNA-seq, with only recent advancement in single-cell visualization and quantification [327]. For cells loaded and stimulated in our device, it is not possible to remove them for single-cell quantification systems such as Fluidigm [328], so we

investigated approaches that could be accomplished on chip for single-cell resolution of the transcriptional response to oscillatory Ca^{2+} stimulation.

To accomplish this, we modified a recently developed protocol based on *in situ* hybridization in which single mRNA molecules can be detected in single-cells [329]. This procedure, known as smFISH, utilizes oligonucleotide probes with a sequence of interest bound to fluorophores for detection with fluorescent microscopy [329]. Multiple fluorophores can be imaged on a single sample, allowing several probes to be used for different mRNA targets in a given cell. We used two probes commercially available to investigate specific molecules involved in T cell activation: FOS and HIF1α (Biosearch Technologies).

FOS expression is dependent on activation of protein kinase C (PKC) during T cell activation [330, 331]. PKC activation is often achieved through phorbol ester stimulation, but it has been shown that Ca^{2+} signals also activate PKC through increased DAG [332, 333] and in a frequency dependent manner [334]. Nuclear Factor of Activated T cells (NFAT) is responsible for downstream transcriptional responses via interactions with other molecules upon activation. NFAT must be dephosphorylated for translocation to the nucleus and binds cooperatively to AP-1 complex (which includes FOS) and binds regulatory domains of inducible genes for immune cell function, such as IL-2 [331, 333, 335]. With the described frequency dependence of PKC on Ca^{2+} signaling, we utilized this previously characterized smFISH probe for monitoring the transcriptional activity of FOS to oscillatory Ca^{2+} activation, ultimately obtaining a functional readout of the cell to frequency stimulation on our microfluidic platform.

Hypoxia-inducible factors (HIF) are known transcription factors, usually heterodimeric in nature, and are constantly degraded in normal O_2 conditions by the von Hippel-Lindau (VHL) complex [336]. In low O_2 environments (hypoxia) the subunits, HIF1α and HIF2α are not targets of VHL and localize to the nucleus upon dimerization with HIF1β. Once in the nucleus, target genes are transcribed to combat the altered O_2 environment [337]. It has also been shown that HIF1α can be upregulated in response to signals facilitated by TCR under hypoxic conditions [338]. While measuring H_2O_2 response in T cells with the recombinant protein HyPer, we can indirectly visualize changes in O_2 homeostasis within the cell. We thus complemented this signaling information with smFISH probes capable of characterizing the downstream activation of HIF1α.

Elucidating the transcriptional response to upstream intracellular signaling is important for understanding the ramifications of Ca^{2+} kinetics in a more informative way. To accomplish this, we demonstrate the ability of our microfluidic device to not only trap and dynamically stimulate T cells, but also to serve as a platform for hybridization with smFISH probes and ultimate high resolution imaging of multiple fluorophores, corresponding to mRNA transcripts, in a single-cell. This highlights our ability to transcend current experimental techniques and combine multiple levels of cellular response with single-cell resolution.

7.2 Materials and Methods

7.2.1 Cell Culture

The Jurkat E6-1 human acute T cell lymphoma cell line was used for all experiments (American Type Culture Collection). Cells were grown in conditions as described before [215] and in previous chapters. Briefly, the cells were cultured in RPMI 1640 without Phenol Red (Lonza) and with L-glutamine (Sigma-Aldrich), supplemented with 10 mM HEPES buffer (Corning), 1 mM sodium pyruvate (Cellgro), 50 units mL-1 penicillin-streptomycin (Cellgro), 1x MEM nonessential amino acids (Cellgro), and 10% fetal bovine serum (Sigma-Aldrich).

For those experiments visualizing cytoplasmic Ca^{2+} concentration in response to varying stimulation, the cells were loaded in 1x calcium and magnesium free HBSS without Phenol Red (Cellgro) with 5 μM Fluo-3 AM, cell permeant (Life Technologies) and 0.05% w/v Pluronic F-127 (Sigma-Aldrich) for 30 minutes at 37°C. Following the incubation, cells were washed once and subsequently resuspended in 1 x calcium and magnesium free HBSS without Phenol Red. Cells were loaded into the device at a density of 1×10^6 cells/mL.

7.2.2 HyPer Transfection and Stable Line Creation

To visualize the dynamics of hydrogen peroxide production in the mitochondria and cytoplasm using fluorescent microscopy, we used stably transfected Jurkat cell lines of either pHyPer-dMito or pHyPer-dCyto plasmids (Evrogen). The original transfections were done in a Neon Transfection System (Life Technologies) as described in Chapter 3. Stable lines were created using neomycin (G418, KSE Scientific) antibiotic selection, as

described in Chapter 3. Upon thawing stocks from cryopreservation, a maintenance concentration of 0.6 mg/mL G418 was continued in cell culture.

To enhance signal for visualization, the stable cell lines were further sorted using a BD FACS Aria IIIu cell sorter (BD Biosciences). Cells were gated based on FSC and SSC using untransfected Jurkat cells as a negative control. The top ~20% of the population was sorted based on GFP fluorescence once and then cultured as described above and used in subsequent experiments.

7.2.3 Ca^{2+} Clamping with Thapsigargin

To inhibit endoplasmic reticulum Ca^{2+} ATPases and irreversibly open CRAC channels, we chemically clamped the cells with thapsigargin (Sigma Aldrich) [22]. HyPer-cyto or HyPer-mito stably transfected cells were suspended with 1 μM thapsigargin at 1 x 10^6 cells/mL in 1 x HBSS without calcium, magnesium, or Phenol Red (Cellgro). Cells were incubated at room temperature for 5 minutes, spun down at 70g, and resuspended in 1 x HBSS without calcium, magnesium, or Phenol Red.

Devices were assembled and autoclaved before use. Devices were primed with sterile filtered PBS in the stimulus layer and 2% BSA in HBSS for the cell trapping layer. Cells were loaded into a primed device according to [220]. Cells were stimulated with either 1.5 mM Ca^{2+} or 2 mM EGTA . The Ca^{2+} solution was prepared with $CaCl_2$ (Sigma-Aldrich) in calcium, magnesium, and Phenol Red free HBSS. The EGTA solution was similarly prepared with EGTA (Boston BioProducts) in calcium, magnesium, and Phenol Red free HBSS. For the EGTA control, only the 2 mM EGTA solution was applied to cells, but it was switched at the designated frequency to control for the mechanical stress cells experience. The HBSS control experiment again controlled for mechanical stress of

solution switching, but cells were exposed to only one solution: HBSS without Phenol Red and with calcium and magnesium (Cellgro).

Cells were stimulated for one hour while being imaged at 20x on a Perkin Elmer UltraVIEW Vox spinning disk confocal microscope and images were acquired on a Hammamatsu C9100-23b back-thinned EM-CCD using the 405 nm and 488 nm laser lines for excitation of the reduced and oxidized version of the protein, respectively. Emission for both channels was obtained using the same emission filter at 525 nm. Images were acquired at the maximal frame rate for two regions of interest within the device using the motorized stage. Images were collected with an exposure time of 800 ms and exported from Volocity as tif files for analysis in MATLAB® (Mathworks) using custom scripts.

7.2.4 smFISH

Protocol was modified from a protocol developed by Loice Chingozha from the Lu Lab.

Following stimulation with oscillatory conditions, cells were incubated for 1 hour at 37°C in EGTA solution before being fixed with 4% PFA (Alfa Aesar) in nuclease free water (Life Technologies) for 10 minutes at room temperature. Following this, methanol is introduced into the device to permeabilize cells for at least 1 hour at 4°C. Following permeabilization, cells are washed for 30 minutes at room temperature with a wash buffer containing 2x SSC (Ambion) and 10% formamide (Ambion) in nuclease free water. Following this, cells are incubated with hybridization buffer and 100 nM concentration of predesigned smFISH probes for Human FOS and Human HIF1α (Biosearch Technologies) overnight at 37°C. Hybridization buffer is prepared with 0.1 g/mL dextran sulfate (Sigma), 2 x SSC solution (Life Technologies), 200 μg/mL UltraPure BSA

(Ambion), and 10% formamide (Ambion) in nuclease free water. Cells are then washed again with the wash buffer for 30 minutes at 37°C and then immersed in an anti-fade imaging buffer. Glox buffer is prepared previously with 2x SSC solution (Life Technologies), 0.4% w/v glucose (Sigma), and 10 mM Tris HCl (Ambion) in nuclease free water. The imaging buffer is then prepared with the addition of 1 μL 3.7 mg/mL glucose oxidase (Sigma) in 50 mM sodium acetate (Ambion), and 1 μL catalase in ammonium sulfate suspension, ≥4000 units/mg (Sigma) to 100 μL glox buffer.

7.2.5 smFISH Image Analysis

Protocol was modified from a protocol developed by Loice Chingozha from the Lu Lab.

Fixed and hybridized cells were imaged at 100x using the Perkin Elmer UltraVIEW Vox spinning disk confocal microscope and images were acquired on a Hammamatsu C9100-23b back-thinned EM-CCD. Z-stacks were obtained with 200 nm spacing using a Piezo stage and 47 images per stack were analyzed for all cells. Cells were focused using the Nikon Perfect Focus System module to account for drift over time in the stage. Cells were hybridized with both FOS and HIF1α smFISH probes simultaneously, and they were imaged in the RFP and Cy5 channels, respectively. The probes used for smFISH are fluorescently labeled and appear bound to target mRNA as diffraction-limited spots [339]. FISH-quant is automatic image analysis software capable of detecting these spots in 3D z-stacks and providing counts of mRNA transcripts present in single-cells [339]. We used this MATLAB® GUI to perform all analysis of smFISH images collected [339]. Briefly, we outline cells using the Outline Designer by identifying cells using the FOS and bright field images obtained. This outline is then applied to both the FOS and HIF1α z-stacks and images are filtered with a two-step approach. The first filter is used to

estimate and remove background with a Gaussian filter of kernel size 5. The second filter is used to increase the signal-to-noise ratio (SNR) with a smaller Gaussian filter with a kernel size of 1. Following this, all spots are identified from the filtered image with sigma xy below 468 and sigma z below 1761. Spots are then further thresholded based on filtered image pixel intensity (between 100 and 1000) and sigma xy (between 35 and 446). These values were chosen from looking at a population of cells and removing the spots that fall outside of the approximately normal distribution according to recommendations in the GUI documentation [339]. Cell location is identified in the device and compared to the HyPer signaling studies.

7.2.6 Clustering

Each device had two positions imaged at 20x to capture more single-cell traces. These cells were combined together for each device and subjected to hierarchical clustering using the built in MATLAB® *clustergram* function (MathWorks). Cells were clustered based on the time series data, with each measurement in time representing a variable. Standardization was performed on variables with the mean centered at zero and a standard deviation of 1. Distance was calculated using the 'cosine' metric and linkage was determined using the default setting, 'average'. These metrics consistently pulled out similar clusters between experiments. There were two clusters in each experiment, corresponding to: 1. cells with high H_2O_2 fluorescence throughout the experiment and 2. cells with consistently lower H_2O_2 fluorescence. The corresponding dendrogram was colored in red and blue, respectively.

7.3 Results

7.3.1 Cells are Chemically Clamped with Thapsigargin

As both the HyPer protein and many cytoplasmic Ca^{2+} dyes both emit in the green visible spectrum, we can reliably only measure one at a time. To image H_2O_2 production in response to Ca^{2+}, we chose to chemically clamp Jurkat T cells and control Ca^{2+} signaling via environmental perturbation with solutions of EGTA and $CaCl_2$. Cells were treated with thapsigargin to inhibit Ca^{2+} ATPases on the endoplasmic reticulum and irreversibly activate CRAC channels [22]. The functional result of this chemical clamping was the inability of cells to store and release intracellular Ca^{2+} and hence, the Ca^{2+} concentration in the extracellular environment controls signaling. To characterize the pre-treatment with thapsigargin and delivery of extracellular Ca^{2+} in our device, we monitored cytoplasmic Ca^{2+} concentration through time for Jurkat cells loaded in the device. Cells were exposed to alternating environment of 2 mM EGTA or 1.5 mM $CaCl_2$ with a frequency of 2.78 mHz, corresponding to a period of 6 minutes (Figure 7-1). The cells are clearly and robustly exhibiting Ca^{2+} signaling upon delivery of $CaCl_2$ (Figure 7-1a). Furthermore, this delivery elicits a functional response at the same frequency as the driving frequency (2.78 mHz) with almost every cell exhibiting this as the dominant frequency when analyzed with spectral analysis (Figure 7-1b). From this characterization we confidently assume all Ca^{2+} signaling corresponds to the extracellular environment being supplied to the cells.

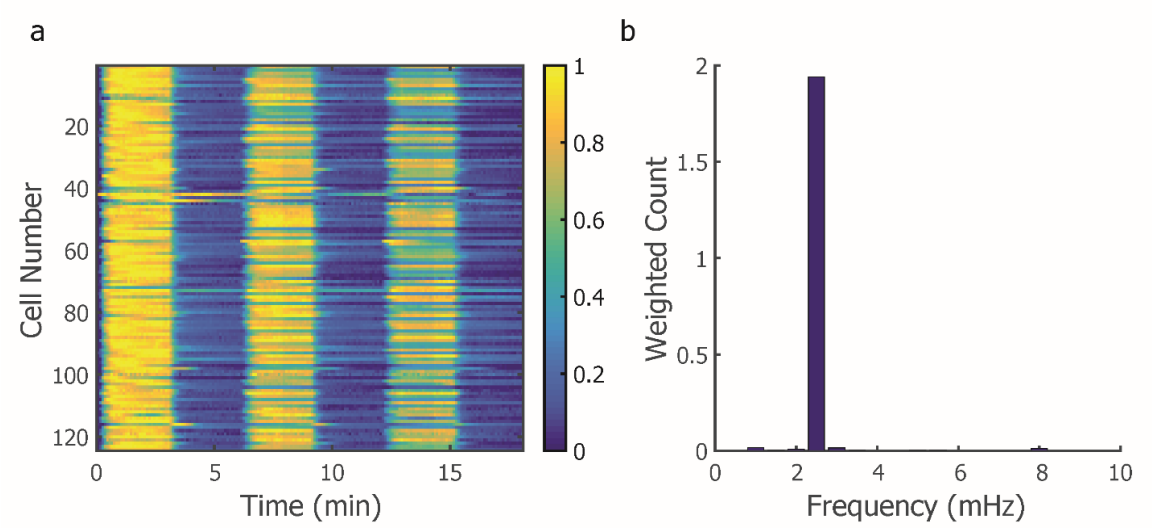

Figure 7-1: Characterization of Ca^{2+} Signaling with Thapsigargin Treatment.
Cells are treated with Thapsigargin followed by oscillatory stimulation with 1.5 mM $CaCl_2$ or 2 mM EGTA. (a) The resulting cytoplasmic Ca^{2+} concentration aligns with $CaCl_2$ treatment in an oscillatory fashion. (b) Cells are stimulated with 2.78 mHz input frequency and dominant frequencies show a robust, repeatable response to stimulation at the driving frequency. Four replicates are combined in (b) and the frequency span is reduced to 10 mHz for easier visualization.

7.3.2 Response of Cytoplasmic H_2O_2 to Ca^{2+} Oscillations

Cells were treated with thapsigargin to inhibit their control of intracellular stores, enabling us to drive intracellular signaling. Cells were first treated with EGTA in a calcium free environment and then exposed to extracellular Ca^{2+} at a specified frequency. We imaged the response of cytoplasmic H_2O_2 production using the recombinant protein HyPer-cyto in stably transfected Jurkat T cells. Cells were normalized to the first time point and expressed as a function of time for easier visualization in Figure 7-2.

It is clear from analyzing individual traces that there is a wide range of variability in the responses, with some cells showing very little variation through time while others show an increasing, decreasing, or oscillatory response. We also noticed a clear drop in cytoplasmic H_2O_2 production upon stimulation with Ca^{2+} following EGTA treatment

(Figure 7-2). For both the 2.78 mHz and 1.67 mHz treatment conditions, at the 3 minute and 5 minute mark we see a subtle but reproducible decrease in cytoplasmic H_2O_2 production, corresponding to the initial exposure of cells to Ca^{2+} in each experimental condition (Figure 7-2a-c,f-h). Two controls were run to ensure the responses seen were due to the Ca^{2+} signaling and not responses to loading or mechanical stimulation in the device. These controls kept the extracellular environment constant for the duration of the experiment (Figure 7-2d,e). Two conditions were used for these controls: constant EGTA or constant HBSS with Ca^{2+}, both of which were mechanically switched at 2.78 mHz to control for any shear stress felt by the cells. The control cell traces showed very little variation through time, with the majority of cells remaining around the same fluorescence through time, suggesting the observed decrease in cytoplasmic H_2O_2 production seen in the treatment conditions was due to the imposed Ca^{2+} signaling Figure 7-2.

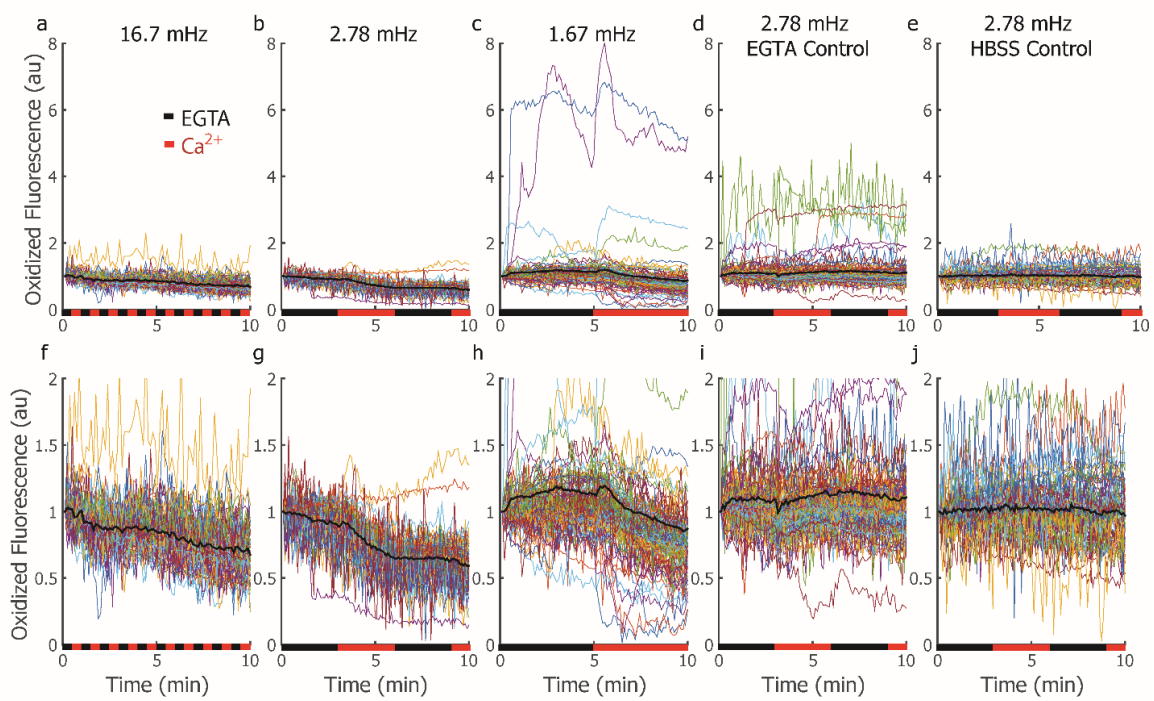

Figure 7-2: Cytoplasmic H_2O_2 Concentration in Response to Oscillatory Ca^{2+} Signals of Different Frequencies.
Each cell is represented by a trace, and the average of all cells is designated with the thick, black line. Cells were exposed to oscillatory conditions of 2 mM EGTA or 1.5 mM $CaCl_2$ with frequencies of (a) 16.7 mHz, (b) 2.78 mHz, or (c) 1.67 mHz. Two controls were obtained for these experiments were the environment was held constant for the cells but it was mechanically switched at a frequency of 2.78 mHz. These constant environmental conditions were (d) 2 mM EGTA and (e) HBSS with Ca^{2+} and Mg^{2+}. Cell traces are normalized to the first time point acquired and visualized for 10 minutes total. For easier visualization, the range of fluorescence is reduced in f-j.

7.3.3 Response of Mitochondrial H_2O_2 to Ca^{2+} Oscillations

As mentioned previously, it has been shown that H_2O_2 production is localized to different organelles and mitochondria are one of the major sources of production during oxidative phosphorylation. Knowing this, we utilized this experimental platform to further explore the mitochondrial H_2O_2 production in response to EGTA and Ca^{2+} oscillatory stimulation using HyPer-mito stably transfected Jurkat T cell lymphocytes. Cells were individually analyzed and results were compiled to visualize dynamics during stimulation (Figure

7-3). Again, there is a striking amount of variability between cells, highlighting the necessity of single-cell analysis to better understand the wide realm of potential responses to oscillatory Ca^{2+} signaling. There were also interesting differences between the two reporter lines, suggesting differences in H_2O_2 production between the cytoplasm and mitochondria. For instance, upon stimulation with Ca^{2+} following EGTA treatment, the HyPer-mito cells first showed a peak of production before a subsequent decrease in production (Figure 7-3). More specifically, for the 16.7, 2.78, and 1.67 mHz conditions, they showed an increase in fluorescence at the 30 second, 3 minute, and 5 minute timepoint, respectively, corresponding to the initial exposure of Ca^{2+} (Figure 7-3a-c). The control experiments with constant exposure to HBSS with EGTA or HBSS with Ca^{2+} showed very little variation through time, suggesting the visualized responses were due to the initial Ca^{2+} exposure and not an experimental artifact of mechanical stimulation in the microfluidic device.

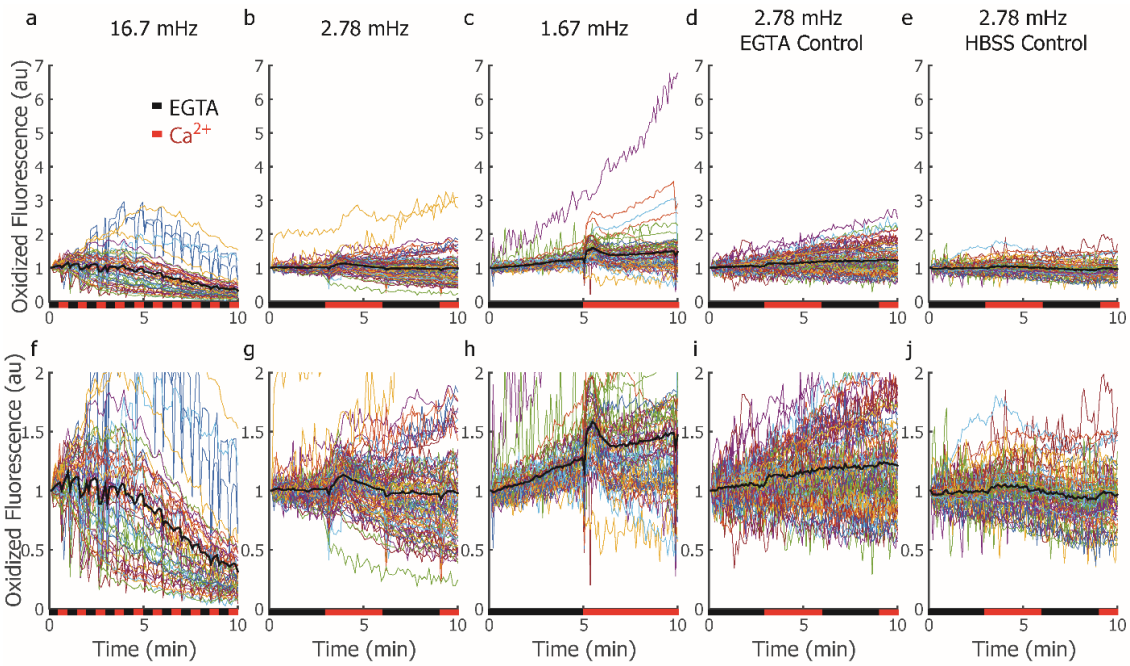

Figure 7-3: Mitochondrial H_2O_2 Concentration in Response to Oscillatory Ca^{2+} Signals of Different Frequencies.
Each cell is represented by a trace, and the average of all cells is designated with the thick, black line. Cells were exposed to oscillatory conditions of 2 mM EGTA or 1.5 mM $CaCl_2$ with frequencies of (a) 16.7 mHz, (b) 2.78 mHz, or (c) 1.67 mHz. Two controls were obtained for these experiments were the environment was held constant for the cells but it was mechanically switched at a frequency of 2.78 mHz. These constant environmental conditions were (d) 2 mM EGTA and (e) HBSS with Ca^{2+} and Mg^{2+}. Cell traces are normalized to the first time point acquired and visualized for 10 minutes total. For easier visualization, the range of fluorescence is reduced in f-j.

7.3.4 smFISH Response to Oscillatory Stimulation

Following dynamic stimulation with a robust delivery of Ca^{2+}, cells were incubated for 1 hour and subsequently fixed and hybridized with two smFISH probes: FOS and HIF1α with a protocol originally developed by Loice Chingozha in the Lu Lab. Cells were imaged using a 100x objective on a Spinning Disk Confocal and individual probes were seen as bright spots within the cells (Figure 7-4). From initial glance at the images collected, it was apparent that different oscillatory frequencies elicited different transcriptional responses. For instance, cells stimulated at a frequency of 2.78 showed

numerous, bright spots representing an increase in mRNA transcript number compared to those stimulated with 16.7 mHz stimulation (Figure 7-4).

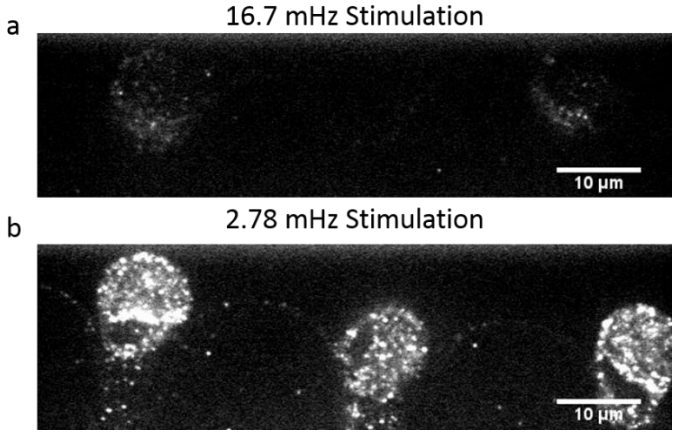

Figure 7-4: smFISH Images Collected Post Stimulation with Different Oscillatory Ca^{2+} Stimulation.

The number of FOS and HIF1α mRNA transcripts was quantified in each identified cell and compiled across reporter lines to demonstrate the dependence of transcript number on treatment condition (Figure 7-5). This analysis on single-cells was completed after they had been exposed to EGTA and Ca^{2+} in an oscillatory pattern with designated period or were confined to the same environmental condition of EGTA or HBSS with Ca^{2+} to control for experimental conditions. It is clear from this analysis that both FOS and HIF1α transcription is upregulated upon stimulation with 6 minute periods of oscillation (2.78 mHz frequency) (Figure 7-5). The 1 minute (16.7 mHz) and 10 minute (1.67 mHz) oscillatory conditions were surprisingly similar to the EGTA and HBSS with Ca^{2+} controls although the range of responses in the 10 minute stimulation was larger than others for the FOS condition (Figure 7-5). It is also surprising that the EGTA control elicited some of the higher HIF1α mRNA counts when compared to treatment conditions. From this visualization, we again highlight how much information

can be lost with population averaged data and demonstrate the wide range of responses capable when single-cells are exposed to oscillatory environmental conditions and subsequently probed for mRNA transcripts of interest using smFISH. We found that the frequency eliciting the highest response in mRNA transcript number for both probes was the 2.78 mHz condition.

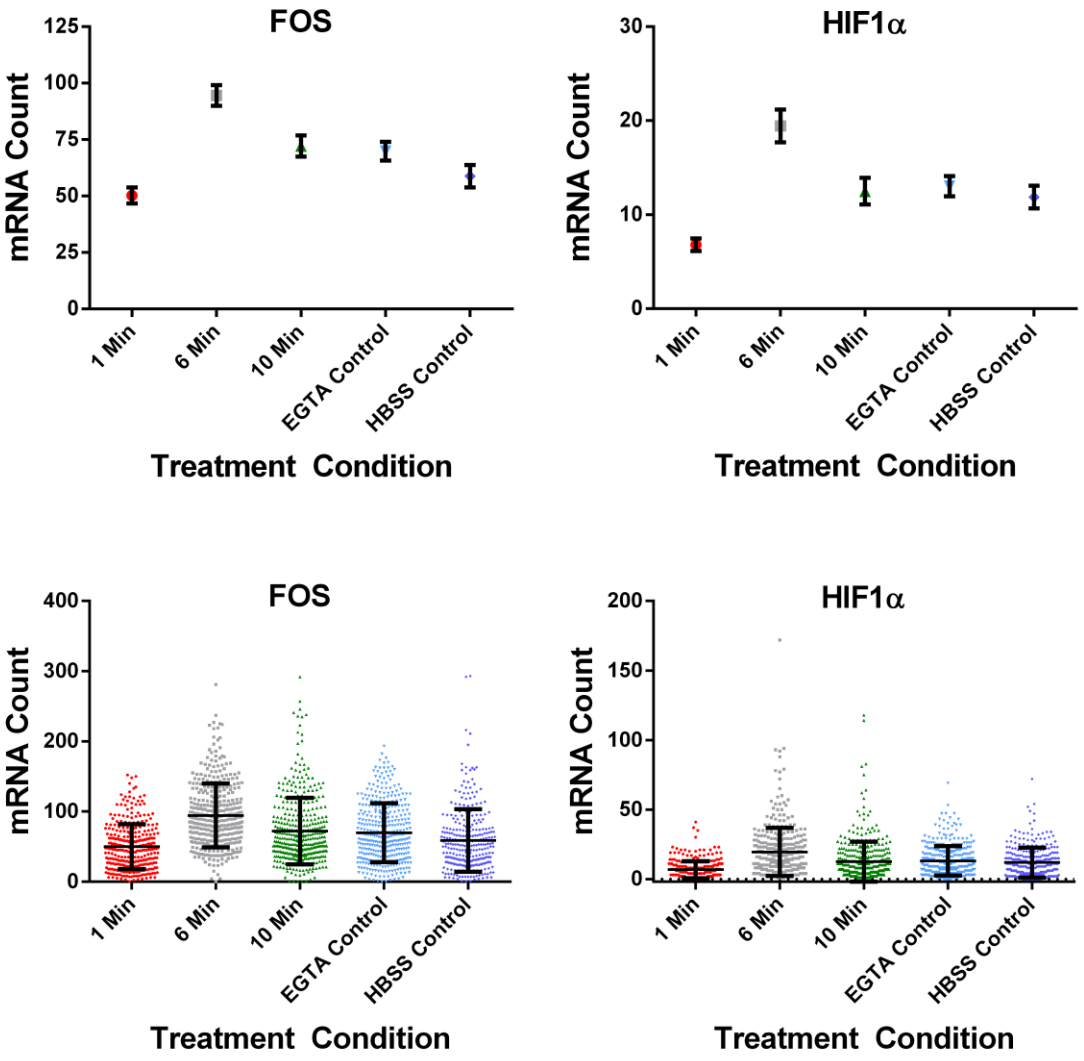

Figure 7-5: Results of smFISH Analysis Following Oscillatory Treatment with Ca^{2+} at Various Frequencies.
Cells were analyzed for smFISH probes subsequent to treatment with EGTA/Ca^{2+} oscillations or control conditions with constant environment. Cells can be seen with the maximal transcriptional response upon 2.78 mHz input of Ca^{2+}.

7.3.5 Clustering Time Course Data

With a plethora of single-cell information, we sought to calculate the similarity between cells to see what phenotypes we observe and what subpopulations might emerge. We used hierarchical clustering to calculate the distance between cells based on the time course data. In other words, each time point was treated as a variable and cells were clustered based on how closely related their dynamic behavior is to others. We chose this approach to compare individual trajectories to compile distinct phenotypes. Using this approach, we pulled out a few distinct subpopulations representing (1) cells that exhibit higher than average H_2O_2 signaling through time (red dendrogram) and (2) cells with lower than average H_2O_2 concentration through time (blue dendrogram) (Figure 7-6 and Figure 7-7).

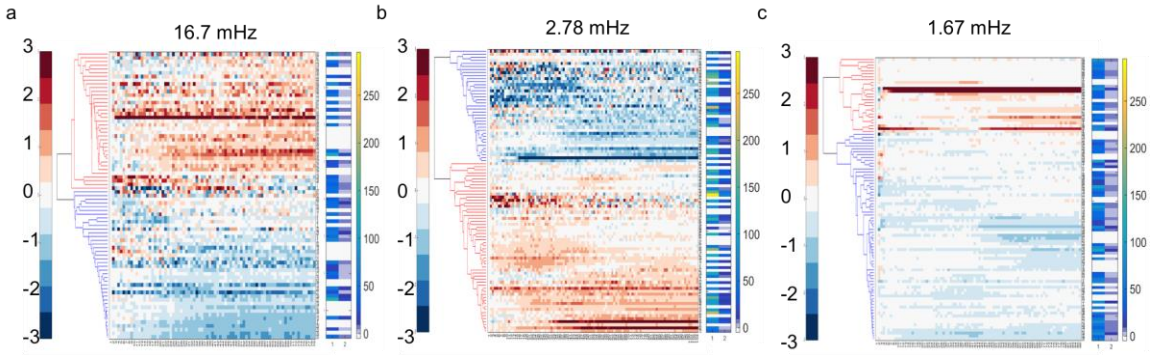

Figure 7-6: Clustered EGTA/Ca^{2+} Treatment Conditions of HyPer-Cyto Response.
Cells (rows of heat-map) were clustered using hierarchical clustering based on time (columns of heat-map) and highlighted different phenotypes within the population of cells. Cells can be seen with lower than average H_2O_2 concentration (blue dendrogram), or higher than average signaling (red dendrogram) through the course of the experiment. Cells were clustered based on the first 10 minutes of stimulation for all conditions: (a) 16.7 mHz, (b) 2.78 mHz, and (c) 1.67 mHz stimulation. The corresponding transcriptional response was identified and added to the right of each clustergram, with the left column corresponding to FOS and the right column corresponding to HIF1α. White values in the transcriptional heatmap correspond to cells that were not present for both signaling event and smFISH measurement.

It was interesting to note that despite investigating two different transcript reporter lines and differences seen in time course data, there were the same dominant phenotypes present in the clustered population of cells for both the HyPer-cyto and HyPer-mito responses (Figure 7-6 and Figure 7-7). However, the distribution in number of cells in each cluster varied between the samples, most notably the high responders (red cluster) were higher in proportion in some treatment conditions of HyPer-cyto cells than the HyPer-mito data. This is at first counterintuitive as the HyPer-mito cells, in general, responded with higher H_2O_2 production than did the HyPer-cyto cells. But with standardization of each time point, cells are clustered based on the distance of their trajectory from the mean, indicating the HyPer-mito cells may have a population subset exhibiting much higher dynamics than in HyPer-cyto and potentially a smaller overall cluster size. This is supported by the evidence in Figure 7-7, where there are clear subsets of the population with large standardized values (deep red), and more of these cells are present in HyPer-mito analysis than in HyPer-cyto results.

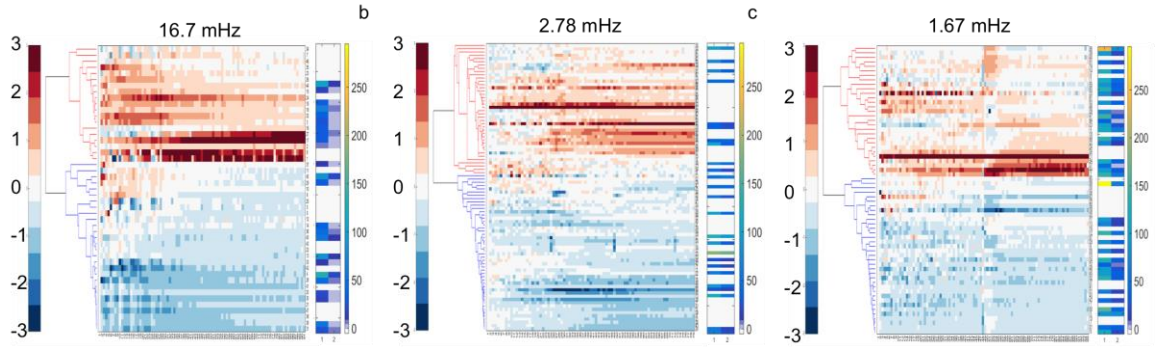

Figure 7-7: Clustered EGTA/Ca^{2+} Treatment Conditions of HyPer-Mito Response.
Cells (rows of heat-map) were clustered using hierarchical clustering based on time (columns of heat-map) and highlighted different phenotypes within the population of cells. Cells can be seen with lower than average H_2O_2 concentration (blue dendrogram), or higher than average signaling (red dendrogram) through the course of the experiment. Cells were clustered based on the first 10 minutes of stimulation for all conditions: (a) 16.7 mHz, (b) 2.78 mHz, and (c) 1.67 mHz stimulation. The corresponding transcriptional response was identified and added to the right of each clustergram, with the left column corresponding to FOS and the right column corresponding to HIF1α. White values in the transcriptional heatmap correspond to cells that were not present for both signaling event and smFISH measurement.

We subsequently calculated the response of cells 10 seconds post activation with the first wave of Ca^{2+} and compared these values with the designated cluster number (Figure 7-8). Although with such a wide range of responses it is difficult to see subtle differences, both cytoplasmic and mitochondrial H_2O_2 production appeared to be higher in the Top cluster, corresponding to sustained response cells (Figure 7-8). It is not surprising that the top responders had a higher H_2O_2 level at 10s post stimulation because this cluster appears to have a higher response throughout the duration of the experiment. Similarly, the bottom cluster cells behaved as expected with this metric, showing a lower level of H_2O_2 present post stimulation with Ca^{2+}. This suggests the cells in the bottom cluster potentially do not have the same initial increase in H_2O_2 production as the top cluster.

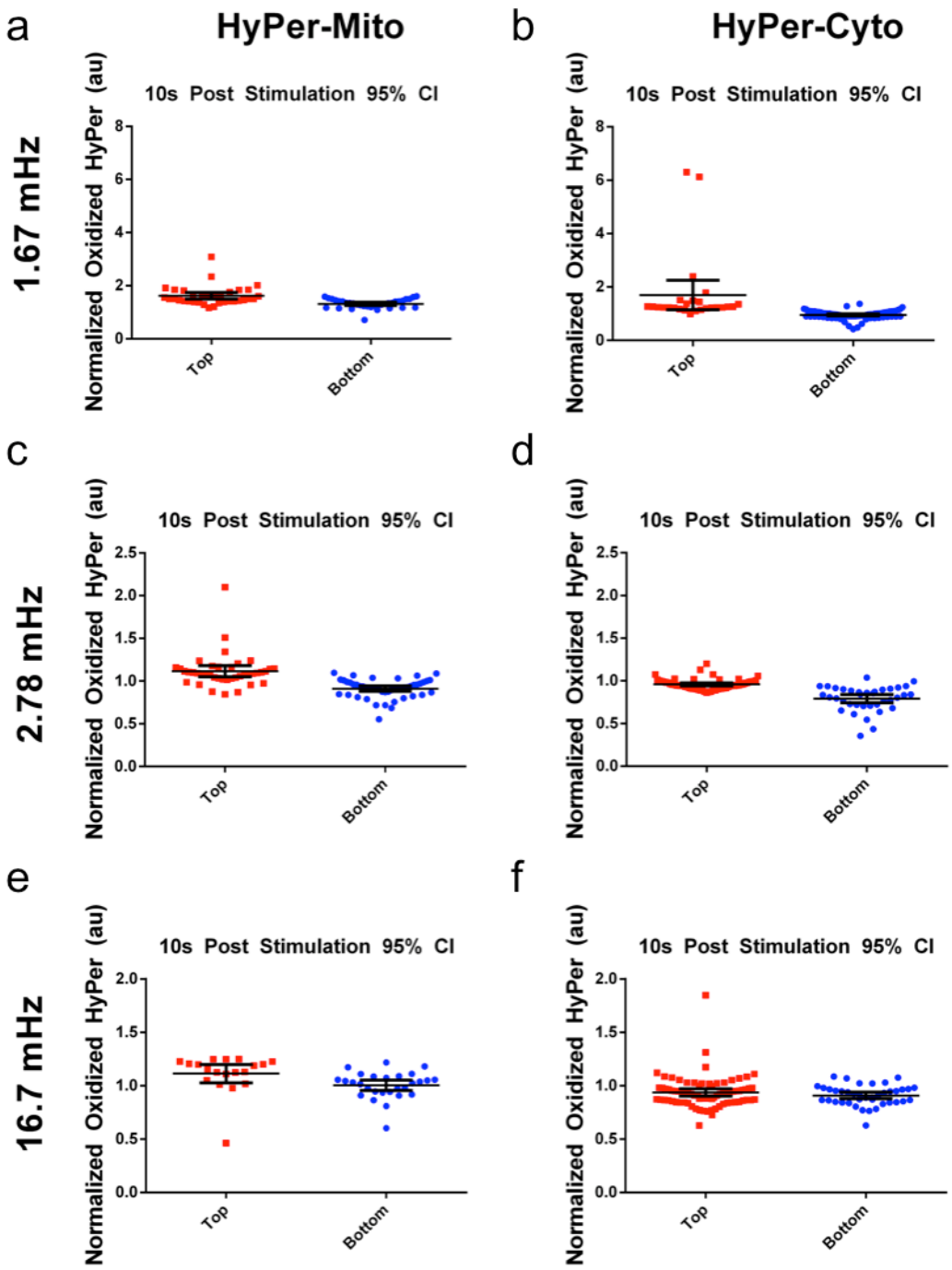

Figure 7-8: 10 s Post Stimulation Response vs. Identified Cluster of Single-cells.
The fluorescence of (a,c,e) HyPer-Myto and (b,d,f) HyPer-Cyto was calculated 10 s post stimulation with the first wave of Ca^{2+} for treatment conditions of (a,b) 1.67 mHz, (c,d) 2.78 mHz, and (e,f) 16.7 mHz stimulation with EGTA/Ca^{2+}.

Finally, we combined the response of the different treatments into a single metric of the value of oxidized HyPer protein 10 seconds post activation with the first wave of Ca^{2+} to compare differences between the cytoplasmic and mitochondrial response. Again, heterogeneity is observable within the population of cells and a wide range of responses is obtained. However, when comparing the response post treatment between the cytoplasmic and mitochondrial localized protein, the mitochondrial protein is significantly more fluorescent than the cytoplasmic protein, suggesting mitochondrial H_2O_2 production is increased in response to Ca^{2+}, at least initially and cytoplasmic H_2O_2 production decreases immediately upon exposure to Ca^{2+} (Figure 7-9).

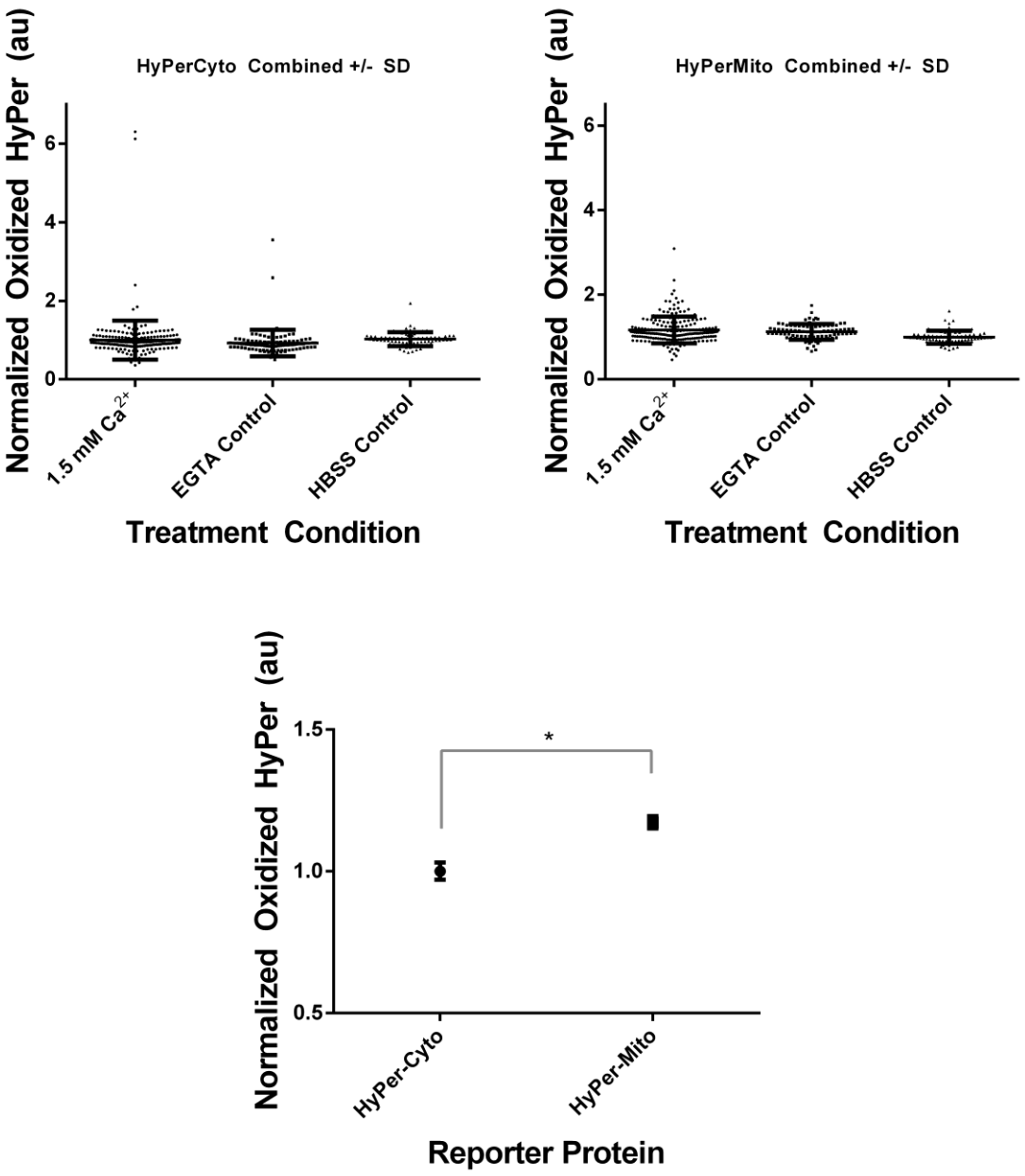

Figure 7-9: Compiled Results for HyPer-Cyto and HyPer-Mito Response to Ca^{2+} Stimulation.

The oxidized fluorescence of HyPer was measured post stimulation for both HyPer-cyto and HyPer-mito cells. All treatment conditions were combined for the first response of cells to Ca^{2+} stimulation and compared across reporter lines. There is a significant increase in mitochondrial H_2O_2 post stimulation as compared to cytoplasmic H_2O_2. A two-tailed t test was performed in GraphPad Prism™ with the resulting p-value < 0.0001.

7.3.6 Correlation of Signaling with Transcriptional Response

We further explored the response of T cells to Ca^{2+} stimulation of various frequencies by analyzing data from both signaling events and downstream transcriptional responses for individual cells. Using the clustering data from above, we compared the transcriptional response for FOS and HIF1α for cells in each cluster, For both HyPer-cyto and HyPer-mito cells, we see a counterintuitive result that cells in the bottom phenotype cluster showed some of the highest FOS and HIF1α transcript numbers, suggesting the peak height 10 seconds post transcription is not necessarily determinant of transcriptional response (Figure 7-10 and Figure 7-11). In other words, cells with lower values of H_2O_2 response to Ca^{2+} still appear to be activated by the treatment to mount a transcriptional response. Overall, cells exposed to 2.78 mHz stimulation have higher numbers of target mRNA for both FOS and HIF1α (Figure 7-10 and Figure 7-11).

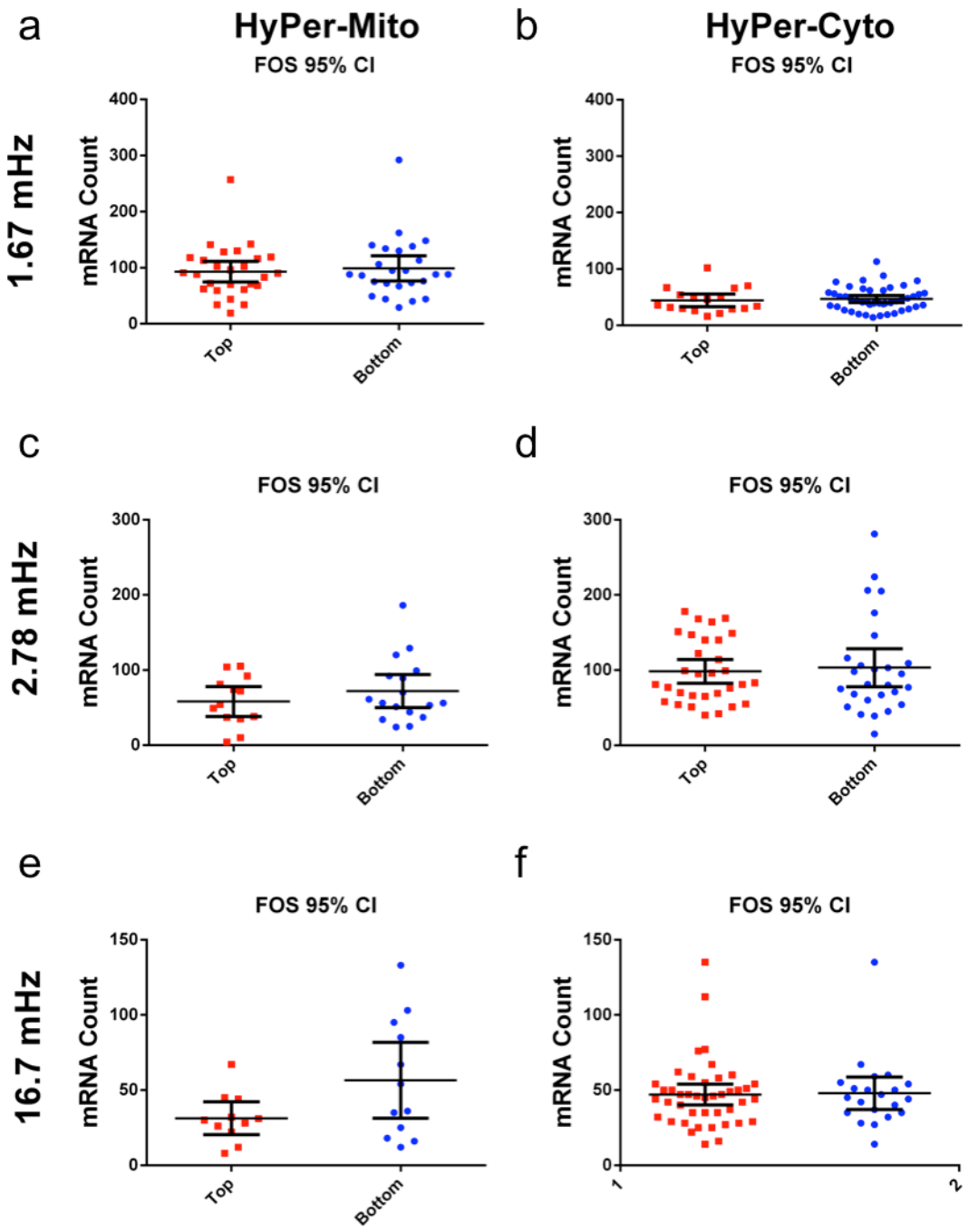

Figure 7-10: Analysis of FOS mRNA Transcript Number Compared to Cluster Number. Cells were clustered based on time course data of cytoplasmic H_2O_2 production into one of two clusters and the resulting smFISH probe transcript number was compared to the identified cluster. FOS smFISH probes were imaged for: (a,c,e) HyPer-Myto and (b,d,f) HyPer-Cyto for treatment conditions of (a,b) 1.67 mHz, (c,d) 2.78 mHz, and (e,f) 16.7 mHz stimulation with EGTA/Ca^{2+}.

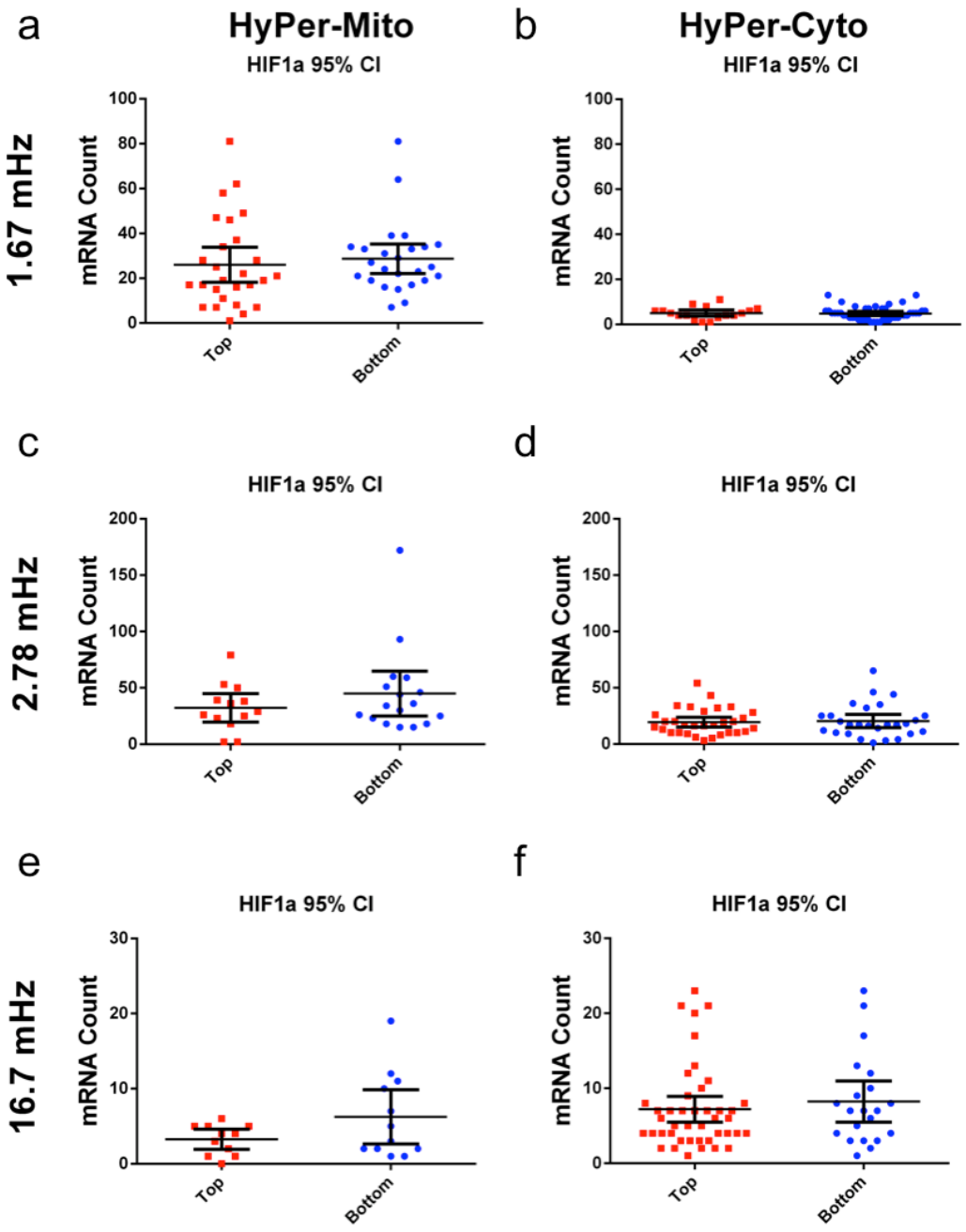

Figure 7-11: Analysis of HIF1α mRNA Transcript Number Compared to Cluster Number.

Cells were clustered based on time course data of cytoplasmic H_2O_2 production into one of two clusters and the resulting smFISH probe transcript number was compared to the identified cluster. HIF1α smFISH probes were imaged for: (a,c,e) HyPer-Myto and (b,d,f) HyPer-Cyto for treatment conditions of (a,b) 1.67 mHz, (c,d) 2.78 mHz, and (e,f) 16.7 mHz stimulation with EGTA/Ca^{2+}.

We investigated the correlation between different metrics mentioned, such as the 10 second post stimulation level and transcript count, but found that the most highly correlated relationship was between FOS and HIF1α levels (Figure 7-12 and Figure 7-13). Cells with high levels of FOS were likely to also have high levels of HIF1α suggesting either cells often express these two genes together, or some cells within the population are more likely to mount higher transcirptional responses for all genes activated.

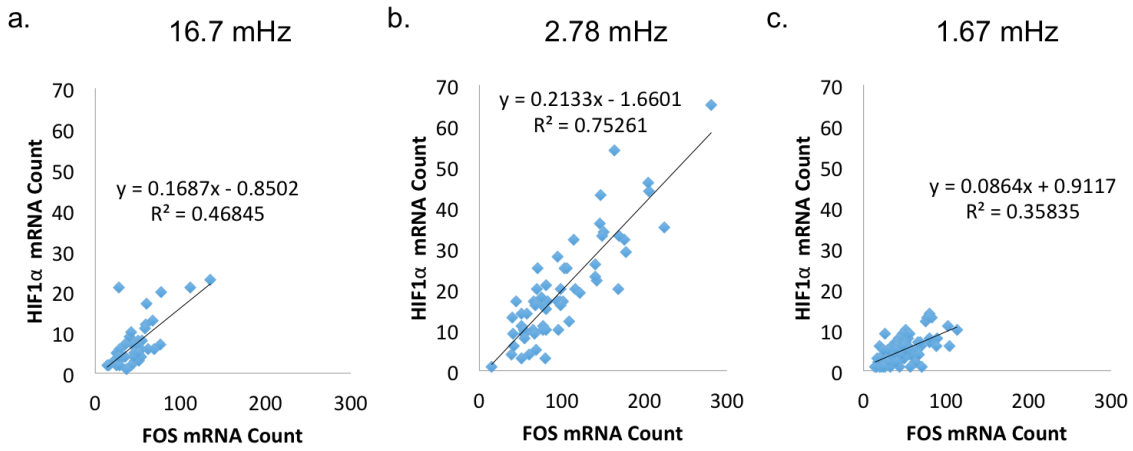

Figure 7-12: Linear Correlation Between mRNA Probes in HyPer-Cyto Transfected Cells.
The mRNA count for FOS and HIF1α was compared for individual cells and showed a strong linear correlation between transcript numbers in HyPer-Cyto stably transfected cells. Each graph is depicted with the resulting linear relationship and R^2 values for (a) 16.7 mHz, (b) 2.78 mHz, and (c) 1.67 mHz condition cells.

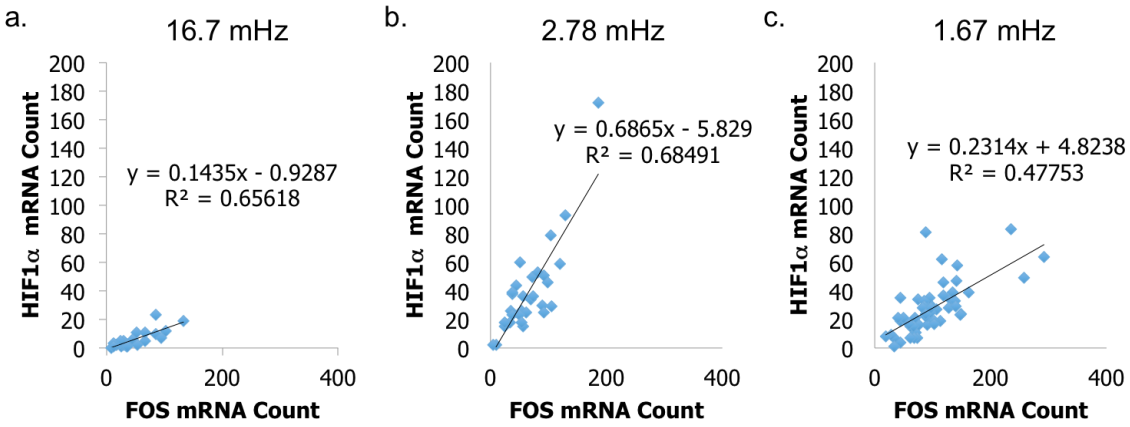

Figure 7-13: Linear Correlation Between mRNA Probes in HyPer-Mito Transfected Cells.
The mRNA count for FOS and HIF1α similarly showed a strong linear correlation between transcript copy numbers in HyPer-Mito cells. Each graph is depicted with the resulting linear relationship and R^2 values for (a) 16.7 mHz, (b) 2.78 mHz, and (c) 1.67 mHz condition cells.

7.4 Discussion

Throughout this work we have hypothesized that we can better characterize the connections and interactions between Ca^{2+} and H_2O_2 during T cell activation using the innovative application of microfluidics and single-cell analysis with recombinant reporter lines. We have shown in earlier chapters that Ca^{2+} responds with oscillatory behavior upon stimulation with H_2O_2, and it appears to be most entrained with a driving frequency of 2.78 mHz, corresponding to a period of 6 minutes. In this work, we interchanged the input and output of our system such that cells were treated with thapsigargin and driven with EGTA and $CaCl_2$ solutions to elicit robust, well defined spikes of Ca^{2+} for a wide range of frequencies. H_2O_2 production was imaged through time with the use of our stably transfected HyPer-mito and HyPer-cyto cells, corresponding to mitochondrial and cytoplasmic localized versions of the recombinant protein, HyPer. We further utilized our microfluidic system to not only image individual cells through time, but also fix and

hybridize cells on chip with smFISH probes to measure downstream transcriptional factors.

We have seen previously that Ca^{2+} signaling is highly heterogeneous and cells within a population vary in frequency, amplitude, and phase shift. We have introduced a new investigational approach to more intelligently probe the system; however fully decoding the whole realm of Ca^{2+} signals is not currently possible. We sought to reduce the number of variations cells experienced such that we could tightly control Ca^{2+} signaling to make conclusions about H_2O_2 production in response to known Ca^{2+} behavior. We were able to characterize the response of Jurkat T cells to EGTA/Ca^{2+} stimulation and found a robust, homogenous population of cells responding at the driving frequency. In fact, almost every cell responded with a single, dominant frequency of signaling that reflected the driving frequency. With this result, we were justified with estimating the population response to Ca^{2+} and assuming all cells were responding similarly with approximately identical Ca^{2+} signaling.

One of the open questions in literature surrounds the effect of Ca^{2+} on H_2O_2 production, with many reports suggesting different results in the presence of different inhibitors of oxidative phosphorylation. To further investigate this, we visualized the response of H_2O_2 reporters, HyPer-cyto and HyPer-mito, to Ca^{2+} oscillations of various frequencies, using the same experimental set up as in previous chapters. Such a view of T cell redox signaling in response to Ca^{2+} perturbations has not been obtained before and signifies a distinct improvement for collecting signaling kinetic information. Time course analysis revealed distinct differences between H_2O_2 production in the mitochondria and cytoplasm. For instance, cytoplasmic H_2O_2 levels were seen to decrease in response to

Ca^{2+} exposure, and although subtle, it was reproducible across many cells and experimental conditions. This suggests there is some kind of inhibitory role of Ca^{2+} in cytoplasmic H_2O_2. This is also in line with previous reports suggesting H_2O_2 does not increase upon exposure to Ca^{2+} unless in the presence of additional inhibitors [320]. However, to our knowledge, such a robust decrease in H_2O_2 has not been reported in literature. This decrease suggests the potential for Ca^{2+} to actively downregulate H_2O_2 levels in the cytoplasm upon exposure, possibly through protein modulation of the redox pathways involved with H_2O_2 metabolism in the cytoplasm, such as activation of the glutathione peroxidase (GPx) and GSH H_2O_2 elimination system. Such a rapid increase in the reducing capacity of the cytoplasm may functionally serve to help harbor the deleterious effects of ROS production during T cell activation.

In contrast to the cytoplasmic results, the mitochondrial H_2O_2 response exhibited a sharp increase in H_2O_2 levels upon exposure to Ca^{2+}, and this was also repeated between experiments and treatment conditions (Figure 7-3). This result suggests that Ca^{2+} signaling differentially affects subcellular localized H_2O_2, suggesting different mechanisms of action or different modifications of the redox systems in place. Ca^{2+} signaling in T cells is one of the steps towards activation, ultimately leading to the upregulation of multiple transcriptional factors, increased proliferation, and cytokine release. These processes all require energy and mitochondria proceed through an oxidative burst upon activation, potentially as the result of an increase in oxidative phosphorylation. However, it has never been shown with this detail of localization and timing that H_2O_2 increases in response to Ca^{2+} signaling, thus providing novel support to this hypothesis.

One of the hypotheses of this work was that the Ca^{2+} signaling could direct downstream transcriptional responses in a frequency dependent manner. To further assess this basis for derivation of our experimental protocol, we measured the transcriptional response of FOS, a protein dependent on Ca^{2+} signaling for complete upregulation during T cell activation, and HIF1α, hypoxia inducible factor protein, by fixing and hybridizing cells in our microfluidic device after stimulation. These cells were first exposed to the oscillatory conditions explained above, and subsequently imaged for mRNA count of smFISH probes of interest. Individual cells were captured for both signaling events and downstream transcriptional activity based on their presence in the cell trap for both procedures. It was evident from the smFISH data that the 6 minute period of oscillation, corresponding to a frequency of 2.78 mHz, for Ca^{2+} signaling elicited the largest response in mRNA count. Not only does this provide useful data to compare to signaling information, but it also reaffirms the conclusions found in Chapter 6: we reported the finding that Ca^{2+} oscillation seems to be naturally entrained to a frequency of H_2O_2 signaling around 6 minutes, and concluded this is important for downstream events. Here we have shown this is in fact the case, and cells appear to respond most robustly to this stimulation condition, highlighting not only the necessity to visualize Ca^{2+} dynamics in the frequency domain, but also the utility of this experimental approach for providing insight into the complex signaling networks to define frequencies of interest and transcriptional ramifications of these signaling patterns.

Furthermore, we explored ways to classify cells into different signaling subpopulations and determine any differences between clusters of downstream transcription. We found three distinct clusters of cells, corresponding to two major

phenotypes of signaling patterns: (1) top cells with higher H_2O_2 signaling through time and (2) bottom cells with lower than average H_2O_2 signaling for the experiment duration. Among these groups, we observed differences in the downstream transcription, with the interesting finding that the cells with decreasing H_2O_2 through time appear to be some of the highest transcriptional responders, highlighting the necessity to further characterize these single-cell traces with additional metrics to find correlations between H_2O_2 response and downstream transcriptional factors. The best correlation we observed was a linear relationship between FOS and HIF1α transcript levels within a single-cell. It was apparent that cells were likely to express similar levels of mRNA counts and this observation may be described with a few different conjectures. First, there is potential for cells to couple these two genes for transcription upon T cell activation to again help with the cellular response to increased energy demands. Another possible explanation is that cells are more likely to be primed to express genes at higher levels overall when compared to other cells. As smFISH is an endpoint assay with inability to collect single-cell information about initial basal transcript levels, we are unaware if these cells were naturally expressing higher levels of both at the initial time point and stimulation only exacerbated this predisposition. Potential future directions to test this hypothesis include better characterization of the initial population of cells, i.e. before any stimulation, to determine the range of mRNA transcript counts. Although this measurement is obtained on a different set of Jurkat T cells than what is stimulated, it would provide additional evidence as to whether or not the population exhibits the same level of heterogeneity initially. Other future experiments could include monitoring an additional signaling molecule upstream of FOS or HIF1α in conjunction with H_2O_2 to more fully characterize

the upstream events of transcription. This may shed light on where the variability in downstream targets arises: whether it be in Ca^{2+}, H_2O_2, or additional, currently unmeasured molecules.

In summary, in this chapter we have demonstrated the utility of this microfluidic system and experimental set up to extract key information regarding the interplay between Ca^{2+} and H_2O_2 upon T cell activation as well as the frequency dependence of downstream transcriptional activity on Ca^{2+} signaling at the single-cell level. Future work can be devoted to defining additional metrics to describe the kinetics of H_2O_2 signaling to find any connection between differential transcriptional responses to these metrics.

CHAPTER 8 CONCLUSIONS AND FUTURE DIRECTIONS

8.1 Conclusions

Throughout this dissertation, we have investigated intracellular signaling in response to various environmental perturbations with single-cell resolution. This work has been made possible through an innovative microfluidic and computational approach, expanding on previously developed techniques to develop a platform for the frequency response analysis of suspension Jurkat T cell lymphocytes. We have expanded the realm of possible perturbations we apply to cells, attempting to decode characteristics of the frequency based Ca^{2+} signaling observed. Our approaches enabled a more systematic approach for probing Ca^{2+} signaling. We were also able to combine signaling studies with markers for downstream transcriptional response by hybridizing smFISH probes on chip with single-cell resolution. We have achieved a more complete view of T cell signaling than previous reports and introduce novel findings in the frequency domain of Ca^{2+} and H_2O_2 signaling networks.

Single-Cell Analysis of H_2O_2 Production

Our first studies aimed at characterizing heterogeneity within a population of cells to ROS stimulation by antimycin A with single-cell resolution. We developed protocols for stably transfecting Jurkat T cells with recently produced recombinant proteins susceptible to reversible oxidation by H_2O_2 [130-132, 340, 341]. These proteins, HyPer-cyto and HyPer-mito, are intracellularly localized within the cytoplasm or mitochondria, respectively, and report spatiotemporal H_2O_2 levels in response to perturbation. We found

that populations of cells responded as expected to varying levels of antimycin A, with more cells reporting higher levels of H_2O_2 as antimycin A concentration increased. Yet, within a population of cells, responses were variable at the single-cell level and there were some nonresponsive cells in both experiments. This observable heterogeneity highlighted the necessity to achieve single-cell resolution to better understand signaling dynamics in complex regulatory networks. Through the use of HyPer, we overcame many current technical limitations regarding ROS measurement [342], and this enabled us to visualize population heterogeneity as well as H_2O_2 dynamics upon stimulation. Our experimental platform can be extended to perturb H_2O_2 production with any soluble cue and provides an advance in better understanding the spatiotemporal ramifications of redox altering stimulation.

Computational Tools for Modeling T cell Ca^{2+} Kinetics

To better understand T cell Ca^{2+} kinetics in response to T cell activation, we also further developed a computational model of T cell activation. This model built upon previous literature to incorporate kinetics that orchestrate Ca^{2+} signaling in response to TCR ligation. We successfully reproduced experimental data *in silico* and perturbed this system to recreate in vivo T cell changes between young and old, senescing, $CD8^+$ T cells. Throughout this process we used the computational model to test predictions of molecular mechanisms by which changes in kinetics occur. The resulting system highlighted the potential for STIM1 to be oxidized during aging, and this was experimentally validated, providing a target for novel redox modification responsible for Ca^{2+} kinetics in older T cells, potentially underscoring differences in T cell effector

function and ultimately a target for reversing age related decline in immune system function. Although only the population average of cells was assayed for model fitting, this finding may also be involved with orchestrating Ca^{2+} oscillations in single-cells. STIM1 is located on the ER membrane and known to translocate from diffuse organization to distinct puncta in close proximity to the plasma membrane upon activation by ER Ca^{2+} depletion. STIM1, upon translocation, is in close proximity to ORAI1 on the plasma membrane and able to elicit CRAC channel opening, flooding the cytoplasm with Ca^{2+} ions from extracellular space as part of the SOCE mechanism [343, 344]. As STIM1 has roles in sensing depleted ER Ca^{2+} and subsequent orchestration of opening CRAC channels, this protein may also play a part in driving the oscillation at which Ca^{2+} signaling occurs in the cytoplasm. With our demonstrated redox regulation of this protein, it also suggests that throughout aging, T cells may respond with differential oscillations compared to the immune system of younger individuals.

Microfluidic and Analysis Tools for Frequency Based Single-Cell Stimulation

We next sought to exploit Ca^{2+} oscillations by investigating signaling kinetics with a frequency response analysis approach, originally developed in control engineering and shown to be useful for analyzing small biological networks [115, 117]. Our application of the cross-talk between Ca^{2+} and ROS during T cell activation represents a more complex mammalian system than has been previously studied. We first developed the microfluidic techniques necessary for oscillatory stimulation of suspension cells and utilized two devices in this thesis: the first device was capable of robustly delivering oscillatory stimulation with diffusion of the step profile as it traversed the device and the second

utilized a two-layer approach for fast fluid switching with top down delivery, providing the same stimulation to all cells regardless of device position. We chose the latter, two-layer device, to eliminate variation in input signal and reduce underlying factors that could contribute to heterogeneity. Despite controlling for a uniform stimulation with oscillatory H_2O_2, we observed a wide realm of potential Ca^{2+} responses with some being entrained to the input frequency and others demonstrating other phenotypes. With hundreds of single-cell traces, we developed a more automatic pipeline for analysis of single-cells and used spectral analysis to extract key features of the frequency response, such as dominant frequencies present in the signal as well as the gain and phase for each input frequency. This suite of analysis scripts represents a novel and complete approach for viewing individual T cell traces with combining previously developed spectral analysis techniques and microfluidic principles [22, 102, 220, 241]. The platform was built with applicability to future and diverse studies in mind; different dynamic stimulation conditions can be easily programmed and applied for single-cell analysis, such as alteration of duty cycle or frequencies assayed.

Ca^{2+} Responds Differentially to Dynamic H_2O_2 Stimulation

We were able to sample multiple frequencies with this modularized device and combine information into Bode plots, representing the filter characteristics of the system. Finally, we used optimization algorithms to fit a second order transfer function to the data, finding a natural frequency of 2.78 mHz for the system, corresponding to a period of 6 minutes. In addition to the transfer function fit to the entire population, subsets of the population were used to fit the same parameters of the transfer function to determine

potential differences between these subsets. We found for the top 25% of the population, as calculated based on the gain response for each frequency, our best fit transfer function parameter set shows a more damped system as compared to the population fit. The bottom 25% of cell values was fit to a model that had a similar damping coefficient to the population fit, but the system gain was much lower than the other fits. Together, these models suggest there could be differences between cells in their filtering behavior, with some cells having a less variable response to stimulation with different frequencies (more damped system). One possible explanation for these differences may arise in oxidative modifications of proteins involved with Ca^{2+} transport, such as STIM1, which we found to be redox sensitive in aging cells. Better characterization of STIM1 oxidation states at the single-cell level within a population of cells may provide evidence to support this hypothesis. Other variations in T cells that would account for these different responses include those molecules involved in Ca^{2+} sensing, such as PLC-γ [75, 76], PKC [77], CaMKII [345], and the mitochondrial Ca^{2+} uniporter [78]. Differences in post translational modification of these proteins may alter the binding kinetics of Ca^{2+} to the sensing portion of the molecule, altering the on-off kinetics that are thought to be responsible for decoding frequency based stimulation.

Frequency Response of Ca^{2+} to H_2O_2

Our computational model of T cell activation was also expanded to incorporate interactions between Ca^{2+} and H_2O_2 into a large mechanistic model of seven nonlinear ODEs. With the application of an oscillatory input to the system *in silico*, we found interesting observations of differential steady state behavior based on input frequency and

amplitude, demonstrating the potential mechanisms by which Ca^{2+} can decode such a diverse array of responses with a universal signaling ion. There are some recent reports that also investigate Ca^{2+} dynamics in the frequency domain, many of which find some kind of band pass filter behavior [324], which aligns with our response: we see the 2.78 mHz frequency most robustly transmitted from input to output signal with attenuation on either side of this frequency. Interestingly, other biological signaling networks also behave as band pass filters in nature, suggesting this is a common network phenomenon [115, 117]. Evolutionarily, it makes intuitive sense that signaling systems would respond only to very specific input signals to spare energy for only specific signaling events, thus providing a robust, efficient response to environmental stimulation.

Other reports demonstrate the functional response of Ca^{2+} signaling, as reported by transcripts of NFAT and NFκB, and find that the frequency of Ca^{2+} signaling elicits differential expression [22, 70]. Although these studies utilized frequency stimulation with varying duty cycle (0.028-0.5), our results lie within the range of reported functional responses, corroborating our conclusion for the natural frequency of Ca^{2+} signaling observed with H_2O_2 stimulation at a constant duty cycle of 0.5. It is interesting to lie within the reported range despite differences in input signal shape, and it would be interesting to more completely characterize this response using our system with a range of duty cycles sampled. As the downstream decoding can be accomplished based on translocation of response elements such as NFAT or NFκB, better understanding of dominant frequencies for each transcription factor may enable a more appropriate mechanistic model to be developed for these dynamics.

We report the first study of Ca^{2+} oscillation in single T cells responding to approximately sinusoidal input signals of H_2O_2 of various frequencies and find novel information previously hidden in the frequency domain. Although our network was much larger with more unknown connections than previous applications, we were able to derive the natural frequency of our data and make conclusions about potential transfer function fits as well as explore dynamics with our complex computational model.

Characterizing Local H_2O_2 Response to Ca^{2+}

Although there are known connections between Ca^{2+} and H_2O_2, literature has incomplete molecular evidence for this interplay, and specifically the response of H_2O_2 to Ca^{2+} signaling [90, 197]. Advances in this field are most likely limited by imaging techniques, as ROS have previously been difficult to study with much debate in literature about proper terminology and reached conclusions based on available, irreversible and nonspecific dyes [342]. To overcome this challenge, we use the stably transfected HyPer lines developed in this thesis to monitor H_2O_2 production in response to Ca^{2+} signaling in Jurkat T cells and find distinct differences dependent on subcellular localization of the protein. Our novel findings demonstrate differences between cytoplasmic and mitochondrial H_2O_2 production, with implications for differentially affected redox regulatory mechanisms between compartments.

Transcriptional Response to Oscillatory Ca^{2+} Stimulation

Finally, we again utilized our two-layer microfluidic device to perform on chip smFISH analysis of downstream transcription factors of interest in T cell activation: FOS and

HIf1α. Our novel findings include the maximal transcriptional response found at 2.78 mHz, corresponding to our proposed natural frequency above. It is not possible to remove specific cells from the device for off chip single-cell gene expression analysis, so we modified an existing smFISH protocol [346] to be used on the device for a more complete view of T cell activation: spanning multiple time scales and different biological processes.

Overall, through the combination of microfluidic and computational approaches, we more accurately depict the signaling processes in T cell activation by probing the system with a frequency response analysis approach. Further, these approaches are applicable to investigate other biological questions and provide unique insight that cannot be garnered using traditional experimental techniques.

8.2 Future Research Directions

8.2.1 Development of Computational Tools for Analyzing Single-Cells

In this work we present the continuation of two computational models of T cell activation. The first was used for demonstrating differences between young and old T cells while the second incorporated added complexity with ROS interactions of Ca^{2+} kinetics. While these models provided useful results here, they were ultimately created based on population averages of cells and could be updated in future work to incorporate more of the observed population heterogeneity. For instance, finding different parameter sets responsible for different kinetic traces would be an interesting exploration of underlying mechanisms that give rise to the plethora of possible responses. Further, this approach will give an unprecedented view into diseased states, potentially finding

parameter sets responsible for driving disease progression and prognosis. Such a view of population heterogeneity will cultivate hypotheses in a more timely fashion than running separate experiments; it is often faster to run *in silico* experiments for model-driven hypotheses that can be experimentally tested.

With an increase in understanding of heterogeneity, it is possible to understand implications of disease treatment based on a personalized assessment of patients' population of cells. With this model toolkit, it may be possible to perform *in silico* drug screens on patient data with the ultimate goal of quickly and confidently ascertaining the most effective treatment option.

8.2.2 Frequency Response Analysis of ROS/Ca^{2+} Signaling

Biological systems have feedback control, robustness, and sensitivity built into network complexity. The ability to reduce this system down to dominant feedback controls is important for advancing understanding of many network topologies. As an investigative approach, we offer a proof of concept that the use of frequency response analysis can model the response of Ca^{2+} signaling to H_2O_2 input without any understanding of molecular basis of the system. Typical approaches for this analysis rely on white noise input signals that are composed of many frequencies. The resulting output signal is analyzed and gain can be calculated for a single-cell across the frequency spectrum. However, without detailed characterization of possible Ca^{2+} signals, it would not be possible to determine if the resulting signal had different frequencies present due to input signal or natural processes within the cell. To overcome this limitation, we first probed only a single frequency for each cell and combined data between experiments to compose the Bode plot representation. The development of better clustering techniques or metrics

to compare cells enables a more complete understanding of potential single-cell responses and could be used for comparison with more advanced stimulatory conditions. An experimental approach to more systematically probe single-cells with multiple frequencies would supply additional information into the hypothesis that different cells exhibit different filtering capabilities, and would also allow us to determine parameters of interest for these transfer function systems.

In this work, we also investigated large mechanistic models using ODE equations to describe the ROS/Ca^{2+} kinetics during T cell activation. We were able to recreate experimental data in the time domain and the response of cells to oscillatory stimulation, however our system was complex with many nonlinearities. Future work should concentrate on reducing the model into different subnetworks to determine how each network contributes to this instability, with the goal of finding stable subnetworks that can be probed individually and combined for a more complete understanding of the underlying topology. It would also give more insight into the dominant feedback regulation and thus highlight novel potential targets for therapeutic intervention of diseased states.

8.2.3 Characterizing H_2O_2 Response to Ca^{2+}

H_2O_2 production was measured in response to Ca^{2+} signaling using a thapsigargin pretreatment condition to chemically clamp the cells. While this pretreatment is not known to alter the redox status of the cell, it would be interesting to activate T cells without thapsigargin and monitor the resulting H_2O_2 response using this well characterized experimental approach to image HyPer transfected cells. However, there are a multitude of potential Ca^{2+} responses that could be occurring and without proper

Ca^{2+} probes that can be used for simultaneous imaging with HyPer, it is difficult to conclude what differences are based on cell specific Ca^{2+} signals and what responses are cell-to-cell variability. Proper characterization of additional Ca^{2+} dyes may make it possible to simultaneously monitor both signaling molecules through time and help alleviate this limitation.

Other controls to assess include providing cells with different amplitude Ca^{2+} signals to determine what information amplitude encodes for H_2O_2 signaling and downstream transcriptional response. As signals in the frequency domain contain both frequency and amplitude, finding a way to systematically sample all possible modes of carrying information in these signals provides an invaluable tool for better characterizing these complex signaling molecules.

To determine potential molecular mechanisms behind this differential response between cytoplasmic and mitochondrial H_2O_2 production, it would be interesting to apply different inhibitors to the system and again collect the H_2O_2 dynamic response with live cell fluorescent microscopy. For instance, applying an inhibitor to a reducing agent of H_2O_2 may result in no difference to H_2O_2 dynamics upon Ca^{2+} signaling, providing the mechanistic details for localized Ca^{2+} modulation of H_2O_2 dynamics. These experiments would be straightforward to complete on the aforementioned microfluidic set up.

8.2.4 Transcriptional Response to Oscillatory Stimulation

To garner as much information as possible, and on as many timescales as possible, we fixed cells post stimulation with oscillatory Ca^{2+} signals and hybridized smFISH probes to count mRNA transcript numbers in single-cells and compare these results with upstream signaling events. We found low correlation between some of the computed

metrics and downstream transcript copy number; it is likely that this is due to the incorrect choice of signaling characterization metrics and more investigation is warranted to find additional measurements, such as area under the curve of H_2O_2 response, time to peak, or decay rate of the response to Ca^{2+}. As single-cell time course data is a new area for research, we are still working to understand what portions of dynamic information provided by the cell are important versus background noise or natural variation. However, with this set up we can systematically test different metrics to the downstream transcriptional events to determine what metrics are useful in conveying important environmental information to the cells.

Experimentally, we observed large heterogeneity between cells with their signaling responses despite approximately the same input signal, which may contain information that we have thus far ignored. Future work in this area should focus to better cluster responses and extract key computed metrics for modeling important regulatory mechanisms responsible for downstream function. This widely applicable platform provides one of the most complete pictures of intracellular T cell signaling dynamics and downstream transcriptional events with single-cell resolution. Many experimental techniques are only capable of accomplishing one of these tasks, highlighting the importance of the work in this dissertation to lay the groundwork for future wide scale studies of cellular behavior.

APPENDIX A: DOCUMENTED CODE

A.1. Device Characterization and Single-cell Identification

A.1.1. Manual Identification

```
%% Load Images to MATLAB

if ~exist('NbImages', 'var')

    NbImages = 305;                              %number of images
    Im = cell(1,NbImages);

    FNAMEFMT1 = 'frame%d.tif';

    for i=1:NbImages
      Im{i} = imread(sprintf(FNAMEFMT1,i));          %Fluorescent
images
    end

%     for i = 10:99
%       Im{i} = imread(sprintf(FNAMEFMT2,i));
%     end
%
%     for i = 100:NbImages
%       Im{i} = imread(sprintf(FNAMEFMT3,i));
%     end

end
% Crop Cells


%Deleted--Makes it more automatic
% Image = Im{NbImages};
% Image2 = Im{1};
%
% [level EM] = graythresh(Image);
% [level2 EM2] = graythresh(Image2);
%
% bw = im2bw(Image,level*1.25);      %%Convert to binary
% bw = bwareaopen(bw,50);              %%Remove small objects
%
% bw2 = im2bw(Image2,level*3);      %%Convert to binary
% bw2 = bwareaopen(bw2,50);
%
% Overlay = imfuse(bw,bw2);

% Imgray = rgb2gray(Im{1});

%Create ROI
```

```
Ncell=21;
for i=21%1:Ncell
    i
[X,Y,Icrop,rect] = imcrop(Im{1});
XX{i}=X;
YY{i}=Y;
IIcrop{i}=Icrop;
Rect{i}=rect;
end

% Apply the ROI to the various pics
for j=1:NbImages
    ImageAnalyze = Im{j};
    Imgray = rgb2gray(ImageAnalyze);
    for i=1:Ncell
        Imcrop{j,i}=imcrop(Imgray,Rect{i});
    end
end


% Get Mean Fluorescent Intensity for each

%define matrices
C=zeros(Ncell-1,NbImages);
CNorm = zeros(size(C));


% calculate intensity, subtract background and normalize
for j=1:NbImages    %step through each picture
    for i=Ncell     %for each picture, the last box drawn is for the
background.
        A=mean(Imcrop{j,i}); %average the rows
        B=mean(A,2);         %average the columns (order?)
        CBack=B;    %Mean background intensity
    end
    for i=1:Ncell-1 %ignore the last box, which is the background
        A=mean(Imcrop{j,i},1);
        B=mean(A,2);
        C(i,j)=B-CBack; %subtract the background from each cell
        CNorm(i, j)=C(i,j)/C(i, 1); %normalize the cell intensity to
the first time point
    end
end

figure(1)
imagesc(C)

% %Plot average of all cells through time
% Cavg = zeros(1,NbImages);
% for j = 1:NbImages
%     Cavg(j)=mean(CNorm(:,j));
% end
%
% figure (2)
% plot(Cavg)
```

A.2. Frequency Response Analysis Pipeline

A.2.1. Step 1: Single-cell Identification

Single-cells are identified using RDFC according to a paper from the Lu Lab that is currently in prep:

Charles L. Zhao, Ariel S. Kniss, Thomas J. Levario, Daniel F. Puleri, Shinsuke Niwa, Kang Shen, Hang Lu. Rapid and Simple Quantitative Phenotyping of Fluorescent Reporters Enabled by Relative Difference Filtering and Clustering. In Prep (2016).

A.2.2. Step 2: Collect Time Lapse Data

```
%Ariel S. Kniss
%Last Edited: January 2015

% %http://www.mathworks.com/help/images/functionlist.html

%Indicate where the L image is from CZ code
%20150521_25uM_6Min_L.mat, originally saved from
20150521_25uM_6Min_TRUNC_CZMethod_20150522T172431

%Indicate what filename you would like the save the results as:
Filename = ['20150521_25uM_6Min_181_CZMethod_',datestr(now,30),'.mat'];

% if ~exist('NbImages', 'var')
%
    NbImages = 211;                              %number of images
    Im = cell(1,NbImages);
    pixelarearange = [30,100];                  %Range of pixel area
values, used below with bwareafilt
    FirstFrame = 31;

    FNAMEFMT1 = '20150521_25h2o2_trial1t00%dxy1c1.tif'; %Change these
to reflect tif images from nd export
    FNAMEFMT2 = '20150521_25h2o2_trial1t0%dxy1c1.tif';
    FNAMEFMT3 = '20150521_25h2o2_trial1t%dxy1c1.tif';

    for i=1:9
      Im{i} = imread(sprintf(FNAMEFMT1,i));          %Fluorescent
images
    end

    for i = 10:99
      Im{i} = imread(sprintf(FNAMEFMT2,i));
    end
```

```
    for i = 100:NbImages
      Im{i} = imread(sprintf(FNAMEFMT3,i));
    end

% end
%
% %Do not change any variables below this line
**************************
%
% figure(1)
% subplot(2,3,1)
% imshow(Im{1})
% title('Grayscale Image')
%
% %first adjust contrast to help pick out cells in binary image
% Imadjust = imadjust(Im{1});
% Imadjustlast = imadjust(Im{NbImages});
%
% ImadjustComb = imadd(Imadjust,Imadjustlast);
%
% subplot(2,3,2)
% imshow(Imadjust)
% title('Grayscale Image Adjusted')
%
% [level EM1] = graythresh(ImadjustComb);     %get the threshold from
graythresh function
% bw = im2bw(ImadjustComb,level);             %Convert to binary
% bwclearborder = imclearborder(bw);      %clear any objects on the
border of image
% bwclear = bwareafilt(bwclearborder,pixelarearange);
%Remove spots not in pixelrange
%
% subplot(2,3,3)
% imshow(bw)
% title('Raw Binary Image')
%
% subplot(2,3,4)
% imshow(bwclearborder)
% title('Binary Image with Clear Borders')
%
% subplot(2,3,5)
% imshow(bwclear)
% title('Binary Image with Sizes Filtered')
%
%
%
% [L, num] = bwlabel(bwclear);               %Label the connected
components, num returns the number of connected components

for ii=1:NbImages

    stats =
regionprops(L,Im{ii},'MeanIntensity','MinIntensity','MaxIntensity','Cen
troid','BoundingBox','Extrema','Area');
```

```
    MeanIntensity(:,ii) = extractfield(stats,'MeanIntensity')';   %This
takes the values from the structure and makes a vector
    BoundingBox(:,ii) = extractfield(stats,'BoundingBox')';
    MinIntensity(:,ii) = extractfield(stats,'MinIntensity');
    MaxIntensity(:,ii) = extractfield(stats,'MaxIntensity');
    Centroid(:,ii) = extractfield(stats,'Centroid');
    Extrema(:,ii) = extractfield(stats,'Extrema');
    Area(:,ii) = extractfield(stats,'Area');

    for i = 0:num-1
        j = i*4+1;                          %Bounding box has 4 values
for every object: 1. x coordinate 2. y coordinate 3. x width 4. y width
        ycoord(i+1) = round(BoundingBox(j+1));   %Find the y value for
all bounding boxes
        xcoord(i+1) = round(BoundingBox(j));     %Find the x value for
all bounding boxes
        if xcoord(i+1) >= 3 && ycoord(i+1)>= 3
            Back(i+1,ii) = mean(mean(Im{ii}(ycoord(i+1)-
2:ycoord(i+1),xcoord(i+1)-2:xcoord(i+1)))); %Take the average of pixel
intensities from the top left, a 3x3 pixel square
            BackSubMeanIntensity(i+1,ii) = MeanIntensity(i+1,ii) -
Back(i+1,ii);
        else
            Back(i+1,ii) = mean(mean(Im{ii}(ycoord(i+1)-
1:ycoord(i+1),xcoord(i+1)-1:xcoord(i+1)))); %Take the average of pixel
intensities from the top left, a 2x2 pixel square
            BackSubMeanIntensity(i+1,ii) = MeanIntensity(i+1,ii) -
Back(i+1,ii);                    %Perform final calculation where the
mean cell intensity subtracts the little background box from it
        end

    end


end

%Now we want to find those cells that become negative, these will be
%removed from the dataset
NegativeCells = BackSubMeanIntensity < 0;
RowsToDelete = [];

for i = 1:num
    if sum(NegativeCells(i,:)) > 0
            RowsToDelete = [RowsToDelete i];
    else
    end
end

NumRowsToDelete=length(RowsToDelete);
BackSubMeanIntensityCorr = BackSubMeanIntensity;
BackCorr = Back;

for i = 1:NumRowsToDelete

        RowNumber = RowsToDelete(i)-(i-1);
```

```
        BackSubMeanIntensityCorr(RowNumber,:)=[];
        BackCorr(RowNumber,:)=[];

end

BackSubMeanIntensityCorrTrunc =
BackSubMeanIntensityCorr(:,FirstFrame:end);

coord = [ycoord' xcoord'];



save(Filename)
```

A.2.3. Step 3: Normalize Traces

```
clear all; close all; clc

File = '20150521_25uM_6Min_181_CZMethod_20150805T114051'; %Insert file
name, but do not include '.mat'

FileToLoad = [File,'.mat']; %Identify the variables you want to bring
in

Matobj = matfile(FileToLoad);   %Load in specific file
BackSubMeanIntensityCorrTrunc = Matobj.BackSubMeanIntensityCorrTrunc;
%Only need one variable here

%Labeled with period listed followed by date BackSubMeanIntensityCorr
was
%created and finally, the date in which the file was created
OutputFilename = [File,'_',datestr(now,30),'.txt'];
SaveFilename = [File,'_',datestr(now,30),'.mat'];

ExpLength = 1080; %Length of the experiment in s
Fs = 6;     %SamplingRate


%Should not need to edit below line
%**********************************


Time = 0:Fs:ExpLength;  %Create your time vector


cellnumber = size(BackSubMeanIntensityCorrTrunc,1);
length = size(BackSubMeanIntensityCorrTrunc,2);
Cminmaxeachnorm2 = zeros(cellnumber + 1,length); %+1 to make room for
the average!!

for i = 1:cellnumber
   M = BackSubMeanIntensityCorrTrunc(i,1:length);
```

```
   Mnorm = minmaxnorm(M);
   Cminmaxeachnorm2(i,:) = (Mnorm);
end

for i = 1:length
    Cminmaxeachnorm2(cellnumber+1,i) =
mean(Cminmaxeachnorm2(1:cellnumber,i));
end

CwTime = [Time' Cminmaxeachnorm2'];

dlmwrite(OutputFilename,CwTime,'\t');

save(SaveFilename)

% %function to accompany this file
% function Mnorm = minmaxnorm(M)
% a = min(min(M));
% b = max(max(M));
% Mnorm = (M-a)/(b-a);
```

A.2.4. Step 4: Spectral Analysis Using Modified GUI

GUI was used from [241] was used with the following modifications:

```
timeError = 0.25;
lowPeriod = 1.0;
autoLevel = 0.75;
pow.increment = 1;

%************************************Added by AK
wordlength = size(pow.file.target,2);
newlength = wordlength - 4;   %Take out the last 4 characers; these
specify the .dat

Filename                                                              =
[pow.file.target(1:newlength),'_SA_',datestr(now,30),'.mat'];

%*****************************************************
%*****************************************Added by AK

NumberCells = pow.noCells;
HistData = [];

%*********************************************
%************************************Added by AK

  HistData = [HistData; pow.peaks];

%*********************************************
%************************************Added by AK
```

```
  % Data was originally stored with three columns
  % Frequency PSDheight RelativePower(in %)
  % Now they are combined for all cells, so take each column and save
as
  % separate variable
  HistFreqVal = HistData(:,1);
  HistPSDVal = HistData(:,2);
  HistRelPower = HistData(:,3);

%***********************************************
save(Filename)
```

A.2.5. Step 5: Combine Gain and Phase Calculations

```
%Ariel S. Kniss
%Last Edited: January 2015

clear all; close all; clc

%Importing files in from the Spectral Analysis .dat files importfile.m
%function needs to be in same folder
%The imported files were creating using SpectralAnalysis.m GUI

ImportFile =
'20150521_25uM_6Min_181_CZMethod_20150805T114051_20150805T114147.spectr
um.dat';

C = importdata(ImportFile);
SineWaveSpectrum = importdata('SIXMINSINWAVEShift_TRUNC.spectrum.dat');

length = size(ImportFile,2);

row = 18; %This is the row that corresponds to the driving frequency,
2.77mHz


Filename = [ImportFile(1:length-4),'_Gains_',datestr(now,30),'.mat'];

cellnumber = size(C.data,2)-2; %Set the cell number based on columns in
%C, but remember the final column in data matrices is the average, so
%subtract 1 from that


%%%%%%%%
for i = 2:cellnumber+2
Cgains(:,i-1) = [C.data(:,i)./SineWaveSpectrum.data(:,2)]; %Second
column of
%SineWaveSpectrum is data; first is frequency


end

%%%%%%
```

```
Gainsdb = 10*log(Cgains);

figure1 = figure;

% Create axes
axes1 = axes('Parent',figure1,'LineWidth',2,'FontSize',12);
hold(axes1,'all');
box(axes1,'off');
plot(C.data(row,1),Gainsdb(row,:),'b.') %Row 18 corresponds to driving
frequency
xlabel('Frequency (mHz)','FontSize',16);

Gainsdb_Drive = Gainsdb(row,:);

% Create ylabel
ylabel('10 * log (P_o_u_t / P_i_n) (dB)','FontSize',16);

% Create title
%title('1 Minute Period - Hanning','FontSize',16);

%%%
save(Filename)
```

A.3. HyPer Signaling Analysis Pipeline

A.3.1. Step 1: Determine Number of Cells

```
%Ariel Kniss 20160314

%AT THE END OF STEP1, YOU NEED TO HAVE THE NUMBER OF CELLS YOU WANT TO
%ANALYZE (WHITE CELLS, NOT ON THE EDGE)

%The input file has the format of 2 channels interwoven
%Exp: Ch1, Ch2, Ch1, Ch2, Ch1, Ch2, Ch1, .... etc

%The goal in this script is to first separate them from a multipage
tif,
%manually identify cells, subtract background, and calculate the ratio
%between the channels

%INPUT YOUR FILE NAME (SHOULD BE A MULTIPAGE TIF WITH INTERWOVEN
CHANNELS)
savedFile = 'XYpoint2.tif';

frameRate_inS = 6.17;

%*****************************************************************
****
```

```
%*************************************************************************
****

%*************************************************************************
****
expDuration = round(600/frameRate_inS);
expLength = frameRate_inS*expDuration;

info = imfinfo(savedFile);
NbImages = numel(info);

NumtoAnalyze = expDuration;

ImEven = cell(1,expDuration);
ImOdd = cell(1,expDuration);

for k = 1:NumtoAnalyze*2
    Mod = mod(k,2);
    if Mod == 1
    ImOdd{(k+1)/2} = imread(savedFile, k);
    elseif Mod == 0
    ImEven{k/2} = imread(savedFile, k);
    end
end

%CHANGE THIS IF YOUR ORDER OF AQUISITION IS DIFFERENT!

Im_red = ImOdd;
Im_ox = ImEven;


%The rest should be relatively automatic
%*************************************************************************
****

% Crop Cells

%*************************************************************************
****
%%THIS SECTION IS ONLY RUN ONCE

%Here we will combine images so the manual picking can be done with the
%first and last frame fused together, this ensures all locations of the
%cell are included in the ROI
Image = imadjust(Im_ox{NumtoAnalyze});
Image2 = imadjust(Im_ox{1});

Overlay = imfuse(Image,Image2);

figure()
imagesc(Overlay)
```

A.3.2. Step 2: Analyze Cell Traces

```
%Ariel Kniss 20160203

%The input file has the format of 2 channels interwoven
%Exp: Ch1, Ch2, Ch1, Ch2, Ch1, Ch2, Ch1, .... etc

%The goal in this script is to first separate them from a multipage
tif,
%manually identify cells, subtract background, and calculate the ratio
%between the channels

%INPUT YOUR FILE NAME (SHOULD BE A MULTIPAGE TIF WITH INTERWOVEN
CHANNELS)
savedFile = 'XYpoint1.tif';

FileName = [savedFile(1:length(savedFile)-4),'_',datestr(now,30),'.mat'
];

%Input the number of cells you would like to manually identify
Ncell = 25;


info = imfinfo(savedFile);
NbImages = numel(info);

NumtoAnalyze = round(NbImages/8);

ImEven = cell(1,NbImages/2);
ImOdd = cell(1,NbImages/2);

for k = 1:NbImages
    Mod = mod(k,2);
    if Mod == 1
    ImOdd{(k+1)/2} = imread(savedFile, k);
    elseif Mod == 0
    ImEven{k/2} = imread(savedFile, k);
    end
end

%CHANGE THIS IF YOUR ORDER OF AQUISITION IS DIFFERENT!

Im_red = ImOdd;
Im_ox = ImEven;


%The rest should be relatively automatic
%*****************************************************************
****

% Crop Cells
```

```
%*********************************************************************
****
%%THIS SECTION IS ONLY RUN ONCE

%Here we will combine images so the manual picking can be done with the
%first and last frame fused together, this ensures all locations of the
%cell are included in the ROI
Image = imadjust(Im_ox{NumtoAnalyze});
Image2 = imadjust(Im_ox{1});

Overlay = imfuse(Image,Image2);

%Create ROI

for i=1:Ncell
    i
[X,Y,Icrop,rect] = imcrop(Overlay);
XX{i}=X;
YY{i}=Y;
IIcrop{i}=Icrop;
Rect{i}=rect;
end


%RUN THIS ONCE FOR EACH CHANNEL
%*****************************************************
%OXIDIZED CHANNEL

% Apply the ROI to the various pics
for j=1:NumtoAnalyze
    ImageAnalyze = Im_ox{j};
    for i=1:Ncell
        Imcrop_ox{j,i}=imcrop(ImageAnalyze,Rect{i});
    end
end

% Get Mean Fluorescent Intensity for each

% calculate intensity, subtract background and normalize
for j=1:NumtoAnalyze    %step through each picture
    for i=1:Ncell     %for each picture, the last box drawn is for the
background.
        A=mean(Imcrop_ox{j,i}); %average the rows
        MeanIntensity_ox(i,j)=mean(A,2);         %average the columns
(order?)
    end

    for i = 1:Ncell
        ycoord_ox(i) = round(Rect{i}(2));   %Find the y value for all
bounding boxes
        xcoord_ox(i) = round(Rect{i}(1));     %Find the x value for all
bounding boxes
        if xcoord_ox(i) >= 3 && ycoord_ox(i)>= 3
```

```
            Back_ox(i,j) = mean(mean(Im_ox{j}(ycoord_ox(i)-
2:ycoord_ox(i),xcoord_ox(i)-2:xcoord_ox(i)))); %Take the average of
pixel intensities from the top left, a 2x2 pixel square
            BackSubMeanIntensity_ox(i,j) = MeanIntensity_ox(i,j) -
Back_ox(i,j);                   %Perform final calculation where the
mean cell intensity subtracts the little background box from it
        else
            Back_ox(i,j) = mean(mean(Im_ox{j}(ycoord_ox(i)-
1:ycoord_ox(i),xcoord_ox(i)-1:xcoord_ox(i)))); %Take the average of
pixel intensities from the top left, a 2x2 pixel square
            BackSubMeanIntensity_ox(i,j) = MeanIntensity_ox(i,j) -
Back_ox(i,j);                   %Perform final calculation where the
mean cell intensity subtracts the little background box from it
        end
    end

end


%Now we want to find those cells that become negative, these will be
%removed from the dataset
NegativeCells_ox = BackSubMeanIntensity_ox < 0;     %Creates a binary
image with 1 if the intensity becomes negative
RowsToDelete_ox = [];                               %Sets up the matrix
to keep track of which rows need to be deleted

for i = 1:Ncell                                    %For each object
found, we want to step through them
    if sum(NegativeCells_ox(i,:)) > 0               %If the cell becomes
negative at any point through the images, we want to write this row
number to another matrix
            RowsToDelete_ox = [RowsToDelete_ox i];    %Keeps track of
the rows we want to delete by writing the row number
    else
    end
end

%*****************************************************
%REDUCED CHANNEL
% Apply the ROI to the various pics
for j=1:NumtoAnalyze
    ImageAnalyze = Im_red{j};
    for i=1:Ncell
        Imcrop_red{j,i}=imcrop(ImageAnalyze,Rect{i});
    end
end

% Get Mean Fluorescent Intensity for each

% calculate intensity, subtract background and normalize
for j=1:NumtoAnalyze    %step through each picture
    for i=1:Ncell     %for each picture, the last box drawn is for the
background.
        A=mean(Imcrop_red{j,i}); %average the rows
```

```
        MeanIntensity_red(i,j)=mean(A,2);         %average the columns
(order?)
    end

    for i = 1:Ncell
        ycoord_red(i) = round(Rect{i}(2));   %Find the y value for all
bounding boxes
        xcoord_red(i) = round(Rect{i}(1));     %Find the x value for
all bounding boxes
        if xcoord_red(i) >= 3 && ycoord_red(i)>= 3
            Back_red(i,j) = mean(mean(Im_red{j}(ycoord_red(i)-
2:ycoord_red(i),xcoord_red(i)-2:xcoord_red(i)))); %Take the average of
pixel intensities from the top left, a 2x2 pixel square
            BackSubMeanIntensity_red(i,j) = MeanIntensity_red(i,j) -
Back_red(i,j);                    %Perform final calculation where the
mean cell intensity subtracts the little background box from it
        else
            Back_red(i,j) = mean(mean(Im_red{j}(ycoord_red(i)-
1:ycoord_red(i),xcoord_red(i)-1:xcoord_red(i)))); %Take the average of
pixel intensities from the top left, a 2x2 pixel square
            BackSubMeanIntensity_red(i,j) = MeanIntensity_red(i,j) -
Back_red(i,j);                    %Perform final calculation where the
mean cell intensity subtracts the little background box from it
        end
    end

end


%Now we want to find those cells that become negative, these will be
%removed from the dataset
NegativeCells_red = BackSubMeanIntensity_red < 0;     %Creates a binary
image with 1 if the intensity becomes negative
RowsToDelete_red = [];                                %Sets up the matrix
to keep track of which rows need to be deleted

for i = 1:Ncell                                      %For each object
found, we want to step through them
    if sum(NegativeCells_red(i,:)) > 0               %If the cell
becomes negative at any point through the images, we want to write this
row number to another matrix
            RowsToDelete_red = [RowsToDelete_red i];    %Keeps track of
the rows we want to delete by writing the row number
    else
    end
end

RowsToDelete_comb_unsort_rep = [RowsToDelete_ox RowsToDelete_red];
%Combine all rows that need to be deleted into one variable, will be
unsorted and include replicates present in more than 1
RowsToDelete_comb_rep = sort(RowsToDelete_comb_unsort_rep);     %This
will sort in ascending order (lowest first, highest last)
RowsToDelete_comb = unique(RowsToDelete_comb_rep); %Removes the
replicates
```

```
NumRowsToDelete_comb=length(RowsToDelete_comb);                %See how
many rows need to be deleted
BackSubMeanIntensityCorr_ox = BackSubMeanIntensity_ox;     %Set up our
new variable to keep track of the cells that don't become negative
BackSubMeanIntensityCorr_red = BackSubMeanIntensity_red;     %Set up our
new variable to keep track of the cells that don't become negative

for i = 1:NumRowsToDelete_comb                              %Step through
all rows that need to be deleted

        RowNumber_comb = RowsToDelete_comb(i)-(i-1);
%Specifies the row number, but after the first deleted it accounts for
the change in row numbers
        BackSubMeanIntensityCorr_ox(RowNumber_comb,:)=[];    %Remove
this row number from our corrected matrix of cell values
        BackSubMeanIntensityCorr_red(RowNumber_comb,:)=[];    %Remove
this row number from our corrected matrix of cell values

end

%Normalize the vectors to the first time point

for i = 1:NumtoAnalyze


NBackSubMeanIntensityCorr_ox(:,i)=BackSubMeanIntensityCorr_ox(:,i)./Bac
kSubMeanIntensityCorr_ox(:,1);

NBackSubMeanIntensityCorr_red(:,i)=BackSubMeanIntensityCorr_red(:,i)./B
ackSubMeanIntensityCorr_red(:,1);

end

%Calculate the ratio for oxidized over reduced

RatioOxoverRed =
NBackSubMeanIntensityCorr_ox./NBackSubMeanIntensityCorr_red;


%************************************************************
%Now we want to save the workspace

figure()
subplot(2,2,1)
imagesc(BackSubMeanIntensityCorr_red)
title('Reduced')
xlabel('Frame')
ylabel('Cell Number')

subplot(2,2,2)
imagesc(BackSubMeanIntensityCorr_ox)
title('Oxidized')
xlabel('Frame')
ylabel('Cell Number')
```

```
subplot(2,2,3)
imagesc(NBackSubMeanIntensityCorr_red)
title('Normalized Reduced')
xlabel('Frame')
ylabel('Cell Number')

subplot(2,2,4)
imagesc(NBackSubMeanIntensityCorr_ox)
title('Normalized Oxidized')
xlabel('Frame')
ylabel('Cell Number')

figure()
imagesc(RatioOxoverRed)
title('Normalized Ratio (Ox/Red)')
xlabel('Frame')
ylabel('Cell Number')

save(FileName)                                          %Filename specified
at the top, saves the entire workspace for future needs

Avg = mean(NBackSubMeanIntensityCorr_ox);

figure()
plot(NBackSubMeanIntensityCorr_ox(:,1:100)')
hold on
plot(Avg(1:100),'LineWidth',2,'Color','k');
title('Normalized Oxidized')
xlabel('Frame')
ylabel('Cell Number')
```

REFERENCES

1. Conley, J.M., M.P. Gallagher, and L.J. Berg, *T cells and gene regulation: the switching on and turning up of genes after T cell receptor stimulation in CD8 T cells.* Frontiers in Immunology, 2016. **7**.
2. Nohara, L.L., et al., *Tweeters, Woofers and Horns: The Complex Orchestration of Calcium Currents in T Lymphocytes.* Front Immunol, 2015. **6**: p. 234.
3. Grupe, M., et al., *Activation of store-operated I(CRAC) by hydrogen peroxide.* Cell Calcium, 2010. **48**(1): p. 1-9.
4. Ray, P.D., B.W. Huang, and Y. Tsuji, *Reactive oxygen species (ROS) homeostasis and redox regulation in cellular signaling.* Cell Signal, 2012. **24**(5): p. 981-90.
5. Kaminski, M.M., et al., *Mitochondria as oxidative signaling organelles in T-cell activation: physiological role and pathological implications.* Arch Immunol Ther Exp (Warsz), 2013. **61**(5): p. 367-84.
6. Trachootham, D., J. Alexandre, and P. Huang, *Targeting cancer cells by ROS-mediated mechanisms: a radical therapeutic approach?* Nature Reviews Drug Discovery, 2009. **8**(7): p. 579-591.
7. Hoogeboom, D. and B.M. Burgering, *Should I stay or should I go: beta-catenin decides under stress.* Biochim Biophys Acta, 2009. **1796**(2): p. 63-74.
8. Haigis, M.C. and B.A. Yankner, *The aging stress response.* Mol Cell, 2010. **40**(2): p. 333-44.
9. Smith, M.A., et al., *Oxidative stress in Alzheimer's disease.* Biochim Biophys Acta, 2000. **1502**(1): p. 139-44.
10. Du, H., et al., *Early deficits in synaptic mitochondria in an Alzheimer's disease mouse model.* Proc Natl Acad Sci U S A, 2010. **107**(43): p. 18670-5.
11. McLellan, M.E., et al., *In vivo imaging of reactive oxygen species specifically associated with thioflavine S-positive amyloid plaques by multiphoton microscopy.* J Neurosci, 2003. **23**(6): p. 2212-7.
12. Chacko, B.K., et al., *Methods for defining distinct bioenergetic profiles in platelets, lymphocytes, monocytes, and neutrophils, and the oxidative burst from human blood.* Lab Invest, 2013. **93**(6): p. 690-700.
13. D'Autreaux, B. and M.B. Toledano, *ROS as signalling molecules: mechanisms that generate specificity in ROS homeostasis.* Nat Rev Mol Cell Biol, 2007. **8**(10): p. 813-824.
14. Bogeski, I., et al., *Differential redox regulation of ORAI ion channels: a mechanism to tune cellular calcium signaling.* Sci Signal, 2010. **3**(115): p. ra24.
15. Finotto, S., et al., *Development of spontaneous airway changes consistent with human asthma in mice lacking T-bet.* Science, 2002. **295**(5553): p. 336-8.
16. Zhu, J. and W.E. Paul, *CD4 T cells: fates, functions, and faults.* Blood, 2008. **112**(5): p. 1557-69.
17. DiPaolo, R.J., et al., *Autoantigen-specific TGF beta-Induced Foxp3(+) regulatory T cells prevent Autoimmunity by inhibiting dendritic cells from activating autoreactive T cells.* Journal of Immunology, 2007. **179**(7): p. 4685-4693.
18. Perl, A., R. Hanczko, and E. Doherty, *Assessment of mitochondrial dysfunction in lymphocytes of patients with systemic lupus erythematosus.* Methods Mol Biol, 2012. **900**: p. 61-89.

19. Zhu, J., H. Yamane, and W.E. Paul, *Differentiation of effector CD4 T cell populations (*).* Annu Rev Immunol, 2010. **28**: p. 445-89.
20. Sena, L.A., et al., *Mitochondria Are Required for Antigen-Specific T Cell Activation through Reactive Oxygen Species Signaling.* Immunity, 2013. **38**(2): p. 225-236.
21. Berridge, M.J., P. Lipp, and M.D. Bootman, *The versatility and universality of calcium signalling.* Nat Rev Mol Cell Biol, 2000. **1**(1): p. 11-21.
22. Dolmetsch, R.E., K. Xu, and R.S. Lewis, *Calcium oscillations increase the efficiency and specificity of gene expression.* Nature, 1998. **392**(6679): p. 933-6.
23. Smith-Garvin, J.E., G.A. Koretzky, and M.S. Jordan, *T cell activation.* Annu Rev Immunol, 2009. **27**: p. 591-619.
24. Vyas, J.M., A.G. Van der Veen, and H.L. Ploegh, *The known unknowns of antigen processing and presentation.* Nat Rev Immunol, 2008. **8**(8): p. 607-18.
25. Woodland, D.L. and R.W. Dutton, *Heterogeneity of CD4+ and CD8+ T cells.* Current Opinion in Immunology, 2003. **15**(3): p. 336-342.
26. Caccamo, N., et al., *Mechanisms underlying lineage commitment and plasticity of human gammadelta T cells.* Cell Mol Immunol, 2013. **10**(1): p. 30-4.
27. Wing, K. and S. Sakaguchi, *Regulatory T cells exert checks and balances on self tolerance and autoimmunity.* Nat Immunol, 2010. **11**(1): p. 7-13.
28. Cools, N., et al., *Regulatory T cells and human disease.* Clin Dev Immunol, 2007. **2007**: p. 89195.
29. Jonuleit, H. and E. Schmitt, *The Regulatory T Cell Family: Distinct Subsets and their Interrelations.* The Journal of Immunology, 2003. **171**(12): p. 6323-6327.
30. Phan, G.Q., et al., *Cancer regression and autoimmunity induced by cytotoxic T lymphocyte-associated antigen 4 blockade in patients with metastatic melanoma.* Proc Natl Acad Sci U S A, 2003. **100**(14): p. 8372-7.
31. Feske, S., E.Y. Skolnik, and M. Prakriya, *Ion channels and transporters in lymphocyte function and immunity.* Nature Reviews Immunology, 2012. **12**(7): p. 532-547.
32. Lewis, R.S., *Calcium oscillations in T-cells: mechanisms and consequences for gene expression.* Biochemical Society Transactions, 2003. **31**: p. 925-929.
33. Finkel, T. and N.J. Holbrook, *Oxidants, oxidative stress and the biology of ageing.* Nature, 2000. **408**(6809): p. 239-247.
34. Jones, D.P., *Radical-free biology of oxidative stress.* American Journal of Physiology - Cell Physiology, 2008. **295**(4): p. C849-C868.
35. Fisher, A.B., *Redox signaling across cell membranes.* Antioxid Redox Signal, 2009. **11**(6): p. 1349-56.
36. Cadenas, E., *Mitochondrial free radical production and cell signaling.* Mol Aspects Med, 2004. **25**(1-2): p. 17-26.
37. Kwon, J., et al., *The nonphagocytic NADPH oxidase Duox1 mediates a positive feedback loop during T cell receptor signaling.* Sci Signal, 2010. **3**(133): p. ra59.
38. Gill, T. and A.D. Levine, *Mitochondria-derived hydrogen peroxide selectively enhances T cell receptor-initiated signal transduction.* J Biol Chem, 2013. **288**(36): p. 26246-55.

39. Kwon, J., S. Devadas, and M.S. Williams, *T cell receptor-stimulated generation of hydrogen peroxide inhibits MEK-ERK activation and lck serine phosphorylation.* Free Radic Biol Med, 2003. **35**(4): p. 406-17.
40. Lee, K. and W.J. Esselman, *Inhibition of PTPs by H(2)O(2) regulates the activation of distinct MAPK pathways.* Free Radic Biol Med, 2002. **33**(8): p. 1121-32.
41. Schieven, G.L., et al., *ZAP-70 tyrosine kinase, CD45, and T cell receptor involvement in UV- and H2O2-induced T cell signal transduction.* J Biol Chem, 1994. **269**(32): p. 20718-26.
42. Griffith, C.E., W. Zhang, and R.L. Wange, *ZAP-70-dependent and -independent activation of Erk in Jurkat T cells. Differences in signaling induced by H2o2 and Cd3 cross-linking.* J Biol Chem, 1998. **273**(17): p. 10771-6.
43. Finkel, T., *Oxygen radicals and signaling.* Curr Opin Cell Biol, 1998. **10**(2): p. 248-53.
44. Simeoni, L. and I. Bogeski, *Redox regulation of T-cell receptor signaling.* Biol Chem, 2015. **396**(5): p. 555-68.
45. Reth, M., *Hydrogen peroxide as second messenger in lymphocyte activation.* Nat Immunol, 2002. **3**(12): p. 1129-34.
46. Lee, M., W.C. Choy, and M.R. Abid, *Direct sensing of endothelial oxidants by vascular endothelial growth factor receptor-2 and c-Src.* PLoS One, 2011. **6**(12): p. e28454.
47. Paulsen, C.E., et al., *Peroxide-dependent sulfenylation of the EGFR catalytic site enhances kinase activity.* Nat Chem Biol, 2012. **8**(1): p. 57-64.
48. Yoo, S.K., et al., *Lyn is a redox sensor that mediates leukocyte wound attraction in vivo.* Nature, 2011. **480**(7375): p. 109-12.
49. Belikov, A.V., B. Schraven, and L. Simeoni, *TCR-triggered extracellular superoxide production is not required for T-cell activation.* Cell Commun Signal, 2014. **12**: p. 50.
50. Williams, M.S. and J. Kwon, *T cell receptor stimulation, reactive oxygen species, and cell signaling.* Free Radic Biol Med, 2004. **37**(8): p. 1144-51.
51. Marnett, L.J., *Oxyradicals and DNA damage.* Carcinogenesis, 2000. **21**(3): p. 361-70.
52. Bedard, K. and K.H. Krause, *The NOX family of ROS-generating NADPH oxidases: physiology and pathophysiology.* Physiol Rev, 2007. **87**(1): p. 245-313.
53. Nordberg, J. and E.S. Arner, *Reactive oxygen species, antioxidants, and the mammalian thioredoxin system.* Free Radic Biol Med, 2001. **31**(11): p. 1287-312.
54. Prakriya, M. and R.S. Lewis, *Store-Operated Calcium Channels.* Physiol Rev, 2015. **95**(4): p. 1383-436.
55. Clapham, D.E., *Calcium signaling.* Cell, 2007. **131**(6): p. 1047-58.
56. Brini, M. and E. Carafoli, *Calcium signalling: a historical account, recent developments and future perspectives.* Cell Mol Life Sci, 2000. **57**(3): p. 354-70.
57. Sarwat, M., et al., *Ca(2+) signals: the versatile decoders of environmental cues.* Crit Rev Biotechnol, 2013. **33**(1): p. 97-109.
58. Gehlert, S., W. Bloch, and F. Suhr, *Ca2+-dependent regulations and signaling in skeletal muscle: from electro-mechanical coupling to adaptation.* Int J Mol Sci, 2015. **16**(1): p. 1066-95.

59. Edwards, J.N. and L.A. Blatter, *Cardiac alternans and intracellular calcium cycling.* Clin Exp Pharmacol Physiol, 2014. **41**(7): p. 524-32.
60. Mishra, P.K., et al., *Cardiac matrix: a clue for future therapy.* Biochim Biophys Acta, 2013. **1832**(12): p. 2271-6.
61. Furukawa, T., *Types of voltage-gated calcium channels: molecular and electrophysiological views.* Curr Hypertens Rev, 2013. **9**(3): p. 170-81.
62. Pinto, M.C., et al., *Studying complex system: calcium oscillations as attractor of cell differentiation.* Integr Biol (Camb), 2016. **8**(2): p. 130-48.
63. Carafoli, E., *Calcium signaling: a tale for all seasons.* Proc Natl Acad Sci U S A, 2002. **99**(3): p. 1115-22.
64. Omilusik, K.D., et al., *Weft, warp, and weave: the intricate tapestry of calcium channels regulating T lymphocyte function.* Front Immunol, 2013. **4**: p. 164.
65. Lewis, R.S., *Calcium signaling mechanisms in T lymphocytes.* Annual Review of Immunology, 2001. **19**: p. 497-521.
66. Brandman, O. and T. Meyer, *Feedback loops shape cellular signals in space and time.* Science, 2008. **322**(5900): p. 390-5.
67. Feske, S., et al., *A mutation in Orai1 causes immune deficiency by abrogating CRAC channel function.* Nature, 2006. **441**(7090): p. 179-85.
68. Prakriya, M., et al., *Orai1 is an essential pore subunit of the CRAC channel.* Nature, 2006. **443**(7108): p. 230-3.
69. Hogan, P.G., R.S. Lewis, and A. Rao, *Molecular basis of calcium signaling in lymphocytes: STIM and ORAI.* Annu Rev Immunol, 2010. **28**: p. 491-533.
70. Smedler, E. and P. Uhlen, *Frequency decoding of calcium oscillations.* Biochim Biophys Acta, 2014. **1840**(3): p. 964-9.
71. Parekh, A.B., *Decoding cytosolic Ca2+ oscillations.* Trends Biochem Sci, 2011. **36**(2): p. 78-87.
72. Skupin, A., H. Kettenmann, and M. Falcke, *Calcium Signals Driven by Single Channel Noise.* Plos Computational Biology, 2010. **6**(8).
73. Skupin, A., et al., *How does intracellular Ca2+ oscillate: By chance or by the clock?* Biophysical Journal, 2008. **94**(6): p. 2404-2411.
74. Dolmetsch, R.E. and R.S. Lewis, *Signaling between intracellular Ca2+ stores and depletion-activated Ca2+ channels generates [Ca2+]i oscillations in T lymphocytes.* J Gen Physiol, 1994. **103**(3): p. 365-88.
75. Cifuentes, M.E., L. Honkanen, and M.J. Rebecchi, *Proteolytic fragments of phosphoinositide-specific phospholipase C-delta 1. Catalytic and membrane binding properties.* J Biol Chem, 1993. **268**(16): p. 11586-93.
76. Rebecchi, M.J., et al., *Hydrolysis of short acyl chain inositol lipids by phospholipase C-delta 1.* J Biol Chem, 1993. **268**(3): p. 1735-41.
77. Kohout, S.C., et al., *C2 domains of protein kinase C isoforms alpha, beta, and gamma: activation parameters and calcium stoichiometries of the membrane-bound state.* Biochemistry, 2002. **41**(38): p. 11411-24.
78. Vinogradov, A. and A. Scarpa, *The initial velocities of calcium uptake by rat liver mitochondria.* J Biol Chem, 1973. **248**(15): p. 5527-31.
79. Dorn, G.W. and C. Maack, *SR and mitochondria: Calcium cross-talk between kissing cousins.* Journal of Molecular and Cellular Cardiology, 2013. **55**: p. 42-49.

80. Csordas, G. and G. Hajnoczky, *SR/ER-mitochondrial local communication: Calcium and ROS.* Biochimica Et Biophysica Acta-Bioenergetics, 2009. **1787**(11): p. 1352-1362.
81. Trebak, M., et al., *Interplay Between Calcium and Reactive Oxygen/Nitrogen Species: An Essential Paradigm for Vascular Smooth Muscle Signaling.* Antioxidants & Redox Signaling, 2010. **12**(5): p. 657-674.
82. Galan, C., et al., *Role of oxidant scavengers in the prevention of Ca(2)+ homeostasis disorders.* Molecules, 2010. **15**(10): p. 7167-87.
83. Hidalgo, C. and P. Donoso, *Crosstalk between calcium and redox signaling: from molecular mechanisms to health implications.* Antioxid Redox Signal, 2008. **10**(7): p. 1275-312.
84. Gerich, F.J., et al., *H(2)O(2)-mediated modulation of cytosolic signaling and organelle function in rat hippocampus.* Pflugers Arch, 2009. **458**(5): p. 937-52.
85. Bootman, M.D., C.W. Taylor, and M.J. Berridge, *The Thiol Reagent, Thimerosal, Evokes Ca2+ Spikes in Hela-Cells by Sensitizing the Inositol 1,4,5-Trisphosphate Receptor.* Journal of Biological Chemistry, 1992. **267**(35): p. 25113-25119.
86. Guo, F., et al., *Probing cell-cell communication with microfluidic devices.* Lab Chip, 2013. **13**(16): p. 3152-62.
87. Abramson, J.J., et al., *Thimerosal Interacts with the Ca2+ Release Channel Ryanodine Receptor from Skeletal-Muscle Sarcoplasmic-Reticulum.* Journal of Biological Chemistry, 1995. **270**(50): p. 29644-29647.
88. Quintana, A., et al., *T cell activation requires mitochondrial translocation to the immunological synapse.* Proc Natl Acad Sci U S A, 2007. **104**(36): p. 14418-23.
89. Gincel, D., H. Zaid, and V. Shoshan-Barmatz, *Calcium binding and translocation by the voltage-dependent anion channel: a possible regulatory mechanism in mitochondrial function.* Biochem J, 2001. **358**(Pt 1): p. 147-55.
90. Brookes, P.S., et al., *Calcium, ATP, and ROS: a mitochondrial love-hate triangle.* Am J Physiol Cell Physiol, 2004. **287**(4): p. C817-33.
91. Dorn, G.W., 2nd and C. Maack, *SR and mitochondria: calcium cross-talk between kissing cousins.* J Mol Cell Cardiol, 2013. **55**: p. 42-9.
92. Grover, A.K. and S.E. Samson, *Peroxide resistance of ER Ca2+ pump in endothelium: implications to coronary artery function.* Am J Physiol, 1997. **273**(4 Pt 1): p. C1250-8.
93. Tong, X., A. Evangelista, and R.A. Cohen, *Targeting the redox regulation of SERCA in vascular physiology and disease.* Curr Opin Pharmacol, 2010. **10**(2): p. 133-8.
94. Cartwright, E.J., D. Oceandy, and L. Neyses, *Plasma membrane calcium ATPase and its relationship to nitric oxide signaling in the heart.* Ann N Y Acad Sci, 2007. **1099**: p. 247-53.
95. Waring, P., *Redox active calcium ion channels and cell death.* Arch Biochem Biophys, 2005. **434**(1): p. 33-42.
96. Lancel, S., et al., *Oxidative posttranslational modifications mediate decreased SERCA activity and myocyte dysfunction in Galphaq-overexpressing mice.* Circ Res, 2010. **107**(2): p. 228-32.
97. Hawkins, B.J., et al., *S-glutathionylation activates STIM1 and alters mitochondrial homeostasis.* J Cell Biol, 2010. **190**(3): p. 391-405.

98. Prins, D., et al., *Modulation of STIM1 and capacitative Ca2+ entry by the endoplasmic reticulum luminal oxidoreductase ERp57.* EMBO Rep, 2011. **12**(11): p. 1182-8.
99. Elowitz, M.B., et al., *Stochastic gene expression in a single cell.* Science, 2002. **297**(5584): p. 1183-6.
100. Altschuler, S.J. and L.F. Wu, *Cellular heterogeneity: do differences make a difference?* Cell, 2010. **141**(4): p. 559-63.
101. Losick, R. and C. Desplan, *Stochasticity and cell fate.* Science, 2008. **320**(5872): p. 65-8.
102. Chung, K.H., et al., *Imaging Single-Cell Signaling Dynamics with a Deterministic High-Density Single-Cell Trap Array.* Analytical Chemistry, 2011. **83**(18): p. 7044-7052.
103. Lubeck, E. and L. Cai, *Single-cell systems biology by super-resolution imaging and combinatorial labeling.* Nat Methods, 2012. **9**(7): p. 743-8.
104. Whitesides, G.M., *The origins and the future of microfluidics.* Nature, 2006. **442**(7101): p. 368-73.
105. Hatakeyama, T., D.L. Chen, and R.F. Ismagilov, *Microgram-scale testing of reaction conditions in solution using nanoliter plugs in microfluidics with detection by MALDI-MS.* J Am Chem Soc, 2006. **128**(8): p. 2518-9.
106. Jovic, A., et al., *Microfluidic interrogation and mathematical modeling of multi-regime calcium signaling dynamics.* Integr Biol (Camb), 2013. **5**(7): p. 932-9.
107. Faley, S., et al., *Microfluidic platform for real-time signaling analysis of multiple single T cells in parallel.* Lab Chip, 2008. **8**(10): p. 1700-12.
108. Taylor, R.J., et al., *Dynamic analysis of MAPK signaling using a high-throughput microfluidic single-cell imaging platform.* Proc Natl Acad Sci U S A, 2009. **106**(10): p. 3758-63.
109. Yang, K., et al., *A microfluidic array for quantitative analysis of human neural stem cell self-renewal and differentiation in three-dimensional hypoxic microenvironment.* Biomaterials, 2013. **34**(28): p. 6607-14.
110. Brewer, L.R. and P.R. Bianco, *Laminar flow cells for single-molecule studies of DNA-protein interactions.* Nat Methods, 2008. **5**(6): p. 517-25.
111. Metto, E.C., et al., *An integrated microfluidic device for monitoring changes in nitric oxide production in single T-lymphocyte (Jurkat) cells.* Anal Chem, 2013. **85**(21): p. 10188-95.
112. Kniss, A., et al., *A microfluidic systems biology approach for live single-cell mitochondrial ROS imaging.* Methods Enzymol, 2013. **526**: p. 219-30.
113. Jeon, N.L., et al., *Generation of Solution and Surface Gradients Using Microfluidic Systems.* Langmuir, 2000. **16**(22): p. 8311-8316.
114. Kuczenski, B., et al., *Probing cellular dynamics with a chemical signal generator.* PLoS One, 2009. **4**(3): p. e4847.
115. Hersen, P., et al., *Signal processing by the HOG MAP kinase pathway.* Proc Natl Acad Sci U S A, 2008. **105**(20): p. 7165-70.
116. LeDuc, P.R., W.C. Messner, and J.P. Wikswo, *How do control-based approaches enter into biology?* Annu Rev Biomed Eng, 2011. **13**: p. 369-96.
117. Mettetal, J.T., et al., *The frequency dependence of osmo-adaptation in Saccharomyces cerevisiae.* Science, 2008. **319**(5862): p. 482-4.

118. Slepchenko, B.M., et al., *Quantitative cell biology with the Virtual Cell.* Trends Cell Biol, 2003. **13**(11): p. 570-6.
119. Tyson, J.J., K. Chen, and B. Novak, *Network dynamics and cell physiology.* Nat Rev Mol Cell Biol, 2001. **2**(12): p. 908-16.
120. Bennett, M.R., et al., *Metabolic gene regulation in a dynamically changing environment.* Nature, 2008. **454**(7208): p. 1119-22.
121. Shimizu, T.S., Y. Tu, and H.C. Berg, *A modular gradient-sensing network for chemotaxis in Escherichia coli revealed by responses to time-varying stimuli.* Mol Syst Biol, 2010. **6**: p. 382.
122. Bielski, B.H.J. and A.O. Allen, *Mechanism of the disproportionation of superoxide radicals.* The Journal of Physical Chemistry, 1977. **81**(11): p. 1048-1050.
123. Ansenberger-Fricano, K., et al., *The peroxidase activity of mitochondrial superoxide dismutase.* Free Radic Biol Med, 2013. **54**: p. 116-24.
124. Sies, H., *Role of Metabolic H2O2 Generation: REDOX SIGNALING AND OXIDATIVE STRESS.* Journal of Biological Chemistry, 2014. **289**(13): p. 8735-8741.
125. Bienert, G.P. and F. Chaumont, *Aquaporin-facilitated transmembrane diffusion of hydrogen peroxide.* Biochimica et Biophysica Acta (BBA) - General Subjects, 2014. **1840**(5): p. 1596-1604.
126. Chauvigne, F., et al., *Mitochondrial aquaporin-8-mediated hydrogen peroxide transport is essential for teleost spermatozoon motility.* Sci Rep, 2015. **5**: p. 7789.
127. Mezencev, R., et al., *Camalexin induces apoptosis in T-leukemia Jurkat cells by increased concentration of reactive oxygen species and activation of caspase-8 and caspase-9.* J Nat Med, 2011. **65**(3-4): p. 488-99.
128. Robinson, K.M., et al., *Selective fluorescent imaging of superoxide in vivo using ethidium-based probes.* Proc Natl Acad Sci U S A, 2006. **103**(41): p. 15038-43.
129. Kalyanaraman, B., et al., *Measuring reactive oxygen and nitrogen species with fluorescent probes: challenges and limitations.* Free Radic Biol Med, 2012. **52**(1): p. 1-6.
130. Belousov, V.V., et al., *Genetically encoded fluorescent indicator for intracellular hydrogen peroxide.* Nat Methods, 2006. **3**(4): p. 281-6.
131. Lukyanov, K.A. and V.V. Belousov, *Genetically encoded fluorescent redox sensors.* Biochim Biophys Acta, 2014. **1840**(2): p. 745-56.
132. Malinouski, M., et al., *Hydrogen Peroxide Probes Directed to Different Cellular Compartments.* Plos One, 2011. **6**(1).
133. Janes, K.A., *Cell-to-Cell Transcript Variability: Seeing Signal in the Noise.* Cell, 2015. **163**(7): p. 1566-8.
134. Raj, A. and A. van Oudenaarden, *Nature, nurture, or chance: stochastic gene expression and its consequences.* Cell, 2008. **135**(2): p. 216-26.
135. Tak, P.P., et al., *Rheumatoid arthritis and p53: how oxidative stress might alter the course of inflammatory diseases.* Immunol Today, 2000. **21**(2): p. 78-82.
136. Simon, A.K., G.A. Hollander, and A. McMichael, *Evolution of the immune system in humans from infancy to old age.* Proc Biol Sci, 2015. **282**(1821).

137. Abbas, A.R., et al., *Immune response in silico (IRIS): immune-specific genes identified from a compendium of microarray expression data.* Genes Immun, 2005. **6**(4): p. 319-31.
138. Janeway, C.A., Jr. and R. Medzhitov, *Innate immune recognition.* Annu Rev Immunol, 2002. **20**: p. 197-216.
139. Riera Romo, M., D. Perez-Martinez, and C. Castillo Ferrer, *Innate immunity in vertebrates: an overview.* Immunology, 2016.
140. Fearon, D.T. and R.M. Locksley, *The instructive role of innate immunity in the acquired immune response.* Science, 1996. **272**(5258): p. 50-3.
141. Louis-Dit-Sully, C., et al., *Activation of the TCR complex by peptide-MHC and superantigens.* Exs, 2014. **104**: p. 9-23.
142. Perez-Villar, J.J. and S.B. Kanner, *Regulated association between the tyrosine kinase Emt/Itk/Tsk and phospholipase-C gamma 1 in human T lymphocytes.* J Immunol, 1999. **163**(12): p. 6435-41.
143. Qi, Q. and A. August, *Keeping the (kinase) party going: SLP-76 and ITK dance to the beat.* Sci STKE, 2007. **2007**(396): p. pe39.
144. Fahrner, M., et al., *The STIM1/Orai signaling machinery.* Channels (Austin), 2013. **7**(5): p. 330-43.
145. Weng, N.P., *Aging of the immune system: how much can the adaptive immune system adapt?* Immunity, 2006. **24**(5): p. 495-9.
146. Salam, N., et al., *T cell ageing: effects of age on development, survival & function.* Indian J Med Res, 2013. **138**(5): p. 595-608.
147. Linton, P.J. and K. Dorshkind, *Age-related changes in lymphocyte development and function.* Nat Immunol, 2004. **5**(2): p. 133-9.
148. Yu, H.T., et al., *T cell senescence and cardiovascular diseases.* Clin Exp Med, 2015.
149. Fulop, T., et al., *Cellular signaling in the aging immune system.* Curr Opin Immunol, 2014. **29**: p. 105-11.
150. Feske, S., *Calcium signalling in lymphocyte activation and disease.* Nat Rev Immunol, 2007. **7**(9): p. 690-702.
151. Larbi, A., J. Kempf, and G. Pawelec, *Oxidative stress modulation and T cell activation.* Exp Gerontol, 2007. **42**(9): p. 852-8.
152. Goronzy, J.J., et al., *Signaling pathways in aged T cells - a reflection of T cell differentiation, cell senescence and host environment.* Semin Immunol, 2012. **24**(5): p. 365-72.
153. Griffiths, H.R., et al., *Thioredoxin as a putative biomarker and candidate target in age-related immune decline.* Biochem Soc Trans, 2014. **42**(4): p. 922-7.
154. Larbi, A., et al., *Impact of age on T cell signaling: a general defect or specific alterations?* Ageing Res Rev, 2011. **10**(3): p. 370-8.
155. Moro-Garcia, M.A., R. Alonso-Arias, and C. Lopez-Larrea, *Molecular mechanisms involved in the aging of the T-cell immune response.* Curr Genomics, 2012. **13**(8): p. 589-602.
156. Henson, S.M., N.E. Riddell, and A.N. Akbar, *Properties of end-stage human T cells defined by CD45RA re-expression.* Curr Opin Immunol, 2012. **24**(4): p. 476-81.

157. Libri, V., et al., *Cytomegalovirus infection induces the accumulation of short-lived, multifunctional CD4+CD45RA+CD27+ T cells: the potential involvement of interleukin-7 in this process.* Immunology, 2011. **132**(3): p. 326-39.
158. Griffiths, H.R., et al., *Free radicals and redox signalling in T-cells during chronic inflammation and ageing.* Biochem Soc Trans, 2011. **39**(5): p. 1273-8.
159. Larbi, A., et al., *Differential role of lipid rafts in the functions of CD4+ and CD8+ human T lymphocytes with aging.* Cell Signal, 2006. **18**(7): p. 1017-30.
160. Rivet, C.A., et al., *Predicting cytotoxic T-cell age from multivariate analysis of static and dynamic biomarkers.* Mol Cell Proteomics, 2011. **10**(3): p. M110.003921.
161. Fulop, T., Jr., et al., *Ageing, autoimmunity and arthritis: Perturbations of TCR signal transduction pathways with ageing - a biochemical paradigm for the ageing immune system.* Arthritis Res Ther, 2003. **5**(6): p. 290-302.
162. Grossmann, A., et al., *Influence of aging on intracellular free calcium and proliferation of mouse T-cell subsets from various lymphoid organs.* Cell Immunol, 1991. **135**(1): p. 118-31.
163. Miller, R.A., *Calcium signals in T lymphocytes from old mice.* Life Sci, 1996. **59**(5-6): p. 469-75.
164. Gupta, S., *Membrane signal transduction in T cells in aging humans.* Ann N Y Acad Sci, 1989. **568**: p. 277-82.
165. Sulger, J., et al., *The calcium response of human T lymphocytes is decreased in aging but increased in Alzheimer's dementia.* Biol Psychiatry, 1999. **45**(6): p. 737-42.
166. Grossmann, A., J.A. Ledbetter, and P.S. Rabinovitch, *Reduced proliferation in T lymphocytes in aged humans is predominantly in the CD8+ subset, and is unrelated to defects in transmembrane signaling which are predominantly in the CD4+ subset.* Exp Cell Res, 1989. **180**(2): p. 367-82.
167. Kim, M., et al., *Colocalization of protein kinase A with adenylyl cyclase enhances protein kinase A activity during induction of long-lasting long-term-potentiation.* PLoS Comput Biol, 2011. **7**(6): p. e1002084.
168. Chay, A., et al., *Control of betaAR- and N-methyl-D-aspartate (NMDA) Receptor-Dependent cAMP Dynamics in Hippocampal Neurons.* PLoS Comput Biol, 2016. **12**(2): p. e1004735.
169. Chay, T.R., *Modeling slowly bursting neurons via calcium store and voltage-independent calcium current.* Neural Comput, 1996. **8**(5): p. 951-78.
170. Holcman, D. and Z. Schuss, *Modeling Calcium Dynamics in Dendritic Spines.* SIAM Journal on Applied Mathematics, 2005. **65**(3): p. 1006-1026.
171. Roussel, C., et al., *Modulation of neuronal excitability by intracellular calcium buffering: from spiking to bursting.* Cell Calcium, 2006. **39**(5): p. 455-66.
172. Rice, J.J. and M.S. Jafri, *Modelling calcium handling in cardiac cells.* Philosophical Transactions of the Royal Society of London A: Mathematical, Physical and Engineering Sciences, 2001. **359**(1783): p. 1143-1157.
173. Hake, J., et al., *Modelling cardiac calcium sparks in a three-dimensional reconstruction of a calcium release unit.* J Physiol, 2012. **590**(18): p. 4403-22.
174. Jafri, M.S., *Models of excitation-contraction coupling in cardiac ventricular myocytes.* Methods Mol Biol, 2012. **910**: p. 309-35.

175. Limbu, S., et al., *Modeling Local X-ROS and Calcium Signaling in the Heart.* Biophys J, 2015. **109**(10): p. 2037-50.
176. Wagner, E., et al., *Stimulated emission depletion live-cell super-resolution imaging shows proliferative remodeling of T-tubule membrane structures after myocardial infarction.* Circ Res, 2012. **111**(4): p. 402-14.
177. Williams, G.S., et al., *Moment closure for local control models of calcium-induced calcium release in cardiac myocytes.* Biophys J, 2008. **95**(4): p. 1689-703.
178. Williams, G.S., et al., *A probability density approach to modeling local control of calcium-induced calcium release in cardiac myocytes.* Biophys J, 2007. **92**(7): p. 2311-28.
179. Williams, G.S., et al., *Models of cardiac excitation-contraction coupling in ventricular myocytes.* Math Biosci, 2010. **226**(1): p. 1-15.
180. Winslow, R.L., et al., *Electrophysiological modeling of cardiac ventricular function: from cell to organ.* Annu Rev Biomed Eng, 2000. **2**: p. 119-55.
181. Cui, J., et al., *Calcium homeostasis and signaling in yeast cells and cardiac myocytes.* FEMS Yeast Res, 2009. **9**(8): p. 1137-47.
182. Groenendaal, W., et al., *Computational modelling identifies the impact of subtle anatomical variations between amphibian and mammalian skeletal muscle on spatiotemporal calcium dynamics.* IET Syst Biol, 2008. **2**(6): p. 411-22.
183. Kuijpers, N.H., et al., *Mechanoelectric feedback as a trigger mechanism for cardiac electrical remodeling: a model study.* Ann Biomed Eng, 2008. **36**(11): p. 1816-35.
184. Schmitz, J.P., et al., *Combined in vivo and in silico investigations of activation of glycolysis in contracting skeletal muscle.* Am J Physiol Cell Physiol, 2013. **304**(2): p. C180-93.
185. van Stiphout, R.G., et al., *Computational model of excitable cell indicates ATP free energy dynamics in response to calcium oscillations are undampened by cytosolic ATP buffers.* Syst Biol (Stevenage), 2006. **153**(5): p. 405-8.
186. Ahnadi, C.E., M.D. Payet, and G. Dupuis, *Effects of staurosporine on the capacitative regulation of the state of the Ca2+ reserves in activated Jurkat T lymphocytes.* Cell Calcium, 1996. **19**(6): p. 509-20.
187. Kim, S., et al., *Modeling of early events in T cell signal transduction after controlled T cell activation by peptide major histocompatibility complex.* Ann Biomed Eng, 2001. **29**(5): p. 373-83.
188. Maurya, M.R. and S. Subramaniam, *A kinetic model for calcium dynamics in RAW 264.7 cells: 1. Mechanisms, parameters, and subpopulational variability.* Biophys J, 2007. **93**(3): p. 709-28.
189. Maurya, M.R. and S. Subramaniam, *A kinetic model for calcium dynamics in RAW 264.7 cells: 2. Knockdown response and long-term response.* Biophys J, 2007. **93**(3): p. 729-40.
190. Pawelec, G., et al., *Cytomegalovirus and human immunosenescence.* Rev Med Virol, 2009. **19**(1): p. 47-56.
191. Pawelec, G., A. Larbi, and E. Derhovanessian, *Senescence of the human immune system.* J Comp Pathol, 2010. **142 Suppl 1**: p. S39-44.

192. Pawelec, G., et al., *T cell immunosenescence in vitro and in vivo.* Exp Gerontol, 1999. **34**(3): p. 419-29.
193. Derhovanessian, E., A. Larbi, and G. Pawelec, *Biomarkers of human immunosenescence: impact of Cytomegalovirus infection.* Curr Opin Immunol, 2009. **21**(4): p. 440-5.
194. Rivet, C.A., *Impaired signaling in senescing T cells: investigation of the role of reactive oxygen species using microfluidic platforms and computational modeling*, in *Bioengineering*. 2012, Georgia Institute of Technology: SMARTech.
195. Abell, E., et al., *Parallel adaptive feedback enhances reliability of the Ca2+ signaling system.* Proc Natl Acad Sci U S A, 2011. **108**(35): p. 14485-90.
196. Liu, W., F. Tang, and J. Chen, *Designing dynamical output feedback controllers for store-operated Ca(2)+ entry.* Math Biosci, 2010. **228**(1): p. 110-8.
197. Marhl, M., et al., *Complex calcium oscillations and the role of mitochondria and cytosolic proteins.* Biosystems, 2000. **57**(2): p. 75-86.
198. Zhang, S.L., et al., *STIM1 is a Ca2+ sensor that activates CRAC channels and migrates from the Ca2+ store to the plasma membrane.* Nature, 2005. **437**(7060): p. 902-5.
199. Quintana, A. and M. Hoth, *Mitochondrial dynamics and their impact on T cell function.* Cell Calcium, 2012. **52**(1): p. 57-63.
200. Quintana, A., et al., *Calcium microdomains at the immunological synapse: how ORAI channels, mitochondria and calcium pumps generate local calcium signals for efficient T-cell activation.* Embo j, 2011. **30**(19): p. 3895-912.
201. Bezprozvanny, I., J. Watras, and B.E. Ehrlich, *Bell-shaped calcium-response curves of Ins(1,4,5)P3- and calcium-gated channels from endoplasmic reticulum of cerebellum.* Nature, 1991. **351**(6329): p. 751-4.
202. De Young, G.W. and J. Keizer, *A single-pool inositol 1,4,5-trisphosphate-receptor-based model for agonist-stimulated oscillations in Ca2+ concentration.* Proc Natl Acad Sci U S A, 1992. **89**(20): p. 9895-9.
203. Atri, A., et al., *A single-pool model for intracellular calcium oscillations and waves in the Xenopus laevis oocyte.* Biophys J, 1993. **65**(4): p. 1727-39.
204. Li, Y.X. and J. Rinzel, *Equations for InsP3 receptor-mediated [Ca2+]i oscillations derived from a detailed kinetic model: a Hodgkin-Huxley like formalism.* J Theor Biol, 1994. **166**(4): p. 461-73.
205. Sneyd, J. and J.F. Dufour, *A dynamic model of the type-2 inositol trisphosphate receptor.* Proc Natl Acad Sci U S A, 2002. **99**(4): p. 2398-403.
206. Sulger, J., et al., *The calcium response of human T lymphocytes is decreased in aging but increased in Alzheimer's dementia.* Biological psychiatry, 1999. **45**(6): p. 737-742.
207. Abell, E., et al., *Parallel adaptive feedback enhances reliability of the Ca2+ signaling system.* Proceedings of the National Academy of Sciences, 2011. **108**(35): p. 14485-14490.
208. Maurya, M.R. and S. Subramaniam, *A kinetic model for calcium dynamics in RAW 264.7 cells: 1. Mechanisms, parameters, and subpopulational variability.* Biophysical Journal, 2007. **93**(3): p. 709-28.

209. Politi, A., et al., *Models of IP3 and Ca2+ Oscillations: Frequency Encoding and Identification of Underlying Feedbacks.* Biophysical Journal, 2006. **90**(9): p. 3120-3133.
210. Kowalewski, J.M., et al., *Modeling the impact of store-operated Ca2+ entry on intracellular Ca2+ oscillations.* Math Biosci, 2006. **204**(2): p. 232-249.
211. Chen, X.-f., et al., *Dynamic simulation of the effect of calcium-release activated calcium channel on cytoplasmic Ca2+ oscillation.* Biophysical Chemistry, 2008. **136**(2–3): p. 87-95.
212. Guse, A.H., E. Roth, and F. Emmrich, *Intracellular Ca2+ pools in Jurkat T-lymphocytes.* Biochem J, 1993. **291 (Pt 2)**: p. 447-51.
213. Petrzilka, G.E. and H.E. Schroeder, *Activation of human T-lymphocytes. A kinetic and stereological study.* Cell Tissue Res, 1979. **201**(1): p. 101-27.
214. Ritchie, M.F., E. Samakai, and J. Soboloff, *STIM1 is required for attenuation of PMCA-mediated Ca2+ clearance during T-cell activation.* EMBO J, 2012. **31**(5): p. 1123-33.
215. He, L.Y., et al., *An automated programmable platform enabling multiplex dynamic stimuli delivery and cellular response monitoring for high-throughput suspension single-cell signaling studies.* Lab on a Chip, 2015. **15**(6): p. 1497-1507.
216. Dolmetsch, R.E., et al., *Differential activation of transcription factors induced by Ca2+ response amplitude and duration.* Nature, 1997. **386**(6627): p. 855-8.
217. Villaverde, A.F. and J.R. Banga, *Reverse engineering and identification in systems biology: strategies, perspectives and challenges.* J R Soc Interface, 2014. **11**(91): p. 20130505.
218. Toettcher, J.E., O.D. Weiner, and W.A. Lim, *Using optogenetics to interrogate the dynamic control of signal transmission by the Ras/Erk module.* Cell, 2013. **155**(6): p. 1422-34.
219. Spiller, D.G., et al., *Measurement of single-cell dynamics.* Nature, 2010. **465**(7299): p. 736-45.
220. Chingozha, L., et al., *A generalizable, tunable microfluidic platform for delivering fast temporally varying chemical signals to probe single-cell response dynamics.* Anal Chem, 2014. **86**(20): p. 10138-47.
221. Bennett, M.R. and J. Hasty, *Microfluidic devices for measuring gene network dynamics in single cells.* Nat Rev Genet, 2009. **10**(9): p. 628-38.
222. Love, J.C., et al., *A microengraving method for rapid selection of single cells producing antigen-specific antibodies.* Nat Biotechnol, 2006. **24**(6): p. 703-7.
223. Di Carlo, D., N. Aghdam, and L.P. Lee, *Single-cell enzyme concentrations, kinetics, and inhibition analysis using high-density hydrodynamic cell isolation arrays.* Anal Chem, 2006. **78**(14): p. 4925-30.
224. Di Carlo, D. and L.P. Lee, *Dynamic single-cell analysis for quantitative biology.* Anal Chem, 2006. **78**(23): p. 7918-25.
225. Di Carlo, D., L.Y. Wu, and L.P. Lee, *Dynamic single cell culture array.* Lab Chip, 2006. **6**(11): p. 1445-9.
226. Wang, G., et al., *In Situ Functionalization of Stable 3D Nest-Like Networks in Confined Channels for Microfluidic Enrichment and Detection.* Advanced Functional Materials, 2014. **24**(7): p. 1017-1026.

227. Taff, B.M. and J. Voldman, *A scalable addressable positive-dielectrophoretic cell-sorting array.* Anal Chem, 2005. **77**(24): p. 7976-83.
228. Voldman, J., et al., *A microfabrication-based dynamic array cytometer.* Anal Chem, 2002. **74**(16): p. 3984-90.
229. Enger, J., et al., *Optical tweezers applied to a microfluidic system.* Lab Chip, 2004. **4**(3): p. 196-200.
230. Irimia, D., et al., *Microfluidic system for measuring neutrophil migratory responses to fast switches of chemical gradients.* Lab Chip, 2006. **6**(2): p. 191-8.
231. Irimia, D. and M. Toner, *Cell handling using microstructured membranes.* Lab Chip, 2006. **6**(3): p. 345-52.
232. Wheeler, A.R., et al., *Microfluidic device for single-cell analysis.* Anal Chem, 2003. **75**(14): p. 3581-6.
233. Rettig, J.R. and A. Folch, *Large-scale single-cell trapping and imaging using microwell arrays.* Anal Chem, 2005. **77**(17): p. 5628-34.
234. Varadarajan, N., et al., *A high-throughput single-cell analysis of human CD8(+) T cell functions reveals discordance for cytokine secretion and cytolysis.* J Clin Invest, 2011. **121**(11): p. 4322-31.
235. Tan, W.H. and S. Takeuchi, *A trap-and-release integrated microfluidic system for dynamic microarray applications.* Proc Natl Acad Sci U S A, 2007. **104**(4): p. 1146-51.
236. Wang, C.J., et al., *Diverse sensitivity thresholds in dynamic signaling responses by social amoebae.* Sci Signal, 2012. **5**(213): p. ra17.
237. Lipan, O. and W.H. Wong, *The use of oscillatory signals in the study of genetic networks.* Proc Natl Acad Sci U S A, 2005. **102**(20): p. 7063-8.
238. Tomida, T., et al., *The temporal pattern of stimulation determines the extent and duration of MAPK activation in a Caenorhabditis elegans sensory neuron.* Sci Signal, 2012. **5**(246): p. ra76.
239. Chung, K., et al., *Microfluidic chamber arrays for whole-organism behavior-based chemical screening.* Lab Chip, 2011. **11**(21): p. 3689-97.
240. Hulme, S.E., S.S. Shevkoplyas, and G.M. Whitesides, *Incorporation of prefabricated screw, pneumatic, and solenoid valves into microfluidic devices.* Lab Chip, 2009. **9**(1): p. 79-86.
241. Uhlén, P., *Spectral Analysis of Calcium Oscillations.* Science Signaling, 2004. **258**: p. pl15.
242. Suzen, M. *histwc, version 1.0*. 2013; Available from: http://www.mathworks.com/matlabcentral/fileexchange/42493-generate-weighted-histogram.
243. Thurley, K., et al., *Reliable encoding of stimulus intensities within random sequences of intracellular Ca2+ spikes.* Sci Signal, 2014. **7**(331): p. ra59.
244. Malek, A.M., S.L. Alper, and S. Izumo, *Hemodynamic shear stress and its role in atherosclerosis.* Jama, 1999. **282**(21): p. 2035-42.
245. Hirsch, A.M., et al., *Parallel multi-time point cell stimulation and lysis on-chip for studying early signaling events in T cell activation.* Lab Chip, 2009. **9**(4): p. 536-44.

246. Dolmetsch, R.E. and R.S. Lewis, *Signaling between Intracellular Ca2+ Stores and Depletion-Activated Ca2+ Channels Generates [Ca2+](I) Oscillations in T-Lymphocytes.* Journal of General Physiology, 1994. **103**(3): p. 365-388.
247. Dolmetsch, R.E., K.L. Xu, and R.S. Lewis, *Calcium oscillations increase the efficiency and specificity of gene expression.* Nature, 1998. **392**(6679): p. 933-936.
248. Kesarwani, P., et al., *Redox Regulation of T-Cell Function: From Molecular Mechanisms to Significance in Human Health and Disease.* Antioxidants & Redox Signaling, 2013. **18**(12): p. 1497-1534.
249. Bootman, M.D., M.J. Berridge, and C.W. Taylor, *All-or-nothing Ca2+ mobilization from the intracellular stores of single histamine-stimulated HeLa cells.* J Physiol, 1992. **450**: p. 163-78.
250. Kobel, S., et al., *Optimization of microfluidic single cell trapping for long-term on-chip culture.* Lab on a Chip, 2010. **10**(7): p. 857-863.
251. Ramji, R., et al., *A passive-flow microfluidic device for imaging latent HIV activation dynamics in single T cells.* Integr Biol, 2015. **7**(9): p. 998-1010.
252. Han, Q., et al., *Multidimensional analysis of the frequencies, dynamics, and rates of cytokine secretion from single cells by quantitative microengraving.* Abstracts of Papers of the American Chemical Society, 2010. **240**.
253. Skelley, A.M., et al., *Microfluidic control of cell pairing and fusion.* Nature Methods, 2009. **6**(2): p. 147-152.
254. Mandikova, J., et al., *Interactions with selected drug renal transporters and transporter-mediated cytotoxicity in antiviral agents from the group of acyclic nucleoside phosphonates.* Toxicology, 2013. **311**(3): p. 135-46.
255. Adimora, N.J., D.P. Jones, and M.L. Kemp, *A Model of Redox Kinetics Implicates the Thiol Proteome in Cellular Hydrogen Peroxide Responses.* Antioxidants & Redox Signaling, 2010. **13**(6): p. 731-743.
256. Jackson, S.H., et al., *T cells express a phagocyte-type NADPH oxidase that is activated after T cell receptor stimulation.* Nat Immunol, 2004. **5**(8): p. 818-27.
257. Raad, H., et al., *Regulation of the phagocyte NADPH oxidase activity: phosphorylation of gp91phox/NOX2 by protein kinase C enhances its diaphorase activity and binding to Rac2, p67phox, and p47phox.* Faseb j, 2009. **23**(4): p. 1011-22.
258. Yin, W., H. Jo, and E.O. Voit, *Systems analysis of the role of bone morphogenic protein 4 in endothelial inflammation.* Ann Biomed Eng, 2010. **38**(2): p. 291-307.
259. Fontayne, A., et al., *Phosphorylation of p47phox sites by PKC alpha, beta II, delta, and zeta: effect on binding to p22phox and on NADPH oxidase activation.* Biochemistry, 2002. **41**(24): p. 7743-50.
260. Roose, J.P., et al., *A diacylglycerol-protein kinase C-RasGRP1 pathway directs Ras activation upon antigen receptor stimulation of T cells.* Mol Cell Biol, 2005. **25**(11): p. 4426-41.
261. Rigutto, S., et al., *Activation of dual oxidases Duox1 and Duox2: differential regulation mediated by camp-dependent protein kinase and protein kinase C-dependent phosphorylation.* J Biol Chem, 2009. **284**(11): p. 6725-34.
262. Camello-Almaraz, C., et al., *Mitochondrial reactive oxygen species and Ca2+ signaling.* Am J Physiol Cell Physiol, 2006. **291**(5): p. C1082-8.

263. Enyedi, B., P. Varnai, and M. Geiszt, *Redox State of the Endoplasmic Reticulum Is Controlled by Ero1L-alpha and Intraluminal Calcium.* Antioxidants & Redox Signaling, 2010. **13**(6): p. 721-729.
264. Csala, M., E. Margittai, and G. Banhegyi, *Redox control of endoplasmic reticulum function.* Antioxid Redox Signal, 2010. **13**(1): p. 77-108.
265. Pollard, M.G., K.J. Travers, and J.S. Weissman, *Ero1p: a novel and ubiquitous protein with an essential role in oxidative protein folding in the endoplasmic reticulum.* Mol Cell, 1998. **1**(2): p. 171-82.
266. Frand, A.R. and C.A. Kaiser, *The ERO1 gene of yeast is required for oxidation of protein dithiols in the endoplasmic reticulum.* Mol Cell, 1998. **1**(2): p. 161-70.
267. Sevier, C.S., et al., *Modulation of cellular disulfide-bond formation and the ER redox environment by feedback regulation of Ero1.* Cell, 2007. **129**(2): p. 333-44.
268. Joseph, S.K., S.K. Nakao, and S. Sukumvanich, *Reactivity of free thiol groups in type-I inositol trisphosphate receptors.* Biochem J, 2006. **393**(Pt 2): p. 575-82.
269. Kaplin, A.I., et al., *Purified reconstituted inositol 1,4,5-trisphosphate receptors. Thiol reagents act directly on receptor protein.* J Biol Chem, 1994. **269**(46): p. 28972-8.
270. Renard-Rooney, D.C., et al., *Effect of oxidized glutathione and temperature on inositol 1,4,5-trisphosphate binding in permeabilized hepatocytes.* Biochem J, 1995. **310 (Pt 1)**: p. 185-92.
271. Barnes, K.A., S.E. Samson, and A.K. Grover, *Sarco/endoplasmic reticulum Ca2+-pump isoform SERCA3a is more resistant to superoxide damage than SERCA2b.* Mol Cell Biochem, 2000. **203**(1-2): p. 17-21.
272. Higo, T., et al., *Subtype-specific and ER lumenal environment-dependent regulation of inositol 1,4,5-trisphosphate receptor type 1 by ERp44.* Cell, 2005. **120**(1): p. 85-98.
273. Kang, S., et al., *Effects of redox potential and Ca2+ on the inositol 1,4,5-trisphosphate receptor L3-1 loop region: implications for receptor regulation.* J Biol Chem, 2008. **283**(37): p. 25567-75.
274. Li, G., et al., *Role of ERO1-alpha-mediated stimulation of inositol 1,4,5-triphosphate receptor activity in endoplasmic reticulum stress-induced apoptosis.* J Cell Biol, 2009. **186**(6): p. 783-92.
275. Xu, K.Y., J.L. Zweier, and L.C. Becker, *Hydroxyl radical inhibits sarcoplasmic reticulum Ca(2+)-ATPase function by direct attack on the ATP binding site.* Circ Res, 1997. **80**(1): p. 76-81.
276. Zaidi, A., et al., *Oxidative inactivation of purified plasma membrane Ca2+-ATPase by hydrogen peroxide and protection by calmodulin.* Biochemistry, 2003. **42**(41): p. 12001-10.
277. Zaidi, A. and M.L. Michaelis, *Effects of reactive oxygen species on brain synaptic plasma membrane Ca(2+)-ATPase.* Free Radic Biol Med, 1999. **27**(7-8): p. 810-21.
278. Adimora, N.J., D.P. Jones, and M.L. Kemp, *A model of redox kinetics implicates the thiol proteome in cellular hydrogen peroxide responses.* Antioxid Redox Signal, 2010. **13**(6): p. 731-43.

279. Blais, J.D., et al., *A small molecule inhibitor of endoplasmic reticulum oxidation 1 (ERO1) with selectively reversible thiol reactivity.* J Biol Chem, 2010. **285**(27): p. 20993-1003.
280. Bootman, M.D., C.W. Taylor, and M.J. Berridge, *The thiol reagent, thimerosal, evokes Ca2+ spikes in HeLa cells by sensitizing the inositol 1,4,5-trisphosphate receptor.* J Biol Chem, 1992. **267**(35): p. 25113-9.
281. Muller, J., C. Kuttler, and B.A. Hense, *Sensitivity of the quorum sensing system is achieved by low pass filtering.* Biosystems, 2008. **92**(1): p. 76-81.
282. Balazsi, G., A. van Oudenaarden, and J.J. Collins, *Cellular decision making and biological noise: from microbes to mammals.* Cell, 2011. **144**(6): p. 910-25.
283. Kang, H.W., L. Zheng, and H.G. Othmer, *The effect of the signalling scheme on the robustness of pattern formation in development.* Interface Focus, 2012. **2**(4): p. 465-86.
284. Zheng, L., M. Chen, and Q. Nie, *External noise control in inherently stochastic biological systems.* J Math Phys, 2012. **53**(11).
285. Selimkhanov, J., et al., *Systems biology. Accurate information transmission through dynamic biochemical signaling networks.* Science, 2014. **346**(6215): p. 1370-3.
286. Boulware, M.J. and J.S. Marchant, *Timing in cellular Ca2+ signaling.* Curr Biol, 2008. **18**(17): p. R769-r776.
287. Tomida, T., et al., *NFAT functions as a working memory of Ca2+ signals in decoding Ca2+ oscillation.* Embo Journal, 2003. **22**(15): p. 3825-3832.
288. Shibasaki, F., et al., *Role of kinases and the phosphatase calcineurin in the nuclear shuttling of transcription factor NF-AT4.* Nature, 1996. **382**(6589): p. 370-3.
289. Richard, M. and G. Yvert, *How does evolution tune biological noise?* Front Genet, 2014. **5**.
290. Bongarzone, E.R., J.M. Pasquini, and E.F. Soto, *Oxidative damage to proteins and lipids of CNS myelin produced by in vitro generated reactive oxygen species.* J Neurosci Res, 1995. **41**(2): p. 213-21.
291. Gutteridge, J.M. and B. Halliwell, *Antioxidants: Molecules, medicines, and myths.* Biochem Biophys Res Commun, 2010. **393**(4): p. 561-4.
292. Gutteridge, J.M. and B. Halliwell, *Free radicals and antioxidants in the year 2000. A historical look to the future.* Ann N Y Acad Sci, 2000. **899**: p. 136-47.
293. Halliwell, B., J.M. Gutteridge, and C.E. Cross, *Free radicals, antioxidants, and human disease: where are we now?* J Lab Clin Med, 1992. **119**(6): p. 598-620.
294. Fleury, C., B. Mignotte, and J.L. Vayssiere, *Mitochondrial reactive oxygen species in cell death signaling.* Biochimie, 2002. **84**(2-3): p. 131-41.
295. Ueda, S., et al., *Redox control of cell death.* Antioxid Redox Signal, 2002. **4**(3): p. 405-14.
296. Brookes, P. and V.M. Darley-Usmar, *Hypothesis: the mitochondrial NO(*) signaling pathway, and the transduction of nitrosative to oxidative cell signals: an alternative function for cytochrome C oxidase.* Free Radic Biol Med, 2002. **32**(4): p. 370-4.
297. St-Pierre, J., et al., *Topology of superoxide production from different sites in the mitochondrial electron transport chain.* J Biol Chem, 2002. **277**(47): p. 44784-90.

298. Turrens, J.F., *Mitochondrial formation of reactive oxygen species.* J Physiol, 2003. **552**(Pt 2): p. 335-44.
299. Muller, F.L., et al., *Architecture of the Qo site of the cytochrome bc1 complex probed by superoxide production.* Biochemistry, 2003. **42**(21): p. 6493-9.
300. Starkov, A.A. and G. Fiskum, *Regulation of brain mitochondrial H2O2 production by membrane potential and NAD(P)H redox state.* J Neurochem, 2003. **86**(5): p. 1101-7.
301. Gunter, T.E., et al., *Mitochondrial calcium transport: mechanisms and functions.* Cell Calcium, 2000. **28**(5-6): p. 285-96.
302. Gunter, T.E., et al., *Mitochondrial calcium transport: physiological and pathological relevance.* Am J Physiol, 1994. **267**(2 Pt 1): p. C313-39.
303. Sparagna, G.C., et al., *Mitochondrial calcium uptake from physiological-type pulses of calcium. A description of the rapid uptake mode.* J Biol Chem, 1995. **270**(46): p. 27510-5.
304. Balaban, R.S., *Cardiac energy metabolism homeostasis: role of cytosolic calcium.* J Mol Cell Cardiol, 2002. **34**(10): p. 1259-71.
305. Das, A.M. and D.A. Harris, *Control of mitochondrial ATP synthase in heart cells: inactive to active transitions caused by beating or positive inotropic agents.* Cardiovasc Res, 1990. **24**(5): p. 411-7.
306. Das, A.M. and D.A. Harris, *Regulation of the mitochondrial ATP synthase in intact rat cardiomyocytes.* Biochem J, 1990. **266**(2): p. 355-61.
307. Hansford, R.G. and D. Zorov, *Role of mitochondrial calcium transport in the control of substrate oxidation.* Mol Cell Biochem, 1998. **184**(1-2): p. 359-69.
308. Griffiths, E.J. and G.A. Rutter, *Mitochondrial calcium as a key regulator of mitochondrial ATP production in mammalian cells.* Biochim Biophys Acta, 2009. **1787**(11): p. 1324-33.
309. McCormack, J.G. and R.M. Denton, *Mitochondrial Ca2+ transport and the role of intramitochondrial Ca2+ in the regulation of energy metabolism.* Dev Neurosci, 1993. **15**(3-5): p. 165-73.
310. Mildaziene, V., et al., *Calcium indirectly increases the control exerted by the adenine nucleotide translocator over 2-oxoglutarate oxidation in rat heart mitochondria.* Arch Biochem Biophys, 1995. **324**(1): p. 130-4.
311. Mildaziene, V., et al., *Ca2+ stimulates both the respiratory and phosphorylation subsystems in rat heart mitochondria.* Biochem J, 1996. **320 (Pt 1)**: p. 329-34.
312. Glancy, B. and R.S. Balaban, *Role of Mitochondrial Ca2+ in the Regulation of Cellular Energetics.* Biochemistry, 2012. **51**(14): p. 2959-2973.
313. Haworth, R.A. and D.R. Hunter, *The Ca2+-induced membrane transition in mitochondria. II. Nature of the Ca2+ trigger site.* Arch Biochem Biophys, 1979. **195**(2): p. 460-7.
314. Hunter, D.R. and R.A. Haworth, *The Ca2+-induced membrane transition in mitochondria. I. The protective mechanisms.* Arch Biochem Biophys, 1979. **195**(2): p. 453-9.
315. Hunter, D.R. and R.A. Haworth, *The Ca2+-induced membrane transition in mitochondria. III. Transitional Ca2+ release.* Arch Biochem Biophys, 1979. **195**(2): p. 468-77.

316. Bereiter-Hahn, J., *Behavior of mitochondria in the living cell.* Int Rev Cytol, 1990. **122**: p. 1-63.
317. Bereiter-Hahn, J. and M. Voth, *Dynamics of mitochondria in living cells: shape changes, dislocations, fusion, and fission of mitochondria.* Microsc Res Tech, 1994. **27**(3): p. 198-219.
318. Perez-Campo, R., et al., *The rate of free radical production as a determinant of the rate of aging: evidence from the comparative approach.* J Comp Physiol B, 1998. **168**(3): p. 149-58.
319. Sohal, R.S. and R.G. Allen, *Relationship between metabolic rate, free radicals, differentiation and aging: a unified theory.* Basic Life Sci, 1985. **35**: p. 75-104.
320. Cadenas, E. and A. Boveris, *Enhancement of hydrogen peroxide formation by protophores and ionophores in antimycin-supplemented mitochondria.* Biochem J, 1980. **188**(1): p. 31-7.
321. De Grey, A.D., *HO2*: the forgotten radical.* DNA Cell Biol, 2002. **21**(4): p. 251-7.
322. Sousa, S.C., et al., *Ca2+-induced oxidative stress in brain mitochondria treated with the respiratory chain inhibitor rotenone.* FEBS Lett, 2003. **543**(1-3): p. 179-83.
323. Starkov, A.A., B.M. Polster, and G. Fiskum, *Regulation of hydrogen peroxide production by brain mitochondria by calcium and Bax.* J Neurochem, 2002. **83**(1): p. 220-8.
324. Sumit, M., et al., *Band-pass processing in a GPCR signaling pathway selects for NFAT transcription factor activation.* Integr Biol (Camb), 2015. **7**(11): p. 1378-86.
325. Zweifach, A. and R.S. Lewis, *Mitogen-regulated Ca2+ current of T lymphocytes is activated by depletion of intracellular Ca2+ stores.* Proc Natl Acad Sci U S A, 1993. **90**(13): p. 6295-9.
326. Kaufmann, B.B. and A. van Oudenaarden, *Stochastic gene expression: from single molecules to the proteome.* Curr Opin Genet Dev, 2007. **17**(2): p. 107-12.
327. Larson, D.R., R.H. Singer, and D. Zenklusen, *A single molecule view of gene expression.* Trends Cell Biol, 2009. **19**(11): p. 630-7.
328. Citri, A., et al., *Comprehensive qPCR profiling of gene expression in single neuronal cells.* Nat Protoc, 2012. **7**(1): p. 118-27.
329. Raj, A., et al., *Imaging individual mRNA molecules using multiple singly labeled probes.* Nat Methods, 2008. **5**(10): p. 877-9.
330. Kvanta, A., et al., *Mitogen stimulation of T-cells increases c-Fos and c-Jun protein levels, AP-1 binding and AP-1 transcriptional activity.* Cell Signal, 1992. **4**(3): p. 275-86.
331. Macian, F., C. Lopez-Rodriguez, and A. Rao, *Partners in transcription: NFAT and AP-1.* Oncogene, 2001. **20**(19): p. 2476-89.
332. Denys, A., et al., *Thapsigargin-stimulated MAP kinase phosphorylation via CRAC channels and PLD activation: inhibitory action of docosahexaenoic acid.* FEBS Letters, 2004. **564**(1–2): p. 177-182.
333. Macian, F., *NFAT proteins: key regulators of T-cell development and function.* Nat Rev Immunol, 2005. **5**(6): p. 472-484.

334. Oancea, E. and T. Meyer, *Protein kinase C as a molecular machine for decoding calcium and diacylglycerol signals.* Cell, 1998. **95**(3): p. 307-18.
335. Rao, A., C. Luo, and P.G. Hogan, *Transcription factors of the NFAT family: regulation and function.* Annu Rev Immunol, 1997. **15**: p. 707-47.
336. Doedens, A.L., et al., *Hypoxia-inducible factors enhance the effector responses of CD8(+) T cells to persistent antigen.* Nat Immunol, 2013. **14**(11): p. 1173-82.
337. Semenza, G.L., *HIF-1 and human disease: one highly involved factor.* Genes Dev, 2000. **14**(16): p. 1983-91.
338. Nakamura, H., et al., *TCR engagement increases hypoxia-inducible factor-1 alpha protein synthesis via rapamycin-sensitive pathway under hypoxic conditions in human peripheral T cells.* J Immunol, 2005. **174**(12): p. 7592-9.
339. Mueller, F., et al., *FISH-quant: automatic counting of transcripts in 3D FISH images.* Nat Methods, 2013. **10**(4): p. 277-8.
340. Mishina, N.M., et al., *Visualization of intracellular hydrogen peroxide with HyPer, a genetically encoded fluorescent probe.* Methods Enzymol, 2013. **526**: p. 45-59.
341. Mishina, N.M., et al., *Imaging H2O2 microdomains in receptor tyrosine kinases signaling.* Methods Enzymol, 2013. **526**: p. 175-87.
342. Rota, C., C.F. Chignell, and R.P. Mason, *Evidence for free radical formation during the oxidation of 2'-7'-dichlorofluorescin to the fluorescent dye 2'-7'-dichlorofluorescein by horseradish peroxidase: possible implications for oxidative stress measurements.* Free Radic Biol Med, 1999. **27**(7-8): p. 873-81.
343. Luik, R.M., et al., *The elementary unit of store-operated Ca2+ entry: local activation of CRAC channels by STIM1 at ER-plasma membrane junctions.* J Cell Biol, 2006. **174**(6): p. 815-25.
344. Brandman, O., et al., *STIM2 is a feedback regulator that stabilizes basal cytosolic and endoplasmic reticulum Ca2+ levels.* Cell, 2007. **131**(7): p. 1327-39.
345. Bradshaw, J.M., et al., *An ultrasensitive Ca2+/calmodulin-dependent protein kinase II-protein phosphatase 1 switch facilitates specificity in postsynaptic calcium signaling.* Proc Natl Acad Sci U S A, 2003. **100**(18): p. 10512-7.
346. Bahar Halpern, K. and S. Itzkovitz, *Single molecule approaches for quantifying transcription and degradation rates in intact mammalian tissues.* Methods, 2015.